



Orgill, Jonathan (2021) *Investigating surface acoustic waves and fluorescence techniques for lab-on-a-chip diagnostics*. PhD thesis.

<http://theses.gla.ac.uk/81933/>

Copyright and moral rights for this work are retained by the author

A copy can be downloaded for personal non-commercial research or study, without prior permission or charge

This work cannot be reproduced or quoted extensively from without first obtaining permission in writing from the author

The content must not be changed in any way or sold commercially in any format or medium without the formal permission of the author

When referring to this work, full bibliographic details including the author, title, awarding institution and date of the thesis must be given

Enlighten: Theses

<https://theses.gla.ac.uk/>
research-enlighten@glasgow.ac.uk



University
of Glasgow

Investigating Surface Acoustic Waves
and Fluorescence Techniques for Lab-
On-A-Chip Diagnostics

Jonathan Marc Orgill

MSc Biotechnology, BSc (Hons) Biochemistry

Submitted in fulfilment of the requirements for the
Degree of Doctor of Philosophy

Division of Biomedical Engineering
School of Engineering
College of Science and Engineering
University of Glasgow

January 2021

Abstract

There is an emerging need for low-cost medical diagnostics for both high and middle to low-resource settings. Surface acoustic waves microfluidics are emerging lab-on-a-chip technologies which have the potential to provide all-in-one solution to actuate liquids and sense biomarkers, thus enabling point-of-care bioassays. DNA has become a key biomarker for a range of medical conditions, including infectious diseases, as it provides critical information on the pathogen or the response of the patients to particular treatment, on a personalized basis.

This thesis will examine the effects of surface acoustic waves on DNA hybridization, with a view to integrate molecular diagnostic assays onto acousto-fluidic devices. The work used fluorescence to characterize the binding of DNA in a range of conditions, and revealed nucleobase-specific quenching (NB-S Quench) of fluorophores when attached to DNA as a double strand. This latter effect was examined as a replacement for common analytical markers used in standard techniques, such as melting curves, which typically rely on dyes which recognize DNA strands non-specifically (such as groove binders). The technique has been shown to be suitable for determine the concentration of DNA, performing DNA amplification and identifying the presence and melting temperature of target DNA.

This work will have an impact on research into low-cost medical diagnostics, and improve the understanding of fluorescence of DNA modified with fluorophores, contributing to the understanding of future work in these areas.

Contents

Abstract	1
List of Tables	7
List of Figures	9
Acknowledgements	24
Authors declaration	25
Commonly used abbreviations	26
1. Background, Introduction to Point-of-Care Diagnostics	27
1.1.DNA	28
1.1.1. Thermodynamics of DNA binding	29
Nearest Neighbour Model	29
1.1.2. DNA Melting	30
1.1.3. DNA Annealing	31
1.1.4. Selected Secondary Structures of DNA	31
1.1.4.1. Model of DNA loop.....	31
1.1.4.2. G-Quadruplex Structures	32
1.2.Polymerase Chain Reaction (PCR)	33
1.2.1. Loop-Mediated Isothermal Amplification (LAMP)	35
1.3.Surface Acoustic Waves (SAW)	37
1.3.1. Modelling of Streaming Within a Droplet	39
1.3.2. Detection Methods for Surface Acoustic Waves (SAW).....	40
1.4.Fluorescence.....	42
1.4.1. Förster / Fluorescence Resonance Energy Transfer (FRET)	43
1.4.2. Total Internal Reflection (TIRF) Microscopy	46
1.4.3 Quenching of Fluorophores	48
1.5.Lab-On-A-Chip (LOC)	49
1.5.1. Microfluidics	49
1.5.2 DNA Microarrays for Diagnostics and Research	49

1.6.Aims and Objectives	50
2. Materials and Methods	52
2.1.Materials.....	53
2.2Buffers and Reagents	54
2.3.DNA	55
2.4.Equipment	60
2.5.Methods.....	61
2.5.1. Microfabrication of IDTs, RTDs and Microfluidic Devices.....	61
2.5.1.1. Interdigitated Transducers (IDTs).....	61
2.5.1.2 Surface Acoustic Waves (SAW)	62
2.5.1.3. Resistance Temperature Devices (RTDs) Design and Fabrication	63
2.5.1.4. RTD Calibration	64
2.5.1.5. Microfluidic Devices	65
2.5.2. Surface Patterning Chemistry	68
2.5.2.1. Hydrophobic and Hydrophilic Surface Patterning	68
2.5.2.2. DNA Attachment Chemistry	70
2.5.3. DNA design, melt curves, amplification.....	72
2.5.3.1. DNA design.....	72
2.5.3.2. Software Predicted DNA Melt Curves	72
2.5.3.3. Measured DNA Melt Curves.....	73
2.5.3.4. OriginPro Curve Fitting of Measured Melt Curves	73
2.5.4 DNA Amplification.....	74
2.5.4.1. PCR	74
2.5.4.2. LAMP	74
2.5.5. Fluorescence and Absorbance.....	75
2.5.5.1. Fluorescence Microscopy.....	75
2.5.5.2. Absorbance	75
2.5.6. LabVIEW Automation.....	76
2.5.6. Modelling of Binding Fluorescence and Melt Curves in OriginPro	79

2.6 Results	79
2.6.1. Microfabrication of IDTs, RTDs and Microfluidic Devices.....	79
2.6.1.1 Interdigitated Transducers (IDTs).....	79
2.6.1.2. Resistance Temperature Device (RTDs) design and fabrication	80
2.6.1.3. RTD Calibration	82
2.6.2. Surface Patterning Chemistry	83
2.6.2.1 Hydrophobic and Hydrophilic Surface Patterning	83
2.6.2.1. DNA Attachment Chemistry	86
2.6.3. Software Predicted DNA Melt Curves.....	86
2.6.4 ABI 7500 Fast PCR Machine Controls.....	88
2.6.5. Photostability of EvaGreen	89
Discussion	90
3. DNA Melting and Annealing with Surface Acoustic Waves.....	91
3.1.Introduction	92
3.2.Results	95
3.2.1 Simulated Melt Curves.....	95
3.2.1. Varying pH.....	97
3.2.2. Peltier Module.....	100
3.2.2.1. Controls.....	100
3.2.2.2. Multiplex	101
3.2.3. Surface Acoustic Waves	101
Detailed melt curve analysis	103
3.2.4. Summary - Comparison of all three methods	107
3.3.Discussion and Conclusion	109
3.4.Fluorescence Energy Resonance Transfer (FRET).....	110
3.4.1 Introduction	110
3.4.2. FRET Results	112
3.4.2.1 Controls.....	112
3.4.2.2 Results.....	113

3.4.3.	Discussion and Conclusion	115
4.	Characterisation of the Nucleobase-Specific Quenching effect (NB-S Quench)	117
4.2.	Comparison with Existing Methods.....	122
4.3.	Modelling of Binding Fluorescence and Melt Curves in OriginPro	123
4.4.	pH Stability	128
4.5.	Labelled Strand, Analysis of Nearest Base Effects on Fluorescence.....	129
Discussion	130
4.6.	Absorption Studies Introduction	133
Results and Discussion	134
4.7.	Complementary Strand Effects	137
4.7.1.	Completely Double-Stranded DNA.....	137
4.7.2.	Double-Stranded Adjacent to Fluorophore	139
Double-Stranded DNA Summary	141
4.7.3.	Single-Stranded Adjacent to Fluorophore.....	141
4.7.3.1.	3 Bases of Single-Stranded DNA, 1nm from Fluorophore	141
4.7.3.2.	3 Bases of Single-Stranded DNA consisting of T bases, 1nm from Fluorophore..	144
4.7.3.3.	6 Bases of Single-Stranded DNA, 2nm from Fluorophore	145
4.7.3.4.	9 Bases of Single-Stranded DNA, 3nm from Fluorophore	148
4.7.3.5.	12 Bases of Single-Stranded DNA, 4nm from Fluorophore	150
4.7.3.6.	Single-Stranded Adjacent to Fluorophore Summary.....	152
4.8.	Structural Similarities to Known Fluorophores	153
4.9.	Conclusion	156
Summary of Melt Curve Analysis for NB-S Quench Fluorescence.....		157
5.	Techniques Utilising the Nucleobase-Specific (NB-S) Quenching Effect	159
5.1.	Using the NB-S Quench Technique to Quantify DNA Concentration	160
5.1.1.	Quantifying Concentration of Labelled DNA using Alexa488 Fluorescence ...	160
5.1.1.1.	Results.....	161
5.1.1.2.	Discussion.....	161

5.1.3. Quantifying Concentration of Complementary Strand using Alexa488 Fluorescence and Melt Curve Analysis	162
5.1.2.1. Results.....	163
5.1.2.2. Discussion.....	166
5.1.3. Quantitative Polymerase Chain Reaction using Alexa488 fluorescence (qPCR)	167
5.1.3.1. Results.....	168
5.1.3.2. Discussion.....	168
5.2. Deriving Melting Temperatures of Partially Single-Stranded DNA.....	169
5.2.1. Results.....	170
5.2.2. Discussion.....	173
5.3. Multiplex Target Sequence Identification.....	174
5.4. DNA amplification using Alexa488 fluorescence	178
5.4.1. Polymerase Chain Reaction (PCR) using Alexa488.....	178
Results and Discussion	181
5.4.2. Loop-Mediated Isothermal Amplification (LAMP) using Alexa488	184
Results and Discussion	184
5.5.Incorporation of the Nucleobase-Specific Quenching Effect in a Reusable Microfluidic Lab-on-a-Chip Device	188
5.5.1. First Generation Microfluidic Device	189
5.5.2. Second Generation Microfluidic Device.....	191
5.6. Conclusion	192
6. Conclusion and Future Work	193
6.1. Surface Acoustic Waves and DNA	193
6.2. Further Characterisation of Alexa488 Fluorescence Effect.....	195
6.3. Conventional Protocols with the Photo-induced Electron Transfer Effect.....	197
6.4. Second and Third Generation Microfluidic Devices	199
7. References	201

List of Tables

Table 2-1 Sequences of designed DNA sequences A, B, C and D.....	55
Table 2-2 DNA used to quantify surface attachment chemistry	55
Table 2-3 Alexa488 and Alexa532-modified DNA used for FRET experiments in section 3.4.....	56
Table 2-4 DNA used for the Completely Double-Stranded DNA experiments in section 4.7.1.....	56
Table 2-5 DNA used for the Completely Double-Stranded Adjacent to Fluorophore experiments in section 4.7.2.....	56
Table 2-6 DNA used for Single-Stranded DNA Adjacent to the Fluorophore experiments in section 4.7.2.	57
Table 2-7 Combinations of DNA used for Single-Stranded DNA Adjacent to the Fluorophore experiments in section 4.7.2.....	57
Table 2-8 Modified BRAC1 sequences used in 5.1.3.....	58
Table 2-9 DNA used for experiments to derive the melting temperature of partially single-stranded DNA in section 5.2.....	58
Table 2-10 DNA used for Chapter 5 experiments, including BRAC1 primers	59
Table 2-11 Design parameters for fabricated IDTs, including frequency.	61
Table 2-12 Predicted melting temperature, GC content, length and estimated mass (GC+backbone = 680Da, AT+backbone = 670Da)	72
Table 3-1 uMelt predicted melting temperature, GC content, length and estimated mass (GC+backbone = 680Da, AT+backbone = 670Da) of DNA A, B, C and D.	93
Table 3-2 Comparison of DNA attributes (length, GC content, mass) and difference in melting temperatures (SAW-Peltier). Standard deviation is shown in brackets. 5 melt curves for 3 replicates were measured for each.	102

Table 3-3 ANOVA Tukey analysis of each method and sample. A low probability close to zero indicates that these are statistically separate samples, whilst a high number close to 1 indicates that they are statistically similar samples.....	108
Table 4-1 Length, GC content, nucleotide and peak comparison of Alexa488-labelled DNA	129
Table 4-2 Difference between melting temperatures derived using EvaGreen and Alexa488	132
Table 4-3 Sequences *of DNA oligonucleotides	138
Table 4-4 Melting points and standard deviation between measurements by DNA and method.....	138
Table 4-5 Structures of Alexa488, ATTO488 and FITC fluorophores. Alexa488- and ATTO488-labelled DNA B exhibited the NB-S Quench effect, allowing the melting temperature to be derived, whilst FITC did not.	155
Table 5-1 Linear correlation between the Alexa488 experiment (Figure 5-9), correlation reduces as the distance from the fluorophore increases.	172
Table 5-2 Second order polynomial correlation between the Alexa488 experiments (Figure 5-9), correlation reduces as the distance from the fluorophore increases.	172
Table 5-3 Difference in melting temperature with Alexa488 experiments with standard deviation between readings (averaged).....	172
Table 5-4 Peak attributes of Alexa488-LPR5F and Alexa488-LPF5R singularly and together for multiplex sequence identification. Analysis performed with OriginPro 2016 using averaged melt curves of data produced with an ABI7500.	178
Table 5-5 BRAC1 PCR primer combinations, product length, weight and melting temperature.....	179
Table 6-1 Example of sequences that could be used to investigate the effect of mismatches of the base closes to the Alexa488 fluorophore on the complementary strand.....	196

List of Figures

Figure 1-1: Hydrogen bonds between DNA bases A, T, G and C. Reproduced from [21]	29
Figure 1-2 Structure of EvaGreen intercalating between DNA strands [26].....	30
Figure 1-3 Model of a DNA hairpin loop showing double-stranded DNA where the sequence is complementary, and 15 base single-stranded loop mostly consisting of A base.	32
Figure 1-4 Illustration of DNA amplification by polymerase chain reaction (PCR) showing exponential DNA amplification [40]	34
Figure 1-5 Illustration of DNA amplification using loop-mediated isothermal amplification (LAMP). 6+ pairs of primers complementary to different regions of DNA, allowing displacement at a single temperature as DNA amplification progresses, forming large products containing multiple copies of the target sequences as well as the loop introduced in the primers. [41].....	36
Figure 1-6 COMSOL model of an IDT illustrating surface displacement of piezoelectric material (lithium niobate) due to surface acoustic waves at 8.5 Mhz. Note that this shows only a single point in time, which will change rapidly as the SAW propagates across the surface. The wave will dissipate as energy is transferred into the sample droplet (not simulated). Red shows pressure wave maxima, dark blue shows minima.....	37
Figure 1-7 Surface acoustic waves (SAW) propagating from an Interdigitated Transducer (IDT) along a substrate and into the droplet. At the interface of the substrate and the droplet some of the energy from the Rayleigh SAW wave as a longitudinal wave which will circulate the droplet. As the energy is transferred from the Rayleigh SAW into the droplet at which point it is termed a Leaky SAW which attenuates as energy is transferred into the sample droplet. Reproduced with permission from [49].....	38
Figure 1-8 A computer model of surface acoustic wave streaming within a 10µl water droplet due to longitudinal wave produced by SAW. Altered from [51] to add a black arrow showing the direction of the SAW wave from the IDT into the droplet that produced the streaming.	40

Figure 1-9 Jablonski diagram showing ground / HOMO (S0) and excited / LUMO (S1) states for electrons, illustrating the energy potentials during photon absorption and emission by a fluorophore.....	42
Figure 1-10 Illustration of FRET principle, highlighting the requirement of spectral overlap between the donor emission and the acceptor excitation (A) and the importance of distance (B). As can be seen in (B), if the fluorophores are far apart, then excitation of the donor fluorophore results in emission of the donor fluorophore, whereas when the fluorophores are close (<10nm) excitation of the donor fluorophore results in the emission of the acceptor fluorophore. By measuring the intensity of the emission in the region of the donor fluorophore and the acceptor fluorophore the efficiency can be calculated under the above conditions.[69]	45
Figure 1-11 A schematic drawing of the TIRF system, reproduced with permission from [117]. The micrometer determines the incident angle of the laser into the substrate to produce the evanescent wave. The refractive index of the immersion oil is matched to the refractive index of the substrate.	46
Figure 1-12 Relationship between the relative intensity of the evanescent wave against z/d which is the ratio of the distance from the interface to the penetration depth of the evanescent wave. At the interface, z/d is zero and the relative intensity is 1.	47
Figure 2-1 Figure showing IDT design parameters aperture (10000 μm), gap to contact pad (300 μm), contact pad (3000 μm), finger width (225 μm) and finger gap (225 μm).	61
Figure 2-2 Mask design for resistance temperature device (RTD). The width of the smallest feature is 100 μm . This mask was used during photolithography, the coloured area remains clear from resist allowing metal (10nm titanium, 100nm platinum) to be deposited	63
Figure 2-3 Figure showing the construction of the First Generation microfluidic device (image modified with permission from Ibidi).	65
Figure 2-4 Illustration of the design of the Second Generation microfluidic device showing the inflow connection (1), the outflow (2), and the 1cm ² reaction chamber shown by a dotted line.....	67
Figure 2-5 Chemical structure of PFOTS silane 1H,1H,2H,2H-Perfluorooctyl-trichlorosilane (reproduced from MERCK, UK). The trichloro binds the molecule to glass	

and lithium niobate, whilst the 13 fluorine molecules are exposed above, creating a highly hydrophobic environment.68

Figure 2-6 Chemical structure of APTES silane (3-Aminopropyl) triethoxysilane (reproduced from MERCK, UK). The triethoxy binds the molecule to glass and lithium niobate whilst the amino group is exposed creating a highly hydrophilic environment. The amino group is also used for DNA attachment via the Sulfo-SMCC linker molecule (see section 2.5.2.2)68

Figure 2-7 DNA attachment using Sulfo-SMCC sulfosuccinimidyl 4-(N-maleimidomethyl)cyclohexane-1-carboxylate (ThermoFisher, Cambridge, UK) and APTES (3-Aminopropyl)triethoxysilane (MERCK, UK). Step 1 is to bind the APTES to the substrate (glass or LiNbO₃). Step 2 joins the Sulfo-SMCC to the APTES/surface. Step 3 binds the thiolated DNA.71

Figure 2-8 Interface of the LabView software written to automate the calibration and experiments for this thesis. The RTD resistance and Thermocouple Temperature are used for calibration, once this is achieved the calibration can be set (“Gradient” and “minus”) so that for experiments the RTD Temperature is automatically calculated. These variables are combined with the fluorescence variables and saved as a spreadsheet file.76

Figure 2-9 Resistance from the RTD is saved as a variable, processed with the calibration data (“Resistance” and “minus”), so that the RTD temperature is available on the interface. This is also exported to the spreadsheet.77

Figure 2-10 Portion of the NI Vision Builder visual inspection loop, showing extraction per frame of the total fluorescence (Total Intensity), minimum pixel values (Min), maximum pixel value (Max) and the Standard Variation.78

Figure 2-11 LabView program subroutine showing collation of variables and export to a spreadsheet for further analysis.....78

Figure 2-12 Frequency response of a fabricated IDT extracted using an Agilent Technologies E5071C ENA series network analyser. The graph shows the 4.4 MHz frequency the IDT was designed for, and the resonant frequency ~12Mhz that was used for SAW.....79

Figure 2-13 Gold IDT fabricated onto LiNbO₃. Early training used gold for the metallisation step, although for this thesis all IDTs used were platinum as the intention would be to fabricate both the IDT and RTD in a single step as in Figure 2-14.80

Figure 2-14 Platinum RTD and IDT fabricated onto LiNbO₃. The IDT and RTD were patterned together using a single S1818 photolithography step by combining the RTD designs and IDT design onto a single mask. Metallisation occurred in a single step, with both the RTD and IDT produced with 10nm of titanium and then 100nm of platinum.80

Figure 2-15 Resistance variation of fabricated Pt100 RTDs at 25°C. RTDs were fabricated using photolithography and 10nm of titanium and 100nm of platinum deposited. Resistance was measured using National Instruments USB-4065 Digital Multimeter.....81

Figure 2-16 Pt100 RTD fabricated on a microscope coverslip.....81

Figure 2-17 Pt100 RTD fabricated on a microscope coverslip with 3mm diameter circle of S1818 over the tip of the RTD. The RTD was patterned with photolithography, metallised (10nm Ti, 100nm Pt) then silanised with APTES. S1818 was patterned to protect the APTES to constrain sample droplet and allow DNA attachment.81

Figure 2-18 Slow (A) and Quick Cool (B) calibration methods showing experimental data (black squares) and extrapolated linear fit (black dashed line). Experiments were performed in 20µl of mineral oil using the Peltier and thermocouple/RTD setup described previously. Linear fit performed with OriginPro. Pearson’s R of Slow Calibration is 0.999, Quick Cool is 0.995.82

Figure 2-19 Comparison of calibration strategies showing alignment of the two calibration methods, “Slow” (black) and Quick Cool (red).83

Figure 2-20 Comparing the hydrophobicity of glass and LiNBO₃ with and without PFOTS silanisation. Images of 1ul water droplets taken using Kruss Easydrop DSA25 (Hamburg, Germany) and contact angles analysed using FIJI DropSnake. 6 measurements were taken for each, error bars show standard deviation. T-tests determined that the silanised substrates were significantly different, Glass P=6E-06, Lithium Niobate P=1E-06. P<0.001 shown by ***.84

Figure 2-21 Comparison of hydrophobicity of non-silanised glass (A), non-silanised LiNbO₃ (B), silanised glass (C) and silanised LiNbO₃ (D) substrates. Images of 1µl RO

water droplets taken using Kruss Easydrop DSA25 (Hamburg, Germany) and contact angles analysed using FIJI DropSnake.	85
Figure 2-22 Relative fluorescence of the DNA attached to the surface with APTES and Sulfo-SMCC (Sample) compared to an unsilanised control (Background). Fluorescence measured in the Cy5 channel. $P=2E-13$, shown by ***.....	86
Figure 2-23 Melt curves of DNA oligonucleotides A (red), B (yellow), C (green) and D (blue) simulated using uMelt.	86
Figure 2-24 Melting curves of DNA A (A) and D (B) predicted using uMelt (University of Utah, v2.0.2) software based on sequence with varying monovalent cation concentrations, (left to right) 10mM, 20mM, 50mM, 100mM and 200mM. Calculations used Weber (Bioinformatics, 2015) thermodynamic set, varying (10mM-200mM) monovalent cation concentration, 3mM Mg^{2+} concentration, 0% DMSO and Owczarzy (2008) salt correction. Datasets visualised using OriginPro. Note that the melting temperature T_m is defined as the point where 50% has melted.	87
Figure 2-25 Melting temperatures of 20 replicates of 10 μ l of 10 μ M DNA A (red), B(yellow), C(green) and D(purple) in Tris EDTA pH 7.8 buffer derived on ABI 7500 using EvaGreen as a reporter molecule. Error bars show standard deviation. $P<0.001$ shown by ***.....	88
Figure 2-26 – ANOVA analysis performed using OriginPro differentiated all 4 DNA samples.....	88
Figure 2-27 Photobleaching of EvaGreen at maximum laser intensity. Absolute fluorescence is shown in black, temperature is shown in red. High laser intensity causes rapid photobleaching of EvaGreen. 2 μ l of DNA and 0.5 μ l EvaGreen in TE buffer, within 20 μ l mineral oil droplet at room temperature	89
Figure 2-28 Photostability of Eva-Green over 20 minutes, performed with 2 μ l of DNA and 0.5 μ l of EvaGreen in TE buffer, within a 20 μ l mineral oil droplet measured at room temperature.....	90
Figure 3-1 Melt curves of DNA A (red), B (yellow), C (green) and D (purple) simulated using uMelt (University of Utah, v2.0.2) software based on sequence.	95

Figure 3-2 Melting temperature of DNA A (red), B (yellow), C (green) and D (purple) simulated using uMelt (University of Utah, v2.0.2) software based on sequence.....96

Figure 3-3 Melting curves of DNA A oligonucleotides predicted using uMelt (University of Utah, v2.0.2) software based on sequence with varying monovalent cation concentrations - left to right, 10mM, 20mM, 50mM, 100mM and 200mM. Calculations used Weber (Bioinformatics, 2015) thermodynamic set, varying (10mM-200mM) monovalent cation concentration, 3mM Mg²⁺ concentration, 0% DMSO and Owczarzy (2008) salt correction. Datasets visualised using OriginPro. Note that the melting temperature T_m is defined as the point where 50% has melted.....97

Figure 3-4 Melting curves of DNA A (green) and D oligonucleotides (purple) predicted using uMelt (University of Utah, v2.0.2) software based on sequence with varying monovalent cation concentrations - left to right, 10mM, 20mM, 50mM, 100mM and 200mM. The change from 10mM to 100mM is the equivalent of increasing pH from 1.0 to 2.0. Calculations used Weber (Bioinformatics, 2015) thermodynamic set, varying (10mM-200mM) monovalent cation concentration, 3mM Mg²⁺ concentration, 0% DMSO and Owczarzy (2008) salt correction. Datasets visualised using OriginPro. Note that the melting temperature T_m is defined as the point where 50% has melted.98

Figure 3-5 Melting temperatures of DNA C (green triangles) and D (purple circles) in varying Tris EDTA buffer pH derived with EvaGreen. 10µl of 10µM double-stranded DNA, melting temperatures measured in 7500 FAST QPCR machine (25-95°C). Higher pH results in a lower melting temperature, due to salt and buffer interactions with the DNA.99

Figure 3-6 Melting temperatures of 20 replicates of 1µl of 10µM DNA A (red), B (yellow), C (green) and D (purple) in Tris EDTA pH7.8 buffer. Samples were heated using a Peltier module under the fluorescence microscope. Temperatures were measured using a calibrated Pt100 RTD. Error bars show standard deviation. P<0.001 shown by ***100

Figure 3-7 Melting temperature using SAW. Melting temperatures of 10µl of 10µM DNA A (red), B (yellow), C (green) and D (purple) in Tris EDTA pH7.8 buffer. Samples were heated using SAW – 23MHz, -2dBm using the IDT previously discussed. Temperature was measured with a calibrated Pt100 RTD. P<0.001 shown by ***.102

Figure 3-8 Melt (A) and Anneal (B) curves of DNA A in pH7.8 Tris EDTA buffer heated with SAW – 23MHz, -2dBm. Graphs show experimental data (black squares),

Origin2016 fitted sigmoidal curve (red line), derivative (blue), and melting point. Experiment was carried out on the fluorescence microscope, with temperature measured using a calibrated Pt100 RTD.104

Figure 3-9 Melt (A) and Anneal (B) curves of DNA B in pH7.8 Tris EDTA buffer heated with SAW – 23MHz, -2dBm. Graphs show experimental data (black squares), origin 2016 fitted sigmoidal curve (red line), derivative (blue), and melting point. Experiment was carried out on the fluorescence microscope, with temperature measured using a calibrated Pt100 RTD.....105

Figure 3-10 Changes in melting (orange circles) and annealing (blue squares) temperatures over 10 experimental cycles of DNA B (A) and D (B) in pH7.8 Tris EDTA buffer heated with SAW – 23MHz, -2dBm. Experiment was carried out on the fluorescence microscope, with temperature measured using a calibrated Pt100 RTD. Each anneal point follows on from the corresponding melt cycle.....106

Figure 3-11 Comparison of melting temperatures measured of DNA A (red), B (yellow), C (green) and D (purple) in pH7.8 Tris EDTA buffer. The controls labelled PCR were measured in an ABI 7500 FAST PCR (solid colour). The source of heating for SAW was SAW actuated at 23MHz -2dBm (diagonal lines), or Peltier module (horizontal lines). * for $P < 0.05$, ** for $P < 0.01$, *** $P < 0.001$, the rest have no significant difference.....107

Figure 3-12 Comparison of Annealing Temperatures of DNA A (red), B (yellow), C (green) and D (purple) in pH7.8 Tris EDTA buffer after being heated to 95°C with the Peltier module (horizontal lines) or SAW (diagonal lines) 23MHz, -2dBm. T-test showed no significant difference within groups, and $P < 0.001$ between (showed by ***).109

Figure 3-13 Comparison of emission spectra of EvaGreen (solid green) and Alexa488 (solid blue) with the excitation spectra of Alexa532 (dotted yellow). Image from SpectraViewer, ThermoFisher. This shows the similarity in emission between the potential FRET donor fluorophores Alexa488 and EvaGreen, and the match with the excitation of the FRET acceptor Alexa532.111

Figure 3-14 Predicted FRET spectra, when the acceptor and donor fluorophores are close together (1-10nm), SpectraViewer (Thermo Fisher). Fluorescence is shown in solid lines and shaded, Alexa488 (green) and Alexa532 (yellow). Dotted lines show absorption spectra, Alexa488 (green) and Alexa532 (yellow). 488nm laser is shown as a solid blue line, 565±18nm filter is shown in yellow.112

Figure 3-15 Absolute fluorescence of Alexa488 and Alexa532 when excited at 488nm, fluorescence for the Alexa488 experiments was measured with the 525±20nm filter whilst the Alexa532 experiments were measured with the 565±18nm emission filter. The “No FRET” experiments included only the named fluorophore; the FRET experiments had both fluorophores, but fluorescence was only measured with the appropriate named emission filter. T-test P<0.001 shown as ***. 113

Figure 3-16 Melting and annealing temperatures of DNA C derived using the appearance of the Alexa488 fluorescence (green) and disappearance of the Alexa532 fluorescence (yellow). The EvaGreen controls are included (blue). Experiment was carried out on the fluorescence microscope, heating supplied by the Peltier module, and temperature measured using a calibrated Pt100 RTD. * shows P<0.05, ** P<0.01, *** P<0.001, the rest showed no significant difference..... 114

Figure 4-1 Green fluorescence of Alexa488 and Alexa532 (yellow fluorescence not shown) FRET experiments normalised between maximum and minimum. Green Square – Alexa488 Fluorophores on opposite ends of DNA A, fluorescence signal similar to EvaGreen. Red Circle – Alexa488 Fluorophores on adjacent ends of DNA A, showing recovery of green signal / alleviation of FRET when DNA melts increasing distance from Alexa532 118

Figure 4-2 Green fluorescence of single-stranded (black squares), and double-stranded (green circles) Alexa-488 labelled DNA C, normalised to maximum of double-stranded fluorescence. Experiments performed on Zeiss upright microscope using EvaGreen filters. Absolute fluorescence from 70-95°C were within experimental variation..... 119

Figure 4-3 (A) Fluorescence of Alexa488 decreases when the DNA is single-stranded. (B) This effect is seen when the fluorophore is attached to the 5’ and 3’ end of the DNA strand. 120

Figure 4-4 Melting points derived using Alexa488 method and EvaGreen controls for DNA C (green) and D (purple). Average of 20 10µl replicates of 10µM DNA in 7.8pH TE buffer measured in Applied Biosciences 7500 PCR Machine. EvaGreen experiments used 1µl of 20x EvaGreen per reaction. * shows P<0.05, ** P<0.01, *** P<0.001, the rest showed no significant difference. 122

Figure 4-5 OriginPro model of G/A quenching adjacent to the fluorophore. The double-stranded model shows higher fluorescence as single-stranded quenching is relieved when

G/A bases are bound to their complements. Black shows the single-stranded model, red shows the average of one single-strand and one double-stranded model, blue shows the average of one single-strand with two double-stranded models, purple shows the average of one single-strand and ten double-stranded model, and green shows the average of one single-strand and one hundred double-stranded model.....124

Figure 4-6 (A) Pictogram showing that Alexa488 fluorescence is reduced when DNA is single-stranded. The higher quenching (A/G) base is on the same strand adjacent to the fluorophore. Fluorescence is relatively higher when the DNA is double-stranded as the A/G base interacts with its complement base.125

Figure 4-7 OriginPro model of G/A quenching on the opposite strand. The single-stranded model shows higher fluorescence as quenching is relieved when G/A bases on the complement strand are not bound. Black shows the single-stranded model, red shows the average of one single-strand and one double-stranded model, blue shows the average of one single-strand with two double-stranded model, purple shows the average of one single-strand and ten double-stranded model, and green shows the average of one single-strand and one hundred double-stranded model.126

Figure 4-8 (A) Pictogram showing that Alexa488 fluorescence is reduced when DNA is double-stranded. The higher quenching base (A/G) is on the complement strand, and interacts with the fluorophore and its complement adjacent to the fluorophore. Fluorescence is relatively higher when the DNA is single-stranded, and the fluorophore only interacts with the weaker quenching base adjacent (T/C).....127

Figure 4-9 Measuring the effects of TE buffer pH on the melting temperature of DNA B (blue) and C (green) using Alexa488 (diamond, triangle) or EvaGreen (square, circle) as a reporter molecule. The linear best fit for Alexa488-derived melting temperatures is shown with a solid line, the linear best fit line for EvaGreen-derived melting temperatures is shown in a dashed line. Average of 10 replicates of 10µl of 10µM DNA in TE buffer. EvaGreen experiments used 1µl of 20x EvaGreen per reaction. Melt curves were measured and analysed using Applied Biosciences 7500 PCR Machine.....128

Figure 4-10 Comparison of melting temperatures of the DNA used to analyse the nearest base effect on the fluorescence. Melting temperatures were derived using the Alexa488 method (blue) and EvaGreen as a control (orange). Average of 10 10µl replicates of 10µM DNA in 7.8pH TE buffer measured in Applied Biosciences 7500 PCR Machine. EvaGreen

experiments used 1µl of 20x EvaGreen per reaction. * shows P<0.05, ** P<0.01, *** P<0.001, the rest showed no significant difference.	129
Figure 4-11 Sequence, fluorophore binding position and EvaGreen derived melting temperature of BRCA1 LAMP DNA oligonucleotides.	130
Figure 4-12 Comparison of GC content (%) and the difference in melting temperature (°C), statistical analysis found no strong correlation.	131
Figure 4-13 Comparison of DNA length (bases) and the difference in melting temperature (°C), statistical analysis found no strong correlation.	131
Figure 4-14 EvaGreen absorption in varying amounts of DNA, reproduced from [14]....	133
Figure 4-15 Averaged absorbance spectra of 1M F3(A) and BIP(B). Single-stranded DNA is shown with black squares, double-stranded DNA is shown with red diamonds. 10µl of 10 µM DNA were prepared in 7.8pH Tris-EDTA buffer and absorbance measured in 1nm steps from 400-600nm (5 replicates of 1µl) using a BioTek Absorbance Reader. Readings were calibrated relative to 400nm and averaged with OriginPro(2016).....	135
Figure 4-16 (A,C) Red shows double-stranded DNA, black shows single-stranded DNA.	136
Figure 4-17 Melting temperatures of completely double-stranded DNA derived using EvaGreen or Alexa488 as a reporter molecule. Averages of 10 replicates of 10µM DNA in 7.8pH Tris-EDTA buffer, measured in Applied Biosciences 7500 PCR Machine. EvaGreen experiments used 1µl of 20x EvaGreen and unlabelled DNA oligonucleotides. * shows P<0.05, ** P<0.01, *** P<0.001, the rest showed no significant difference.	138
Figure 4-18 Sequence (A) and melting temperatures (B) of DNA that is double-stranded adjacent to the fluorophore derived using EvaGreen (green) or Alexa488 (blue) as a reporter molecule. Averages of 10 replicates of 10µM DNA in 7.8pH Tris-EDTA buffer, measured in ABI 7500. EvaGreen experiments used 1µl of 20x EvaGreen and unlabelled oligonucleotides. * shows P<0.05, ** P<0.01, *** P<0.001, the rest showed no significant difference.	139
Figure 4-19 (A) Example derivative curve from Experiment 1 and (B) Experiment 2 showing a melt peak at 58°C (A) and 50°C (B). 10µM DNA in 7.8pH TE buffer, measured in ABI 7500.....	140

Figure 4-20 Sequence (A) and melting temperatures (B) of DNA that has 3 single-stranded bases adjacent to the fluorophore derived using EvaGreen (green) or Alexa488 (blue) as a reporter molecule. Averages of 10 replicates of 10µM DNA in 7.8pH Tris-EDTA buffer, measured in ABI 7500. EvaGreen experiments used 1µl of 20x EvaGreen and unlabelled oligonucleotides. * shows P<0.05, ** P<0.01, *** P<0.001, the rest showed no significant difference. 142

Figure 4-21 Example derivative curve from Experiment 3A (3A) and Experiment 3B (3B) showing a melt peak at 70°C (3A) and 66°C (3B). 10µM DNA in 7.8pH Tris-EDTA buffer, measured in ABI 7500 143

Figure 4-22 Sequence and melting temperatures of DNA that has 3 single-stranded T bases adjacent to the fluorophore derived using EvaGreen (green) or Alexa488 (blue) as a reporter molecule. Averages of 10 replicates of 10µM DNA in 7.8pH Tris-EDTA buffer, measured in ABI 7500. EvaGreen experiments used 1µl of 20x EvaGreen and unlabelled oligonucleotides. * shows P<0.05, ** P<0.01, *** P<0.001, the rest showed no significant difference. 144

Figure 4-23 Averaged derivative curves from Experiment 3T showing a false peak around 27°C. 10µM DNA in 7.8pH Tris-EDTA buffer, measured in ABI 7500..... 145

Figure 4-24 Sequences (A) and melting temperatures (B) of DNA that has 6 single-stranded bases adjacent to the fluorophore derived using EvaGreen (green) or Alexa488 (blue) as a reporter molecule. Averages of 10 replicates of 10µM DNA in 7.8pH Tris-EDTA buffer, measured in ABI 7500. EvaGreen experiments used 1µl of 20x EvaGreen and unlabelled oligonucleotides..... 146

Figure 4-25 Example derivative curve from Experiment 6A and 6B with melt peak at 66°C (6A) and 58°C (6B). 10µM DNA in 7.8pH Tris-EDTA buffer, measured in ABI 7500.. 147

Figure 4-26 Sequence (A) and melting temperatures (B) of DNA that has 9 single-stranded bases adjacent to the fluorophore derived using EvaGreen (green) or Alexa488 (blue) as a reporter molecule. Averages of 10 replicates of 10µM DNA in 7.8pH Tris-EDTA buffer, measured in ABI 7500. EvaGreen experiments used 1µl of 20x EvaGreen and unlabelled oligonucleotides. All results P<0.001 148

Figure 4-27 Example derivative curves from Experiment 9A, 9B, 9C and 9D showing a melt peak at 54°C (9A) and false peaks due to signal noise around 27°C (9B/C/D). 10µM DNA in 7.8pH TE buffer, measured in ABI 7500149

Figure 4-28 Sequence (A) and melting temperatures (B) of DNA that has 12 single-stranded bases adjacent to the fluorophore derived using EvaGreen (green) or Alexa488 (blue) as a reporter molecule. Averages of 20 replicates of 10µM DNA in 7.8pH Tris-EDTA buffer, measured in ABI 7500. EvaGreen experiments used 1µl of 20x EvaGreen and unlabelled oligonucleotides. T test $P < 0.001$ shown by ***.150

Figure 4-29 Derivative curve for 12 single-stranded base experiment showing a false peak due to signal noise around 27°C. 10µM DNA in 7.8pH TE buffer, measured in ABI 7500151

Figure 4-30 Peak height / baseline median for the melt curves for experiments detailed in 0 with partially single-stranded DNA adjacent with the Alexa488 fluorophore.153

Figure 4-31 Absorption (A) and Emission (B) spectra of Alexa488 (black square), FITC (red circles) and Atto488 (blue triangles) fluorophores, drawn and analysed with OriginPro. The standard deviation between these fluorophores and an imaginary average was 3.22 for the absorption between 420-540nm and 3.46 for the emission between 480-600nm, showing the close alignment.154

Figure 4-32 Model showing melt curves seen using the photo-induced fluorescence quenching effect. Red lines show the fluorescence signal seen when the fluorophore attached to double-stranded DNA is adjacent to a G or A base, blue line shows the fluorescence signal seen when the fluorophore attached to double-stranded DNA is opposite to a G or A base, grey shows the fluorophore attached to single-stranded DNA. dF shows the change in fluorescence between the double-stranded and single-stranded state. Points *A* show the absolute fluorescence when the DNA is double-stranded, *B* and *C* will be single-stranded. The melting temperature is shown by the dotted line, marked T_m 157

Figure 5-1 – Variations in concentrations (10 µM, 5 µM, 1 µM, 500 nM and 100 nM) of Alexa488-labelled DNA C in 7.8pH Tris-EDTA buffer. The concentration of the unlabelled complementary strand was the same as the DNA. Total fluorescence was measured using the Applied Biosciences 7500 Fast Real-Time PCR machine at 25°C.

Each point shown is the average of 4 replicates, with the fluorescence for each read 10 times. Dotted line shows linear best fit, error bars show standard deviation.....161

Figure 5-2 Varied concentrations of Alexa488-labelled DNA C with varied concentrations of unlabelled complementary DNA - 10 μ M (green), 5 μ M (orange), 1 μ M grey), 500nm (yellow) and 100nm (blue) - in pH 7.8 Tris-EDTA buffer. Total fluorescence was measured using the Applied Biosciences 7500 Fast Real-Time PCR machine at 25°C. 4 replicates, fluorescence for each read 10 times. Tukey ANOVA analysis for each group showed P>0.001 showed by ***164

Figure 5-3 (A) and (C) are the derivative curves with high concentrations of complementary DNA (10 μ M) with 10 μ M (A) and 500nM (C) of Alexa488-labelled DNA C. (B) and (D) are the derivative melt curves with lower concentrations of complementary DNA (100nM) with 10 μ M (B) and 500nm (D) of Alexa488-labelled DNA C. Grey shaded area shows standard deviation between derived melt curves. All experiments were performed in quadruplicate with an Applied Biosciences 7500 Fast PCR machine at the 480nm excitation/530nm emission, measurements taken from 20-95°C.165

Figure 5-4 Derivative of the melt curve at the melting peak and 60°C. 10 μ M (green), 5 μ M (orange), 1 μ M (grey), 500nM (yellow).....166

Figure 5-5 Primer (F3 in red, B3 in Green) and template sequence of modified BRCA1 used to perform qPCR. Modified base indicated by *. Polymerase direction indicated by arrow.167

Figure 5-6 40 cycle qPCR performed in ABI 7500 using Alexa488-labelled primer (green) or unlabelled primers with EvaGreen (black) as a control. The amount of template DNA was varied, 400ng (circle), 100ng (square), 10ng (triangle). PCR was otherwise performed as described in 2.5.4.....168

Figure 5-7 Figure showing the sequences of the DNA sequences used. The green strand is Alexa488 modified or unlabelled for the EvaGreen controls. The light blue represents the unlabelled complementary strand, which is the same for both the control and the Alexa488 experiments.170

Figure 5-8 Melting temperatures of DNA with sequential deletions on the complementary strand derived using EvaGreen reporter molecule on the ABI 7500 PCR machine. * shows P<0.05, ** P<0.01, *** P<0.001, the rest showed no significant difference.171

Figure 5-9 Melting temperatures of DNA with sequential deletions on the complementary strand derived using Alexa488 effect on the ABI 7500 PCR machine. -n indicates that a number of bases that have been removed from adjacent to the fluorophore on the complementary strand. * shows $P < 0.05$, ** $P < 0.01$, *** $P < 0.001$, the rest showed no significant difference.....172

Figure 5-10 Derivative curves of standard unlabelled BRCA1 LAMP primers without (A) and with (B) LPR5F and LPF5B complement strands (see 0. for full sequences). No significant peak is observed.175

Figure 5-11 Averaged derivative curve of BRCA1 LAMP primers Alexa488-LPRF5 and Alexa488-LPF5B with the unlabelled LPR5F complement strand showing a distinct melt peak at 44.4°C. 10µM dsDNA in pH7.8 TE buffer175

Figure 5-12 Average derivative curve of BRCA1 LAMP primers Alexa488-LPRF5 and Alexa488-LPF5B with their unlabelled complement strands showing two distinct melt peak at 44.4 °C and 51.0°C. 10µM dsDNA in pH7.8 TE buffer176

Figure 5-13 Averaged derivative curve of BRCA1 LAMP primers Alexa488-LPRF5 and Alexa488-LPF5B with the unlabelled LPF5B complement strand showing a distinct melt peak at 51.0°C. 10µM dsDNA in pH7.8 TE buffer176

Figure 5-14 Example of analysis in OriginPro of the averaged melt curve of BRCA1 LAMP primers Alexa488-LPRF5 and Alexa488-LPF5B with their unlabelled complement strands. The centre points of the two peaks are shown by red lines and numbered, the separation line is in blue, and the areas are shaded in grey.177

Figure 5-15 BRCA1 template and primer sequences. Colour indicates primer sequences and arrow indicates amplification direction and strand. FIP and BIP were only used for LAMP DNA amplification (5.4.3) and so are not highlighted here.....179

Figure 5-16 Melting temperature of BRAC1 PCR products measured with Alexa488 (blue) or EvaGreen (green) fluorescence in ABI 7500. EvaGreen with F3 and B3 are controls. *** shows $p < 0.001$ between combinations.....181

Figure 5-17 Spectra of normalised fluorescence (A) and derivative (B) curves of the products of Combination 1. In A and B, F3+B3+EvaGreen (control) is shown in black, Alexa488-labelled F3+B3 is shown in red, and F3+Alexa488-labelled B3 is in green. PCR was performed as described, with a melt curve performed between 25-95 °C. Origin 2016

performed smoothing with 10 point adjacent-averaging in Origin 2016, and derivative. Peakfinding function was limited to a single peak, shown.182

Figure 5-18 Spectra of normalised fluorescence (A) and derivative (B) curves of the products of Combination 2. In A and B, F3+LPF5B+EvaGreen (control) is shown in black, F3+Alexa488-labelled LPF5B is shown in green, and Alexa488-labelled F3+LPF5B is shown in red. PCR was performed as described, with a melt curve performed between 25-95 °C. Origin 2016 performed smoothing with 10 point adjacent-averaging in Origin 2016, and derivative plotted. Peakfinding function was limited to a single peak, shown.183

Figure 5-19 Amplification plots (left) and melt curves (right) of BRCA1 LAMP EvaGreen controls with (3 and 4) and without (1 and 2) template DNA performed on ABI 7500. Total reaction time was 20 min (40 cycles of 30 seconds). The control without template DNA showed no increase in fluorescence (1), nor a distinguishable melt curve (2). The EvaGreen control used unlabelled primers and worked as expected with positive LAMP amplification seen after 5 minutes and complete after 10 minutes (3), producing melt curve (4) with a single peak around 85°C.185

Figure 5-20 Amplification plots (left) and melt curves (right) of BRCA1 LAMP reaction performed using Alexa488-labelled primers in ABI 7500. Total reaction time was 20min (40 cycles of 30 seconds), with positive LAMP amplification seen after 0.5-1 minute and complete after 3-5 minutes, producing melt curves as seen on the right. LAMP (A) utilised Alexa488-labelled LPF5B (1 and 2), LAMP (B) utilised Alexa488-labelled LPF5B (3 and 4), LAMP (C) utilised Alexa488-labelled LPF5B (5 and 6).186

Figure 5-21 Restored averaged melt curves of Alexa488-labelled LAMP (A), (B) and (C) products – samples were photobleached and EvaGreen added to measure the melt curves in an ABI7500. The Alexa488 produced melt curves seen in the previous graph reverted to the expected curves, suggesting that the differences seen previously were due to specific position of the labelled primers within the overall LAMP product.187

Figure 5-22187

Figure 5-23 Schematic representation of the potential stages of a microfluidic DNA microarray using Alexa488 fluorescence to monitor DNA binding.188

Figure 5-24 Melt curve derived using the First-Generation microfluidic device. Sigmoidal curve (red) fitted by OriginPro(2016).189

Figure 5-25 Testing the First-Generation Microfluidic device. Temperature (black line) and DNA content (blue squares) over the course of an experiment (A) and the control (B). Temperature measured using J-type thermocouple, fluorescence measured using the microscope and software previously described.190

Figure 5-26 Complete Second Generation single input/output PDMS microfluidic device with DNA test chip enclosed in the centre (labelled). The inlet port and outlet ports are shown and are interchangeable.191

Acknowledgements

Within the research group I would like to thank Jon Cooper and Julien Reboud, for supervision and encouragement, Rab Wilson, for effectively running the lab and Dave, for brainstorming over pints and microfluidic device fabrication. For providing training, I thank Gabby for help with surface chemistry, Eloise for surface acoustic wave training, and Andrew for optics.

I thank my mother, Tracey, for always answering the phone when my experiments were going particularly well, or particularly poorly. My gratitude to Neil, for cooking dinner and keeping me sane. My friends and family, who were always there.

Authors declaration

I declare that, except where explicit reference is made to the contribution of others, that this dissertation is the result of my own work and has not been submitted for any other degree at the University of Glasgow or any other institution.

Printed Name: _____

Signature: _____

Commonly used abbreviations

Å – Angstroms

A base – Adenine

APTES – (3-aminopropyl)triethoxysilane

BRCA – Human breast cancer risk gene

C base – Cytosine

DNA – Deoxyribonucleic acid

dsDNA – double-stranded DNA

EDTA – ethylenediaminetetracetic acid

FRET – Forster / Fluorescence Energy Resonance Transfer

G base – Guanine

HIV – Human Immunodeficiency Virus

IDT – Interdigitated transducer

IPA – isopropanol

LAMP – Loop-mediated Isothermal Amplification

LiNbO₃ – Lithium niobate

ml – millilitres

NB-S Quench – Nucleobase-Specific Quenching

NGS – Next Generation Sequencing

nm – nanometre

PBS – phosphate buffered saline

PCR – Polymerase Chain Reaction

PFOTS – 1H,1H,2H,2H-Perfluorooctyl-trichlorosilane

POC – Point of care

RFU – relative fluorescence units

RTD – Resistance Temperature Detector

SAW – Surface Acoustic Waves

ssDNA – single-stranded DNA

T base – Thymine

TE – Tris-EDTA (tris(hydroxymethyl)aminomethane ethylenediaminetetracetic acid)

TIRF – Total Internal Reflection Fluorescence

T_m – melting temperature

UV – ultraviolet light

µl – microliters

1. Background, Introduction to Point-of-Care Diagnostics

There is increasing demand for miniaturised, portable diagnostic medical devices. Developed countries are challenged by medical budgets restricted by increasing drug and treatment costs and ageing populations [1]. Developing countries are challenged by a lack of infrastructure, trained medical technicians and funding combined with growing populations which are increasingly aging, increasingly mobile and demand higher standards of living, including medical-related quality of life [2].

Lab-on-a-Chip technologies such as surface acoustic waves (SAW) can meet the needs of point-of-care diagnostics for mobile populations whilst also reducing the cost and training required to diagnose disease [3–5]. SAW is particularly versatile and can be used to heat, move and mix droplets, as well as measure mass changes to monitor DNA or antigen binding [6,7].

This chapter provides an introduction to the current state of point-of-care diagnostics, and an overview of selected relevant diseases. As DNA, fluorescence and Surface Acoustic Waves (SAW) are important for this thesis, an overview of each is included.

1.1. DNA

Deoxyribonucleic acid (DNA), and ribonucleic acid (RNA) are the chemical storage of genetic information for all of life. In eukaryotes, DNA encodes genes which are transcribed into messenger RNA, which is then translated into proteins which may act as enzymes. The genetic information of many viruses, such as Influenza and Human Immunodeficiency Virus (HIV) are stored as RNA [3,8]. In order to replicate, Influenza viruses copy their genetic RNA, and this is used directly to transcribe proteins needed for replication. In contrast, HIV is a retrovirus so the genetic RNA is used to create complementary DNA (cDNA) by an enzyme reverse transcriptase, which integrates into the host genome [9–11]. This research examined diagnostics using DNA, if, in the future, additional RNA-based infections are to be studied then the additional step of converting the RNA to cDNA will be required.

At physiological conditions (above annealing temperature, but below the melting temperature), single strands DNA (ssDNA) that are complementary will, with non-covalent bonds, form double-stranded DNA (dsDNA). The strength of these bonds depends on the base pair (A=T or G=C), in addition to base stacking and solvent interactions [12]. The salt concentration of the buffer, GC content, and the number of DNA bases all have an effect on the DNA melting temperature, and will be considered individually in this work, with these factors varied individually as far as possible [13]. In order to measure if the DNA is in a double- or single-stranded form, a reporter molecule (EvaGreen [14]) is used, which binds preferentially to dsDNA, resulting in a change in EvaGreen conformation and fluorescence which can be monitored using a fluorescent microscope. To quantify the melting point the fluorescence and temperature must be accurately measured. Characterisation of the system requires accurate calibration of the RTDs against a thermocouple as well as analysing the fluorescence of the system to take into account photobleaching.

In order to investigate the use of surface acoustic waves for DNA-based diagnostics, it is necessary to understand nucleic acid thermodynamics. The temperature at which 50% of the DNA is single stranded (ssDNA) is defined as the melting temperature (T_m), and this depends on the primary and secondary structure [15]. The DNA in this thesis was designed to avoid complicated secondary structures that would influence the melting temperature, although this is a requirement for Loop-mediated Isothermal Amplification (LAMP).

1.1.1. Thermodynamics of DNA binding

The transition of single-stranded DNA to double-stranded DNA at the melting temperature can be described using $A + B \leftrightarrow AB$ therefore $K = \frac{[A][B]}{[AB]}$ (Eq 1)

where A and B are single-stranded DNA, AB is the double-stranded form. At the melting temperature T_m , double-stranded DNA equals single-stranded DNA. At the equilibrium.

$$T_m = \Delta H^\circ / (\Delta S^\circ + R \ln C_T) \text{ (Eq 2)}$$

where R is the gas constant ($1.987 \text{ kcal K}^{-1} \text{ mol}^{-1}$) and C_T is the total oligonucleotide concentration [12,15,16].

Nearest Neighbour Model

As there are 4 DNA bases, there are 16 possible neighbour pairs, although the formation energy of 6 pairs are identical due to symmetry – leaving AA/TT, AC/TG, AG/TC, AT/TA, CA/GT, CC/GG, CG/GC, GA/CT, GC/GC and TA/AT [17]. The entropic and enthalpic (ΔS° and ΔH°) values of every one of the 10 possible neighbour pairs, and the final/initial nucleotides have been experimentally determined under various conditions and the total value can be calculated with

$$\Delta G^\circ(\text{total}) = \Delta H^\circ(\text{total}) - T\Delta S^\circ(\text{total}) \text{ (Eq 3) [17–20].}$$

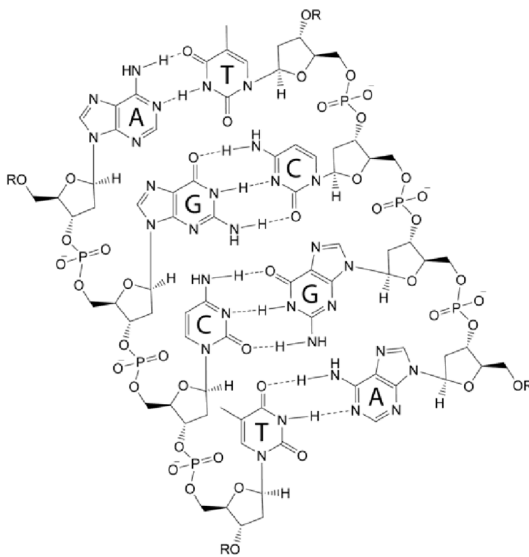


Figure 1-1: Hydrogen bonds between DNA bases A, T, G and C. Reproduced from [21]

1.1.2. DNA Melting

Thermal denaturation of DNA is the sequential breaking of A=T and G≡C base pairs between complementary DNA strands, and the additional stacking effects of adjacent bonds of the neighbouring bases to either side [22]. Mismatched bases within a strand also lower the binding efficiency of adjacent bases, or repeated bases which allow multiple potential binding patterns, along with secondary structures, such as single stranded loops, or overlap of strands, can change the overall DNA melting temperature [16,23,24]. In addition, where the DNA is modified, such as with fluorophores, there may be steric hindrance between these molecules which will lower the overall melting temperature. In addition to the DNA sequence, salt-buffer interactions, and increased bond vibration due to temperature also contribute to the melting temperature [24,25].

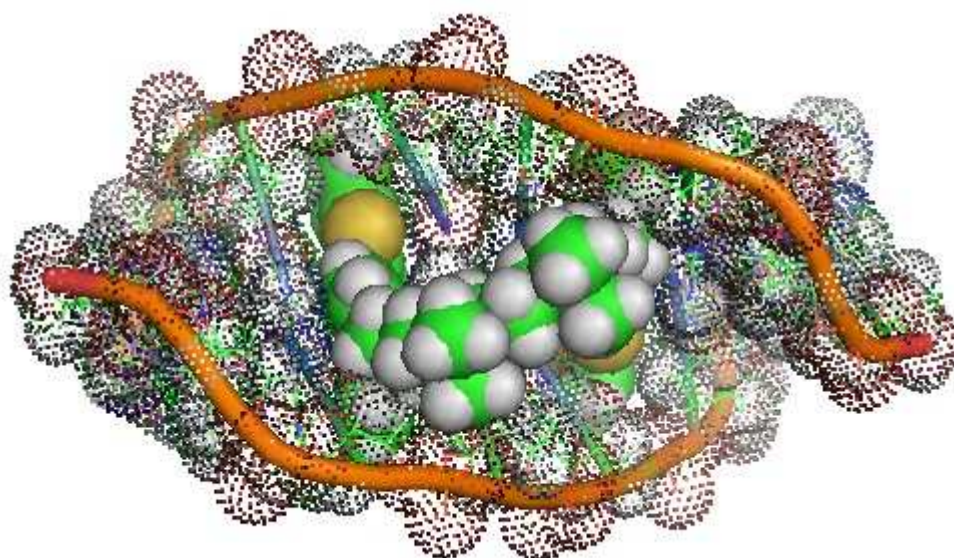


Figure 1-2 Structure of EvaGreen intercalating between DNA strands [26]

1.1.3. DNA Annealing

Whilst DNA melting is the sequential breaking of A=T or G≡C bonds between complementary strands, annealing is the renaturation of complementary strands. The rate for DNA strands binding is dependent on the temperature, viscosity, pH of the solution, the concentration and sequence of each strand. The fluorescent dsDNA reporter molecule EvaGreen is used in high concentration, with multiple molecules of EvaGreen to each molecule of dsDNA [14,27].

1.1.4. Selected Secondary Structures of DNA

DNA can form secondary structures, within or between complementary strands. These can affect gene regulation *in vivo*, and have research applications such as LAMP and DNA Molecular Beacons which are designed so that a hairpin loop to bring a fluorophore and quencher into proximity when the complementary strand is absent [28]. These secondary structures could explain the novel fluorescent effect in Chapters 4 and 5, where G-Quadruplex structures could result in aggregation of the fluorophores resulting in a decrease in fluorescence.

1.1.4.1. Model of DNA loop

DNA hairpin loops (also known as stem loops, see Figure 1-3) are a secondary structure of DNA and RNA. They consist of a short sequence that is non-complementary and usually A-rich, which forms a single stranded loop [24]. These are used for self-quenching DNA molecular beacons, which contain adjacent FRET paired fluorophores at the double-stranded end. If the complementary sequence is present, the fully double-stranded DNA has a higher binding energy which is more favoured, moving the FRET (see 1.4) fluorophores away from each other [28]. These loops are also important in LAMP reactions, as they allow the primers to loop around to the opposite strand, producing long LAMP products (see 1.2.1). Some research has examined photoinduced charge transfer quenching of fluorophores in DNA hairpin loops [29].

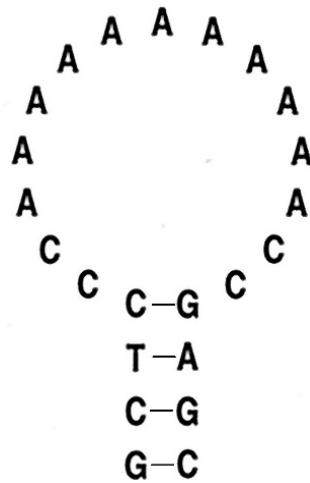


Figure 1-3 Model of a DNA hairpin loop showing double-stranded DNA where the sequence is complementary, and 15 base single-stranded loop mostly consisting of A base.

1.1.4.2. G-Quadruplex Structures

GC rich DNA regions can also form G-quadruplex structures, which can influence gene regulation, so may be important for inherited eukaryote disease [30–32]. Guanine-rich sequences can form tetrads containing up to 4 strands of DNA through Guanine interactions. These could form temporarily between DNA strands at low temperatures but would be transient at higher temperatures due to relatively low binding energy. G-quadruplex structures are considered in Chapters 4 and 5, as they could result in aggregation of G-rich single-stranded DNA which could be responsible for the Alexa488 fluorescence effect discovered.

1.2. Polymerase Chain Reaction (PCR)

Polymerase chain reaction (PCR) is an indispensable technique used for DNA amplification using a heat-stable polymerase enzyme and thermal cycling (see Figure 1-4). It requires 2 primers (short, specific DNA usually 10-20 bases), source DNA (including cDNA, which could be created from RNA using reverse polymerase), polymerase (usually Taq) and active heating / cooling to allow cycles between 60-65°C and 95°C [3,27,33–35].

Traditional PCR relies on cycles of a high temperature denaturation step of around 90-95°C followed by an annealing step of 50-60°C and an extension step at 72°C – the optimal temperature for Taq polymerase. 30 cycles have been shown to be possible in 10 minutes in small droplets (5µl) with specialised heating and cooling equipment, unsuitable for non-research laboratory [33]. If substrate and reagents (target DNA, primers, dNTPs) are not limiting then the amount of amplified DNA is doubled each cycle, leading to 2^n amplification of the target sequence where n is the number of PCR cycles. The final amount of target DNA will depend on the number of copies present in the sample – this has led to quantitative PCR (qPCR) which uses the fluorescence after each cycle to measure the DNA increase and hence the level within the original sample [36–38].

PCR in a droplet using SAW has already been shown, and results suggest that streaming within the droplet may be influencing the melting temperature [39].

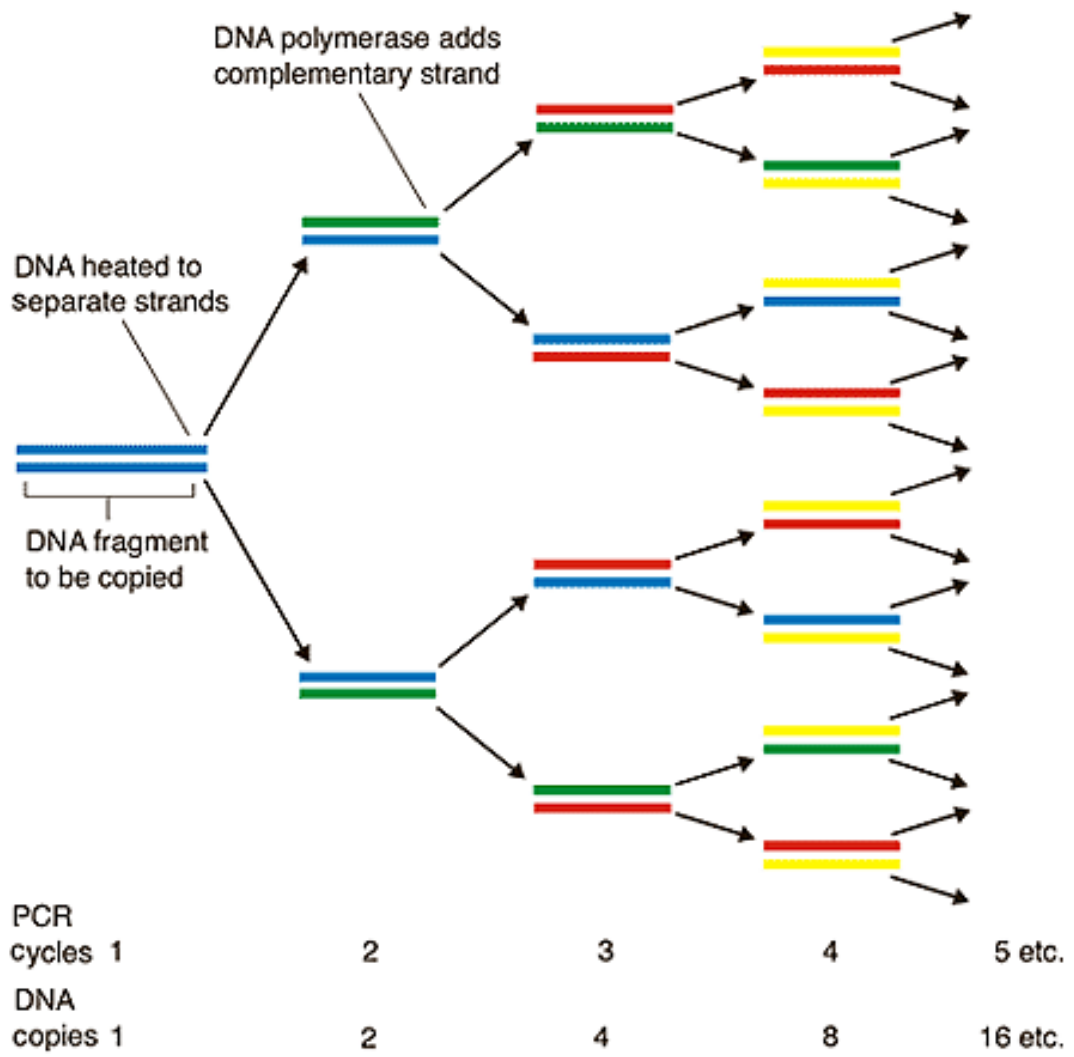


Figure 1-4 Illustration of DNA amplification by polymerase chain reaction (PCR) showing exponential DNA amplification [40]

1.2.1. Loop-Mediated Isothermal Amplification (LAMP)

LAMP is an alternative method of DNA amplification. Whilst PCR makes use of two primers on opposite strands to amplify the DNA in the middle, LAMP uses upwards of 4 primers, designed with loops which are important for strand displacement. As one primer is extended it will displace another, using loops to bind partway through the sequence, so this DNA amplification can be done at a single temperature, usually 60-65°C. The primers are more complicated to design as they include loops and non-complementary sequences to allow strand displacement. Each reaction requires at least 4, so multiplexing is more difficult than PCR. In addition, LAMP results in a large, repetitively looped product, which is unsuitable for many further applications such as cloning as it contains multiple copies of the DNA of interest in long chains which include various loops introduced by the primers [41–44].

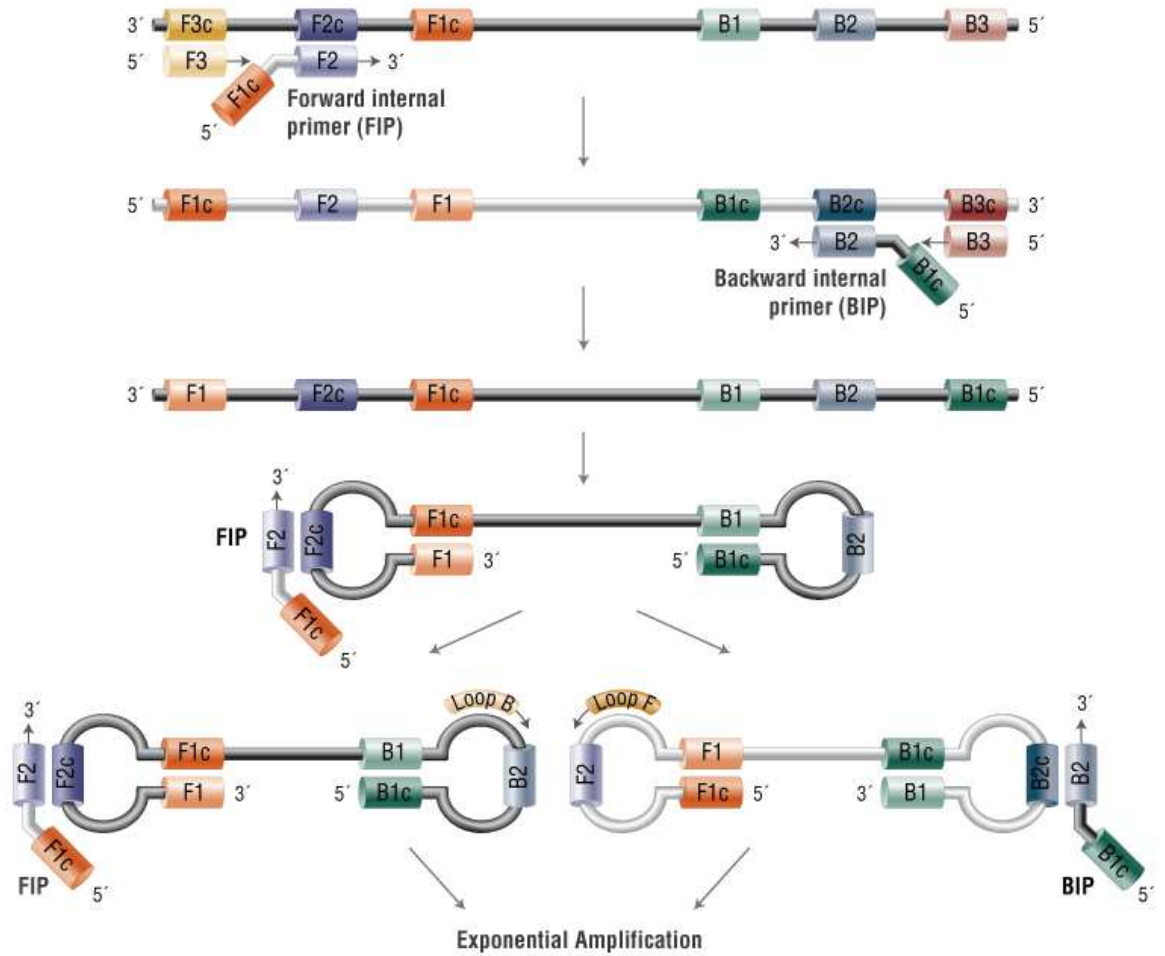


Figure 1-5 Illustration of DNA amplification using loop-mediated isothermal amplification (LAMP). 6+ pairs of primers complementary to different regions of DNA, allowing displacement at a single temperature as DNA amplification progresses, forming large products containing multiple copies of the target sequences as well as the loop introduced in the primers. [41]

1.3. Surface Acoustic Waves (SAW)

Surface acoustic waves (SAW) are 10 MHz to 1GHz ultrasonic waves produced by an Interdigital Transducer (IDT) with applications from radio, mobile phones, and lab-on-a-chip diagnostics [6,45]. When a SAW wave travelling along a piezoelectric substrate (one point of a travelling SAW wave is shown in Figure 1-6) interfaces with the sample droplet, some of the energy is transferred as a longitudinal wave and the remaining Leaky SAW attenuates in the direction of propagation [46].

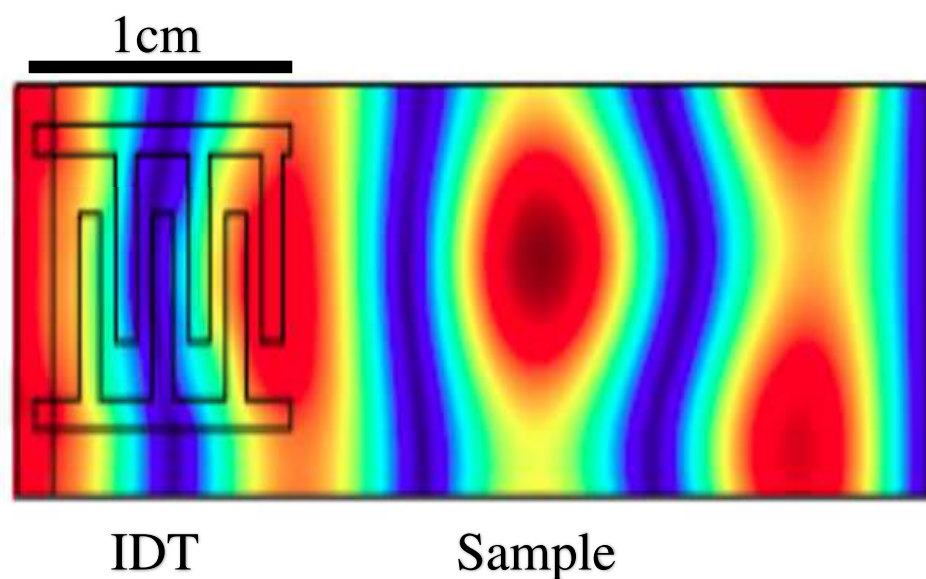


Figure 1-6 COMSOL model of an IDT illustrating surface displacement of piezoelectric material (lithium niobate) due to surface acoustic waves at 8.5 Mhz. Note that this shows only a single point in time, which will change rapidly as the SAW propagates across the surface. The wave will dissipate as energy is transferred into the sample droplet (not simulated). Red shows pressure wave maxima, dark blue shows minima.

Previous work has shown that SAW can be used for moving particles by size, weight or charge, mixing, centrifuging, heating and atomising droplets, with recent advances replicating PCR in a droplet [39,47,48]. SAW has also been shown to reduce non-specific antibody interactions by an unknown mechanism [49]. These applications for SAW in droplets could also allow on chip sample preparation as whole cells could be lysed and centrifuged to concentrate proteins of interest [7,49].

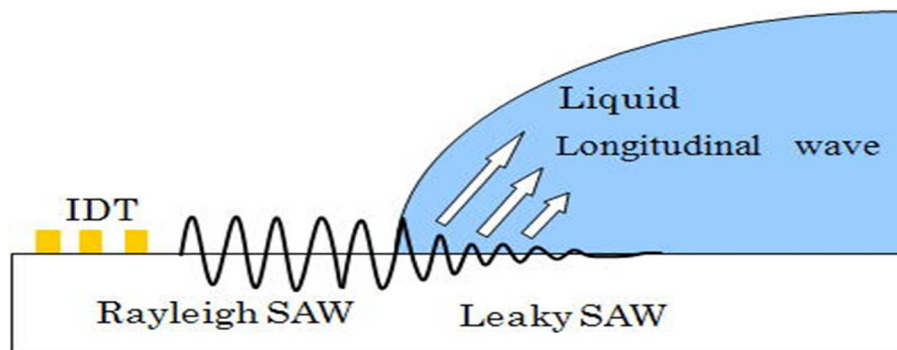


Figure 1-7 Surface acoustic waves (SAW) propagating from an Interdigitated Transducer (IDT) along a substrate and into the droplet. At the interface of the substrate and the droplet some of the energy from the Rayleigh SAW wave as a longitudinal wave which will circulate the droplet. As the energy is transferred from the Rayleigh SAW into the droplet at which point it is termed a Leaky SAW which attenuates as energy is transferred into the sample droplet. Reproduced with permission from [49].

It is hypothesised that the energy from SAW could disrupt DNA binding instead of melting the DNA through simply heating the droplet. If so, there will be several advantages over using heat. The speed of SAW in water is 3995ms^{-1} , meaning the binding of DNA could be disrupted extremely quickly, potentially with nanosecond pulses. The thermal conductivity of water, even in a small droplet, means that it takes significantly longer to heat and cool a sample than for SAW to travel through. The heating energy will be varied even across the droplet depending on the position and efficiency of the heating source.

Therefore, if SAW can disrupt DNA binding at low or lower temperatures then there would be time and energy advantages, potentially allowing PCR to proceed at room temperature with only a second or two between cycles. If SAW can disrupt DNA binding, this effect would depend on the binding energy between strands. Longer dsDNA, and higher GC content (Guanine-Cytosine pair has three hydrogen bonds, whereas Thymine-Adenine pair has two hydrogen bonds) result in higher binding energy.

There are several models for predicting the melting temperature of a DNA strand given its sequence, including the 2+1 rule of thumb, linear regression and nearest neighbour [16,17,23,51].

By altering the frequency, amplitude or time that the SAW is applied it could be possible to selectively target DNA of a certain sequence and length, although it is likely that any shorter sequences with lower binding energy would also melt. For the field of medical diagnostics there would be a relatively simple solution to work around this problem. For example, targeting DNA shorter than the target would allow background noise to be removed, thereafter DNA of increasing length would be targeted and previous signal subtracted. In this way DNA of different lengths could be targeted sequentially, whilst taking into account non-specific binding and general background noise such as dNTPs and failed PCR products.

PCR amplification is required for genetic tests in order for a binding event to be measurable with non-specific fluorescent reporter molecules. If SAW can disrupt DNA binding as suggested it could be possible to specifically target DNA within a mixed sample, disrupting the binding between the strands and resulting in a loss of fluorescence and subsequent recovery when the SAW is no longer applied. If we could focus SAW disruption like this, we could measure this fluorescent signal repeatedly as SAW is pulsed, forgoing the need for PCR completely.

1.3.1. Modelling of Streaming Within a Droplet

Mansuor et al. have produced detailed modelling (an example is shown in Figure 1-8) of the hydrodynamics of surface acoustic wave streaming in microfluidic droplets[52]. DNA within the droplet will be influenced by streaming within the droplet, DNA attached to the surface will additionally be affected by leaky SAW waves from the substrate. In addition to streaming, Mansuor modelling also showed differences in temperature and pressure within these droplets which could affect DNA binding.

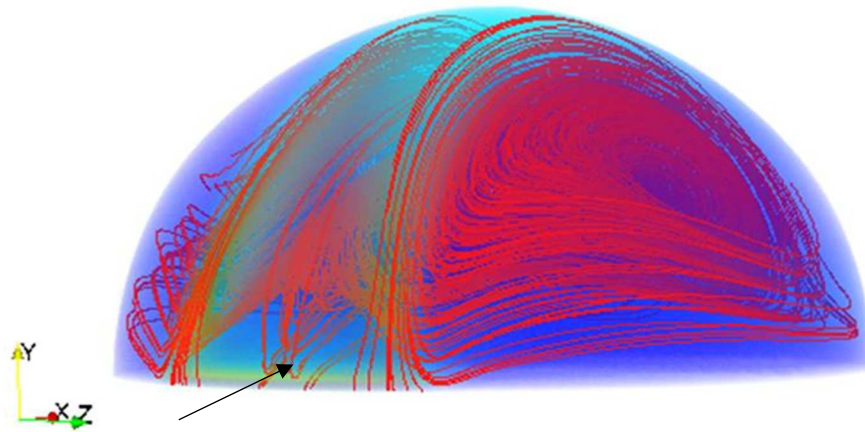


Figure 1-8 A computer model of surface acoustic wave streaming within a 10 μ l water droplet due to longitudinal wave produced by SAW. Altered from [51] to add a black arrow showing the direction of the SAW wave from the IDT into the droplet that produced the streaming.

1.3.2. Detection Methods for Surface Acoustic Waves (SAW)

Various detection methods have been used with SAW Lab-On-A-Chip devices including antibody, colour/light, pH, temperature, or crystal/salt/gas formation [44,52]. Antibodies are commonly used as they are readily available and do not require complicated protocols [53–55].

For example, a fluorescently labelled secondary antibody can be incubated on the chip, binding to the primary antibody attached to the surface if the disease antigen is absent but not binding if the disease antigen is present. Antibodies are not without their drawbacks – binding could be too specific and so not bind to all serotypes such as emerging sub-populations. Antibody orientation is important, attaching antibodies to a surface often results in sub-optimal orientation reducing efficiency. Lastly, antibodies cannot be easily reused, so antibody paper devices are single use [7,49].

An alternative approach to measure if an antigen has bound to the antibody on the surface of the diagnostic device without secondary antibodies are Love wave (horizontally polarised SAW) devices. These measure the difference in the acoustic wave produced before the

sample and received afterwards, but they are more difficult to use and manufacture than using a secondary antibody which could be visually or chemically detected [4,6,56,57].

The literature includes several chemical based detection methods that rely on a colour or pH change, endo- or exothermic reaction significant enough to alter the sample temperature. Studies also make use of crystal, salt or bubble formation, or phosphorescence [6,57–60]. These detection methods are difficult to apply to preliminary experiments involving DNA binding as they will not be able to show the reversal between single and double stranded DNA. If the required catalysts and reagents could not be applied to the device in advance and stored, this would greatly decrease the reliability and usefulness of a diagnostic kit. Lastly, potential cross-reactions, oxidation, dehydration and heat instability could mean a requirement for a specialist storage such as a continuous cold-storage chain.

An interesting approach to detection is magnetic – either labelled antibodies or inherent to the parasite. Hemozoin is produced by blood borne pathogens (malaria, Chagas) and forms crystals. There is potential to bind “seed” hemozoin crystals onto a diagnostic device – if there is hemozoin present this would be sequestered from the sample, crystallize on the reaction chamber and alter the magnetic properties. The crystal formation and altered magnetic properties of infected red blood cells are understood but using this approach to diagnose an infection in a LOC format is untested with a SAW device [61–63].

The most attractive approach would be label-free, to avoid relying on complex sample preparation, optics and sensing. A mass-based detection method, such as the single virus particle detection using microresonators could be employed as dsDNA has a greater mass than ssDNA, allowing differentiation of the binding states [64]. Another potential method is to use a simple camera and lens to visualise beads with antibodies attached in order to distinguish between presence and absence of an antigen, similar to the antibody agglutination test to identify blood types [53]. Alternative approaches could be based on light (light absorption / emission / scattering), such as the commonly used spectrophotometric method for estimating DNA concentration in a solution [65]. EvaGreen is a non-specific fluorescent DNA dye commonly used to quantify PCR reactions. The fluorescence allows quantification of the concentration of DNA, and differentiation of dsDNA and ssDNA, although this does require a light source with a peak emission at 488nm and sensing filtration with a peak at 530nm.

1.4. Fluorescence

Absorption of a photon promotes an electron from the ground state to an excited state (see Figure 1-9) [66]. Excitation: $S_0 + h\nu_{excitation} \rightarrow S_1$ (Eq 4) where h is Planck's constant, ν is the frequency of photon absorbed.

Energy can be transferred from the excited state S_1 to a lower energy state S_0 as shown in Figure 1-9 through processes such as:

- vibrational relaxation (transferred within the same molecule, or surrounding molecules)
- internal conversion (radiationless transitioning)
- intersystem crossing (singlet \leftrightarrow triplet state, can lead to phosphorescence)
- fluorescence

Fluorescence occurs when the excited singlet electron emits a photon with lower energy / longer wavelength than the excitation photon, relaxing to its ground state (see Figure 1-9). Emission: $S_1 \rightarrow S_0 + h\nu_{emission} + \text{heat}$ (Eq 5) where h is Planck's constant, ν is the frequency of photon emitted.

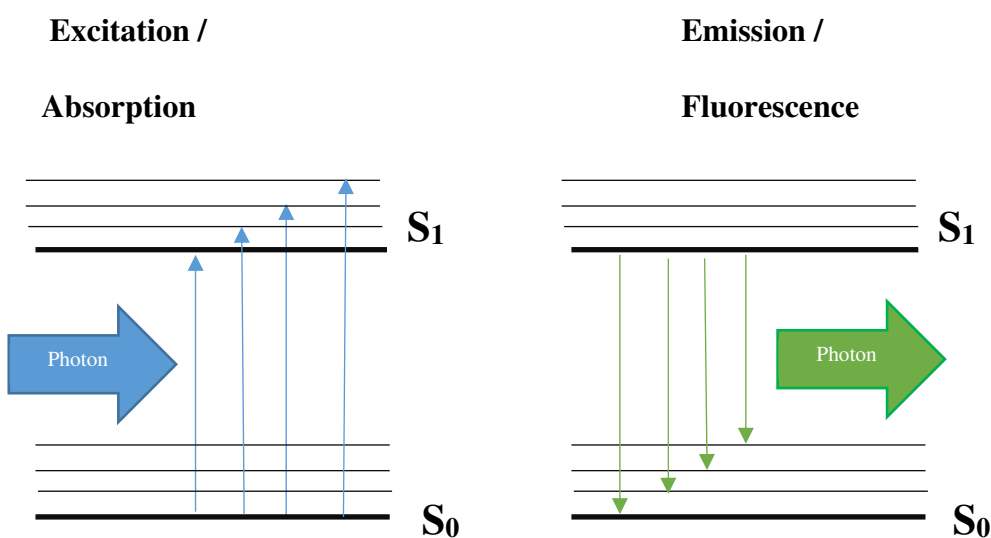


Figure 1-9 Jablonski diagram showing ground / HOMO (S_0) and excited / LUMO (S_1) states for electrons, illustrating the energy potentials during photon absorption and emission by a fluorophore

The quantum yield of a fluorophore is defined as the proportion of excited fluorophores that emit a photon to return to the ground state, which can also be described as the ratio of emitted photons to absorbed photons. Intramolecular vibrations, and transference of energy to surrounding molecules via vibrational relaxation, are more efficient at higher temperatures, therefore increasing temperature generally results in a decrease in fluorescence. Other parameters such as viscosity, pH (collisional quenching), hydrogen bonds and quenchers (such as O₂) can also decrease fluorescence quantum yield as energy from the fluorophore electron in the excited state is transferred to molecules surrounding the fluorophore which do not fluoresce [66].

1.4.1. Förster / Fluorescence Resonance Energy Transfer (FRET)

Förster / Fluorescence Resonance Energy Transfer (FRET) is a dipole-dipole coupling mechanism which transfers energy from the excited electron in the donor fluorophore, to a ground state electron in the acceptor fluorophore, which is promoted to an excited state [67]. The excited electron in the acceptor fluorophore emits a photon when it relaxes to the ground state. FRET cannot be directly measured, but the transfer of energy from the donor fluorophore results in a reduction in fluorescence, at the same time as the acceptor fluorophore fluorescence increases. The FRET efficiency is defined as the ratio between the number of excited donors transferring energy to the receptor to the number of photons absorbed by the donor [68]. This can also be expressed as a ratio of the transfer rate to the transfer rate and decay rate:

$$FRET\ Efficiency = \frac{k_{Transfer}}{k_{Transfer} + k_{Decay}} \quad (Eq\ 6)$$

where the decay rate refers to energy lost to FRET by relaxation or photon emission by the donor fluorophore. This in turn can be shown to be equal to the Förster Radius (R_0), which is the distance where the FRET efficiency is 50%. Förster radii have been characterised for pairs of donor and acceptor fluorophores [68].

This equation:

$$Fret\ Efficiency = \frac{R_0^6}{R_0^6 + r^6} \quad (Eq\ 7)$$

shows that the efficiency reduces by r^6 [43]. Considering a system where the fluorophores are in solution, this distance would be dependent on concentration – the average distance between molecules free-flowing in solution decreases as the number of molecules within the solution increases. At low concentrations, for example $1\mu\text{M}$ where R_0 is 5nm , the average distance between donor and acceptor molecules means that FRET is highly unlikely to occur. Even a concentration of 1mM would mean $<1\%$ FRET efficiency. In Chapter 4, the theory that the quenching seen is due to fluorophore – fluorophore interactions is discussed, these would increase with concentration so the fluorescence would exhibit a non-linear relationship in this case.

The Förster Radius (R_0) depends on several factors [27,35,43,67,68] such as the:

- Refractive index of the media [68] – this is 1.331-1.335 (PubChem SID 329770217) for TE buffer pH 8.0 (Sigma-Aldrich, UK) at 25°C .
- Orientation factor between the fluorophores - important when the fluorophores are attached to large molecules which rotate relatively slowly in solution, but this should not be an issue with fluorophores attached to DNA oligonucleotides [68].
- Overlap integral – a measurement of overlap between the donor fluorophore emission spectra and the acceptor fluorophore excitation spectra [68]

FRET does not depend on a photon emitted by the donor fluorophore, the overlap between the spectra is due to the possible energy states of the electrons within the fluorophore (see Figure 1-9). [27]

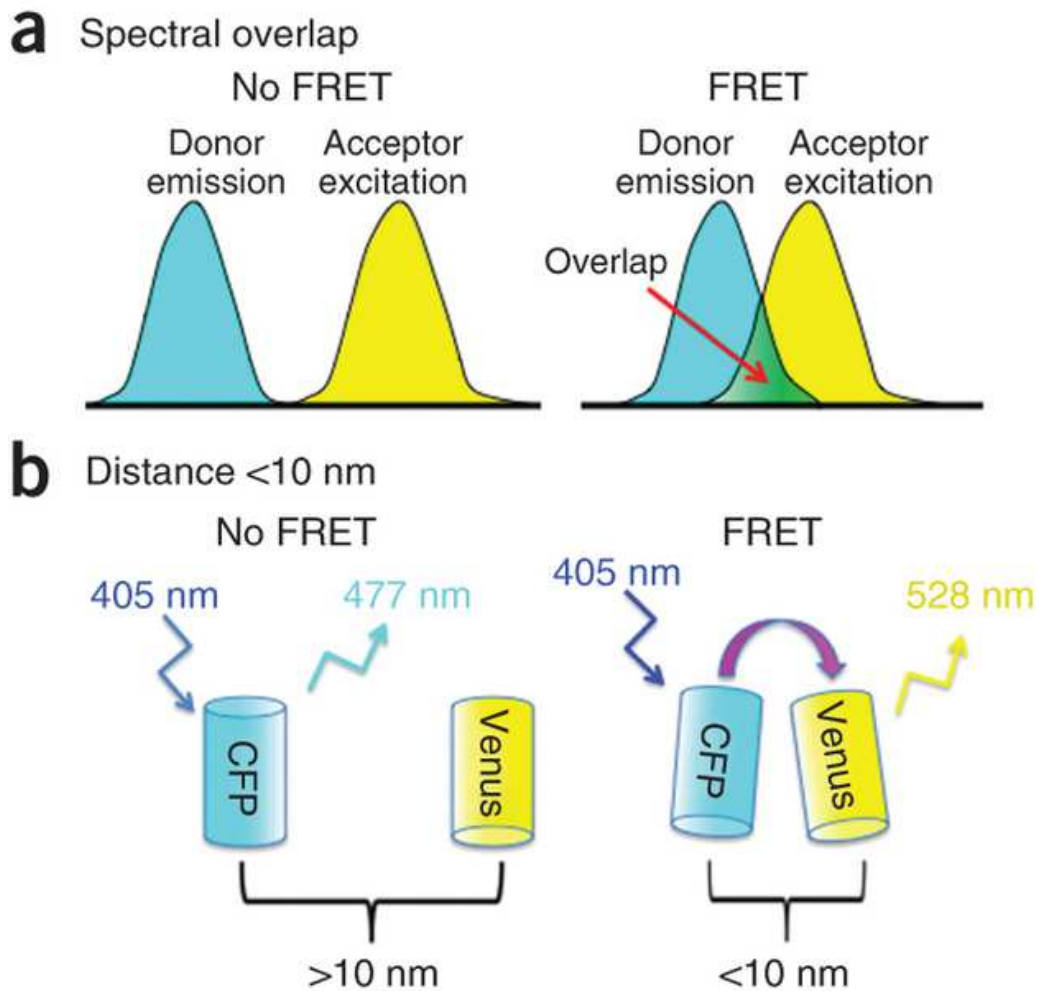


Figure 1-10 Illustration of FRET principle, highlighting the requirement of spectral overlap between the donor emission and the acceptor excitation (A) and the importance of distance (B). As can be seen in (B), if the fluorophores are far apart, then excitation of the donor fluorophore results in emission of the donor fluorophore, whereas when the fluorophores are close (<10nm) excitation of the donor fluorophore results in the emission of the acceptor fluorophore. By measuring the intensity of the emission in the region of the donor fluorophore and the acceptor fluorophore the efficiency can be calculated under the above conditions.[69]

1.4.2. Total Internal Reflection (TIRF) Microscopy

TIRF microscopy uses totally internally reflected light to excite fluorophores. Light is directed into the material such as glass or clear lithium niobate, in order to excite only the fluorophores adjacent to the substrate/aqueous interface, without exciting all the molecules in the sample. The depth-specific excitation is achieved as at the incident angle an evanescent wave is produced decays exponentially from the surface (Figure 1-12). This was accomplished for this thesis through directing the angle of the laser beam with an immersion lens of an inversion fluorescence microscope (Figure 1-11), although an alternative method coupling the laser to the superstrate through a prism was attempted [70,71].

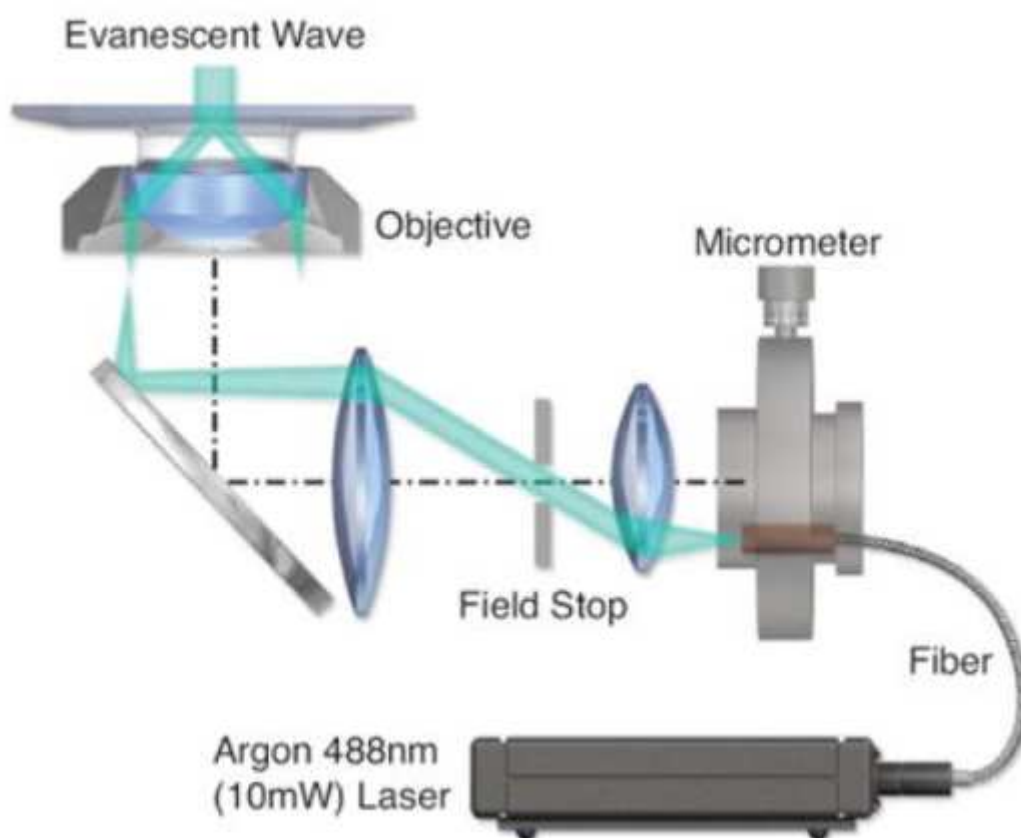


Figure 1-11 A schematic drawing of the TIRF system, reproduced with permission from [117]. The micrometer determines the incident angle of the laser into the substrate to produce the evanescent wave. The refractive index of the immersion oil is matched to the refractive index of the substrate.

The decay of the evanescent wave can be described with the equation [70]:

$$I_z = I_0 e^{-z/d} \quad (\text{Eq 8})$$

where I_0 is the initial intensity, I_z is the intensity at depth z , and d is the penetration depth which is in turn a function of the incident angle and wavelength of the light and refractive indexes of the substrate and sample (assuming that the refractive indexes of the immersion oil and substrate are equal). At the interface of the substrate and the sample, $z/d = 0$ and $I_z = I_0$ - the intensity of the evanescent wave is equal to the initial intensity (this is relative intensity 1 on Figure 1-12), after this the intensity decays exponentially.

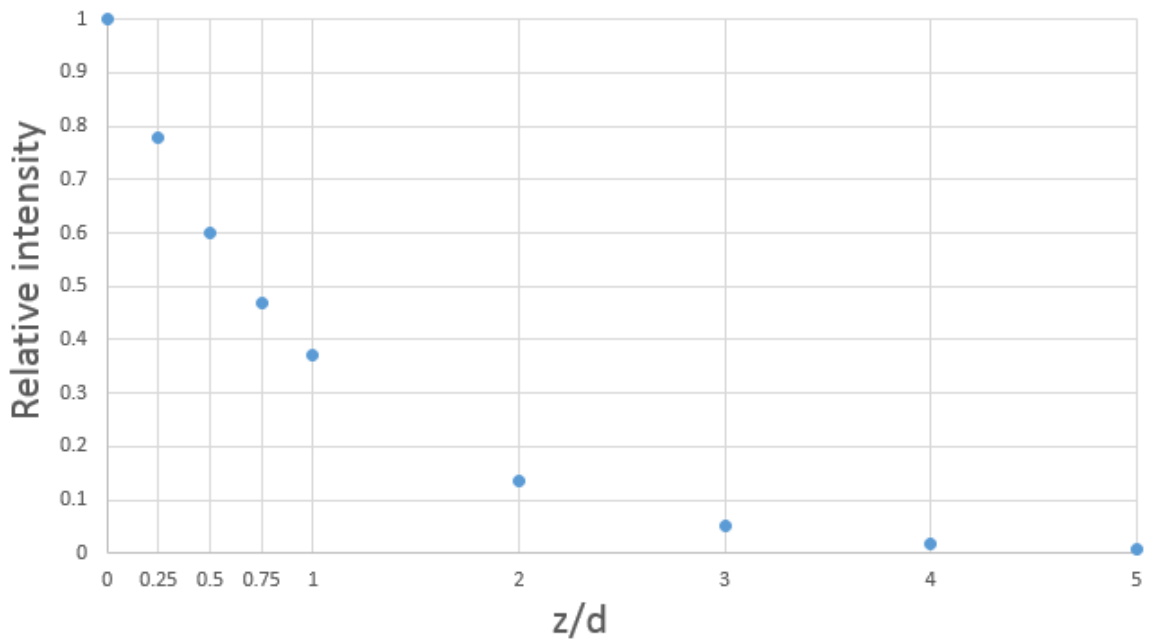


Figure 1-12 Relationship between the relative intensity of the evanescent wave against z/d which is the ratio of the distance from the interface to the penetration depth of the evanescent wave. At the interface, z/d is zero and the relative intensity is 1.

1.4.3 Quenching of Fluorophores

Organic fluorophores can be quenched in a variety of ways, such as conformational change/denaturing, absorbance of excitation light, absorbance of fluorescence, FRET, or photoinduced charge transfer [72]. EvaGreen changes confirmation in the presence of double-stranded DNA, resulting in a change in absorption area and peak, along with a corresponding shift in emission area and peak. Extremes of pH, temperature and photobleaching denature EvaGreen so that it is unable to fluoresce [14,27,28].

Molecular beacons and TaqMan probes rely on DNA hairpins with a fluorophore at one end and a quencher on the other, in the absence of the target DNA the quencher and fluorophore are brought within close proximity, resulting in a loss of fluorescence [27,28,73]. This can also be achieved with a FRET pair, although this would result in fluorescence at a longer wavelength [35,43,68].

π -stacking between the same fluorophores can also quench fluorophores, due to close alignment of the benzene rings in organic fluorophores, this occurs in a concentration-dependant manner – higher concentration of fluorophores results in a higher number of fluorophores that are close enough to interact. If π -stacking between fluorophores was responsible for the Alexa488 effect discussed in this thesis, then this would depend solely on the concentration of the fluorophores – a linear increase in the concentration of double- or single-stranded DNA would result in a linear decrease in fluorescence and not a linear increase in fluorescence.

Previous research has focussed on G-base quenching, through π -stacking between some fluorophores and G-base, allowing electrons excited by fluorescence to transfer to and from the DNA bases [29,74–76]. Chapter 4 will examine if this is the case with Alexa488 nucleospecific quenching.

1.5. Lab-On-A-Chip (LOC)

Lab-on-a-chip devices miniaturise and simplify lab-based diagnostics, in order to bring diagnostics closer to the patient. There is a growing private market for home-based testing that can be performed without medical or technical training, such as the now commonplace pregnancy tests, blood sugar level test for diabetics, BioSure HIV test or date rape drug test kits [34,77]. In the US alone the market for blood testing is worth billions of dollars per year, with similar markets for bacterial, viral and parasitic infection diagnosis, and an increasing market for genetic screening. The World Health Organisation publishes a list of Essential In Vitro Diagnostics to encourage more effective low cost diagnostics with Tuberculosis and HIV as priorities which will be discussed later as potential applications for this research [78,79].

1.5.1. Microfluidics

The field of microfluidics began with early devices miniaturising existing assays [80]. The compact size has many advantages, from saving money on equipment and work space, to the small reagent and sample volumes required, and researchers can exploit unique characteristics of fluids in small channels [80]. There are several emerging biotechnology applications including sequencing, synthesis of molecules, and the production and analysis of biomimetic vesicles for parasite research, or drug development which have emerged from this field [77,78,81–83].

1.5.2 DNA Microarrays for Diagnostics and Research

Microarrays allow multiplex DNA tests to be automatically carried out, however it requires a full laboratory, and training in the correct handling of reagents and samples [90]. Fluorescence is used to detect if the target DNA has bound or not to the microarray probe, although additional sequence information such as deletions or mismatches is unavailable [91].

Recent research has discovered that DNA from cancerous cells is more likely to adopt unique 3D structures due to epigenetic differences in methylation, and subsequently bind to gold particles [92]. Several paper and flow microfluidic strategies have been developed for separation of blood plasma from whole blood [81,93,94], which could be incorporated into

a single microfluidic platform to determine the presence of a cancer cell or infection with integrated DNA microarrays to identify specific cell types and aid identification of medical treatment regimes.

1.6. Aims and Objectives

A broad aim of this work is to develop a SAW-based microfluidics technique to perform amplification and detection of DNA strands specifically within a biological sample. As the fluidic manipulation of DNA has been developed separately, this thesis focuses on research for the optimisation and detection of DNA hybridization events. This has the potential to generate knowledge applicable to DNA processing (such as in PCR which relies on primers binding to targets) as well as detection (e.g. in DNA microarrays and melting analysis).

The thesis addresses the following objectives:

- Using SAW to affect DNA hybridization (using acoustic heating and streaming)
- Developing techniques to monitor these effects, focussed primarily on fluorescence
- Investigating nucleotide specific quenching effects linked to fluorophore tagging in melting curve analysis.

More specifically, the document is structured as follows:

Chapter 3 will:

- Design DNA oligonucleotides for the experiments, and simulate melt curves
- Confirm surface acoustic wave experimental methods, including temperature and fluorescence sensing and processing
- Examine the difference in melting temperature with surface acoustic waves with control systems

It was hoped that experiments using TIRF and FRET could be used to examine this further, but when the FRET experiments were started it became obvious that there was something additional to understand before continuing – the nucleobase-specific quenching (NB-S Quench) effect.

Chapter 4 will characterise the NB-S quench effect by

- Comparison with existing methods
- Modelling to explain melt curve change and direction
- Examining pH stability
- Investigating absorption and nearest base effects
- Comparing structural similarities with other fluorophores

Chapter 5 will use the Nucleobase-Specific (NB-S) quenching effect to:

- Quantify DNA concentration
- Identify multiple target sequences
- Amplify DNA using PCR and LAMP
- Incorporate into a microfluidic device

Chapter 6 will examine how these may be further examined in the future.

2. Materials and Methods

This chapter contains the methods and materials used, including protocols to calibrate the fabricated Resistance Temperature Devices (RTDs) and surface patterning. SAW devices are produced using Interdigitated Transducers (IDTs) which were designed then fabricated onto lithium niobate (LiNbO_3) using photolithography followed by metallisation with titanium and platinum. Temperature was measured using Resistance Temperature Devices which were designed and then fabricated using the photolithography method. The surfaces were further patterned and salinized in order to produce hydrophobic and hydrophilic patterns on the surface, allowing attachment of DNA via the linker molecule. Fluorescence was quantified using a fluorescence microscope, automated with temperature measurements in LabVIEW.

2.1. Materials

Reagents chemicals were obtained from Sigma Aldrich (Dorset, UK) unless otherwise stated in the text and below.

For microfabrication, S1818 photoresist was from Microposit (Paris, France) and M319 developer from Shipley (Marlborough, USA) and were used to pattern the substrates lithium niobate – 3 inch, 128° Y-cut wafers from Si-Mat (Kaufering, Germany) and superstrates of Menzel-Glaser Microscope slides and coverslips from ThermoFisher (Perth, UK) using photolithography.

For surface chemistry, APTES - (3-Aminopropyl)triethoxysilane and PFOTS - 1H,1H,2H,2H-Perfluorooctyl-trichlorosilane were from Merck (Darmstadt, Germany) and were used to obtain a hydrophilic and hydrophobic surface respectively. Sulfo-SMCC linker molecule - 4-(*N*-Maleimidomethyl) cyclohexane-1-carboxylic acid 3-sulfo-*N*-hydroxysuccinimide ester sodium salt (Sigma Aldrich, Dorset, UK) was used for DNA binding.

For the microfluidic devices, PDMS (Polydimethylsiloxane) was purchased from Sigma Aldrich (Dorset, UK).

For attaching electrical connections, Electrodag was used from Agar Scientific (Stansted, UK) and Blackspar superglue from Hamble Distribution (Glasgow, UK).

The LiNbO₃ substrates were coupled to the glass superstrates using lubricant KY Jelly (Thornton and Ross, Huddersfield)

Unmodified DNA oligonucleotides were purchased from Eurofins (Ebersberg, Germany), modified DNA oligonucleotides (thiolated, fluorescently labelled) were purchased from IDT (MA, USA). PCR amplification was performed with Brilliant 3 Ultrafast qPCR master mix with low ROX from Agilent (Stockport, UK). LAMP amplification was performed using ISO-004nd Master Mix from Optigene (Horsham, UK).

2.2 Buffers and Reagents

Tris-EDTA (tris(hydroxymethyl)aminomethane-ethylenediaminetetraacetic acid) pH 8.0 buffer was used from Sigma Aldrich (Dorset, UK). TE buffers of other pH were made in the laboratory at 10x strength - 15.759 g of Tris from Sigma Aldrich (Dorset, UK), 2.92 g of EDTA from Sigma Aldrich (Dorset, UK) were added to 800ml distilled water, then made up to 1 l. 1 ml of this stock was adjusted to the correct pH and made up to 10ml with distilled water for use.

PBS buffer was made in the laboratory – a 5 g PBS tablet from Gibco (MA, USA) was dissolved in 200 ml of distilled water, pH corrected using an Edge pH meter from Hanna Instruments (RI, USA), and then made up to 500 ml with distilled water.

Buffer pH was assured using a 2002 Edge pH Meter from Hanna Instruments (RI, USA) and further sterilised using a fume hood UV light for 1 hour before being used.

2.3. DNA

Chapter 3 examined the following DNA sequences in Table 2-1, from Optigene (Horsham, UK). As is convention, all sequences are written 5' to 3'. The DNA sequences were designed so as to vary the length, GC content and melting temperatures.

DNA	Sequence and Modification
A	GGG CCC CAG CGC CAA CAG TCG GCG CTT GTG CGC GGC GGC G
A-Complement	CGC CGC CGC GCA CAA GCG CCG ACT GTT GGC GCT GGG GCC C
B	GGG CCC CAG CGC CAA CAG TCG GCG CTT GTG CGC T
B-Complement	AGC GCA CAA GCG CCG ACT GTT GGC GCT GGG GCC C
C	GGG CCC CAG CGC CAA CAG TCG GCG CTT GTG
C-Complement	CAC AAG CGC CGA CTG TTG GCG CTG GGG CCC
D	GGG CCC CAG CGC CAA CAG TCG
D-Complement	CGA CTG TTG GCG CTG GGG GCC C

Table 2-1 Sequences of designed DNA sequences A, B, C and D.

DNA attached to the surface for section 2.6.2 was ordered from IDT DNA (Iowa, USA), with a thiol group on the primary strand to attach to the APTES via the Sulfo-SMCC linker molecule. The complementary strand was labelled with Cy5 for imaging. Sequences are in Table 2-2.

DNA	Sequence and Modification
Primary	GGG CCC CAG CGC CAA CAG TCG GCG CTT GTG - thiol
Complement	CAC AAG CGC CGA CTG TTG GCG CTG GGG CCC – Cy5

Table 2-2 DNA used to quantify surface attachment chemistry

For the FRET experiments in section 3.4, the primary strand was labelled with Alexa488, and the complementary strand was labelled with Alexa532 from IDT DNA (Iowa, USA) as in Table 2-3. Alexa488 or Alexa532 were covalently attached via NHS Ester chemistry (without additional carbon spacers). The oligo was synthesised with an amino modifier at

either the 5' or 3' end, this was then tagged with the required fluorophore. Controls were performed with unmodified DNA from Optigene (Horsham, UK). Alexa488 and 532 were chosen as FRET pairs as previously discussed and were placed so that they would be adjacent when the primary strand is attached to a surface.

DNA	Sequence and Modification
Primary	Alexa488 - GGG CCC CAG CGC CAA CAG TCG GCG CTT GTG - thiol
Complement	CAC AAG CGC CGA CTG TTG GCG CTG GGG CCC – Alexa532

Table 2-3 Alexa488 and Alexa532-modified DNA used for FRET experiments in section 3.4

For experiments examining completely double-stranded Alexa488-modified DNA (Table 2-4) in section 4.7.1. These are completely complementary.

DNA	Sequence and Modification
C	Alexa488-GGG CCC CAG CGC CAA CAG TCG GCG CTT GTG
C-Reverse	GGG CCC CAG CGC CAA CAG TCG GCG CTT GTG-Alexa488
D	Alexa488-GGG CCC CCA GCG CCA ACA GTC G
C-Complement	CAC AAG CGC CGA CTG TTG GCG CTG GGG CCC
D-Complement	CGA CTG TTG GCG CTG GGG GCC C

Table 2-4 DNA used for the Completely Double-Stranded DNA experiments in section 4.7.1

For experiments examining completely double-stranded DNA adjacent to the Alexa488 fluorophore (Table 2-4) in section 4.7.2

DNA	Sequence and Modification
C	Alexa488-GGG CCC CAG CGC CAA CAG TCG GCG CTT GTG
1-Complement	CGA CTG TTG GCG CTG GGG CCC
C-Reverse	GGG CCC CAG CGC CAA CAG TCG GCG CTT GTG-Alexa488
2-Complement	CAC AAG CGC CGA CTG TTG

Table 2-5 DNA used for the Completely Double-Stranded Adjacent to Fluorophore experiments in section 4.7.2.

For experiments examining single-stranded DNA adjacent to the fluorophore (Table 2-4) in section 4.7.2.

DNA	Sequence and Modification
3T	GGG CCC CAG CGC CAA CAG TCG GCG CTT GTG TTT-Alexa488
3-Complement	CAC AAG CGC CGA CTG TTG GCG CTG GGG CCC
C	Alexa488-GGG CCC CAG CGC CAA CAG TCG GCG CTT GTG
C-Reverse	GGG CCC CAG CGC CAA CAG TCG GCG CTT GTG-Alexa488
D	Alexa488-GGG CCC CCA GCG CCA ACA GTC G
3A/B -Complement	AAG CGC CGA CTG TTG GCG CTG GGG
6A/B -Complement	CGC CGA CTG TTG GCG CTG
9A-Complement	CGACTGTTGGCGCTGGGGCCC
9B/C/D -Complement	CGA CTG TTG GCG
12 -Complement	CGC CGA CTG TTG GCG CTG

Table 2-6 DNA used for Single-Stranded DNA Adjacent to the Fluorophore experiments in section 4.7.2.

Overview of combinations used to examine single-stranded DNA adjacent to the fluorophore in 4.7.2 is listed in Table 2-7.

Experiment	Alexa488-labelled DNA	Unlabelled Complement DNA
3A	C	3A/B -Complement
3B	C-Reverse	3A/B -Complement
3T	3T	3-Complement
6A	C	6A/B -Complement
6B	C-Reverse	6A/B -Complement
9A	C-Reverse	9A-Complement
9B	C	9B/C/D -Complement
9C	C-Reverse	9B/C/D -Complement
9D	D	9B/C/D -Complement
12	C	12 -Complement

Table 2-7 Combinations of DNA used for Single-Stranded DNA Adjacent to the Fluorophore experiments in section 4.7.2.

Template and primer sequences (Table 2-8) used for qPCR experiments in section 5.1.3 using Alexa488 based on modified BRAC1

DNA	Sequence and Modification
F3	TCC TTG AAC TTT GGT CTC C
Modified B3	Alexa488-GAG TTC ATA AAG GAA TTG ATA GC

Table 2-8 Modified BRAC1 sequences used in 5.1.3

Modified BRAC1 Template sequence:

1 TCCTGAACT TTGGTCTCCC AAAATGCTGG GATTATAGAT GTGAGCCACC
 1 AGGAACTTGA AACCAAGAGGG TTTTACGACC CTAATATCTA CACTCGGTGG

51 TCGCCTGGCC TCTGGTTCTG TTATTATCCC AATTTACAG ACTGGGGATA
 51 AGCGGACCGG AGACCAAGAC AATAATAGGG TTAAAGTGTC TGACCCCTAT

101 CTGAAACTGT GCAGCAGAAA GATTATTAAC TTGGGAGGCA GATAGGCTTA
 101 GACTTTGACA CGTCGTCTTT CTAATAATTG AACCTCCGT CTATCCGAAT

151 GACTCAAACC CTAATCTTCC ATTTACTTAC CAACTGTGCT ATCAATTCCT
 151 CTGAGTTTGG GATTAGAAGG TAAATGAATG GTTGACACGA TAGTTAAGGA

201 TTATGAACTC
 201 AATACTTGAG

Overview of DNA used to derive the melting temperatures of partially single-stranded DNA in 5.2 are listed in Table 2-9.

DNA	Sequence and Modification
C	Alexa488-GGG CCC CAG CGC CAA CAG TCG GCG CTT GTG
C-Complement	CAC AAG CGC CGA CTG TTG GCG CTG GGG CCC
-1 Complement	CAC AAG CGC CGA CTG TTG GCG CTG GGG CC
-2 Complement	CAC AAG CGC CGA CTG TTG GCG CTG GGG C
-3 Complement	CAC AAG CGC CGA CTG TTG GCG CTG GGG
-4 Complement	CAC AAG CGC CGA CTG TTG GCG CTG GG
-5 Complement	CAC AAG CGC CGA CTG TTG GCG CTG G
-6 Complement	CAC AAG CGC CGA CTG TTG GCG CTG

Table 2-9 DNA used for experiments to derive the melting temperature of partially single-stranded DNA in section 5.2

For experiments throughout Chapter 5 is listed in Table 2-10, BRCA1 DNA and unmodified template.

DNA	Sequence and Modification
F3	Alexa488-TCC TTG AAC TTT GGT CTC C
F3-Complement	GGA GAC CAA AGT TCA AGG A
B3	Alexa488-CAG TTC ATA AAG GAA TTG ATA GC
B3-Complement	GCT ATC AAT TCC TTT ATG AAC TG
LPR5F	Alexa488-AGG CAG ATA GGC TTA GAC TCA A
LPR5F-Complement	TTG AGT CTA AGC CTA TCT GCC T
LPF5B	Alexa488-AGA ACC AGA GGC CAG GCG AG
LPF5B-Complement	CTC GCC TGG CCT CTG GTT CT
FIP	Alexa488- ATC CCC AGT CTG TGA AAT TGG GCA AAA TGC TGG GAT TAT AGA TGT
FIP-Complement	ACA TCT ATA ATC CCA GCA TTT TGC CCA ATT TCA CAG ACT GGG GAT
BIP	Alexa488- GCA GCA GAA AGA TTA TTA ACT TGG GAG TTG GTA AGT AAA TGG AAG A
BIP-Complement	TCT TCC ATT TAC TTA CCA ACT CCC AAG TTA ATA ATC TTT CTG CTG C

Table 2-10 DNA used for Chapter 5 experiments, including BRAC1 primers

Unmodified BRCA1 template sequence

1 TCCTTGA ACT TTGGTCTCCC AAAATGCTGG GATTATAGAT GTGAGCCACC
1 AGGAACTTGA AACCCAGAGGG TTTTACGACC CTAATATCTA CACTCGGTGG

51 TCGCCTGGCC TCTGGTTCTG TTATTATCCC AATTCACAG ACTGGGGATA
51 AGCGGACCGG AGACCAAGAC AATAATAGGG TTAAAGTGTC TGACCCCTAT

101 CTGAAACTGT GCAGCAGAAA GATTATTAAC TTGGGAGGCA GATAGGCTTA
101 GACTTTGACA CGTCGTCTTT CTAATAATTG AACCCCTCCGT CTATCCGAAT

151 GACTCAAACC CTAATCTTCC ATTTACTTAC CAACTGTGCT ATCAATTCCT
151 CTGAGTTTGG GATTAGAAGG TAAATGAATG GTTGACACGA TAGTTAAGGA

201 TTATGAACTG
201 AATACTTGAC

2.4. Equipment

For microfabrication, equipment included a Headway Research (Texas, USA) PWM32 spinner for applying resist, a mask aligner from Microtec UV MA6 from Karl Suss (Andover, UK), Plasmafab505 plasma asher from Electrotech (Bristol, UK) and Plassys MEB 400S Electron Beam Evaporator from UK Photonics (Glasgow, UK).

For SAW experiments, the frequency response of fabricated IDTs were extracted with an E5071C ENA series network analyser from Agilent Technologies (California, USA), and the frequency provided by a TG5011 function generator from Aim-TTi (Huntingdon, UK) and a ZHL-5W-1 amplifier from Mini-circuits (New York, USA).

Microfluidics experiments required two New Era 1000 Syringe Pumps (NY, USA) and μ -Slide 4 wells with glass bottom from Ibidi (Planegg, Germany).

For the both fluorescence measurements a Grasshopper 3 monochrome camera was used from FLIR (Kent, UK).

For temperature measurements a Type J Thermocouple was from Omega, (Manchester, UK) was used in conjunction with a TC-08 Thermocouple Data Logger from Pico Technologies (St Neots, UK), whilst the resistance of fabricated RTDs was measured using a USB-4065 Digital Multimeter from National Instruments (Berkshire, UK).

The microscopes used were a Scope A1 (upright, used most experiments) or the Axio Observer Z1 (inverted, used in TIRF experiments) both from Zeiss (Jena, Germany).

For DNA experiments, concentration was quantified using a Nanodrop 1000 from Thermofisher (MA, USA) and size/mass quantified using a Bioanalyzer 1000 from Agilent (Stockport, UK). DNA amplification and melt curve analysis was performed in the 7500 FAST qPCR machine from Applied Biosystems (CA, USA). Absorbance was measured using a Synergy HTX Absorbance Reader from Biotek (VT, USA). The pH of buffers was measured using a 2002 Edge pH Meter from Hanna Instruments (RI, USA).

2.5. Methods

2.5.1. Microfabrication of IDTs, RTDs and Microfluidic Devices

2.5.1.1. Interdigitated Transducers (IDTs)

An Interdigitated Transducer (IDT) for a low frequency was designed for ultrasonic generation with a finger gap of $225\mu\text{m}$ which should work at 4.41MHz , with the parameters listed in Table 2-11 and illustrated in Figure 2-1. The wavelength of the resultant SAW depends on distance between each IDT finger (kept constant) and the speed of sound on lithium niobate (LiNbO_3) of 3995ms^{-1} [6,45,127].

Frequency	4.407 MHz
Number of fingers	30
Finger width	$225\mu\text{m}$
Finger gap	$225\mu\text{m}$
Finger length	$700\mu\text{m}$
Aperture	$10000\mu\text{m}$
Contact pad width	$3000\mu\text{m}$
Gap to contact pad	$300\mu\text{m}$

Table 2-11 Design parameters for fabricated IDTs, including frequency.

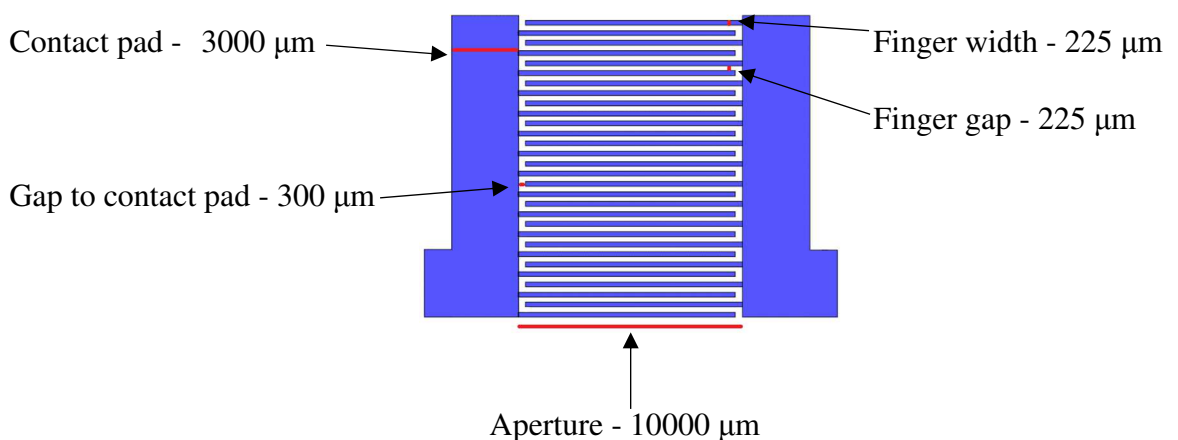


Figure 2-1 Figure showing IDT design parameters aperture ($10000\mu\text{m}$), gap to contact pad ($300\mu\text{m}$), contact pad ($3000\mu\text{m}$), finger width ($225\mu\text{m}$) and finger gap ($225\mu\text{m}$).

IDTs were fabricated on 128-Y cut 3inch LiNbO₃ wafers (Si-Mat, Kaufering, Germany) in the University of Glasgow's James Watt Nanofabrication Centre. The LiNbO₃ was cleaned in sonicator (3min acetone, 3min methanol, 3min IPA) and ashed in a Plasmafab505 plasma asher (Electrotech, Bristol, UK) for 2min at 100W) to remove organic contamination.

S1818 photoresist (Microposit, Paris, France) was applied by spinning (30seconds, 4000rpm) which should result in an 18nm layer as per manufacturers protocols, dried on a hotplate (1min, 80°C) and patterned (4-6seconds) using UV light on Karl Suss Microtec MA6 (UK) through a predesigned acetate mask.

The pattern was developed using M319 developer (Shipley, Marlborough, MA) for 75 seconds, washed with RO water and dried using nitrogen before being cleaned in a Plasmafab505 plasma asher (Electrotech, Bristol, UK) for 2min at 100W to clean the surface to allow metal deposition [45,128].

10nm of titanium and 100nm of platinum were coated using Plassys MEB 400S Electron Beam Evaporator (UK Photonics). Samples were cleaned again as above to remove remaining S1818, and metal bound to the resist.

2.5.1.2 Surface Acoustic Waves (SAW)

Working frequencies were extracted using an Agilent Technologies E5071C ENA series network analyser. Microscope coverslip superstrate with calibrated RTDs were coupled to the LiNbO₃ substrate with KY Jelly (Thornton and Ross, Huddersfield) and electrical connections were made using Electrodag (Agar scientific, UK) and superglue (Blacksparr, Hamble). The LiNbO₃ was fixed with thermal paste to a copper heatsink to avoid overheating. A TTI TG5011 function generator was attached to a Mini-circuits ZHL-5W-1 amplifier to provide the signal for the IDT.

2.5.1.3. Resistance Temperature Devices (RTDs) Design and Fabrication

Preliminary experiments used thermocouples (type J) to measure temperatures but when it was found that SAW waves disrupt thermocouples (, it was decided to use Pt100 Resistance Temperature Devices [129,130].

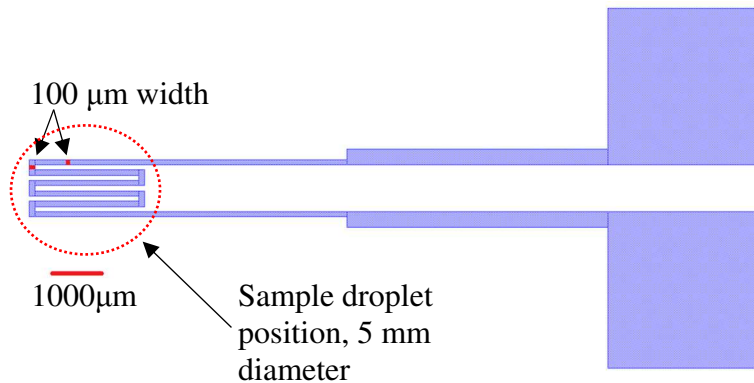


Figure 2-2 Mask design for resistance temperature device (RTD). The width of the smallest feature is 100 μm . This mask was used during photolithography, the coloured area remains clear from resist allowing metal (10nm titanium, 100nm platinum) to be deposited

RTDs were fabricated onto 128-Y cut 3-inch LiNbO_3 wafers, microscope slides or coverslips in the University of Glasgow's JWNC clean room facility. The substrate was cleaned in sonicator (3 min acetone, 3 min methanol, 3 min IPA) then 18nm (not measured, as per Microposit protocols) of S1818 photoresist (Microposit, Paris, France) was applied by spinning (30 secs, 4000rpm), dried on a hotplate (1 min, 80°C) and patterned (4-6 secs) using UV light on Karl Suss Microtec MA6 (UK). The pattern was developed using M319 developer (Shipley, Marlborough, MA) for 75 secs, washed with RO (Gibco, UK) water and dried before cleaned in a plasma asher (2 min, 100W). 10nm of titanium and 100nm of platinum were coated using Plassys MEB 400S Electron Beam Evaporator (UK Photonics). Samples were cleaned again as described above to remove the S1818, and any metal bound to the resist, cycled between room temperature and 200°C in an oven. Resistance readings were taken using a National Instruments USB-4065 digital multimeter (Berkshire, UK) at 25°C, as shown in Figure 2-15. As stated, RTDs and IDTs on LiNbO_3 were fabricated at the same time for some experiments.

2.5.1.4. RTD Calibration

Several strategies were devised to calibrate the RTD against a Type J thermocouple, three were examined and termed “Slow”, “Hot Quick” and “Quick Cool”. For all strategies 20 μ l of mineral oil is pipetted onto the substrate on the RTD and the thermocouple tip is then carefully positioned within the mineral oil but not in contact with the surface. Additional data points will always result in increased accuracy and require increased time. Heating LiNbO₃ repeatedly strains the structure of the substrate inducing cracks and breaks, so cooling for calibration was proposed using the Peltier module. Each experiment relied on 20-30 cycles, if the “Slow” calibration were performed in between every cycle then each experiment would take 3-4 days of continuous heating and cooling, severely reducing the viability of the DNA, reporter molecules and LiNbO₃. The Peltier can cool to 10-15°C below room temperature after which additional power input results in heating which overcomes the cooling, raising the temperature of the system.

For the “Slow” calibration method temperatures of between 10°C and 110°C are used, with the calibration taking around 2-3 hours (Figure 2-18 A). The Peltier was used to slowly cool the substrate to as close to 10°C as possible before being heated to 110°C, at a rate of ~2°C per minute. Whilst this is accurate, a quicker calibration method was investigated so that the calibration could be checked after and between experiments.

For the “Hot Quick” method the substrate is quickly heated to around 100°C at experimental power settings by turning the Peltier on to maximum heating (12.5V, 2Amp). Once the thermocouple shows the temperature was around 100°C the Peltier connections were reversed and maximum cooling (12.5V, 2Amp) used to return the chip to ambient temperatures.

This compared favourably with the slow method, but fast heating and cooling cycles are known to stress LiNbO₃ resulting in breaking of the substrate, so this method is not best for the longevity of the test chip.

Another method, termed Quick Cool, was devised where the chip was slowly cycled between room temperature and 10-15°C below room temperature repeatedly (Figure 2-18 B). This reduced stress on the chip, was significantly faster at around 20 minutes than the slow method, and gave a calibration that was at most within 0.45°C (0-100°C), 0.3°C of the relevant melting temperatures (70°C-80°C), of the Slow method (Figure 2-19).

2.5.1.5. Microfluidic Devices

Microfluidics experiments were performed with upright microscope described in 2.4, the 5ml syringes were pumped using New Era Syringe Pump (Farmingdale, NY).

First Generation:

A 100 μ l volume open well type device was built, using one well of a “ μ -Slide 4 well” with glass bottom (Ibidi, Germany). Outflow from the open well to a pump was added just above the base (~2mm) of the well. Temperature was measured using a type-J thermocouple inserted into the channel. DNA was attached to an 8mm by 8mm coverslip (ThermoFisher, UK) as per the protocol in section 2.5.2 and placed on the bottom of the well. This open well design was chosen due to ease of use - the thermocouple could be placed within the well, flow rate could be controlled, and the DNA sample could be easily placed in the well.

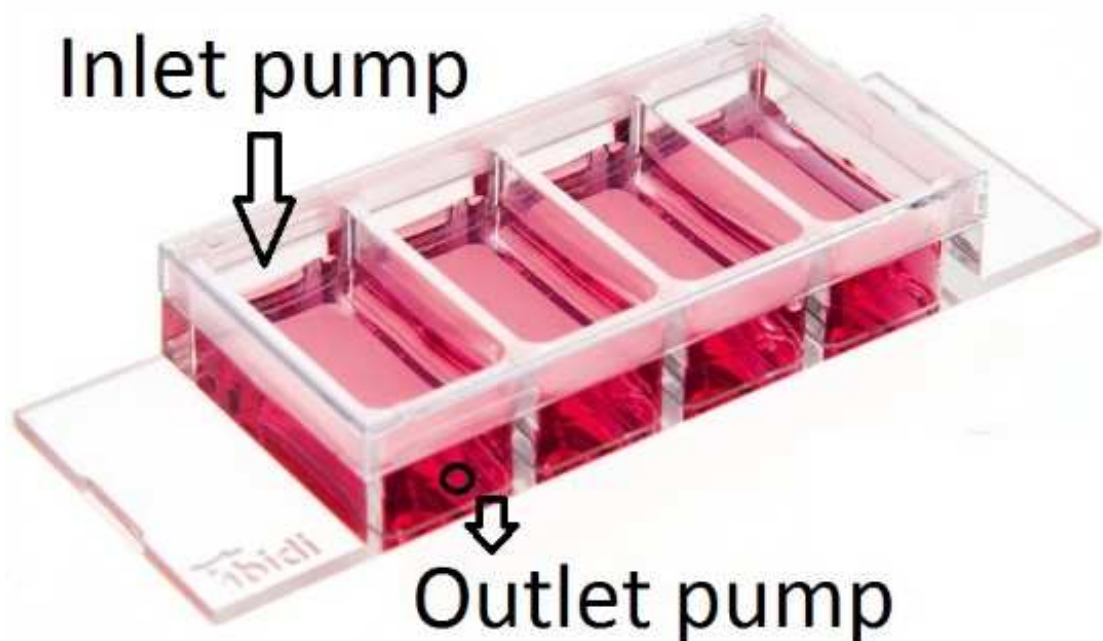


Figure 2-3 Figure showing the construction of the First Generation microfluidic device (image modified with permission from Ibidi).

TE buffer (pH 7.8) was flowed into the well at a rate of 20 $\mu\text{l}/\text{min}$ by a New Era 1000 Syringe Pump (NY, USA). After 5min the pump to remove the buffer from the well was started, also at a rate of 20 $\mu\text{l}/\text{min}$, in order to keep the volume of buffer in the system at 100 μl . This was run for 10 minutes at the beginning so that the volume in the chamber was steady and non-specifically bound DNA would be extracted to the waste outlet.

Once the experiment was begun, every 10 minutes the drainage pump was paused for a minute and 20 μl samples were removed by pipette from the well before the drainage pump was restarted, allowing sampling of the buffer at these time points. Each sample was split into 2 so that DNA concentration of these samples was measured on 10 μl with the ThermoFisher Nanodrop 1000, melt curves performed 10 μl with 1 μl EvaGreen to look for double stranded DNA on the ABI 7500 PCR machine, and melt curves with the non-labelled probe strand with EvaGreen to look for single-stranded DNA again with the ABI 7500 PCR machine.

3 control samples were taken at 10, 20, 30 minutes. At 40 minutes the inflow pump was paused for 30 seconds and 10 μl of 100 μM unlabelled complementary strand was added so that the final concentration of the complementary DNA in the well was 10 μM / 9.21 μg (MW 9210). The well was heated using a Peltier module, varied up to 2amp / 10volts until the temperature reached 95°C. During the control experiments it was noted that the heating was relatively rapid, and so this was slowed down and better controlled in the final experiments.

Second Generation:

A single input and single output PMDS microfluidic device was designed with a 1 cm^2 chamber in the middle where the 8 mm by 8 mm coverslip with DNA attached (as in the first generation) was placed, as per published protocols [131–134]. The PDMS device was fabricated from a mould that was formed by photolithography – silicon wafer was cleaned as above, then a 50 μm layer of SU8-3050 was patterned with UV by an MA6 (Karl Suss, UK), developed in Microposit EC solvent (Shipley, MA, USA) and silanised using PFOTS (Sigma Aldrich, UK).

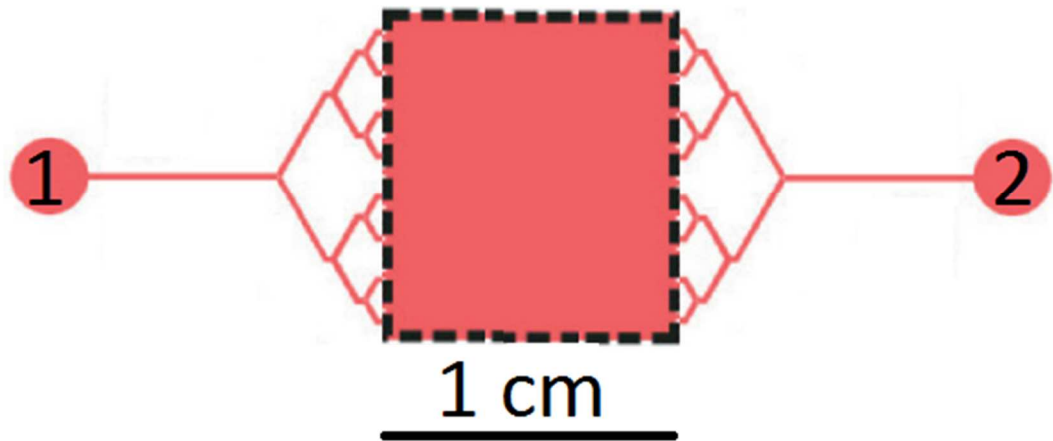


Figure 2-4 Illustration of the design of the Second Generation microfluidic device showing the inflow connection (1), the outflow (2), and the 1cm^2 reaction chamber shown by a dotted line.

The resultant PDMS device and a microscope slide were cleaned for 5 minutes at 100W in a Plasmafab505 plasma asher (Electrotech, Bristol, UK), before bonding these together the DNA coverslip was introduced in between the microscope slide and the PDMS device. The chamber was filled with TE pH 7.8 buffer, then washed through with the same buffer at a rate of $20\mu\text{l}/\text{min}$ for several minutes, whilst the outflow was collected.

2.5.2. Surface Patterning Chemistry

2.5.2.1. Hydrophobic and Hydrophilic Surface Patterning

The surface was patterned to keep the sample only on top of the RTD without spreading across the whole surface to ensure accurate temperature readings. A hydrophobic silane, PFOTS 1H,1H,2H,2H-Perfluorooctyl-trichlorosilane (MERCK, UK) [50,135–138], and a hydrophilic silane APTES (3-Aminopropyl)triethoxysilane (MERCK, UK) [137,139–142] were chosen based on previous work [50,135–137,139,141,142] and the structures are shown below in Figure 2-6 and Figure 2-5. APTES allows DNA attachment using a linker molecule to thiolated DNA as discussed below in section 2.5.2.2

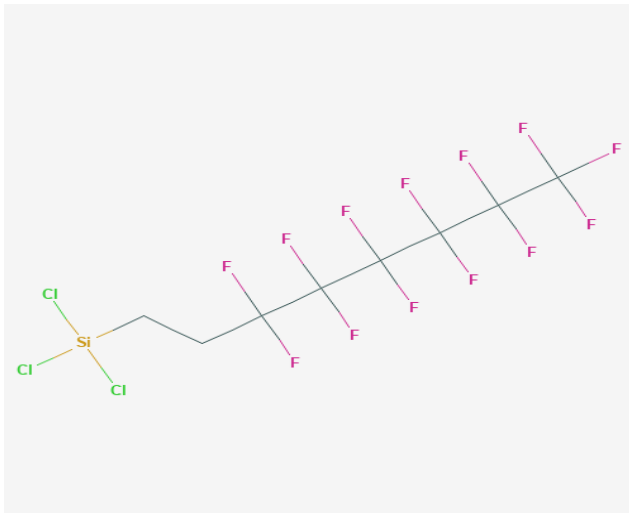


Figure 2-5 Chemical structure of PFOTS silane 1H,1H,2H,2H-Perfluorooctyl-trichlorosilane (reproduced from MERCK, UK). The trichloro binds the molecule to glass and lithium niobate, whilst the 13 fluorine molecules are exposed above, creating a highly hydrophobic environment.

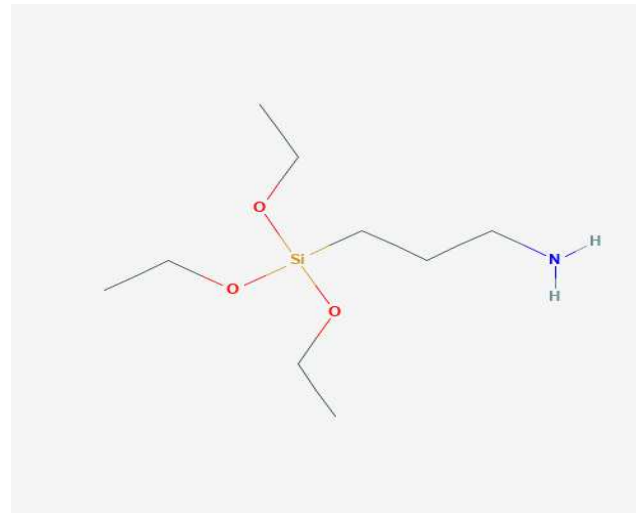


Figure 2-6 Chemical structure of APTES silane (3-Aminopropyl) triethoxysilane (reproduced from MERCK, UK). The triethoxy binds the molecule to glass and lithium niobate whilst the amino group is exposed creating a highly hydrophilic environment. The amino group is also used for DNA attachment via the Sulfo-SMCC linker molecule (see section 0)

Samples were patterned as described in sections 2.5.1.1 – 2.5.1.3 with s1818 photoresist (Microposit, Paris, France), plasma ashed (2min, 100W). 5µl of silane was placed with the sample in a vacuum desiccator for one hour, after which the sample was incubated at 60°C to encourage cross-linking monolayers. The sample was then cleaned by washing in acetone for 3 min, methanol for 3 min, IPA for 3min and RO water for 3 min, then dried using N₂ gas.

These experiments required a hydrophilic circle with a 5mm diameter on the superstrate to keep the droplet in place and enable DNA binding. If the hydrophobic silane PFOTS is applied first, no further patterning with S1818 can occur – the high hydrophobicity results in a near-complete loss of S1818 resist when it is subsequently spun on to coat the surface.

The cleaned surface (as described above) was silanised with APTES, and a 5mm diameter circle was patterned above this with S1818 to protect the APTES underneath. As APTES is hydrophilic, this resulted in a slightly thicker layer of S1818 resist, requiring a longer (6.5 seconds) MA6 exposure and additional (90 secs) development time.

After this the APTES around the circle was removed by ashing (2W, 60 secs) which did not significantly degrade the S1818 circle, and the surface was silanised with PFOTS as described above. Lastly the superstrate was cleaned as described above, removing the S1818, leaving a 5mm diameter hydrophilic circle surrounded by a hydrophobic surface.

2.5.2.2. DNA Attachment Chemistry

Thiolated DNA was attached to APTES on the surface of the glass superstrate via a Sulfo-SMCC linker, sequences detailed in Table 2-2. A 5mm diameter circle patterned using S1818 photolithography as described in section 2.5.1.1 before being silanised with PFOTS and APTES as described in section 2.5.1.3. Sulfo-SMCC sulfosuccinimidyl 4-(N-maleimidomethyl)cyclohexane-1-carboxylate (ThermoFisher, Cambridge, UK) was used as a linker as per literature [15,143–146] and shown in Figure 2-7.

1mM sulfo-SMCC (ThermoFisher, Cambridge, UK) PBS pH 9.0 solution was incubated where the APTES is bound for 2 hours. Unbound linker was rinsed off with 3 washes of PBS. 10 μ l of 10 μ M thiolated DNA in 7.8pH TE buffer (Merck, UK) was then incubated for 2 hours at 4°C. The sample was then rinsed 3 times with additional TE buffer to remove unbound DNA. 10 μ l of 10 μ M Cy5-labelled complementary DNA in 7.8pH TE buffer (Merck, UK) was then incubated for 30 minutes at 4°C, unbound DNA was rinsed off with TE buffer as before. This protocol was based on ThermoFisher Sulfo-SMCC manual, and antibody attachment protocols [147,148]. To ensure DNA binding chemistry, controls were performed using DNA with a Cy5 fluorescent tag that could be imaged.

For DNA attached to the 8 mm by 8mm microscope slide coverslip for the microfluidic devices in section 2.5.1.5 the surface was only silanised with APTES without prior S1818 patterning as a circle was not required to keep a droplet in place. DNA for the microfluidic devices was thiolated at the 5' end and labelled with Alexa488 fluorophore on the 3' end and attached as above.

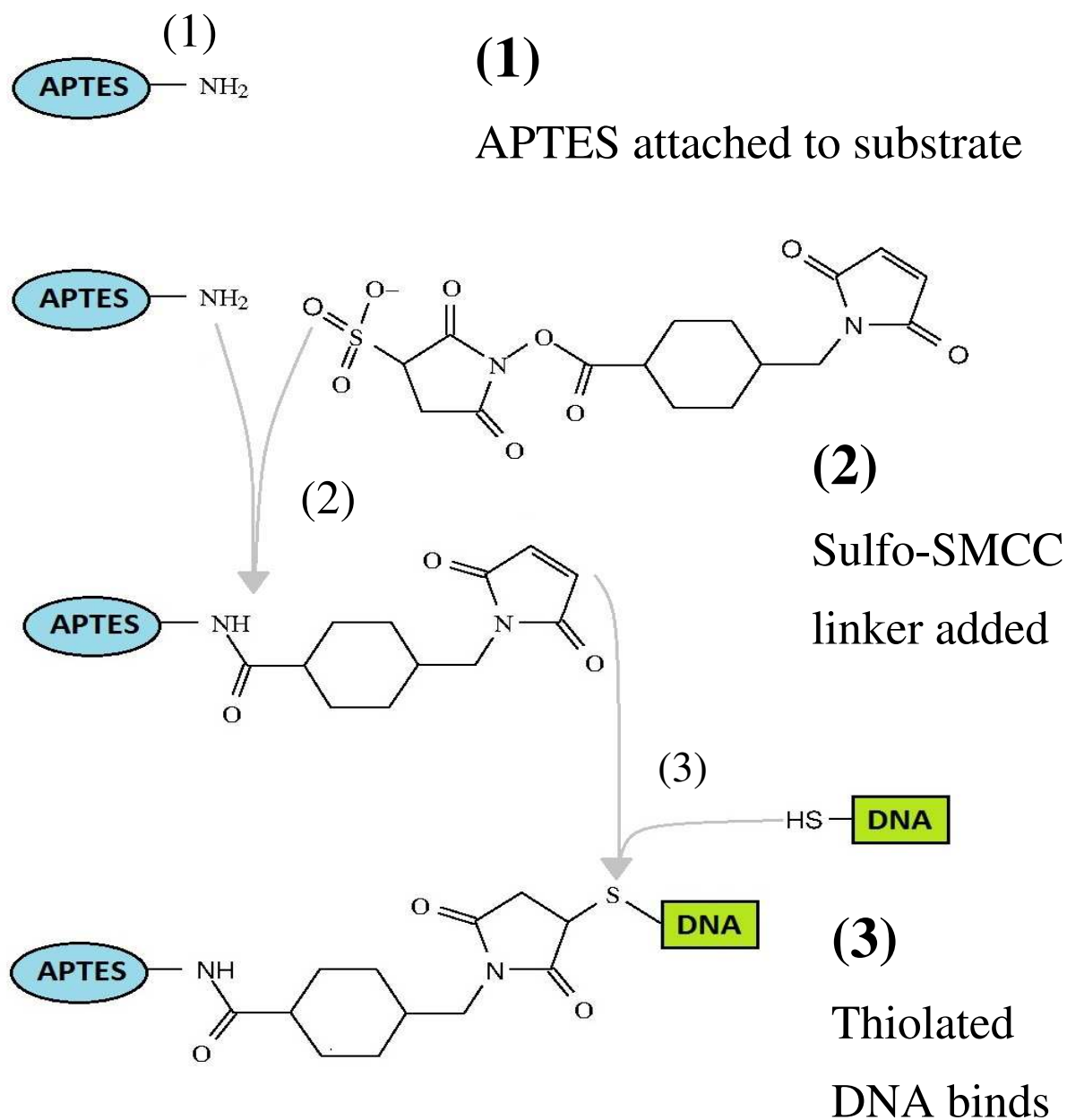


Figure 2-7 DNA attachment using Sulfo-SMCC sulfosuccinimidyl 4-(N-maleimidomethyl)cyclohexane-1-carboxylate (ThermoFisher, Cambridge, UK) and APTES (3-Aminopropyl)triethoxysilane (MERCK, UK). Step 1 is to bind the APTES to the substrate (glass or LiNbO₃). Step 2 joins the Sulfo-SMCC to the APTES/surface. Step 3 binds the thiolated DNA.

2.5.3. DNA design, melt curves, amplification

2.5.3.1. DNA design

The melting temperature (T_m) of DNA is dependent on the length and sequence (GC content, mismatches/insertions/deletions). Unmodified DNA was ordered from Optigene (Horsham, UK), see Table 2-12 and Table 2-1. Modified DNA was ordered from IDT DNA (Iowa, USA) and were thiolated for surface attachment, the complementary strand was labelled with Cy5, FITC, ATTO488 or Alexa488 for quantification.

Name	Melting Temperature (predicted)	GC Content (%)	Bases	Mass (Daltons)
A	84.7	80	40	27120
B	79.6	74	34	23030
C	62.2	73	30	20320
D	40.0	76	21	14230

Table 2-12 Predicted melting temperature, GC content, length and estimated mass (GC+backbone = 680Da, AT+backbone = 670Da)

2.5.3.2. Software Predicted DNA Melt Curves

Melting of DNA oligonucleotides A, B, C and D (Table 2-12 and Table 2-1) were predicted using uMelt (University of Utah, v2.0.2) software based on sequence [149]. Sequence and conditions are used to calculate relative helicity with respect to temperature. Calculations used Weber (Bioinformatics, 2015) thermodynamic set, 20mM monovalent cation concentration, 3mM Mg^{2+} concentration, 0% DMSO and Owczarzy (2008) salt correction. To predict the melt curves with differing salt concentrations, the monovalent cation concentration was set to 10mM, 20mM, 50mM, 100mM and 200mM.

2.5.3.3. Measured DNA Melt Curves

ABI 7500 controls

Melt curves and melting temperatures (Figure 2-25) were obtained using the 10 μ l of 10 μ M DNA in pH 7.8 TE buffer on an ABI 7500 real time fast PCR (ThermoFisher, UK) machine using 7500 software v2.0.6 using EvaGreen as the reporter molecule [14,150]. EvaGreen controls included 1 μ l of 20x EvaGreen. The temperature was increased by 1 $^{\circ}$ C per minute from 20 $^{\circ}$ C to 95 $^{\circ}$ C with three readings taken per $^{\circ}$ C. DNA was ordered through Eurofins EU and was rehydrated with ThermoFisher Nuclease Free water.

These experiments act as a control for the experimental setup which uses droplet fluorescence microscopy with a calibrated RTD to measure temperature and are analysed using OriginPro sigmoidal curve fitting. If the results from the fluorescence microscope using the Peltier module had differed significantly from those found with the commercial PCR machine, then further improvement and validation would be required before it could be used for SAW.

Peltier module controls

Melting temperatures (Figure 3-6) of 1 μ l of 10 μ M DNA with 10 μ M EvaGreen as the reporter molecule in 20 μ l of mineral oil detailed in the materials and methods on the upright microscope (section 2.4). Samples were heated using a Peltier module (5W). All measurements were taken using the automated LabVIEW program, and subsequently analysed using Origin2016 sigmoidal curve fitting and peak identification. Peltier heating controls can be performed between SAW heating to ascertain if there are permanent changes to the DNA due to SAW.

2.5.3.4. OriginPro Curve Fitting of Measured Melt Curves

OriginPro (2016) was used to plot and analyse the data produced by the fluorescence microscopes. As DNA transitions between two states – dsDNA and ssDNA – the Poisson-Boltzmann equation is used. The Sigmoidal fit function is used to align a Boltzmann curve to the melt data, and the 1st derivative plotted to allow melt peak melting temperature identification. OriginPro Peakfinding feature was used to identify peaks and calculate statistics on area.

2.5.4 DNA Amplification

2.5.4.1. PCR

100 μ M primers and 1ng/ μ l template DNA were ordered from Eurofins (Hamburg, Germany). 0.2 μ l of the forward primer (100 μ M), 0.2 μ l of the reverse primer (100 μ M) and 5 μ l of template DNA (1 ng / μ l) all from Eurofins (Germany) were added to 15 μ l of Mastermix (Brilliant 3 Ultrafast qPCR master mix with low ROX, Agilent, UK) with an additional 0.6 μ l of TE buffer (pH7.8) to give a final volume of 30 μ l per reaction. To amplify the DNA by PCR, a denaturing step at 95°C for 1 min was followed by 20 cycles of the PCR steps (60°C for 20sec for primers to anneal, 72°C for 1 min for DNA extension, 95°C for 20 secs to melt DNA strands) with the fluorescence quantified each cycle.

Afterwards amplification a melt curve from 25 to 95°C (1°C increase per min, 3 fluorescence readings per °C) was performed. Both the amplification and melt curve were performed in the ABI 7500 Fast PCR Machine (ThermoFisher, UK) [27].

2.5.4.2. LAMP

100 μ M LAMP primers and 1ng/ μ l template DNA were ordered from Eurofins (Hamburg, Germany). The primer concentrations were originally based on previous literature concentrations. These primers were further varied in pairs, F3 with B3, FIP with BIP, LPR5F with LPF5B, to confirm that they are optimum – defined as the time for the amplification curve to reach the midpoint between the start of amplification and the end of amplification. The following volumes were used for the BRAC LAMP Primer Mix: 0.2 μ l F3, 0.2 μ l B3, 0.8 μ l FIP, 0.8 μ l BIP, 1.0 μ l LPR5F, 1.0 μ l LPF5B. This BRAC LAMP Primer Mix (total volume 4 μ l) was added to 5 μ l Template DNA (Eurofins, Germany), 15 μ l Master Mix (ISO-004nd, Optigene, UK) with 1.0 μ l dH₂O (Agilent, UK) to give a final reaction volume of 30 μ l. To perform amplify the DNA by LAMP, this was heated at 60°C for 20 min, with fluorescence quantified every minute.

Afterwards amplification a melt curve from 25 to 95°C (1°C increase per min, 3 fluorescence readings per °C) was performed. Both the amplification and melt curve were performed in the ABI 7500 Fast PCR Machine (ThermoFisher, UK) [41].

Further analysis to quantify the concentration of the final product was performed on the Nanodrop (ThermoFisher, UK), and the size and concentration of products was also examined using the Agilent 2100 Bioanalyzer (1µl sample run on DNA 1000 kit)

2.5.5. Fluorescence and Absorbance

2.5.5.1. Fluorescence Microscopy

An upright Scope A1 microscope from Zeiss (Jena, Germany) with a 20x objective (NA0.4) was used for all experiments apart from TIRF. The TIRF experiments were performed with an Axio Observer Z1 inverted microscope from Zeiss (Jena, Germany) with a 20x objective (NA0.4), connected to a Coherent (CA, USA) 0.45µm laser. Both microscope systems quantified fluorescence with the Grasshopper 3 monochrome camera (FLIR, UK). Temperature measured with a calibrated RTD device. Fluorescence and temperature were both recorded using LabVIEW and the melt curves analysed using OriginPro (2016).

2.5.5.2. Absorbance

10 µM DNA were prepared in 7.8pH TE buffer. Melt curves were confirmed using Applied Biosciences 7500 Fast PCR machine as a control. The absorbance (5 replicates of 1µl sample) was measured in 1nm steps from 400-600nm using Synergy HTX Absorbance Reader from Biotek (VT, USA). Readings were calibrated relative to 400nm and an average spectrum from the 5 replicates produced using OriginPro2016. OriginPro2016 was also used to measure peak height, peak wavelength, and area under the peak.

2.5.6. LabVIEW Automation

In order calculate DNA melt curves, precise measurements of temperature and fluorescence were automated with LabVIEW (2016) using the Zeiss inverted microscope, Grasshopper 3 camera (FLIR, UK), TC-08 thermocouple adapter (Pico, UK) and NI 4065 USB multimeter (NI, UK). In order to calibrate the RTDs against a type-J thermocouple (Omega, UK), and perform the experiments, a program was written in LabVIEW to automate this and save the data for analysis (see interface in Figure 2-8).

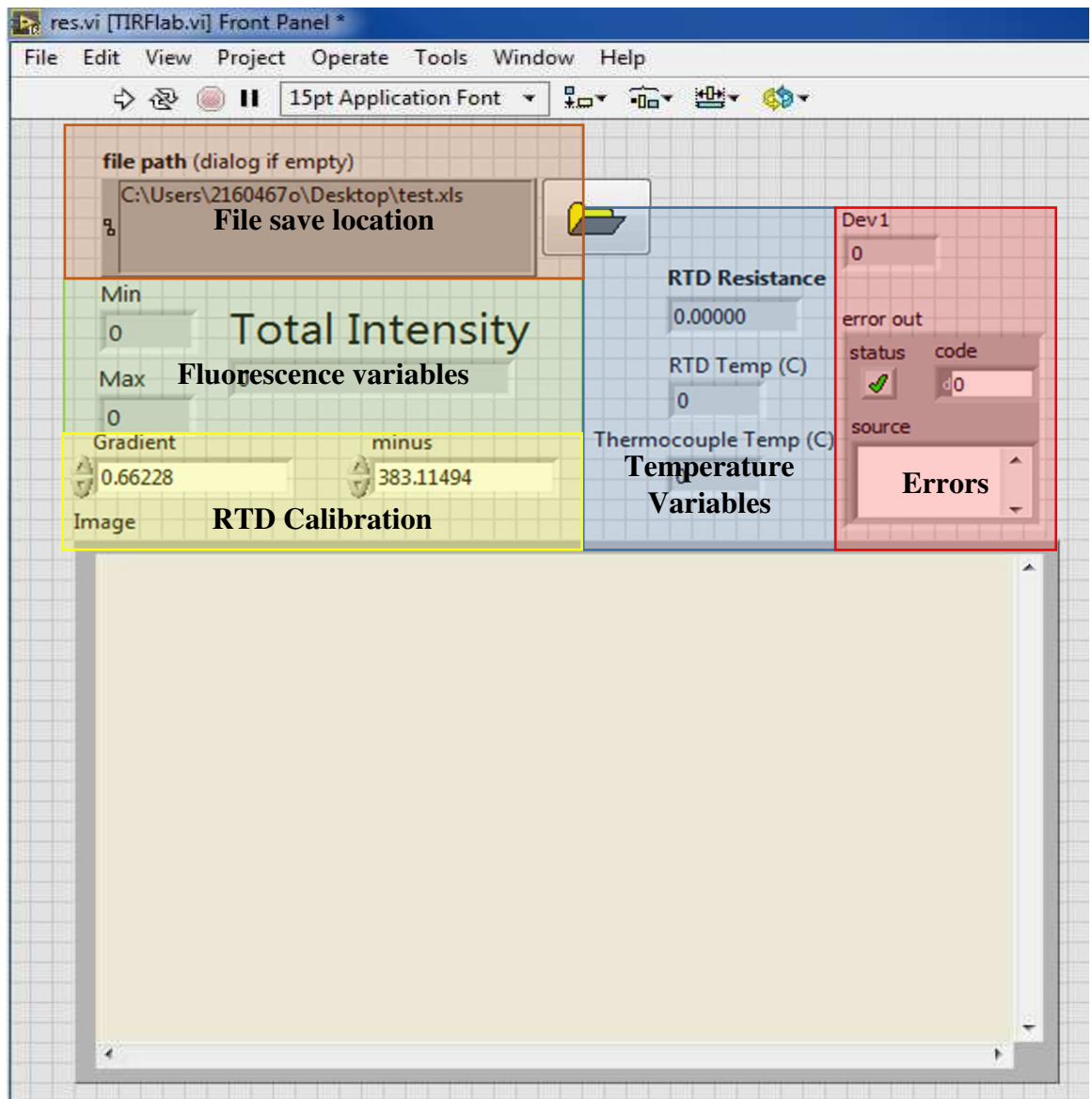


Figure 2-8 Interface of the LabVIEW software written to automate the calibration and experiments for this thesis. The RTD resistance and Thermocouple Temperature are used for calibration, once this is achieved the calibration can be set (“Gradient” and “minus”) so that for experiments the RTD Temperature is automatically calculated. These variables are combined with the fluorescence variables and saved as a spreadsheet file.

In order to measure temperature, the Type-J Thermocouple was connected to a TC-08 USB data logger was interfaced using the manufacturer’s LabView program, the thermocouple temperature is sampled every 100ms and this variable was made available on the interface and saved as part of the experimental results file. The resistance from the USB resist meter is recorded using NI-DMM/Switch Express at intervals of 100ms, variables and formula were added so that, once calibrated, the correct RTD temperature is automatically calculated on the interface (Figure 2-9).

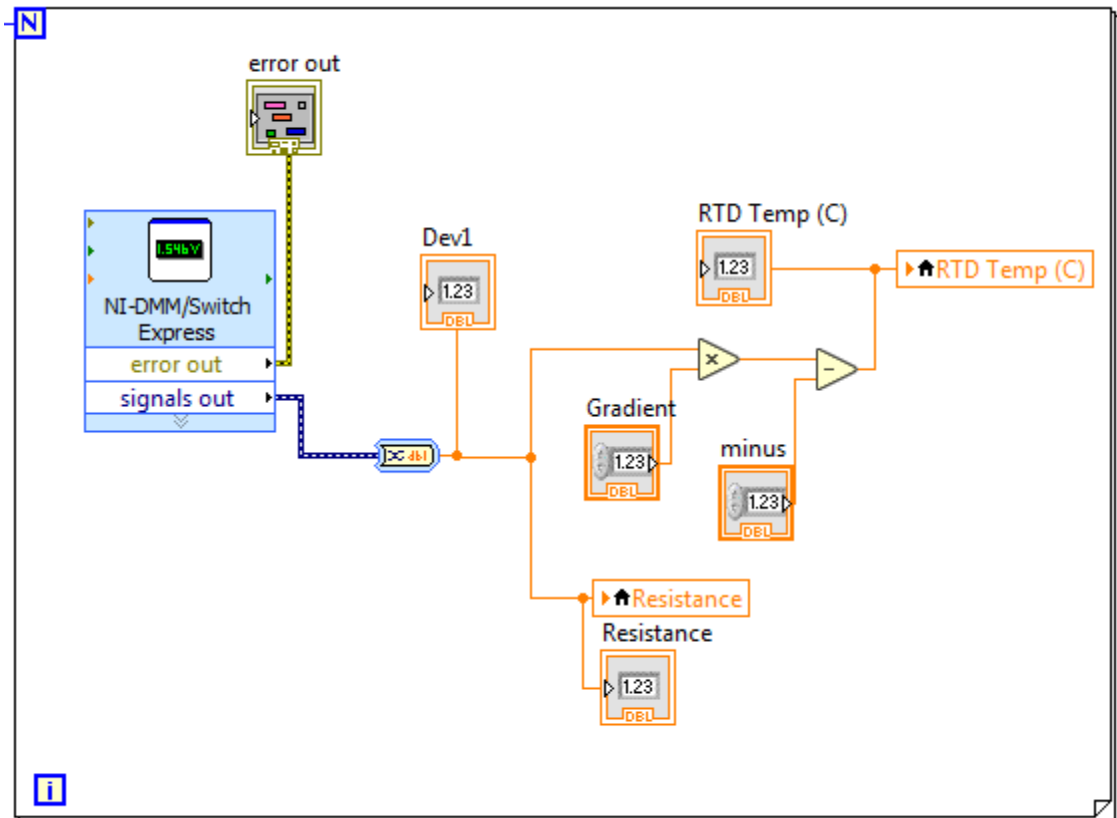


Figure 2-9 Resistance from the RTD is saved as a variable, processed with the calibration data (“Resistance” and “minus”), so that the RTD temperature is available on the interface. This is also exported to the spreadsheet.

For fluorescence, NI Vision Builder 2014 was used to create the subroutine to collect 100 fluorescence readings per second, which were converted into monochrome to allow the total fluorescence across the image, minimum pixel values, maximum pixel values (to ensure that no pixels are saturated) and standard deviation to be extracted from each frame (Figure 2-10). These variables are available directly to the experimenter and are also saved as part of the final experiment results file. Colour video is available, and images can be saved directly from the interface (Figure 2-8).

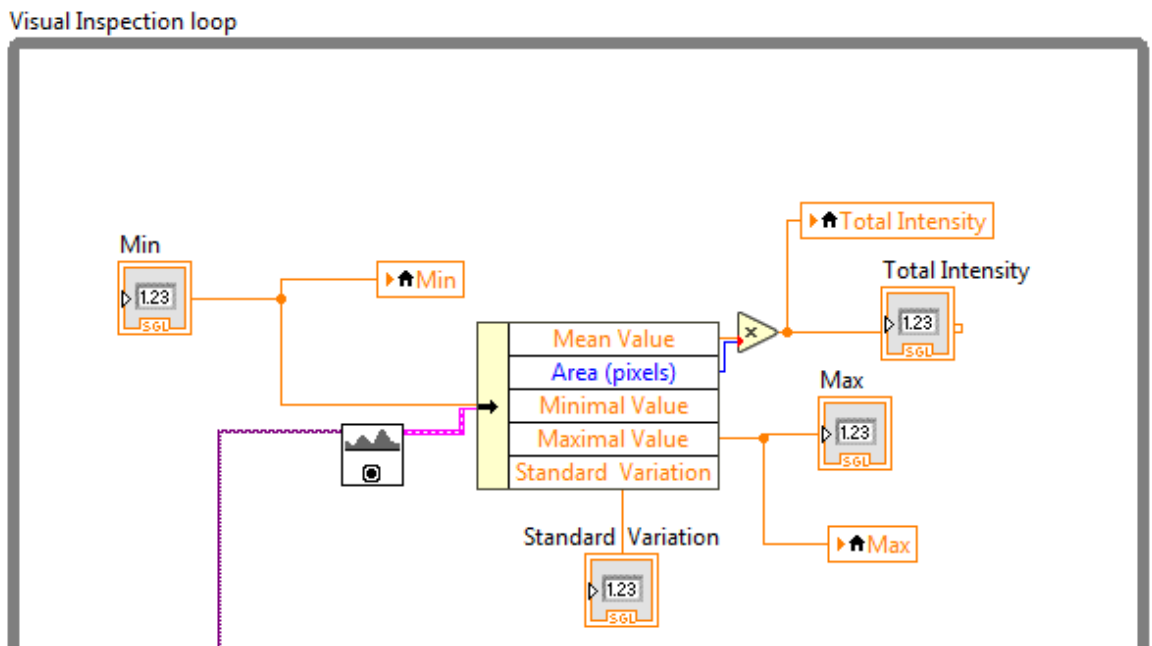


Figure 2-10 Portion of the NI Vision Builder visual inspection loop, showing extraction per frame of the total fluorescence (Total Intensity), minimum pixel values (Min), maximum pixel value (Max) and the Standard Variation.

Last, all the variables were collated and exported with the time onto a spreadsheet file specified by the user on the interface (Figure 2-11).

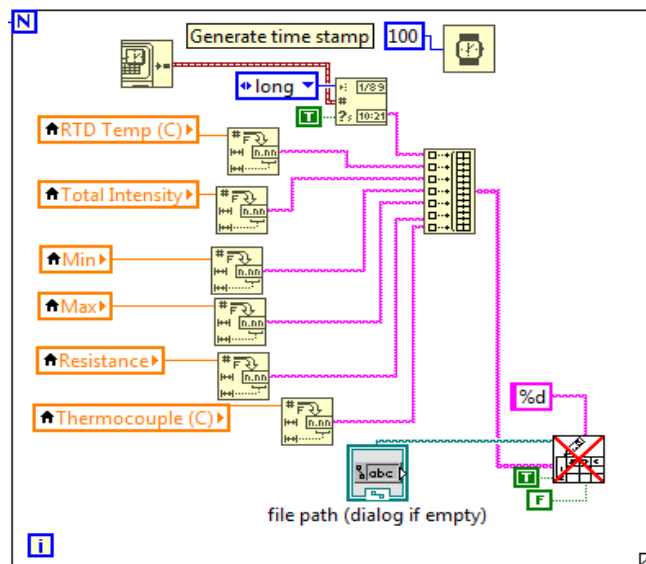


Figure 2-11 LabView program subroutine showing collation of variables and export to a spreadsheet for further analysis

2.5.6. Modelling of Binding Fluorescence and Melt Curves in OriginPro

Modelling was performed in OriginPro (2016). The reduction in fluorescence when heat is applied was seen to be $20\pm 2\%$ during single-stranded DNA experiments, so this was used as the basis between 0-100°C. The melting point was set at 50°C, with a 20% reduction as seen in experiments between 40-60°C. For this, a sigmoidal curve was produced using the curve fitting function, with close resemblance to those seen experimentally. Ratios were produced by averaging the base-line heat fluorescence with the simulated melt curve – for example, double-stranded 1:2 is the average of one double-strand model and 2 single-strand model. The derivatives of the simulated curves were analysed using OriginPro, peak height and peak area measured.

2.6. Results

2.6.1. Microfabrication of IDTs, RTDs and Microfluidic Devices

2.6.1.1 Interdigitated Transducers (IDTs)

IDTs were fabricated individually (Figure 2-13) and combined with RTDs (Figure 2-14), with a success rate of 84%, which worked as designed at $4.4\pm 0.4\text{MHz}$, Figure 2-12. In the literature, IDTs are usually fabricated with gold and RTDs with platinum, in order to fabricate both with a single step it was decided to focus on fabricating both with platinum.

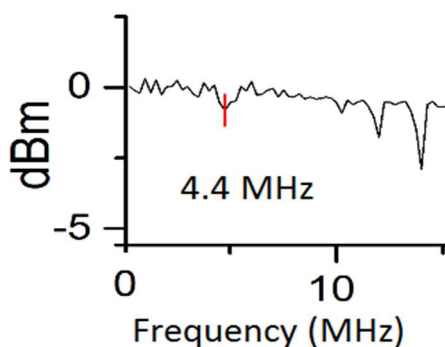


Figure 2-12 Frequency response of a fabricated IDT extracted using an Agilent Technologies E5071C ENA series network analyser. The graph shows the 4.4 MHz frequency the IDT was designed for, and the resonant frequency $\sim 12\text{MHz}$ that was used for SAW.

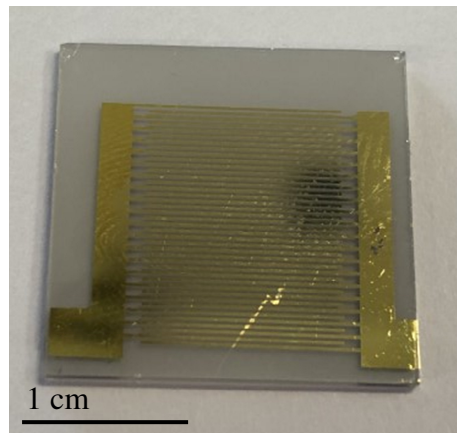


Figure 2-13 Gold IDT fabricated onto LiNbO₃. Early training used gold for the metallisation step, although for this thesis all IDTs used were platinum as the intention would be to fabricate both the IDT and RTD in a single step as in Figure 2-14.

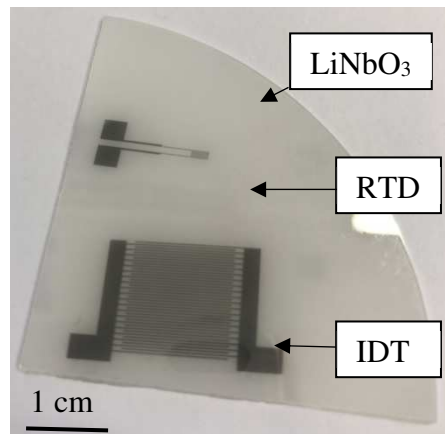


Figure 2-14 Platinum RTD and IDT fabricated onto LiNbO₃. The IDT and RTD were patterned together using a single S1818 photolithography step by combining the RTD designs and IDT design onto a single mask. Metallisation occurred in a single step, with both the RTD and IDT produced with 10nm of titanium and then 100nm of platinum.

2.6.1.2. Resistance Temperature Device (RTDs) design and fabrication

The resistance of the fabricated RTD is limited by the smallest width produced by photolithography (see Figure 2-2), assuming that the depth and quality of metal deposited during metallisation is equal over the sample. Each RTD requires calibration as in practice the resistance of the fabricated RTDs at 25°C vary by $\pm 7.8\%$ (Figure 2-15). RTD designs were patterned on to the photolithography mask so that fabrication could be achieved at the same time as the IDTs were fabricated (Figure 2-14). Stages of fabrication are shown below, with a fabricated RTD in Figure 2-16, and an RTD after silanisation with APTES with S1818 circle to protect the sample droplet area in Figure 2-17.

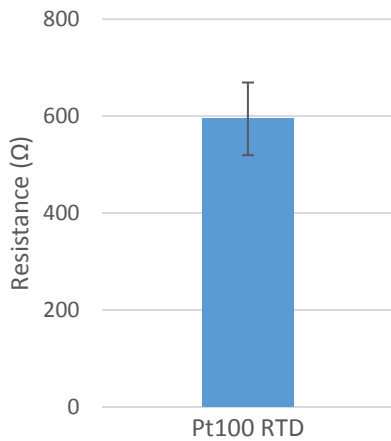


Figure 2-15 Resistance variation of fabricated Pt100 RTDs at 25°C. RTDs were fabricated using photolithography and 10nm of titanium and 100nm of platinum deposited. Resistance was measured using National Instruments USB-4065 Digital Multimeter

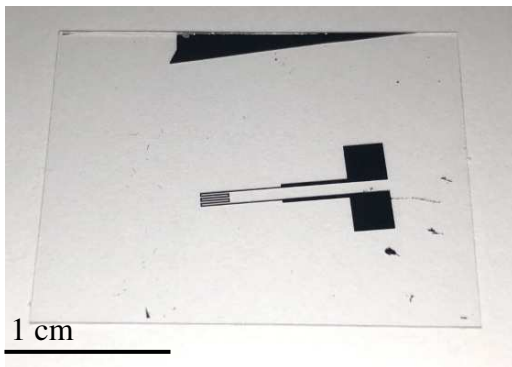


Figure 2-16 Pt100 RTD fabricated on a microscope coverslip.

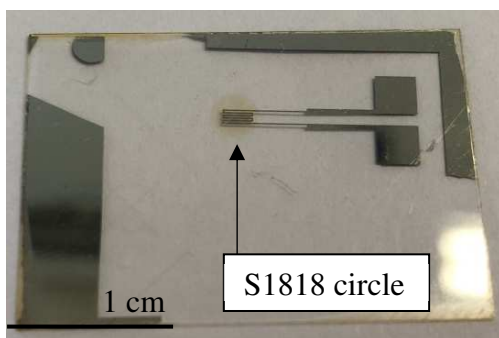


Figure 2-17 Pt100 RTD fabricated on a microscope coverslip with 3mm diameter circle of S1818 over the tip of the RTD. The RTD was patterned with photolithography, metallised (10nm Ti, 100nm Pt) then silanised with APTES. S1818 was patterned to protect the APTES to constrain sample droplet and allow DNA attachment.

2.6.1.3. RTD Calibration

For experiments in this thesis new RTDs were first calibrated using the Slow method and this was validated regularly using the Quick Cool method (both described fully in 2.5.1.4). The substrate would break if stressed by repeatedly and quickly changing temperatures, so alternative methods were devised which did not result in broken substrate.

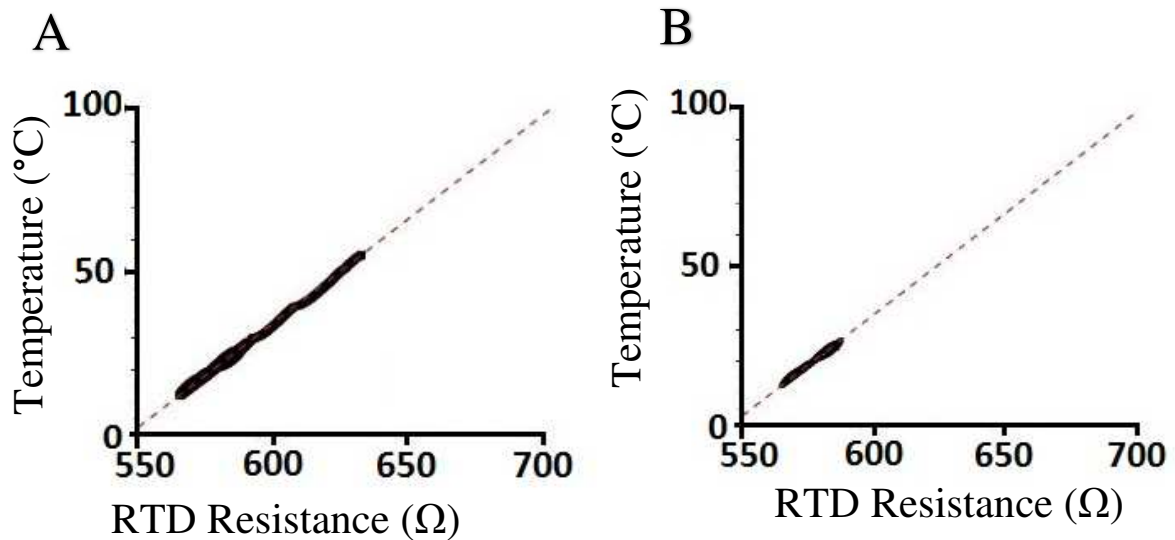


Figure 2-18 Slow (A) and Quick Cool (B) calibration methods showing experimental data (black squares) and extrapolated linear fit (black dashed line). Experiments were performed in 20 μ l of mineral oil using the Peltier and thermocouple/RTD setup described previously. Linear fit performed with OriginPro. Pearson's R of Slow Calibration is 0.999, Quick Cool is 0.995.

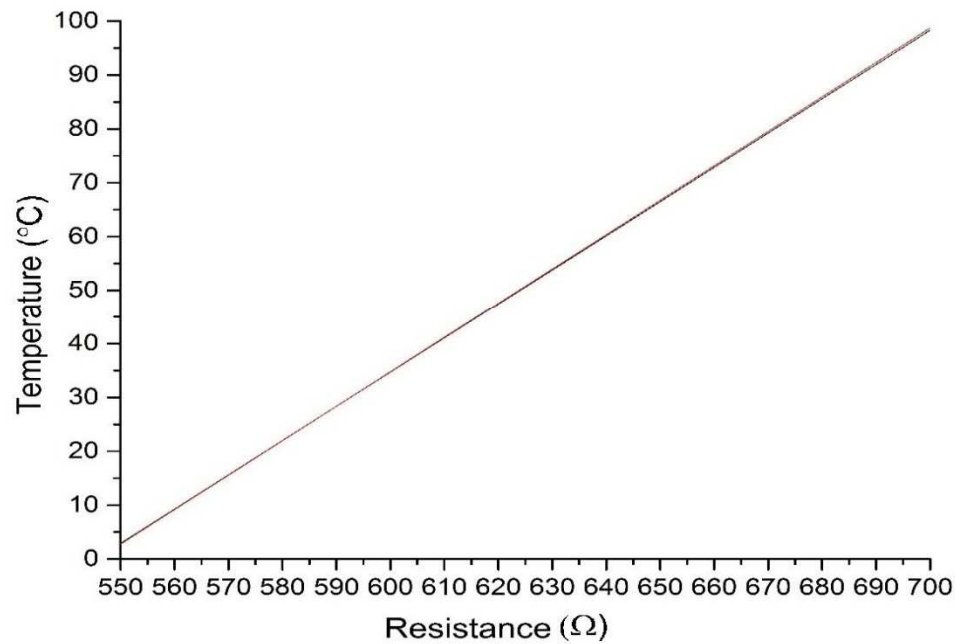


Figure 2-19 Comparison of calibration strategies showing alignment of the two calibration methods, “Slow” (black) and Quick Cool (red).

2.6.2. Surface Patterning Chemistry

2.6.2.1 Hydrophobic and Hydrophilic Surface Patterning

The hydrophobicity of glass and LiNbO_3 was increased after silanisation to become significantly more hydrophobic, Figure 2-21 and Figure 2-20. For glass, silanisation increased the contact angle from $26.2^\circ \pm 3.8$ to $105.8^\circ \pm 7.2$. For lithium niobate, the contact angle increased from $28.9^\circ \pm 3.6$ to $102.7^\circ \pm 7.4$.

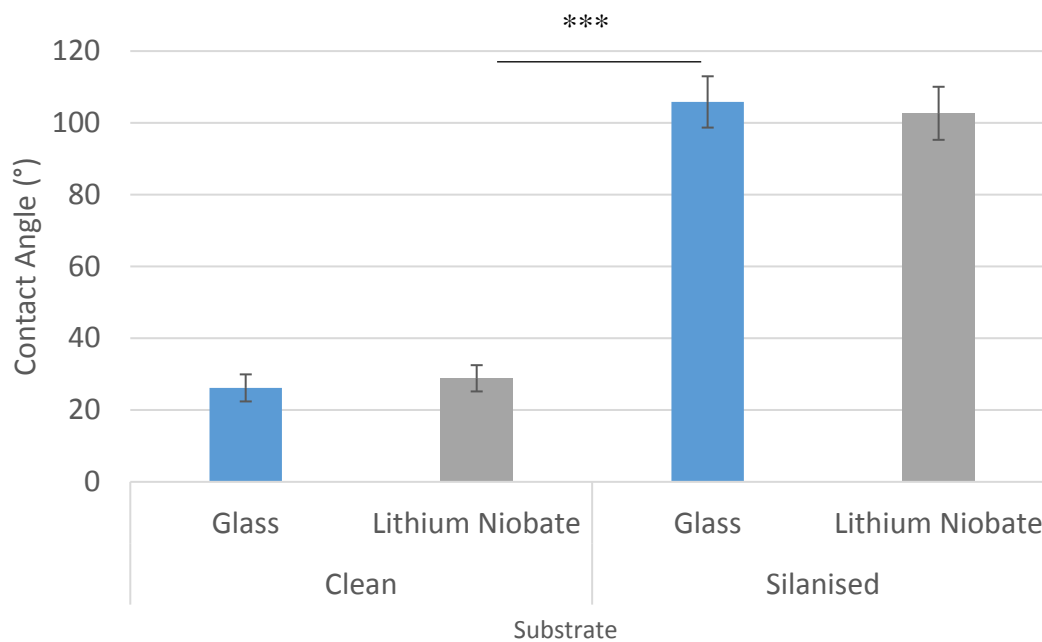


Figure 2-20 Comparing the hydrophobicity of glass and LiNbO_3 with and without PFOTS silanisation. Images of 1ul water droplets taken using Kruss Easydrop DSA25 (Hamburg, Germany) and contact angles analysed using FIJI DropSnake. 6 measurements were taken for each, error bars show standard deviation. T-tests determined that the silanised substrates were significantly different, Glass $P=6\text{E-}06$, Lithium Niobate $P=1\text{E-}06$. $P<0.001$ shown by ***.

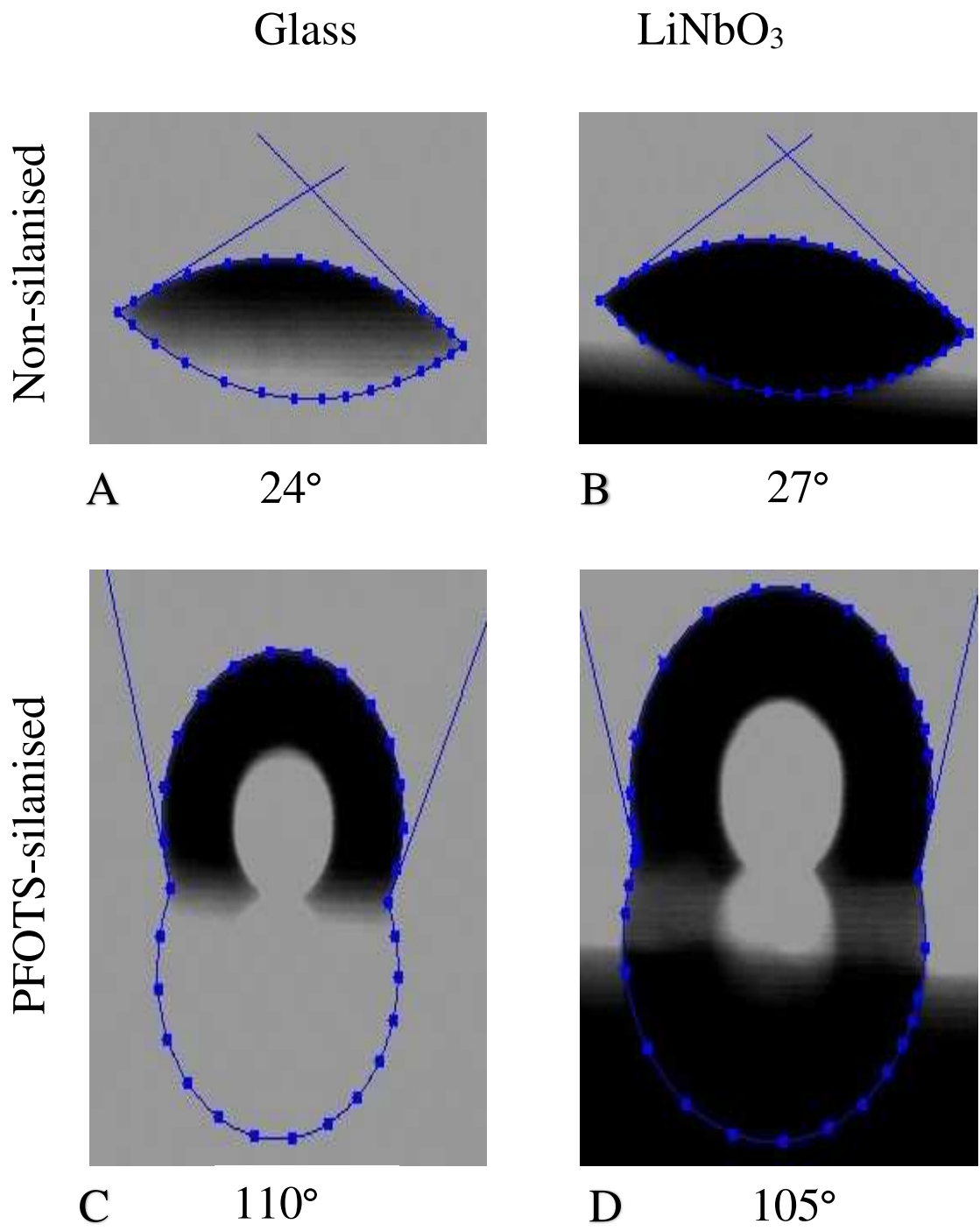


Figure 2-21 Comparison of hydrophobicity of non-silanised glass (A), non-silanised LiNbO₃ (B), silanised glass (C) and silanised LiNbO₃ (D) substrates. Images of 1µl RO water droplets taken using Kruss Easydrop DSA25 (Hamburg, Germany) and contact angles analysed using FIJI DropSnake.

2.6.2.1. DNA Attachment Chemistry

5 regions in an unsilanised control were averaged to give Figure 2-22, showing high fluorescence in the DNA attachment circle with an RFU of 87 ± 3 and showed minimal background fluorescence of 9 ± 1 due to DNA sticking to the glass surface. Full sequences are in Table 2-2.

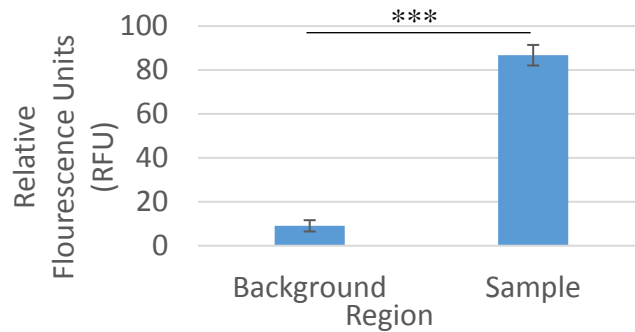


Figure 2-22 Relative fluorescence of the DNA attached to the surface with APTES and Sulfo-SMCC (Sample) compared to an unsilanised control (Background). Fluorescence measured in the Cy5 channel. $P=2E-13$, shown by ***

2.6.3. Software Predicted DNA Melt Curves

Melt curves for the DNA oligonucleotides were simulated using uMelt (University of Utah, v2.0.2) software (Figure 2-23), including with a range of cation concentrations to examine the effect of pH changes (Figure 2-24).

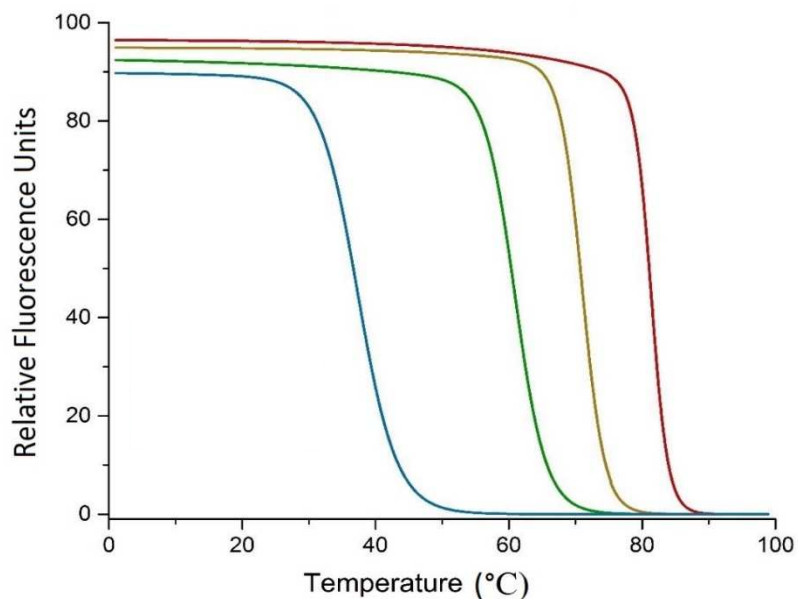


Figure 2-23 Melt curves of DNA oligonucleotides A (red), B (yellow), C (green) and D (blue) simulated using uMelt.

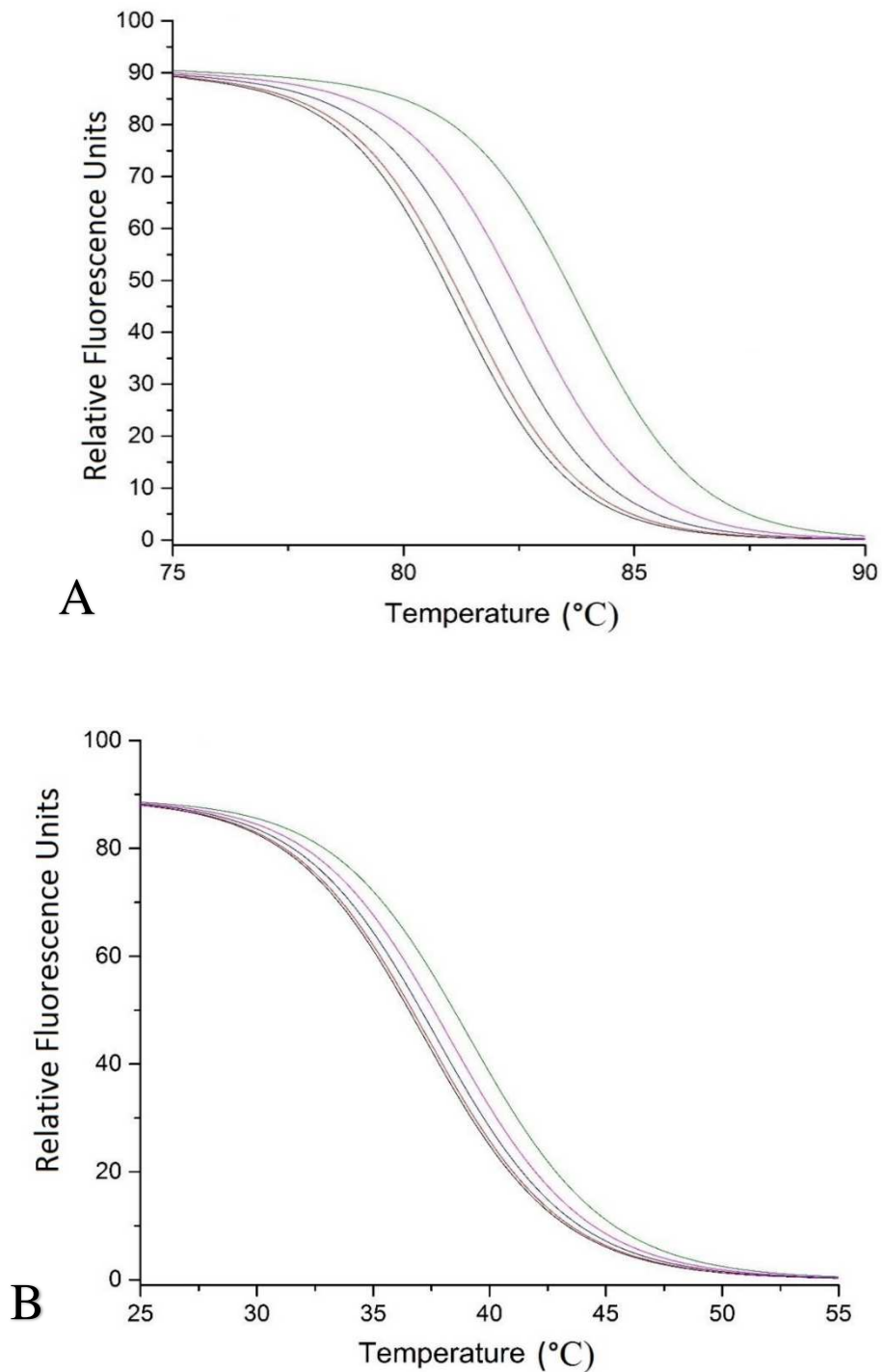


Figure 2-24 Melting curves of DNA A (A) and D (B) predicted using uMelt (University of Utah, v2.0.2) software based on sequence with varying monovalent cation concentrations, (left to right) 10mM, 20mM, 50mM, 100mM and 200mM. Calculations used Weber (Bioinformatics, 2015) thermodynamic set, varying (10mM-200mM) monovalent cation concentration, 3mM Mg^{2+} concentration, 0% DMSO and Owczarzy (2008) salt correction. Datasets visualised using OriginPro. Note that the melting temperature T_m is defined as the point where 50% has melted.

2.6.4 ABI 7500 Fast PCR Machine Controls

Melting temperatures (Figure 2-25) were obtained using the 10 μ l of 10 μ M DNA with 10 μ M EvaGreen on an ABI 7500 real time fast PCR machine using 7500 software v2.0.6 [14,150]. ANOVA Tukey analysis and T tests confirmed that each are significantly different, $P < 0.001$.

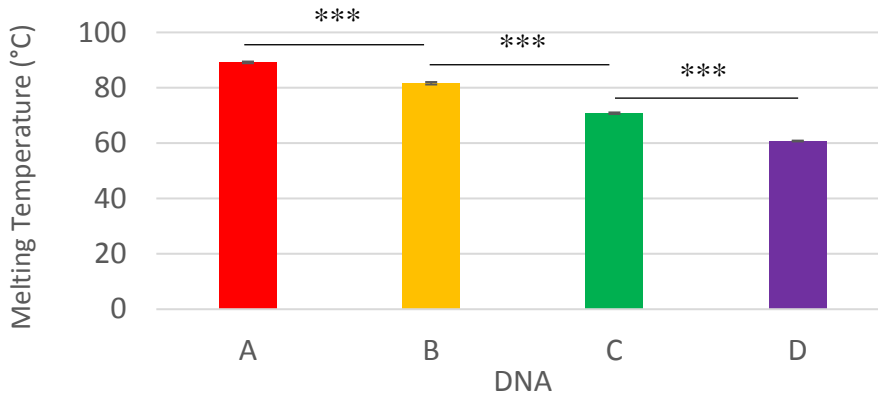


Figure 2-25 Melting temperatures of 20 replicates of 10 μ l of 10 μ M DNA A (red), B(yellow), C(green) and D(purple) in Tris EDTA pH 7.8 buffer derived on ABI 7500 using EvaGreen as a reporter molecule. Error bars show standard deviation. $P < 0.001$ shown by ***.

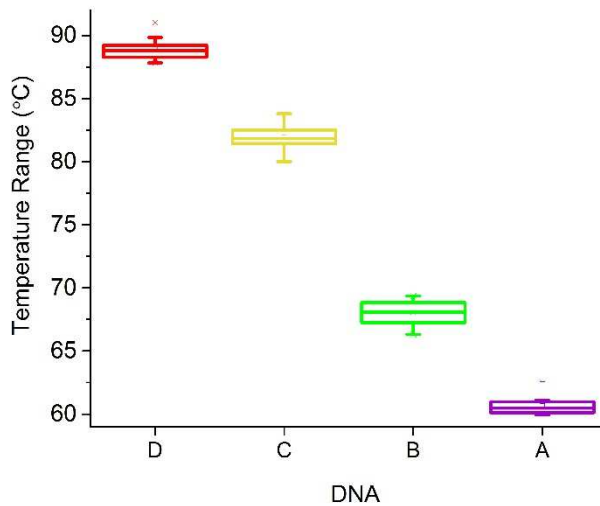


Figure 2-26 – ANOVA analysis performed using OriginPro differentiated all 4 DNA samples

2.6.5. Photostability of EvaGreen

In order to show that there is a difference between SAW and Peltier heating it would be helpful to show in a single experiment the melting temperature for both using the same sample. Multiple Peltier heating cycles, followed by multiple SAW cycles, followed by multiple cold-SAW cycles, in a single experiment could take a few hours. At high intensity (the maximum available laser power setting), EvaGreen is quickly photobleached (Figure 2-27). In order to discuss any changes in fluorescence during these experiments, it must be confirmed that there will not be significant reduction in fluorescence of the reporter molecule or fluorophores under experimental conditions.

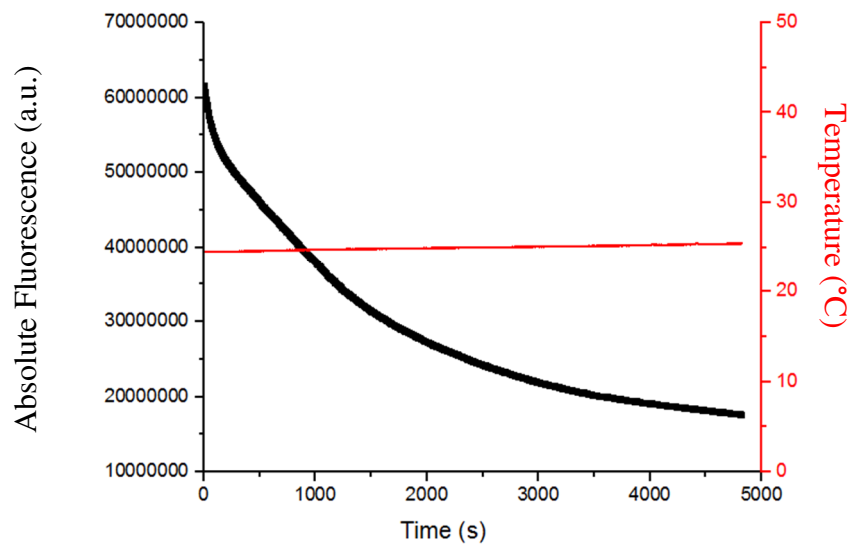


Figure 2-27 Photobleaching of EvaGreen at maximum laser intensity. Absolute fluorescence is shown in black, temperature is shown in red. High laser intensity causes rapid photobleaching of EvaGreen. 2 μ l of DNA and 0.5 μ l EvaGreen in TE buffer, within 20 μ l mineral oil droplet at room temperature

EvaGreen (Biotium, Cambridge Bioscience) photobleaching was carried out over 20 minutes (Figure 2 18), with the gradient of the fitted line suggesting that at room temperature and in the presence of double-stranded DNA Eva-Green would be photostable for around 200 minutes.

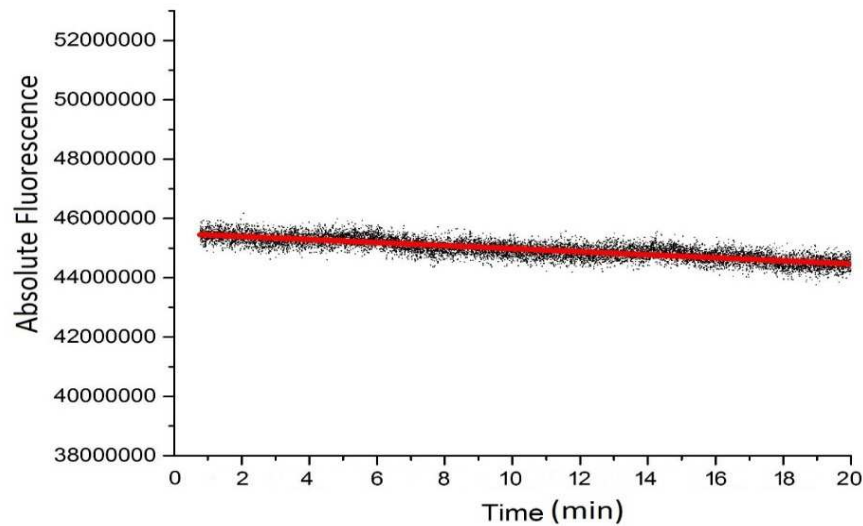


Figure 2-28 Photostability of Eva-Green over 20 minutes, performed with 2 μ l of DNA and 0.5 μ l of EvaGreen in TE buffer, within a 20 μ l mineral oil droplet measured at room temperature.

Discussion

If DNA is fragmented by SAW, lowering the melting point, then this would also be seen in a subsequent Peltier melting experiment, as well as a shift in the annealing temperature. The light intensity was reduced so that there were measurable melt curves, but the fluorescence was stable. EvaGreen (Biotium, Cambridge Bioscience) photobleaching was carried out over 20 minutes (Figure 2-28), with the gradient of the fitted line suggesting that at room temperature and in the presence of double-stranded DNA Eva-Green would be photostable for around 200 minutes. A Peltier heat and cooling cycle takes approximately 5-6 minutes (depending on the Peltier input power), and the calibration curve does not require fluorescence. Therefore, a Peltier heating and cooling experiment (5-10 cycles, ~30min) could be performed on the same sample and act as a control for the SAW experiments.

3. DNA Melting and Annealing with Surface Acoustic Waves

This chapter examines melting and annealing DNA using SAW. 4 DNA sequences (A, B, C and D) were investigated with different lengths, GC melting temperatures and melting temperatures. Melting curves were simulated under standard conditions, and in varying monocation concentrations in order to show how changes in pH affect DNA melt curves.

DNA C and D showed a reduced melting temperature with SAW compared to the Peltier controls whilst DNA B showed a higher melting temperature. There was no clear relationship between the difference in SAW melting temperature and GC content, although results did suggest a potential link with length / mass that should be further investigated.

SAW-induced streaming influencing pressure and pH did not cause the change in DNA melting temperatures as there was not a uniform pattern across all DNA sequences. DNA fragmentation induced by SAW would have affected subsequent heating and annealing temperatures in subsequent cycles, but this was not seen and expected melting temperatures returned when the DNA was heated using a Peltier module. Post-experiment analysis of the DNA size further agreed that fragmentation is not an issue.

Examination of the melt curves in detail showed that there was not lower total fluorescence when SAW was applied, suggesting that collisional quenching was not a significant factor. This is further supported by the results that suggest a relationship between length/size – collisional quenching, as seen with increases in temperature, is linear and would reduce total fluorescence without changing the melting temperature.

In order to investigate whether SAW was affecting the binding of DNA strands, or of the reporter molecule EvaGreen to DNA, FRET experiments were explored.

3.1. Introduction

In order to investigate the use of SAW for point-of-care diagnostics, it is necessary to understand nucleic acid thermodynamics. The temperature at which 50% of DNA is single stranded (ssDNA) is defined as the melting temperature (T_m), and this depends on the primary and secondary structure [15]. DNA melting using a Peltier module is a reproducible technique; this work will examine using SAW (SAW). Previous work has examined SAW heating [151,152] and streaming [153] in a droplet.

For this project, the DNA was designed to avoid secondary structures as discussed in Chapter 1 that would influence the melting temperature, although this may be investigated at a later stage. It is hypothesised that if SAW affects the melting temperature of DNA (as measured using the reporter molecule EvaGreen), then this could occur due in different ways.

SAW could:

- fragment DNA, resulting in decreased melting temperatures
- directly disrupt binding between DNA strands, or between EvaGreen and dsDNA
- indirectly affect DNA binding, through streaming, or streaming-induced differences in pressure, salt concentration/pH or temperature within the droplets [52]
- quench EvaGreen fluorescence, streaming could increase collisional quenching by increasing interactions of the fluorophore with the surrounding buffer [66,72,150]

To ascertain if DNA is fragmented by SAW, melt and annealing curves will be monitored, and Peltier module controls performed between SAW cycles. If the DNA is fragmented, the subsequent annealing curve will also show a lower annealing temperature, as will melt curves performed using a Peltier module as the heat source instead of SAW. Fragmentation of DNA would result in a reduction in melting and annealing temperatures that would not recover when the sample is heated using the Peltier module. This will additionally be checked after experiments by analysis in the Agilent Bioanalyzer 1000.

At physiological conditions, lower than the melting temperature, single strands of Complementary DNA (ssDNA) will form non-covalent bonds to form double-stranded DNA (dsDNA). The strength of these bonds depends on the base pair ($A=T$ or $G=C$), in addition to base stacking and water interactions with the buffer solution [12]. If SAW is disrupting the binding of DNA strands, then this effect would be dependent on the length, and GC

content of the DNA. The DNA used in these experiments were designed to have differing GC content and length/mass and melting temperature as shown in Table 3-1. The full sequences are in Table 2-1.

Name	Predicted Melting Temperature (uMelt)	GC Content (%)	Bases	Mass (Daltons)
A	84.7	80	40	27120
B	79.6	74	34	23030
C	62.2	73	30	20320
D	40.0	76	21	14230

Table 3-1 uMelt predicted melting temperature, GC content, length and estimated mass (GC+backbone = 680Da, AT+backbone = 670Da) of DNA A, B, C and D.

DNA exists in vivo as a dsDNA, although in some viruses it can be single-stranded. In prokaryotes (archaea and bacteria) DNA is a supercoiled structure, usually a ring such as plasmids, and interacts directly with the cytosol of the bacterial cell and so is exposed to varying sugar and salt concentrations, and different pH levels. In contrast, eukaryotic DNA is packaged with histones as chromosomes, and compartmentalised within the nucleus. The packaging means that some parts of the DNA are open to the nucleus environment, and available for DNA transcription, whilst other parts are silenced. Protein and enzyme access to the nucleus is tightly controlled to the point where there is even a difference in pH – the nucleus usually being 0.3-0.5 pH higher than the cytosol [154]. SAW-induced changes in salt concentration/pH would not be sequence specific, so DNA of different lengths and GC content would be affected in a predictable manner.

There is evidence in the literature that SAW streaming induces changes in pressure (which could lead to changes in salt concentration, pH) that allow concentration of particles within droplets, and regions with temperature variations ($\pm 0.2^\circ\text{C}$) [52] within droplets, so this should be investigated [52,155,156]. There is potential for this work to have further applications on biological research, to replicate some of the in vivo conditions within a droplet.

In this chapter the melting curve of the DNA was predicted using software, with the pH and salt concentrations kept under experimental conditions. Experiments were performed in buffer which resist changes in pH, so significant differences of pH within the buffer is unlikely to have a measurable effect on DNA melting temperature. Higher pressure and/or higher salt concentration would mean a lower pH which in turn would mean a higher melting temperature. Chapter 4 will examine these using the reporter molecule EvaGreen, whilst Chapter 5 will use the photo-induced electron transfer effect (NB-S Quench) to try and distinguish if any effects seen are due to EvaGreen.

The differences in melting temperature with SAW could also be explained by SAW affecting the fluorescent reporter molecule. In order to measure if the DNA is in a double- or single-stranded configuration a reporter molecule Eva-Green was used which binds preferentially to dsDNA causing a change in conformation and increase in fluorescence which can be monitored using a fluorescence microscope [14].

To quantify the melting point, the fluorescence and temperature must be accurately measured. Characterisation of the system required careful calibration of the fabricated RTDs against a thermocouple of traceable calibration as well as analysing the fluorescence of the system to take into account of photobleaching. The binding of EvaGreen to DNA is difficult to measure directly, additional experiments will examine the use of FRET – DNA labelled directly with fluorophores – in order to investigate if the binding of the EvaGreen reporter molecule was responsible for the reduction in melting temperature with SAW.

3.2. Results

3.2.1 Simulated Melt Curves

In order to design the DNA for these experiments, the melting point of the DNA was predicted using uMelt (Figure 3-2) as described in section 2.5.3.2 at high resolution (intervals of 0.1°C). In order to study the effects of SAW on DNA, we must be able to study DNA with different GC content, lengths and melting temperatures (shown in Figure 3-2).

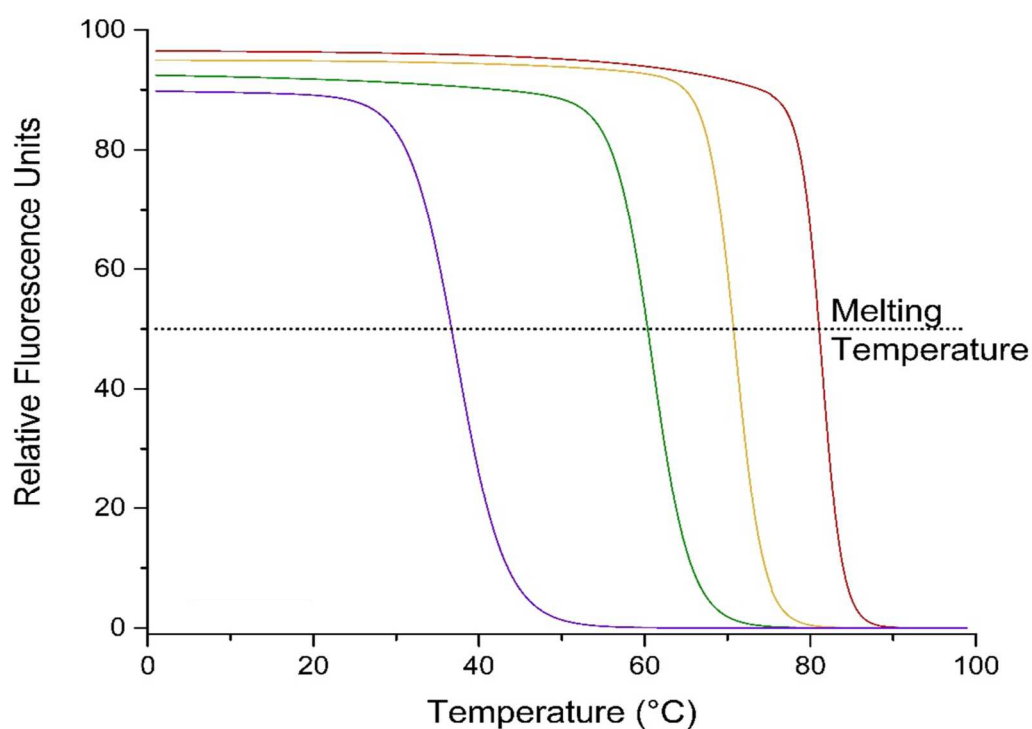


Figure 3-1 Melt curves of DNA A (red), B (yellow), C (green) and D (purple) simulated using uMelt (University of Utah, v2.0.2) software based on sequence.

Calculations used Weber (Bioinformatics, 2015) thermodynamic set, 20mM monovalent cation concentration, 3mM Mg^{2+} concentration, 0% DMSO and Owczarzy (2008) salt correction.

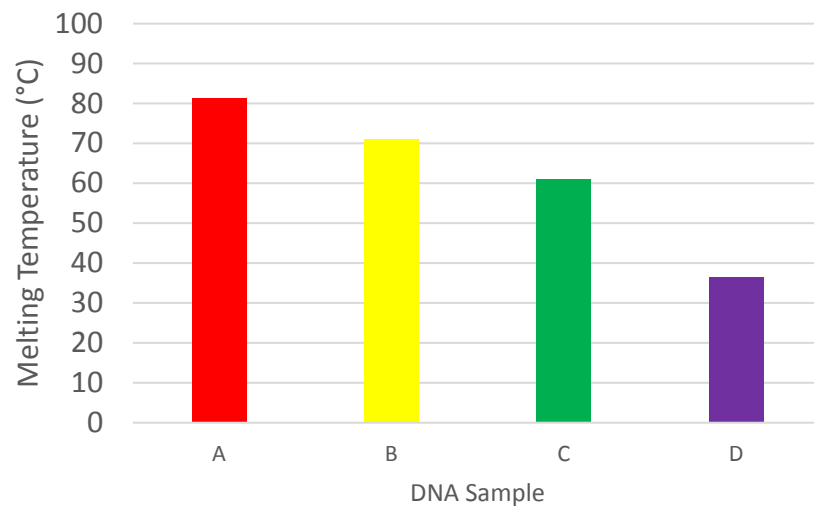


Figure 3-2 Melting temperature of DNA A (red), B (yellow), C (green) and D (purple) simulated using uMelt (University of Utah, v2.0.2) software based on sequence.

The melting point (T_m) is defined as 50% single stranded and 50% double-stranded.

Calculations used Weber (Bioinformatics, 2015) thermodynamic set, 20mM monovalent cation concentration, 3mM Mg^{2+} concentration, 0% DMSO and Owczarzy (2008) salt correction.

3.2.1. Varying pH

Mansoor modelling of SAW-induced streaming in microdroplets shows microregions within the droplet with increased temperature and pressure due to streaming pressure – this allows movement and concentration of particles [52]. As differences in salt concentration, and pH can also affect melting temperature these were modelled by uMelt software (Figure 3-3 and Figure 3-4) by varying the cation concentration. The effect of pH is shown in the following section, showing higher cation / H⁺ concentration (lower pH) increases the melting temperature for DNA.

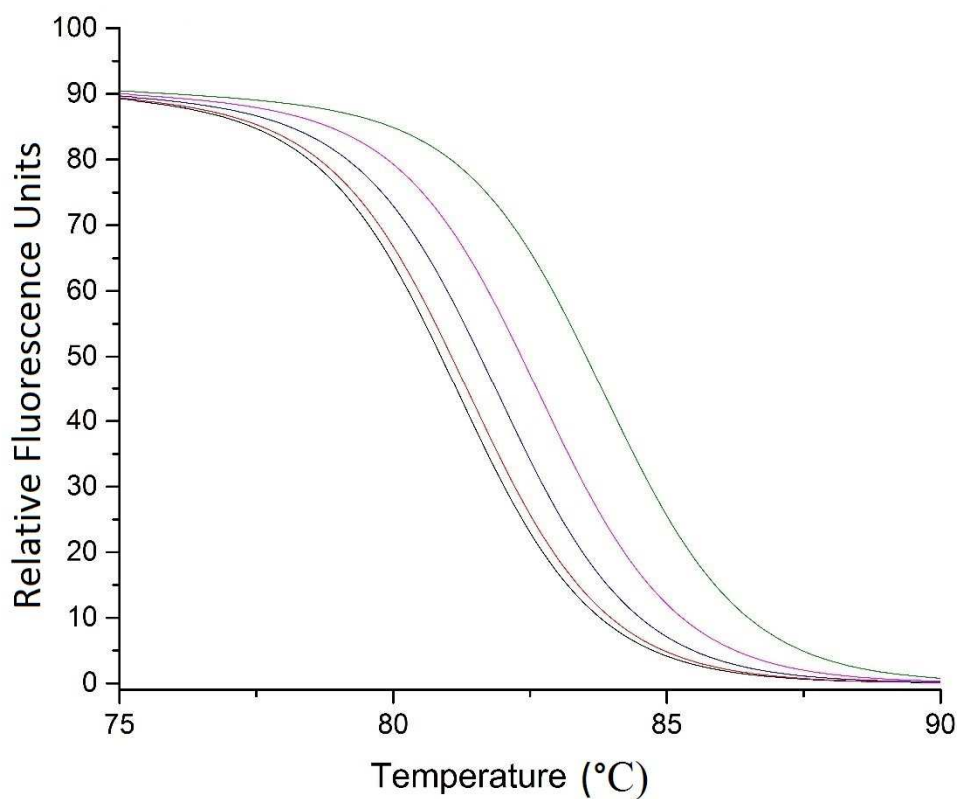


Figure 3-3 Melting curves of DNA A oligonucleotides predicted using uMelt (University of Utah, v2.0.2) software based on sequence with varying monovalent cation concentrations - left to right, 10mM, 20mM, 50mM, 100mM and 200mM. Calculations used Weber (Bioinformatics, 2015) thermodynamic set, varying (10mM-200mM) monovalent cation concentration, 3mM Mg²⁺ concentration, 0% DMSO and Owczarzy (2008) salt correction. Datasets visualised using OriginPro. Note that the melting temperature T_m is defined as the point where 50% has melted.

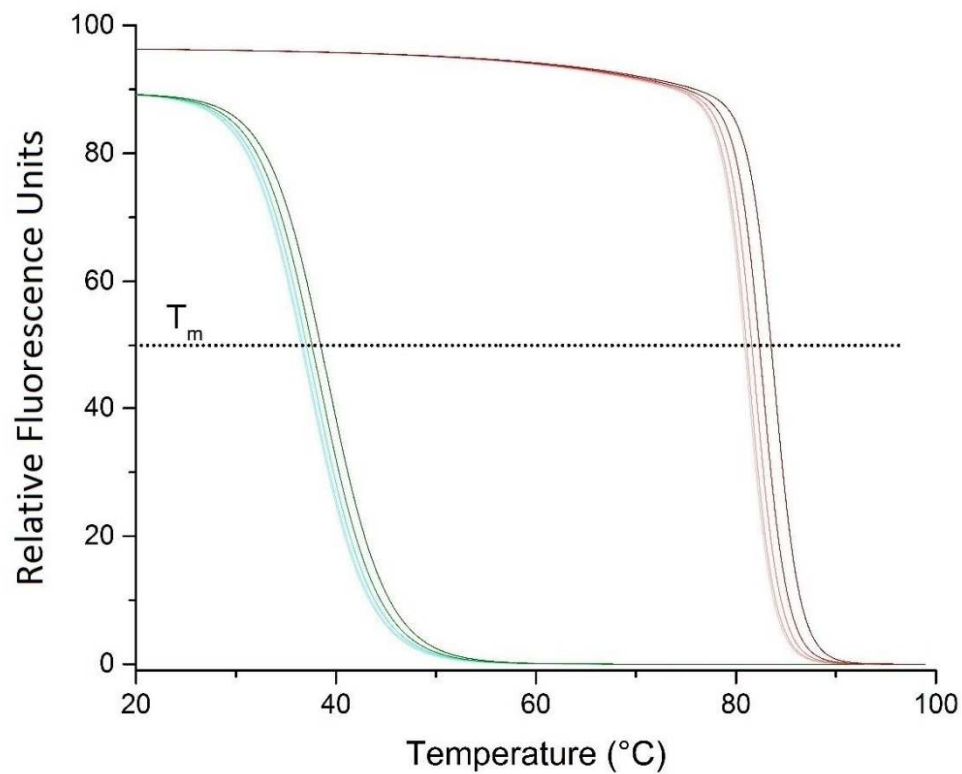


Figure 3-4 Melting curves of DNA A (green) and D oligonucleotides (purple) predicted using uMelt (University of Utah, v2.0.2) software based on sequence with varying monovalent cation concentrations - left to right, 10mM, 20mM, 50mM, 100mM and 200mM. The change from 10mM to 100mM is the equivalent of increasing pH from 1.0 to 2.0. Calculations used Weber (Bioinformatics, 2015) thermodynamic set, varying (10mM-200mM) monovalent cation concentration, 3mM Mg^{2+} concentration, 0% DMSO and Owczarzy (2008) salt correction. Datasets visualised using OriginPro. Note that the melting temperature T_m is defined as the point where 50% has melted.

Figure 3-5 shows the effect of varying the pH on the melting temperature of DNA C and D experimentally derived using the ABI7500 with EvaGreen as the reporter molecule. Increasing the pH reduces the melting temperature, as found by the simulated curves and in the literature [25,157]. The linear fit of DNA C had an R^2 of 0.69, and the T_m reduced by 2.0°C per pH. The linear fit of DNA D had an R^2 of 0.72, and the T_m was found to reduce by 4.5°C per pH. The pH effect on melting temperature is consistent with the changes predicted by uMelt software in the previous section (Figure 3-3 and Figure 3-4), as a low pH is a high cation/ H^+ concentration. SAW effects will be compared to the effects seen with pH changes.

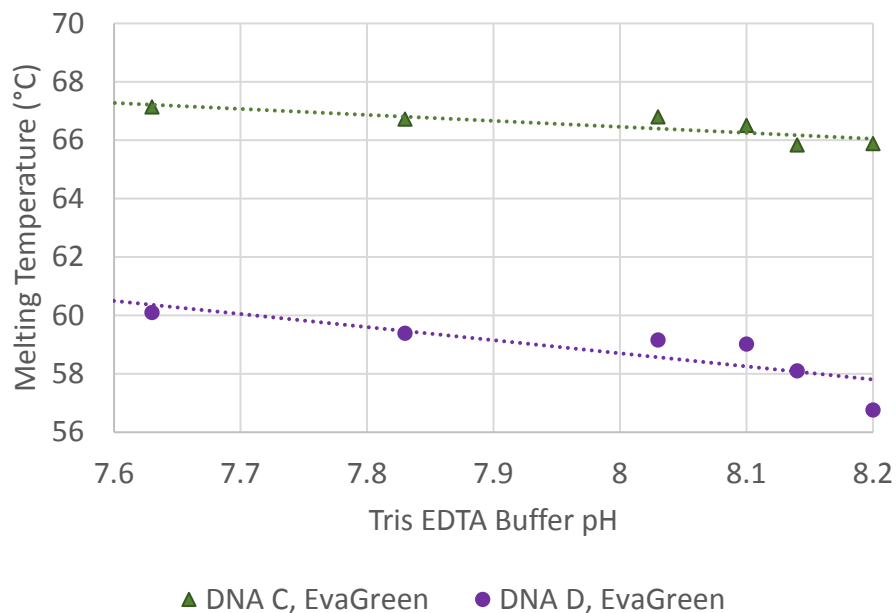


Figure 3-5 Melting temperatures of DNA C (green triangles) and D (purple circles) in varying Tris EDTA buffer pH derived with EvaGreen. $10\mu\text{l}$ of $10\mu\text{M}$ double-stranded DNA, melting temperatures measured in 7500 FAST QPCR machine ($25\text{-}95^\circ\text{C}$). Higher pH results in a lower melting temperature, due to salt and buffer interactions with the DNA.

3.2.2. Peltier Module

3.2.2.1. Controls

Melting temperatures (Figure 3-6) of 1 μ l of 10 μ M DNA with 10 μ M EvaGreen as the reporter molecule in 20 μ l of mineral oil detailed in the materials and methods on the upright fluorescence microscope (section 2.4). Samples were heated using a Peltier module (5W), temperatures quantified using a calibrated Pt100 RTD (section 0). DNA A melted at 88.9 \pm 0.8 $^{\circ}$ C, B at 81.6 \pm 0.9 $^{\circ}$ C, C at 68.6 \pm 0.8 $^{\circ}$ C and D at 60.9 \pm 0.5 $^{\circ}$ C. ANOVA analysis confirms these to be statistically separate groups, P<0.001 of being the same samples.

The melting temperatures derived using the upright fluorescence microscope varied by \pm 0.6 $^{\circ}$ C on average from those derived using the ABI 7500 PCR machine, validating the experimental method. All measurements were taken using the automated LabVIEW program, and subsequently analysed using Origin2016 sigmoidal curve fitting and peak identification. Peltier heating controls were performed between SAW heating to ascertain if the DNA is fragmented due to SAW.

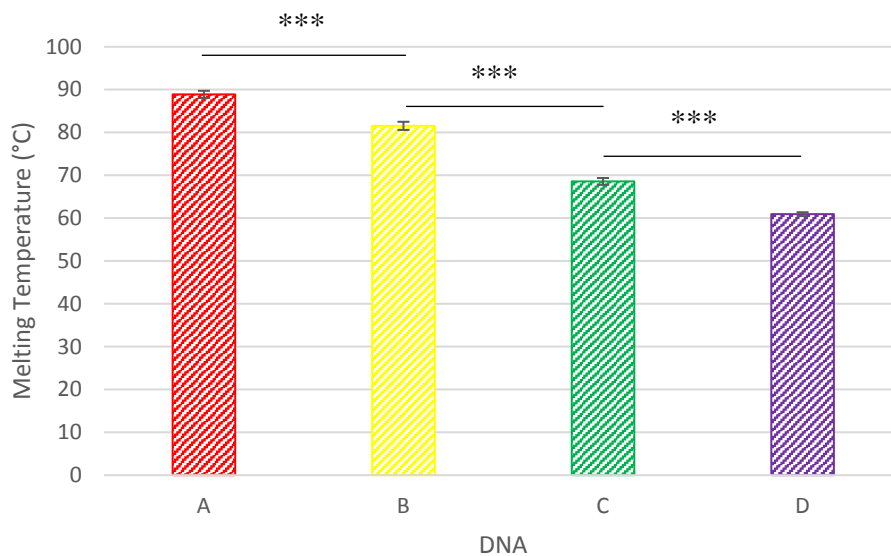


Figure 3-6 Melting temperatures of 20 replicates of 1 μ l of 10 μ M DNA A (red), B (yellow), C (green) and D (purple) in Tris EDTA pH7.8 buffer. Samples were heated using a Peltier module under the fluorescence microscope. Temperatures were measured using a calibrated Pt100 RTD. Error bars show standard deviation. P<0.001 shown by ***

3.2.2.2. Multiplex

Multiplex refers to the ability to monitor the melting of multiple DNA oligonucleotides within the same sample. This is possible with reporter molecules such as EvaGreen, as long as the melting temperatures are different enough to be distinguished, usually around 5°C. A, B, C and D were all able to be multiplexed with the ABI 7500 and using the upright fluorescence microscope. Multiplex is an advantage for diagnostics, as the cost per test is decreased and coinfections or different variants can be simultaneously tested. It also allows additional tests to be performed to act as positive or negative controls in the reaction. Multiplex PCR for diagnostics is still a developing field, and currently relies on reporter molecules such as EvaGreen which will interact with contaminating genomic material [34]. In Chapter 5.3 and 5.4 multiplex target identification and PCR are examined using the novel photo-induced nucleo-specific quenching effect (NB-S Quench). Chapter 5 examines LAMP DNA amplification, which requires upwards of 6 primers per reaction. As the number of primers increases, the likelihood that a primer will be specific decreases, and the potential for partial matches (primer-dimers) increases. For this reason, LAMP reactions are not routinely multiplexed, as two LAMP reactions would require 12 primers, three LAMP reactions would require 18 primers etc. 6 primers would be sufficient to perform 3 pairs of PCR amplifications, which would be attractive in a Lab-on-a-Chip diagnostic device.

3.2.3. Surface Acoustic Waves

Melting temperatures (Figure 3-7) of 1µl of 10µM DNA in 20µl of mineral oil detailed in the materials and methods on the microscope setup discussed above, using EvaGreen as the reporter molecule. SAW was applied (23MHz, -2dBm) resulting in streaming and heating of the droplet. All measurements were taken using the automated LabVIEW program, analysed using Origin 2016 as for the Peltier heated controls above. SAW melting results are summarised in Figure 3-7 and Table 3-2.

DNA A melted at a slightly higher (+0.2°C) temperature, but this was lower than the variation between samples, which for DNA A using SAW was ±1.7°C. T-test P=0.6, ANOVA Tukey analysis confirmed that DNA A melted with SAW was still the same group (P=0.999). DNA B had a higher melting temperature (+1.8°C) than the Peltier controls,

which was above the variation of $\pm 0.8^{\circ}\text{C}$, T-test $P=0.02$, ANOVA Tukey analysis suggested this was most likely still the same group with a $P<0.995$. DNA C had a lower melting temperature (-4.7°C), which was significantly above the variation seen of $\pm 0.1^{\circ}\text{C}$, T-test $P<0.01$, ANOVA Tukey test $P=0.22$. DNA D melted at a lower temperature (-6.1°C), which was higher than the variation of $\pm 0.6^{\circ}\text{C}$, T-test $P<0.001$, statistically the most different when analysed with ANOVA with $P<0.001$. There is no obvious link between the differences in melting temperature and the Guanine and Cytosine (GC) content – DNA A and D have the same GC content but were affected by SAW differently. There does seem to be a link with length/size as seen in Table 3-2, and there is potentially a link between the variation in SAW measurements and length.

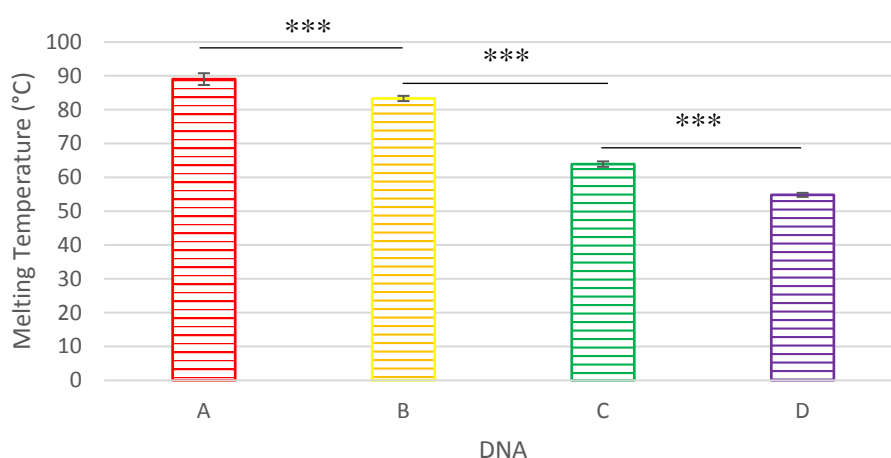


Figure 3-7 Melting temperature using SAW. Melting temperatures of $10\mu\text{l}$ of $10\mu\text{M}$ DNA A (red), B (yellow), C (green) and D (purple) in Tris EDTA pH7.8 buffer. Samples were heated using SAW – 23MHz, -2dBm using the IDT previously discussed. Temperature was measured with a calibrated Pt100 RTD. $P<0.001$ shown by ***.

Name	Melting Temperature Difference ($^{\circ}\text{C}$)	GC Content (%)	Length (bases)	Mass (Daltons)
A	0.2 (± 1.7)	73	30	20325
B	1.8 (± 0.8)	76	21	14234
C	-4.7 (± 0.1)	80	15	10173
D	-6.1 (± 0.6)	73	12	7451

Table 3-2 Comparison of DNA attributes (length, GC content, mass) and difference in melting temperatures (SAW-Peltier). Standard deviation is shown in brackets. 5 melt curves for 3 replicates were measured for each.

Detailed melt curve analysis

Examples of the melt and annealing curves when SAW were used as the source of temperature control are shown in Figure 3-8 and Figure 3-9. The melt curves were examined for several variables at this stage, including the number, size and temperature of derivative peaks. The total fluorescence and change in fluorescence were also noted.

The annealing curves were also examined, and it was found that the annealing temperature is close to the annealing temperature measured with the Peltier module in the absence of SAW. If subsequent melting curves and annealing curves showed lower melting temperatures, this would suggest degradation of the DNA by SAW, but this was not seen (Figure 3-10). Agarose gel electrophoresis were performed after SAW experiments, and these agreed with the Peltier-controlled experiments that did not show any significant breakdown of the DNA into smaller fragments.

For these experiments, after heating with SAW controls were performed with the same sample where the sample was heated with a Peltier module, which showed a reversion of the melting temperature to that expected. This evidence, along with the annealing temperatures, suggests that SAW DNA fragmentation does not explain the lower melting temperature observed with SAW.

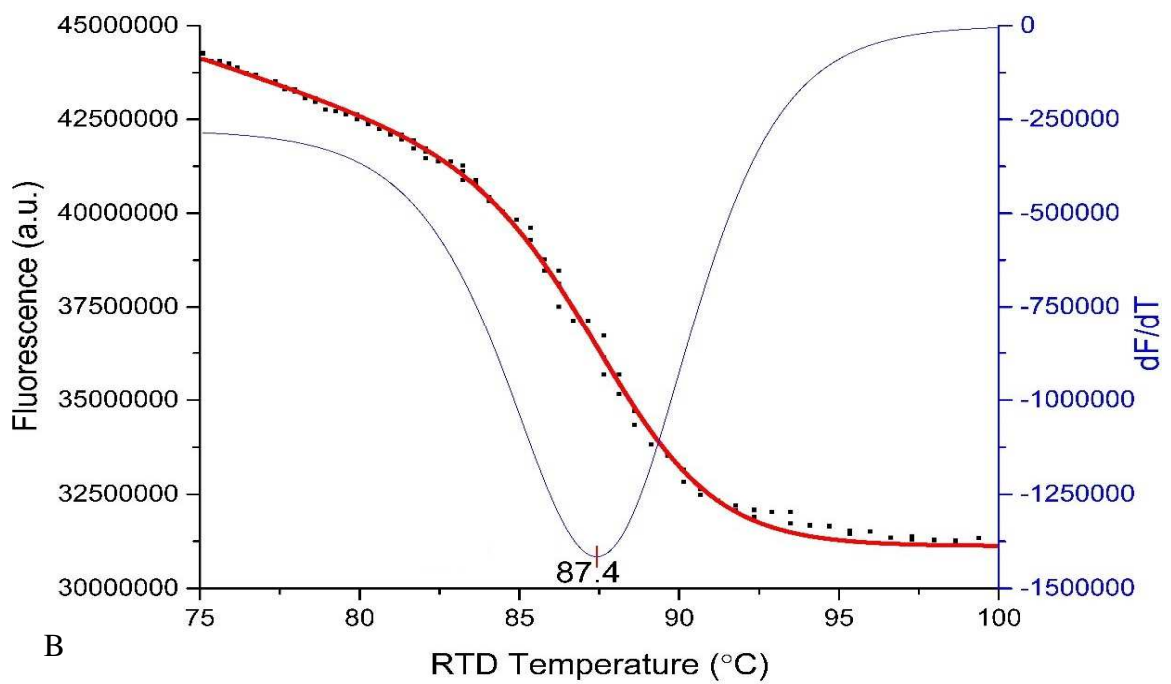
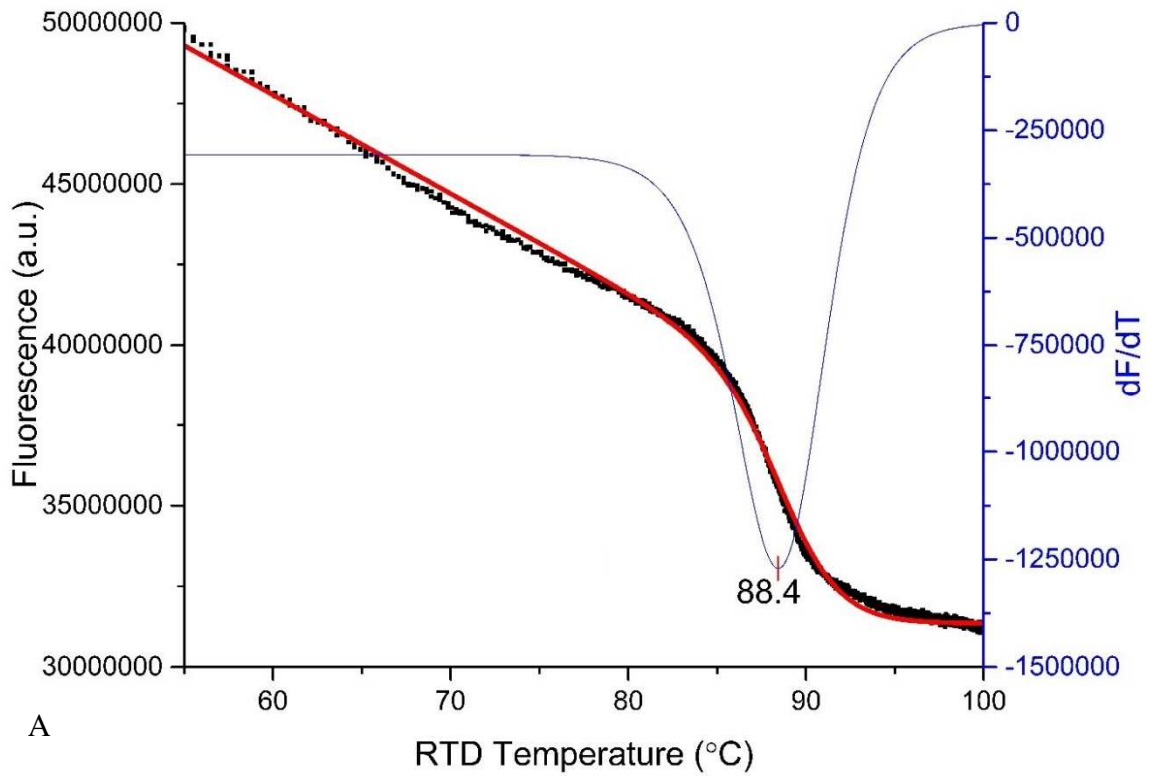


Figure 3-8 Melt (A) and Anneal (B) curves of DNA A in pH7.8 Tris EDTA buffer heated with SAW – 23MHz, -2dBm. Graphs show experimental data (black squares), Origin2016 fitted sigmoidal curve (red line), derivative (blue), and melting point. Experiment was carried out on the fluorescence microscope, with temperature measured using a calibrated Pt100 RTD.

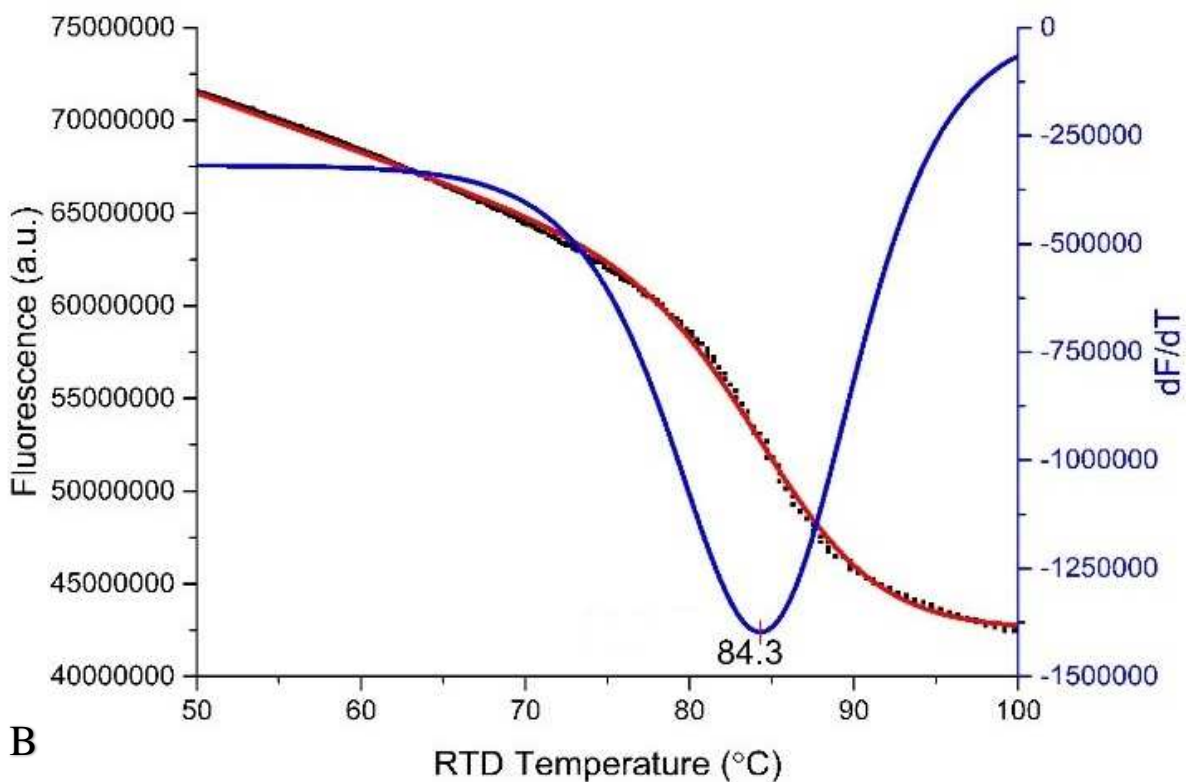
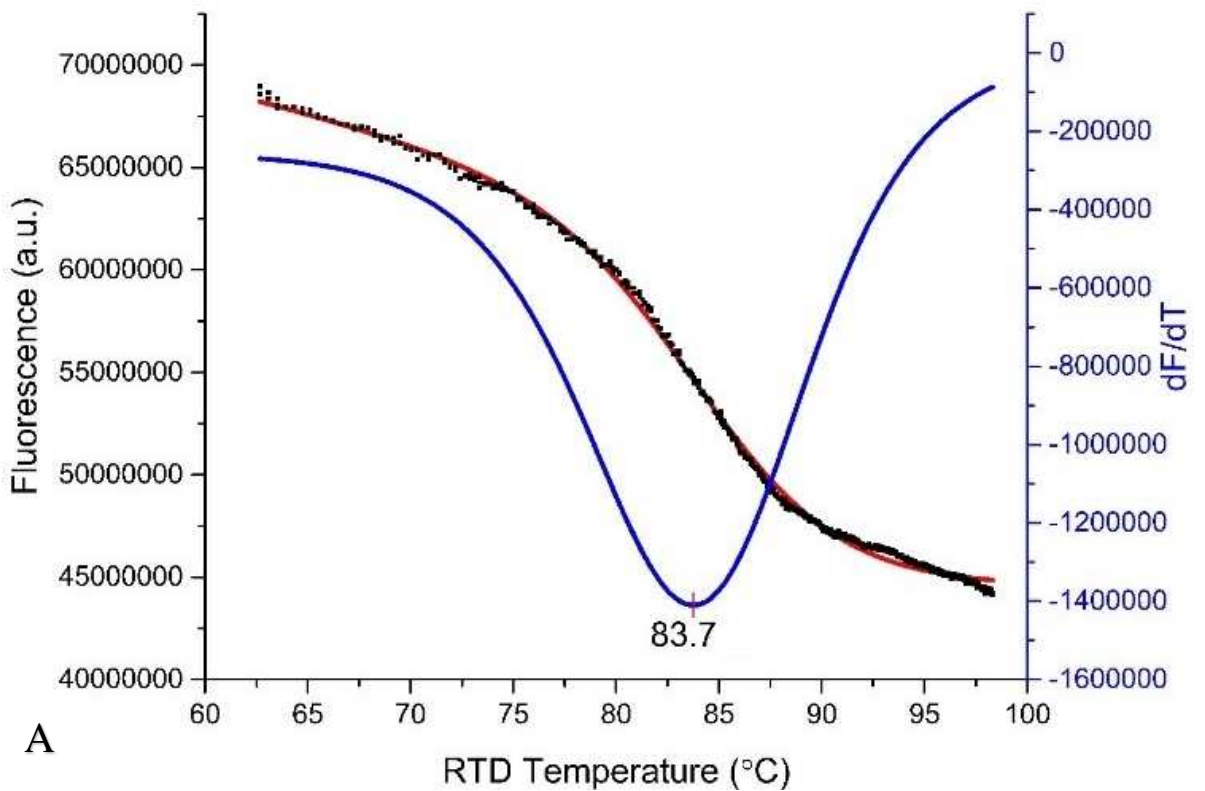
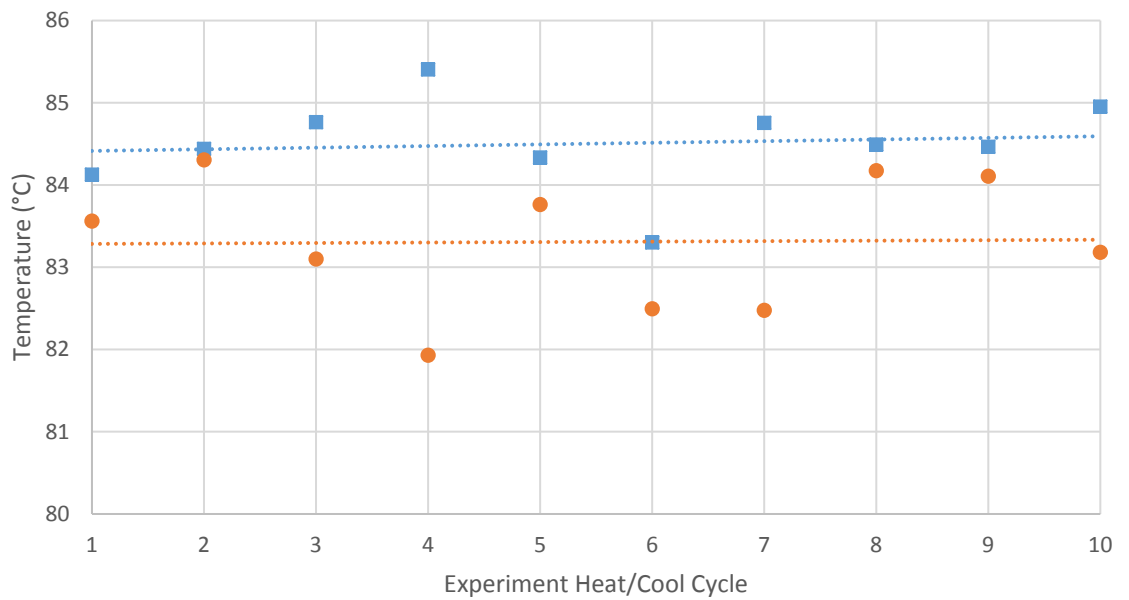
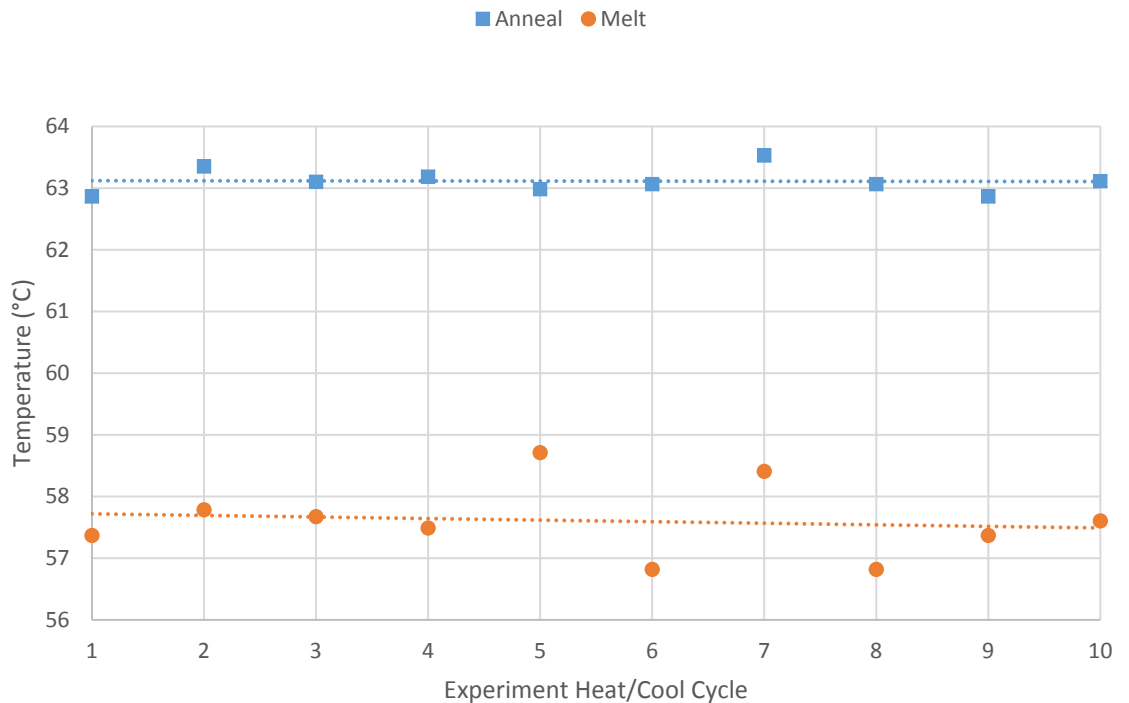


Figure 3-9 Melt (A) and Anneal (B) curves of DNA B in pH7.8 Tris EDTA buffer heated with SAW – 23MHz, -2dBm. Graphs show experimental data (black squares), origin 2016 fitted sigmoidal curve (red line), derivative (blue), and melting point. Experiment was carried out on the fluorescence microscope, with temperature measured using a calibrated Pt100 RTD.



A



B

Figure 3-10 Changes in melting (orange circles) and annealing (blue squares) temperatures over 10 experimental cycles of DNA B (A) and D (B) in pH7.8 Tris EDTA buffer heated with SAW – 23MHz, -2dBm. Experiment was carried out on the fluorescence microscope, with temperature measured using a calibrated Pt100 RTD. Each anneal point follows on from the corresponding melt cycle.

3.2.4. Summary - Comparison of all three methods

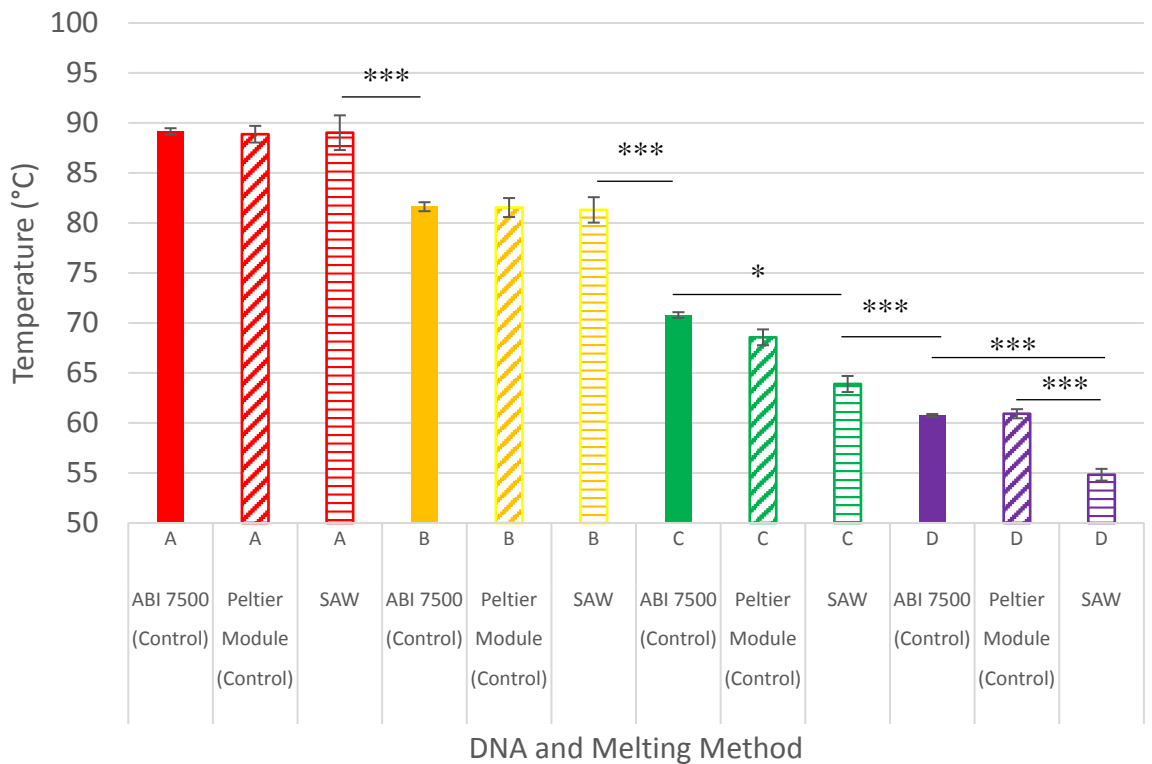


Figure 3-11 Comparison of melting temperatures measured of DNA A (red), B (yellow), C (green) and D (purple) in pH7.8 Tris EDTA buffer. The controls labelled PCR were measured in an ABI 7500 FAST PCR (solid colour). The source of heating for SAW was SAW actuated at 23MHz -2dBm (diagonal lines), or Peltier module (horizontal lines). * for $P < 0.05$, ** for $P < 0.01$, *** $P < 0.001$, the rest have no significant difference.

SAW were found to affect the melting temperature of some DNA oligonucleotides (Figure 3-11), although this was not seen in the annealing (Figure 3-12). There was a higher variation between measurements made with the Peltier heater than the commercial PCR machine, and the variation between measurements made with SAW was higher still. For DNA A the standard deviation was $\pm 0.3^\circ\text{C}$ for the PCR machine, $\pm 0.8^\circ\text{C}$ for the Peltier module and $\pm 1.7^\circ\text{C}$ for SAW. For DNA B the standard deviation was $\pm 0.4^\circ\text{C}$ for the PCR machine, $\pm 0.9^\circ\text{C}$ for the Peltier module and $\pm 0.8^\circ\text{C}$ for SAW. For DNA C the standard deviation was $\pm 0.3^\circ\text{C}$ for the PCR machine, $\pm 0.8^\circ\text{C}$ for the Peltier module and $\pm 0.8^\circ\text{C}$ for SAW. For DNA D the standard deviation was $\pm 0.1^\circ\text{C}$ for the PCR machine, $\pm 0.5^\circ\text{C}$ for the Peltier module and $\pm 0.6^\circ\text{C}$ for SAW.

ANOVA analysis was performed for each method, and for each DNA sample. Across all DNA samples tested using the ABI7500, ANOVA analysis confirmed that there is a low to zero (<0.05) probability that DNA samples A, B, C and D are the same groups. DNA samples A and B were found to have a high probability ($P>0.995$) of being the same group across all methods. DNA C heated with SAW only showed a low probability of being the same group as DNA C heated with the Peltier or PCR machine ($P=0.22$), whilst DNA D heated with SAW was even more statistically different with a probability approaching zero ($P<0.01$).

Increased variation in the experimental setup with the Peltier module compared to the ABI 7500 PCR machine was expected as the PCR machine performs melt curve analysis over ~90 minutes, in a highly controlled environment including sealed tubes, whilst the microscope melt curves are performed in 2-3 minutes on a sample droplet covered in mineral oil to prevent evaporation. It is interesting that SAW showed a higher variation than the Peltier module experiment. The SAW variation did increase with DNA oligo length, so this should be investigated further. It is possible that SAW is affecting the folding or binding of the EvaGreen reporter molecule, or SAW could be increasing the partial melting of the DNA, resulting in single-stranded DNA that can still influence the fluorescence of EvaGreen (this will be discussed again in the experiments in Chapter 4 where there are portions of single-stranded DNA). For DNA A the variation between measurements was greater than the difference in melting temperature seen when SAW was applied, suggesting that the effect is not constant.

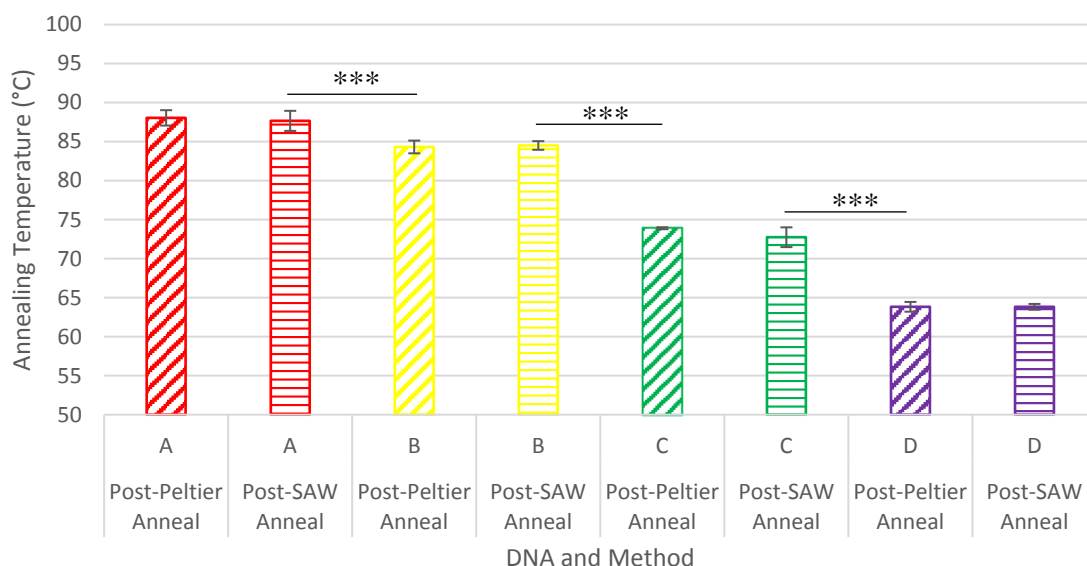


Figure 3-12 Comparison of Annealing Temperatures of DNA A (red), B (yellow), C (green) and D (purple) in pH7.8 Tris EDTA buffer after being heated to 95°C with the Peltier module (horizontal lines) or SAW (diagonal lines) 23MHz, -2dBm. T-test showed no significant difference within groups, and $P < 0.001$ between (showed by ***).

3.3. Discussion and Conclusion

Any deviation of melting temperature due to surface acoustic waves will have implications for designing SAW lab-on-a-chip devices, or applications such as sequencing which are currently in development. It was suggested that SAW may lower the melting temperature of DNA through streaming, or through the differences in pressure and temperature within the droplet due to streaming. If this were the case, longer DNA oligonucleotides A and B would be more affected or equally affected, so the results do not support this theory. It was thought that the DNA could be fragmented by SAW, this effect has been seen before but relies on a frozen DNA sample or rough surface to encourage shearing of DNA, and longer DNA oligonucleotides were found to be more affected than short. Annealing curves and post-experiment gel analysis do not support the theory that the DNA is becoming fragmented – melting with a Peltier after SAW restored the expected melt curve.

The melt curves are measured using the reporter molecule EvaGreen, the binding or conformation of which could be affected by SAW. As discussed in Chapter 1, EvaGreen changes conformation in the presence of double-stranded DNA, resulting in a shift in absorption and increase in emission, if the structure or binding of EvaGreen is affected this would result in altered melt curves.

In order to understand if this was due to concentration of DNA within the droplet, potentially changing the pH microenvironment, or SAW influencing the binding of the EvaGreen reporter molecule, Total Internal Reflection Fluorescence (TIRF) microscopy experiments were planned. TIRF experiments illuminate fluorophores such as the EvaGreen reporter molecule within 10nm of the surface, so DNA attached to the surface (and subject to maximum streaming by SAW) could have been studied. However, TIRF microscopy uses immersion oil between the glass or clear LiNbO₃ and the lens, which was also subjected to SAW. Heating the immersion oil and microscope lens to the temperatures required to study DNA melt curves is neither possible nor recommended due to damage to the LiNbO₃ and microscope lens. As TIRF was not possible at that time (see Future Work) it was decided to use FRET to further study this phenomenon, as this would remove the requirement to use a non-specific reporter molecule such as EvaGreen.

3.4. Fluorescence Energy Resonance Transfer (FRET)

3.4.1 Introduction

Fluorescence/Förster Resonance Energy Transfer (FRET) experiments were designed when difficulties were encountered preparing experiments with TIRF.

As discussed in Chapter 1, FRET involves energy transfer between two fluorophores, with the efficiency of this energy transfer directly proportional to the distance between the fluorophores. In FRET, a donor fluorophore is excited, and the energy may be transmitted to an acceptor fluorophore as a virtual photon, resulting in fluorescence of the acceptor fluorophore [43,68]. The efficiency of this transfer depends on the distance between the fluorophores and the available electron energy states (see Figure 1-9) of the FRET donor and acceptor.

In order to discover if the lower SAW melting temperatures were due to changes in EvaGreen fluorescence the FRET experiments were designed so that they could use either EvaGreen as the donor fluorophore or a fluorophore attached to the DNA with similar fluorescent properties. If the SAW effect was due to disruption of the binding of EvaGreen to dsDNA, then the effect would also be noted with EvaGreen FRET to an acceptor fluorophore. If the SAW effect was due to collisional quenching due to streaming then controls exciting the acceptor fluorophore alone would exhibit a similar change.

Of the commercially available DNA modifications, EvaGreen and Alexa 488 show similar excitation and emission spectra (Figure 3-13), therefore Alexa488 was chosen as the donor fluorophore. The absorption spectra of Alexa532 aligned very closely with the emission spectra of Alexa488/EvaGreen (Figure 3-14), with an acceptable difference in emission spectra so they could be distinguished using a standard FITC/EvaGreen emission filter $525\pm 20\text{nm}$ (Thorlabs, US) and a $565\pm 18\text{nm}$ filter (Chroma, US). Crosstalk between filters will be removed using controls of each fluorophore with each filter. The addition of the fluorophores adds mass to the DNA strands, so this could give insight into the SAW effect seen previously if it is due to streaming.

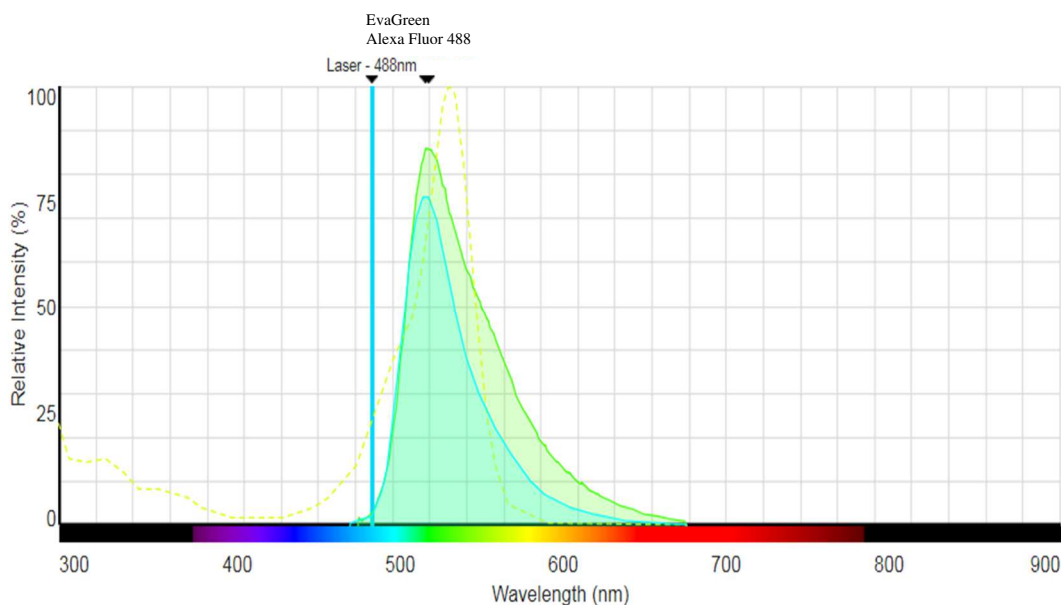


Figure 3-13 Comparison of emission spectra of EvaGreen (solid green) and Alexa488 (solid blue) with the excitation spectra of Alexa532 (dotted yellow). Image from SpectraViewer, ThermoFisher. This shows the similarity in emission between the potential FRET donor fluorophores Alexa488 and EvaGreen, and the match with the excitation of the FRET acceptor Alexa532.

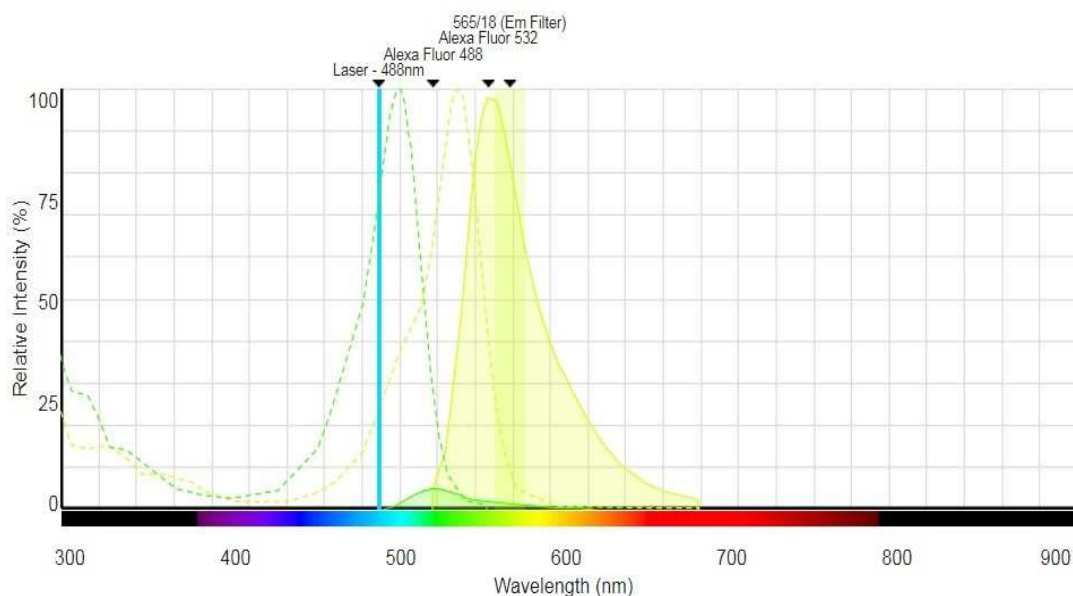


Figure 3-14 Predicted FRET spectra, when the acceptor and donor fluorophores are close together (1-10nm), SpectraViewer (Thermo Fisher). Fluorescence is shown in solid lines and shaded, Alexa488 (green) and Alexa532 (yellow). Dotted lines show absorption spectra, Alexa488 (green) and Alexa532 (yellow). 488nm laser is shown as a solid blue line, 565±18nm filter is shown in yellow.

3.4.2. FRET Results

3.4.2.1 Controls

The control experiments showed that the Alexa532 alone was only excited 1.0% of Alexa488, barely distinguishable from background. With FRET, the fluorescence of Alexa488 was quenched significantly, to 12.9% of fluorescence without FRET. Quenching of around 87% is consistent with the literature [158]. The Alexa532 was excited by FRET with an efficiency of 81.2%.

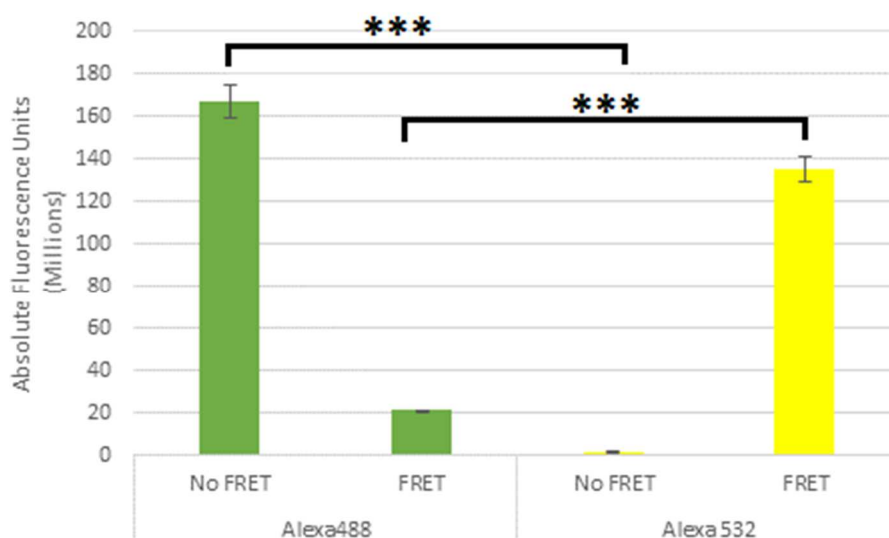


Figure 3-15 Absolute fluorescence of Alexa488 and Alexa532 when excited at 488nm, fluorescence for the Alexa488 experiments was measured with the 525±20nm filter whilst the Alexa532 experiments were measured with the 565±18nm emission filter. The “No FRET” experiments included only the named fluorophore; the FRET experiments had both fluorophores, but fluorescence was only measured with the appropriate named emission filter. T-test $P < 0.001$ shown as ***.

3.4.2.2 Results

The DNA C FRET experiments using a Peltier module compared favourably with those using EvaGreen as a reporter molecule (Figure 3-16). The reduction in the green channel fluorescence of the FRET donor Alexa488 produced a melting temperature at $68.5 \pm 0.5^\circ\text{C}$ whilst the increase in the yellow channel fluorescence of the FRET acceptor Alexa532 produced a melting temperature of $68.7 \pm 0.7^\circ\text{C}$. The EvaGreen control melting temperature was $68.6 \pm 0.8^\circ\text{C}$. The annealing temperature was $73.9 \pm 0.6^\circ\text{C}$ derived with Alexa488 fluorescence, was $73.2 \pm 0.8^\circ\text{C}$ derived with Alexa532 fluorescence and was $73.9 \pm 0.1^\circ\text{C}$ derived with the control EvaGreen reporter. ANOVA Tukey analysis confirmed that the annealing temperature were the same group, which was significantly different from the melting temperatures.

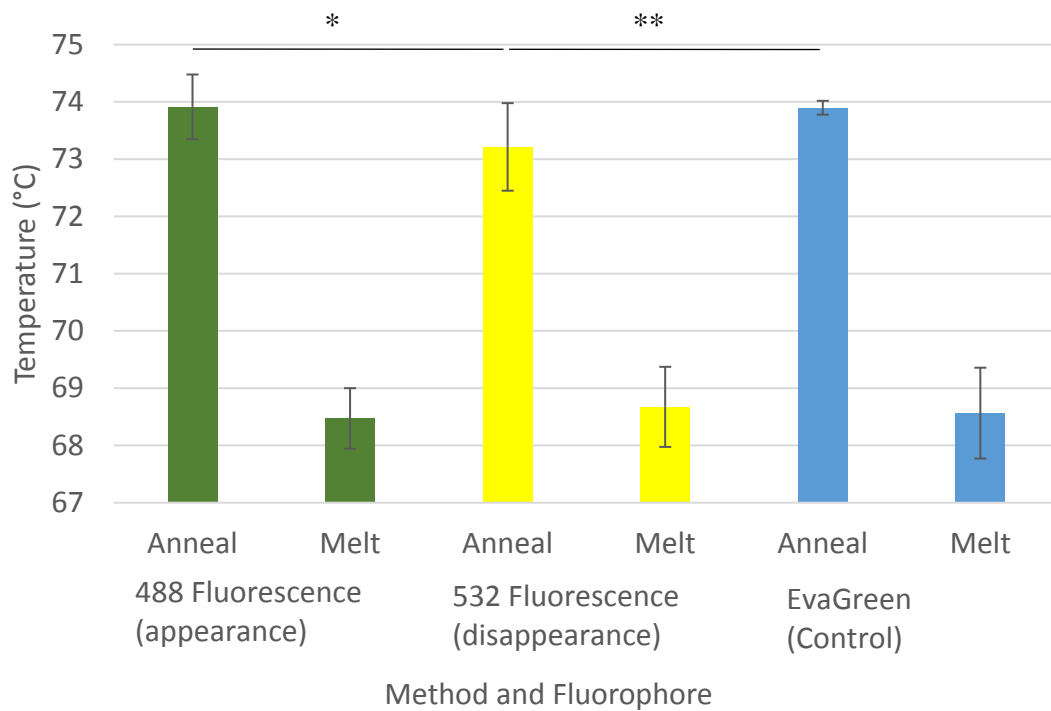


Figure 3-16 Melting and annealing temperatures of DNA C derived using the appearance of the Alexa488 fluorescence (green) and disappearance of the Alexa532 fluorescence (yellow). The EvaGreen controls are included (blue). Experiment was carried out on the fluorescence microscope, heating supplied by the Peltier module, and temperature measured using a calibrated Pt100 RTD. * shows $P < 0.05$, ** $P < 0.01$, *** $P < 0.001$, the rest showed no significant difference.

The absolute fluorescence of Alexa488 at the end (~80°C) of the FRET experiment in the green filter was noted to be significantly lower than expected, the resultant fluorescence of the Alexa532 in the yellow filter throughout was also lower than expected, and controls using only one of the FRET fluorophores produced unexpected results. Single-stranded Alexa488-labelled DNA exhibited a linear reduction in fluorescence as temperature increased due to increased buffer-fluorophore interactions at higher temperatures, as did single-stranded Alexa532-labelled. This was also confirmed with controls with double-strand Alexa532 controls - one strand labelled with Alexa532, the other unlabelled.

However, the double-stranded Alexa488 controls did not work as expected, producing a sigmoidal curve with a melting temperature similar to that seen with the EvaGreen reporter

molecule instead of a linear seen with the other controls. Alexa488 was chosen due to a similar excitation and emission spectra to EvaGreen, but a covalently attached Alexa fluorophore was not expected to produce an EvaGreen-like melt curve. In addition, the total fluorescence of the double-stranded Alexa488 control was 18.2% higher than the single-stranded control. The control results that relied on Alexa488/EvaGreen excitation and emission were further confirmed using the ABI 7500 PCR machine. Whilst the results seem promising, these discrepancies call the FRET experiments into question.

If the FRET donor Alexa488 fluorophore emission decreases by 18.2% in a sigmoidal curve, then that would need to be taken into account as the Alexa532 FRET acceptor fluorescence would also follow a similar pattern even if the fluorophores are still adjacent. The underlying fluorescence “melt curve” of the Alexa488 when double-stranded requires investigation and modelling if these experiments are to be used to investigate SAW melting temperatures.

3.4.3. Discussion and Conclusion

During the experiment it was noted that the absolute fluorescence for the green filter was significantly lower than expected. Controls measuring temperature dependent fluorescence of only the ssDNA with each fluorophore showed the expected decrease in fluorescence from room temperature to 100°C of around 10%, yet when the green fluorescence recovered in the FRET experiments it was around 20% lower than expected, suggesting that there was still FRET between the Alexa488 and Alexa532. Additional experiments noted that the Alexa488-labelled DNA with unlabelled secondary DNA produced a melt curve similar to that seen if FRET were working as expected, or if EvaGreen were used (see Figure 4-1). Whilst the experiment FRET appeared to work, this unexpected signal from the negative controls needed further research – was the fluorescence of the acceptor Alexa532 fluorescence decreasing because the fluorophores were moving apart as predicted, or was the fluorescence of the Alexa532 fluorophore decreasing as the fluorescence of the Alexa488 donor fluorophore decreased? If Alexa488 changes fluorescence depending on the binding of an unlabelled complementary strand, then why persist with FRET if a single fluorophore could be used to perform the same experiment?

The preliminary results from the FRET experiments suggested that there wasn't a significant difference in melting temperature with SAW when the fluorescence of the FRET fluorophores was examined, which would mean that the SAW effect seen was due to the reporter molecule EvaGreen, but no definitive answer can be given until the Alexa488 effect is better understood. Work in Chapter 4 aims to characterise this effect, whilst Chapter 5 aims to utilise it to perform existing techniques. Once the Alexa488 fluorescence effect is understood, or an alternative fluorophore identified for FRET that doesn't exhibit the same effect, then these experiments should be completed with SAW in the future.

4. Characterisation of the Nucleobase-Specific Quenching effect (NB-S Quench)

The melt curves produced by Alexa488 in the FRET experiments were unexpected and unexplained. Alexa488 was chosen for its similar excitation and emission spectra to EvaGreen, although the production of melt curves is not assumed to be directly related – EvaGreen changes confirmation in the presence of double-stranded DNA, the excitation/emission profile is incidental. This chapter compares the fluorescence phenomenon described in Chapter 3 to known fluorescence effects such as FRET-like π -stacking (photoinduced electron transfer when donor and acceptor fluorophores are π -stacked) between two or more Alexa488 fluorophores and guanine/nucleotide quenching / enhancement between Alexa488 fluorophores and DNA, both noted in literature [75,76,159,160]. In brief, the aim is to determine if this novel fluorescence behaviour is due to Alexa488-Alexa488 fluorophore interactions, or Alexa488-DNA (likely guanine) interactions.

A model based on the work in this chapter was introduced to explain the different derivative peak directions, based on experimental conclusions that the direction of the peak is likely due to DNA base adjacent/opposite to the fluorophore.

The melting temperatures derived using the nucleospecific fluorescence quenching technique were compared with those derived using the control EvaGreen reporter molecule to confirm reproducibility and reliability against an established standard technique. The effects of pH were examined (Alexa488 fluorophores are particularly pH stable [161]), and absorption was investigated and compared again to EvaGreen as EvaGreen is the industry standard.

Established protocols using reporter molecules, such as EvaGreen or FRET, were used to quantify the concentration of both strands of DNA, allowing concentration-dependant FRET-like quenching to be determined.

Lastly, the sequence effect on Alexa488 fluorescence was elicited by varying the complementary strands, including LAMP primers so that LAMP with Alexa488 can be examined in Chapter 5. There are several theories as to the mechanism behind this observed fluorescence effect, by changing the sequence of the DNA more can be understood about what is happening at the nucleotide level.

4.1. Introduction

Whilst examining controls using the Peltier module for the DNA for FRET experiments (Chapter 3) an unusual fluorescence signal was noted as the DNA melted. When the fluorescent molecules are close together on the same ends of the DNA strands, as the DNA melted the expected FRET signal of an increase in the fluorescence of the donor fluorophore was seen as (shown by the red points in Figure 4-1), and the expected decrease in fluorescence of the acceptor fluorophore was seen. However, when the fluorophores were far apart, instead of a constant, steady decrease in fluorescence (as seen in the black points of ssDNA labelled with Alexa488 in Figure 4-2) a DNA melt curve similar to that seen with EvaGreen was found (shown by the green points in Figure 4-1 and Figure 4-2). At 95°C the absolute fluorescence signals show in Figure 4-1 were equivalent - varying by 1.2% which is comparable to the variation between melt curve repeats ($\pm 0.9\%$).

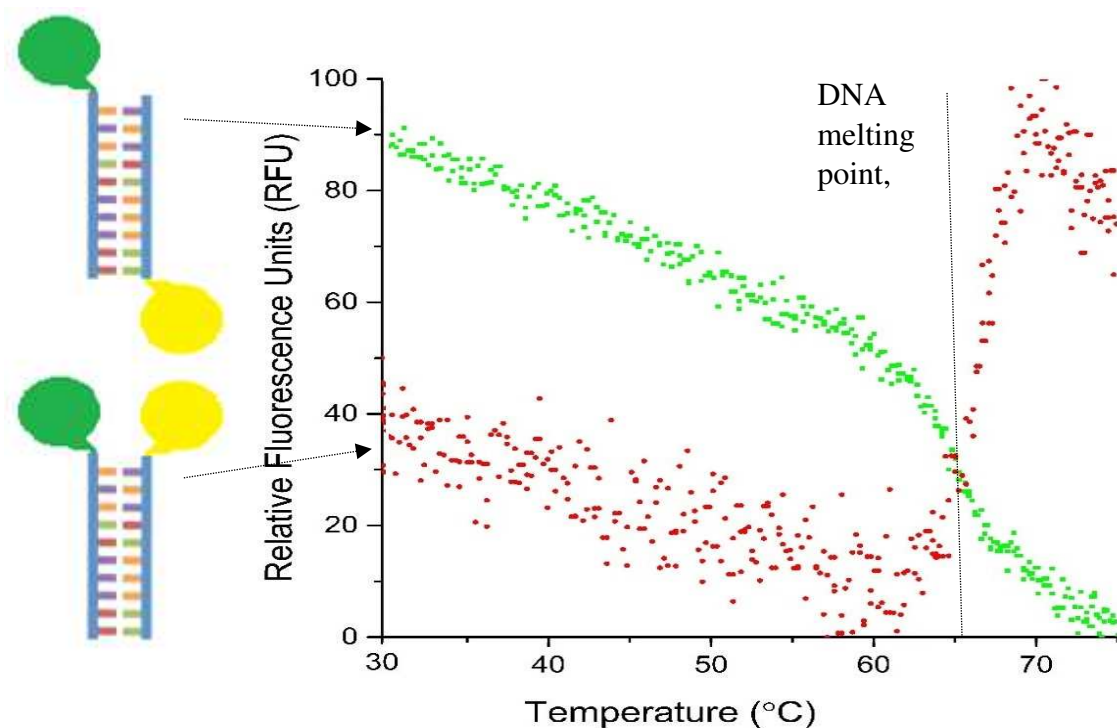


Figure 4-1 Green fluorescence of Alexa488 and Alexa532 (yellow fluorescence not shown) FRET experiments normalised between maximum and minimum. Green Square – Alexa488 Fluorophores on opposite ends of DNA A, fluorescence signal similar to EvaGreen. Red Circle – Alexa488 Fluorophores on adjacent ends of DNA A, showing recovery of green signal / alleviation of FRET when DNA melts increasing distance from Alexa532

This phenomenon was limited to double-stranded DNA labelled with Alexa488, whilst Alexa532 and single-stranded DNA produced the expected results. Double-stranded DNA with Alexa488 gave a fluorescent signal similar to EvaGreen, with similar melting temperatures as with EvaGreen (Figure 4-4). The absolute fluorescence signal of single-stranded Alexa488 labelled DNA above the melting temperature was equivalent to that seen from the double-stranded experiments, suggesting that the Alexa488 fluorescence was enhanced in double-stranded DNA compared to the single-stranded state, or that the Alexa488 fluorescence was inhibited in the single-stranded state as can be seen in Figure 4-2.

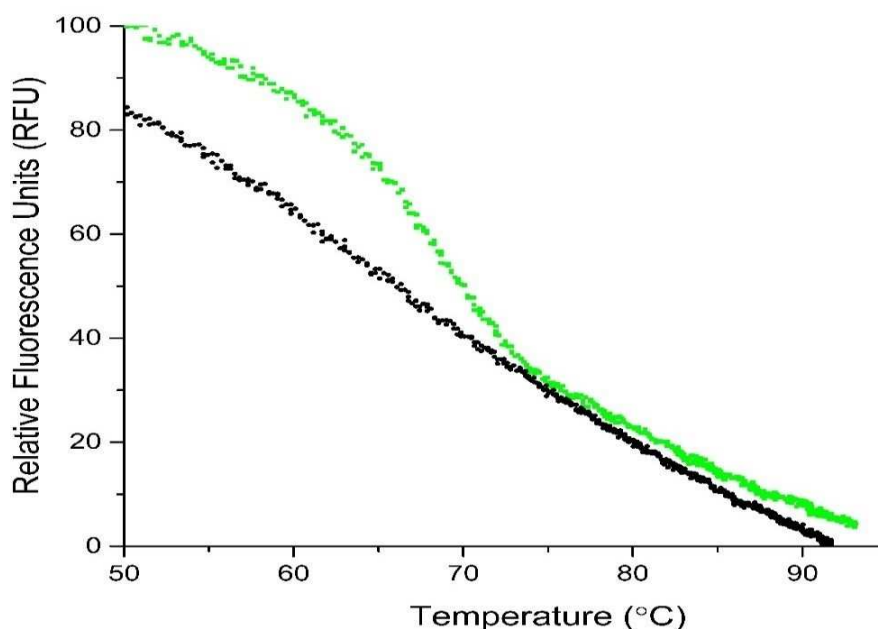


Figure 4-2 Green fluorescence of single-stranded (black squares), and double-stranded (green circles) Alexa-488 labelled DNA C, normalised to maximum of double-stranded fluorescence. Experiments performed on Zeiss upright microscope using EvaGreen filters. Absolute fluorescence from 70-95°C were within experimental variation.

Nucleotide quenching of nearby fluorophores has been noted previously and where the complementary strand overlap so free DNA nucleotides are able to interact with the fluorophore – donating electrons or protons [20,76,162,163]. Dyes have also been noted with nucleobase-specific fluorescence lifetimes, allowing all 4 bases to be distinguished [162]. In these experiments, the fluorescence intensity decreases on addition of the complementary strand, with fluorescence increasing when the DNA strands melt. Conversely, DNA tagged with Alexa488 shows increased fluorescence intensity with addition of the complementary strand, which reduces as the DNA melts. In addition to this, short secondary strand with no overlap of nucleotides as discussed in section 0 still exhibit an EvaGreen-like signal.

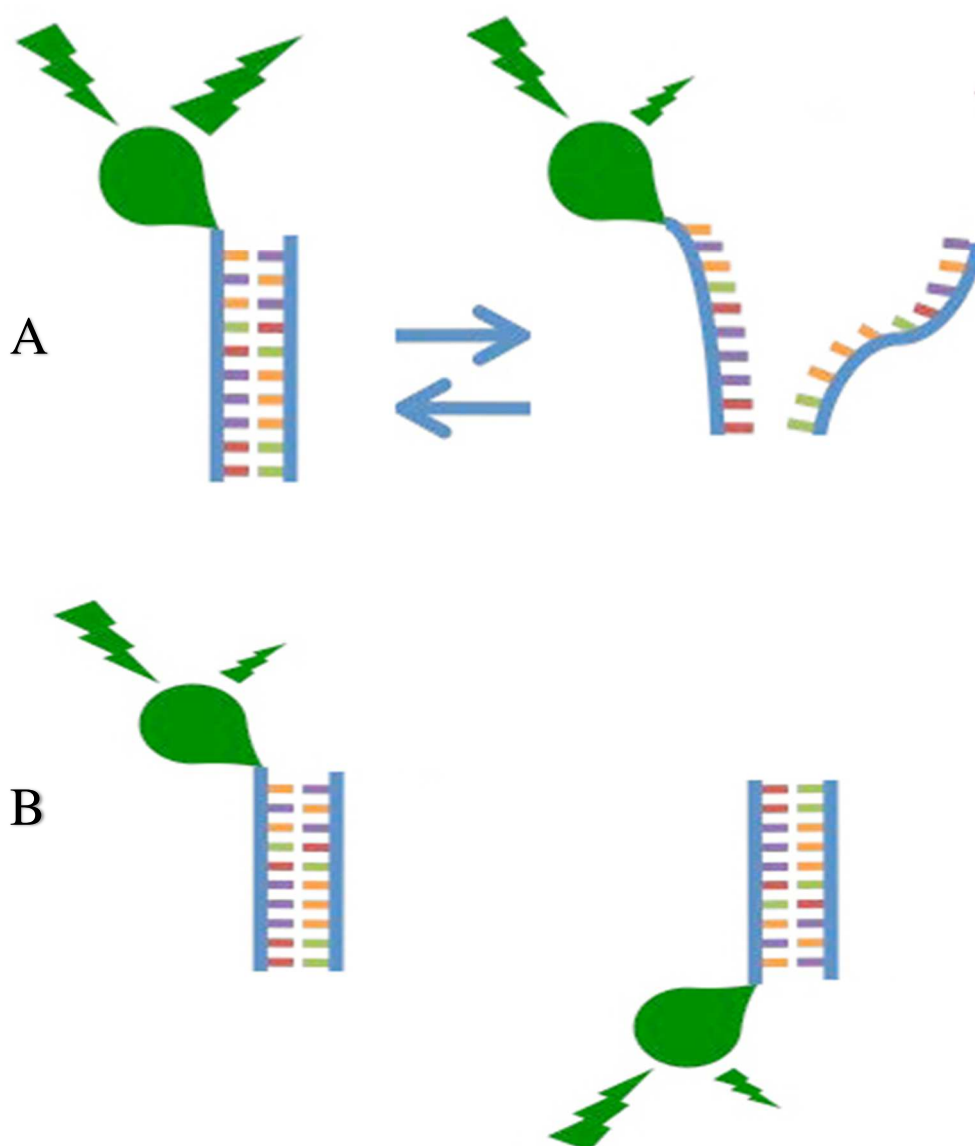


Figure 4-3 (A) Fluorescence of Alexa488 decreases when the DNA is single-stranded. (B) This effect is seen when the fluorophore is attached to the 5' and 3' end of the DNA strand.

π -stacking of the Alexa488 fluorophores, as happens in FRET, can produce self-quenching in a concentration dependant manner [76]. If the Alexa488 fluorophores were interacting with each other, and self-quenching, then this quenching would increase as the concentration increased. This could explain the change in fluorescence when the DNA is single-stranded, as absence of the complementary strand would allow the fluorophores to interact more closely in solution, perhaps through partial binding of the GC rich region close to the fluorophore or secondary structure formation. Quenching due to π -stacking between fluorophores and adjacent bases has been noted [164], and methods to reduce this effect investigated [20], but there has been no suggestion that this quenching would be relieved when the complementary strand were added, nor that it could be used to determine if the labelled DNA strand was double- or single-stranded in solution.

It is possible to interpret the data show in Figure 4-2 in two ways, as the fluorescence increases on addition of the complementary strand of DNA this suggests that the phenomenon seen involves suppression of fluorescence when the DNA is single-stranded (modelled in 4.3), or enhancement of fluorescence when DNA is bound. Intercalating reporter molecules such as EvaGreen show enhancement of absorbance and subsequent fluorescence as the dye changes confirmation to sit in the presence of double-stranded DNA to sit in the hydrophobic groove.

This chapter will examine the basis of this fluorescence effect, by comparing the Alexa488 derived melting temperatures to established techniques; how buffer pH affects the fluorescence; and if the absorption of the fluorophore is changed. These results allow a model to be suggested in 4.3. Later experiments will look specifically at altering the sequence of the labelled and complementary strands, and the structural similarities to known fluorophores, such as Atto488 and FITC.

4.2. Comparison with Existing Methods

As shown in Figure 4-4, Alexa488 derived melting temperatures of DNA C at $64.5^{\circ}\text{C} \pm 0.49$ whilst unlabelled DNA and EvaGreen reporter molecule was found to be $67.1^{\circ}\text{C} \pm 1.14$, ANOVA Tukey analysis found that the probability that they were the same group was 0.2198, showing there is some difference. For DNA D, the EvaGreen derived melting temperature was $59.39^{\circ}\text{C} \pm 0.80$ whilst using the Alexa488 method it was $58.7^{\circ}\text{C} \pm 0.02$. ANOVA Tukey analysis was that these were the same group, with $P=0.9522$. Whilst the temperature found using Alexa488 was lower, there was less variation than with EvaGreen. Further experiments looking at comparing the melting temperatures will be discussed in 4.5 and 4.7. If the melting temperature derived using Alexa488 fluorescence is less variable than existing methods, then it could replace reporter molecules such as EvaGreen for common laboratory techniques such as PCR and LAMP (discussed further in Chapter 5).

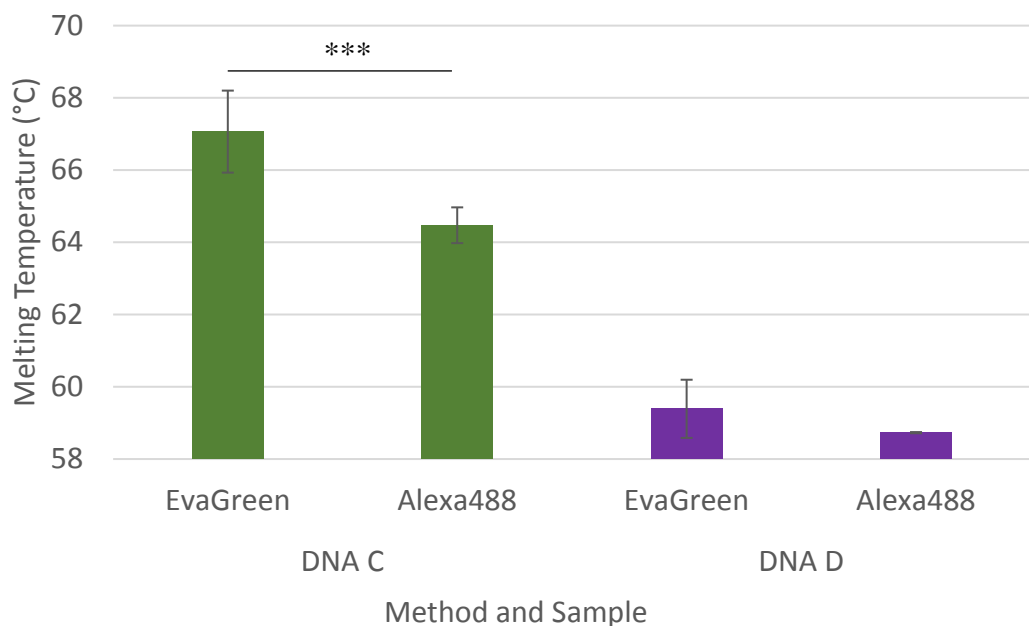


Figure 4-4 Melting points derived using Alexa488 method and EvaGreen controls for DNA C (green) and D (purple). Average of 20 10 μl replicates of 10 μM DNA in 7.8pH TE buffer measured in Applied Biosciences 7500 PCR Machine. EvaGreen experiments used 1 μl of 20x EvaGreen per reaction. * shows $P < 0.05$, ** $P < 0.01$, *** $P < 0.001$, the rest showed no significant difference.

4.3. Modelling of Binding Fluorescence and Melt Curves in OriginPro

The results throughout this chapter (particularly 4.5) suggest that G and A bases are quenching the Alexa488 fluorophore when adjacent or opposite (on the complementary strand) [20,76,163]. The Nearest Neighbour model for DNA binding states that the base closest to the end of the DNA has a lower binding energy, due to base stacking and solvent effects, so it is proposed that the nucleobase hydrogen bonds transition between the fluorophore and complementary base resulting in quenching, as has been suggested before [76,162,163].

For this proposed model, the fluorophore fluorescence parameters were based on previous experiments. These parameters included decreasing by 20% between 0-100°C, with the melt curve changing fluorescence by 20% in a sigmoidal function generated by Origin between 40-60°C. Quenching of up to 40% by G bases has been noted [163], whilst quenching by A bases of up to 95% has also been shown in the literature [75]. The intermediate curves were produced by averaging the simulated sigmoidal curve with the linear model based on temperature dependant quenching of fluorophores.

The area:peak ratio for adjacent nucleotide quenching is $2.8 \pm 5 \times 10^{-6}$ and $3 \pm 4 \times 10^{-6}$ for opposite nucleotide quenching. This ratio will be determined experimentally for EvaGreen and Alexa488, to provide assurance that the melt curves seen are significantly different from background noise.

Quenching from adjacent nucleotide when DNA is single-stranded

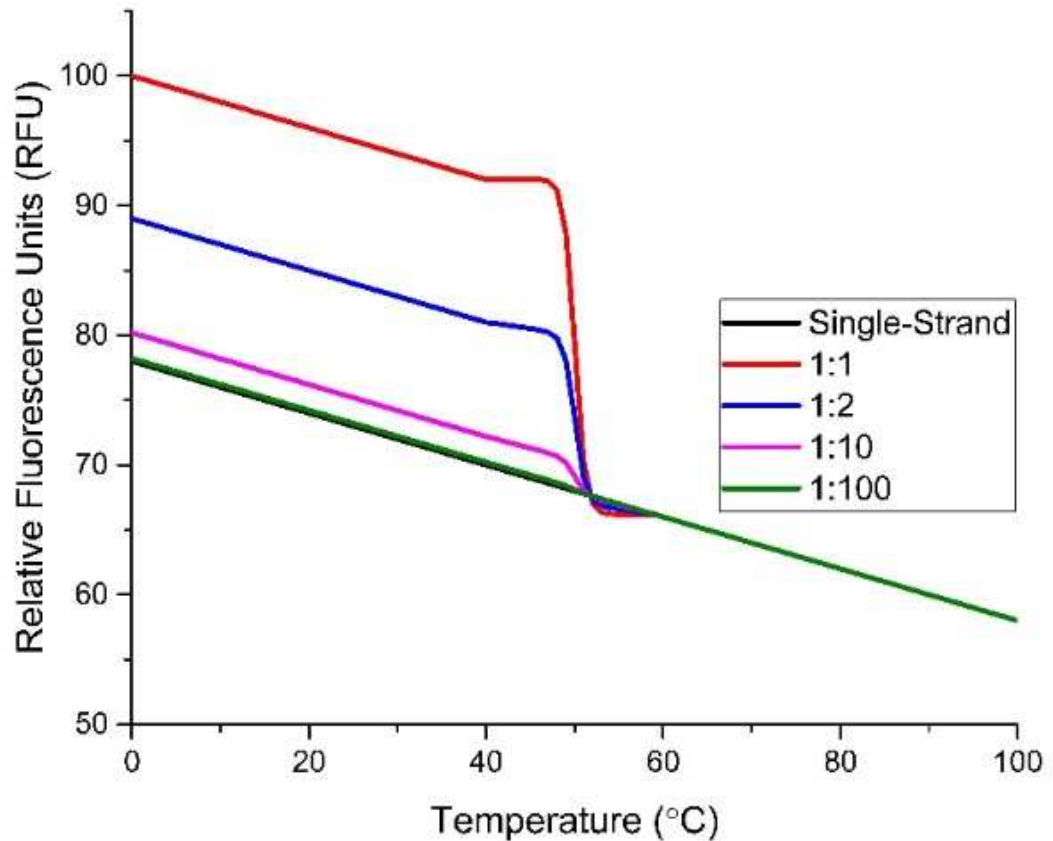


Figure 4-5 OriginPro model of G/A quenching adjacent to the fluorophore. The double-stranded model shows higher fluorescence as single-stranded quenching is relieved when G/A bases are bound to their complements. Black shows the single-stranded model, red shows the average of one single-strand and one double-stranded model, blue shows the average of one single-strand with two double-stranded models, purple shows the average of one single-strand and ten double-stranded model, and green shows the average of one single-strand and one hundred double-stranded model.

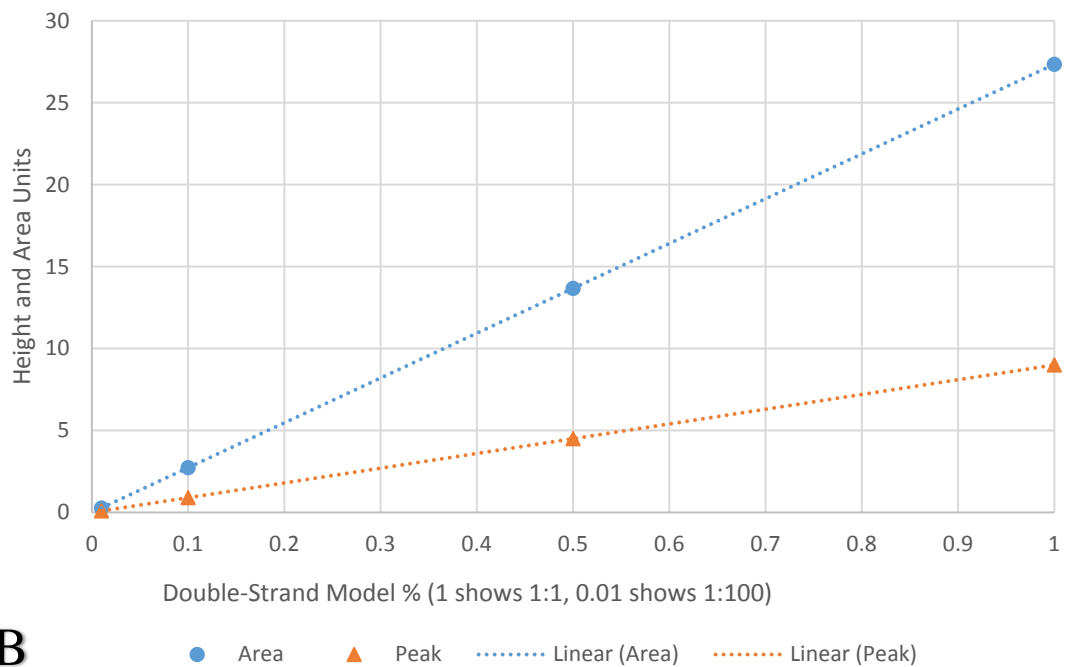
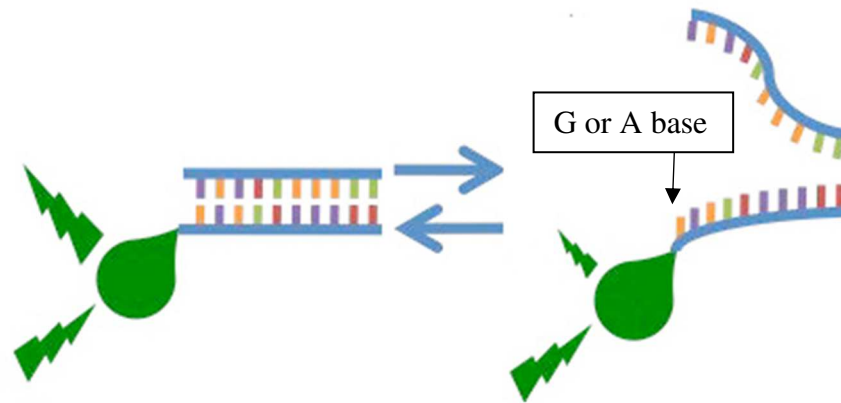
A**B**

Figure 4-6 (A) Pictogram showing that Alexa488 fluorescence is reduced when DNA is single-stranded. The higher quenching (A/G) base is on the same strand adjacent to the fluorophore. Fluorescence is relatively higher when the DNA is double-stranded as the A/G base interacts with its complement base.

(B) Peak height (orange triangle) and area (blue circle) of derivative peaks from those simulated, measured using OriginPro. Height and area of the derivatives are recorded as negative to differentiate between a positive direction melt peak and negative direction “melt valley”.

Quenching from complementary nucleotide when DNA is double-stranded

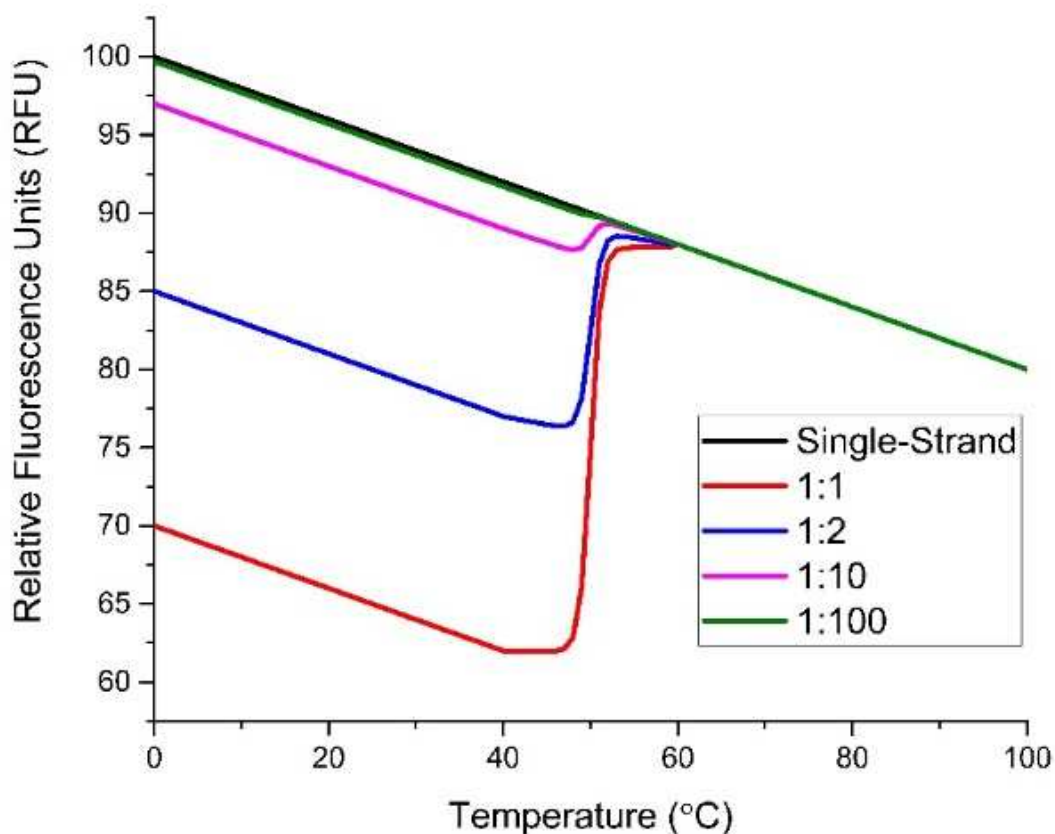
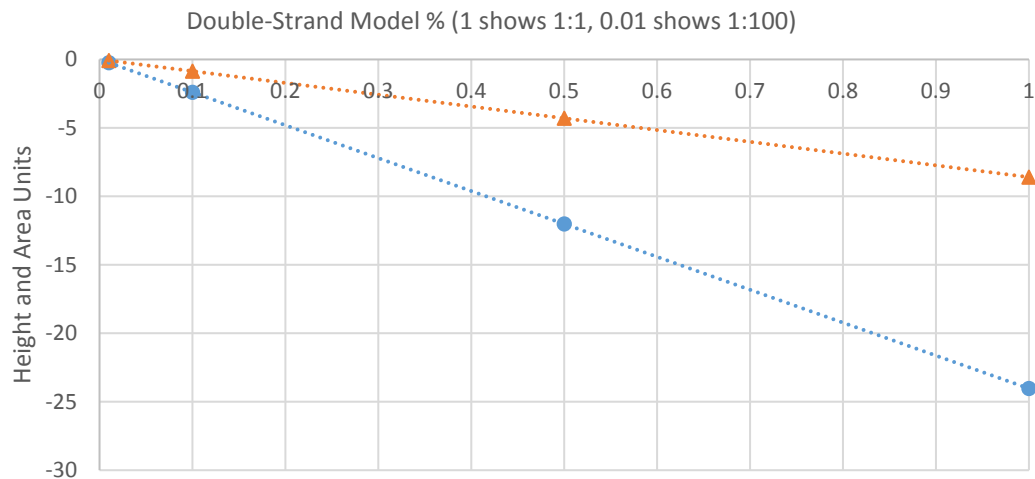
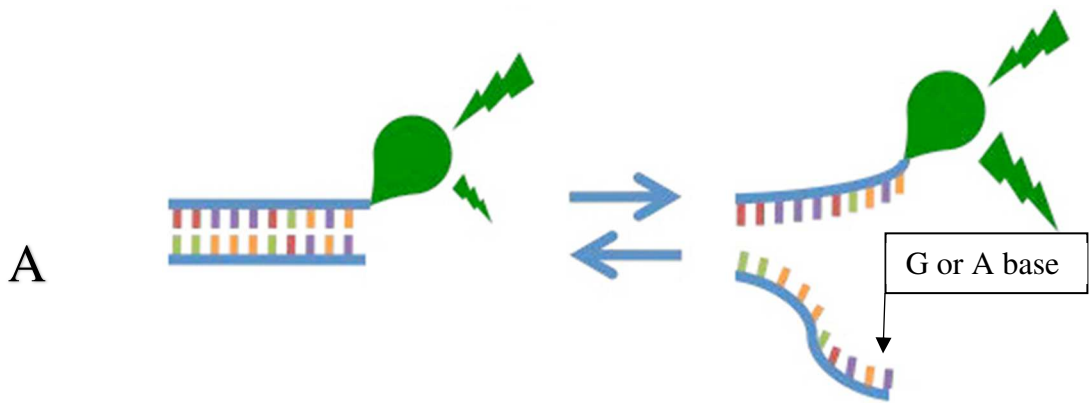


Figure 4-7 OriginPro model of G/A quenching on the opposite strand. The single-stranded model shows higher fluorescence as quenching is relieved when G/A bases on the complement strand are not bound. Black shows the single-stranded model, red shows the average of one single-strand and one double-stranded model, blue shows the average of one single-strand with two double-stranded model, purple shows the average of one single-strand and ten double-stranded model, and green shows the average of one single-strand and one hundred double-stranded model.



B

● Area ▲ Peak Linear (Area) Linear (Peak)

Figure 4-8 (A) Pictogram showing that Alexa488 fluorescence is reduced when DNA is double-stranded. The higher quenching base (A/G) is on the complement strand, and interacts with the fluorophore and its complement adjacent to the fluorophore. Fluorescence is relatively higher when the DNA is single-stranded, and the fluorophore only interacts with the weaker quenching base adjacent (T/C).

(B) Peak height (orange triangle) and area (blue circle) of derivative peaks from those simulated, measured using OriginPro. Height and area of the derivatives are recorded as negative to differentiate between a positive direction melt peak and negative direction “melt valley”.

4.4. pH Stability

Alexa fluorophores are known to be relatively pH stable when compared to other dyes including EvaGreen, and are described as pH insensitive between pH 4.0 and 10.0 [161]. The changes in melting temperatures seen using 488-labelled DNA follow that seen with EvaGreen, the gradients for the trend lines of EvaGreen and Alexa488 methods varied by 6.9% for DNA B and 3.7% for DNA C. Alexa488 had a higher R^2 of 0.89 (DNA B) and 0.96 (DNA C) compared to 0.72 (DNA B) and 0.60 (DNA C) for EvaGreen, suggesting that Alexa488 method is more reliable over the pH ranges measured. These results suggest that the solvent effect is similar to that seen with EvaGreen.

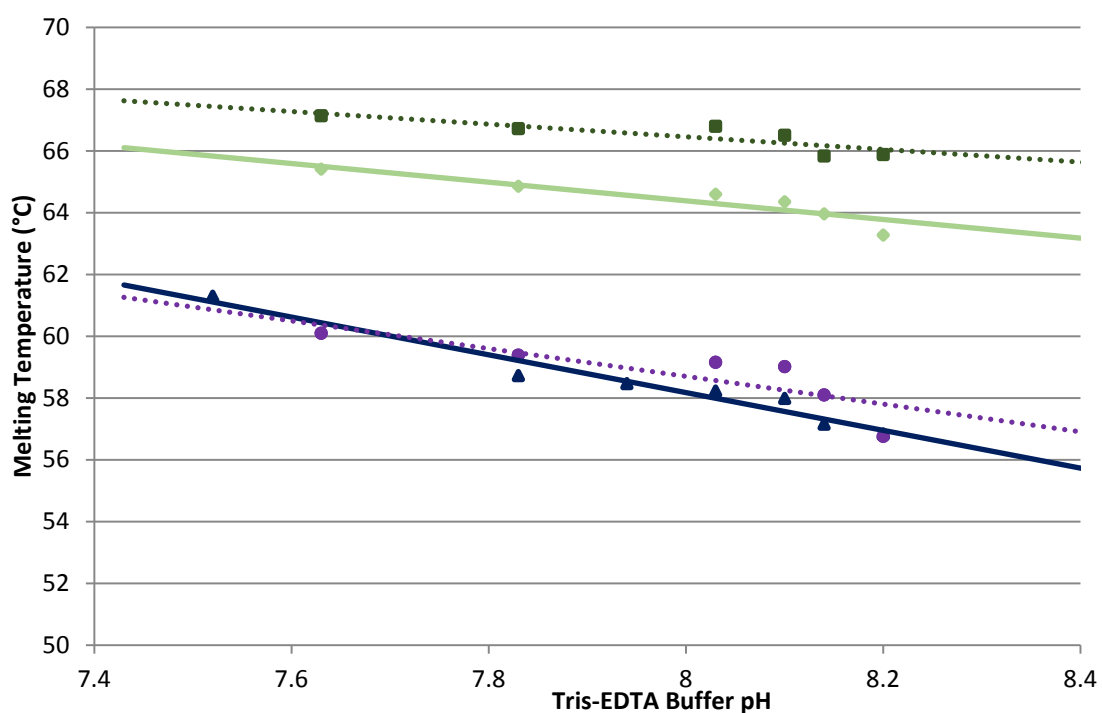


Figure 4-9 Measuring the effects of TE buffer pH on the melting temperature of DNA B (blue) and C (green) using Alexa488 (diamond, triangle) or EvaGreen (square, circle) as a reporter molecule. The linear best fit for Alexa488-derived melting temperatures is shown with a solid line, the linear best fit line for EvaGreen-derived melting temperatures is shown in a dashed line. Average of 10 replicates of 10 μ l of 10 μ M DNA in TE buffer. EvaGreen experiments used 1 μ l of 20x EvaGreen per reaction. Melt curves were measured and analysed using Applied Biosciences 7500 PCR Machine.

4.5. Labelled Strand, Analysis of Nearest Base Effects on Fluorescence

In order to further study the effect of the sequence adjacent to the fluorophore, additional DNA oligonucleotides based on DNA B, C, and BRCA1 LAMP primers were designed as in Table 4-1 below. Full sequences are in Figure 4-11.

Name	Length (base pairs)	GC Content %	Adjacent Base	Complement Base	Defined Melt Curve	Derivative Peak
C	30	73.3	G	C	Yes	+(Peak)
C-reverse	30	73.3	G	C	Yes	+(Peak)
D	21	76.2	G	C	Yes	+(Peak)
LPF5B	20	65	A	T	Yes	+(Peak)
LPR5F	22	45.5	A	T	Yes	+(Peak)
FIP	45	42.2	A	T	Yes	+(Peak)
BIP	47	38.3	G	C	Yes	+(Peak)
F3	19	47.4	T	A	Yes	-(Valley)
B3	23	34.88	C	G	Yes	-(Valley)

Table 4-1 Length, GC content, nucleotide and peak comparison of Alexa488-labelled DNA

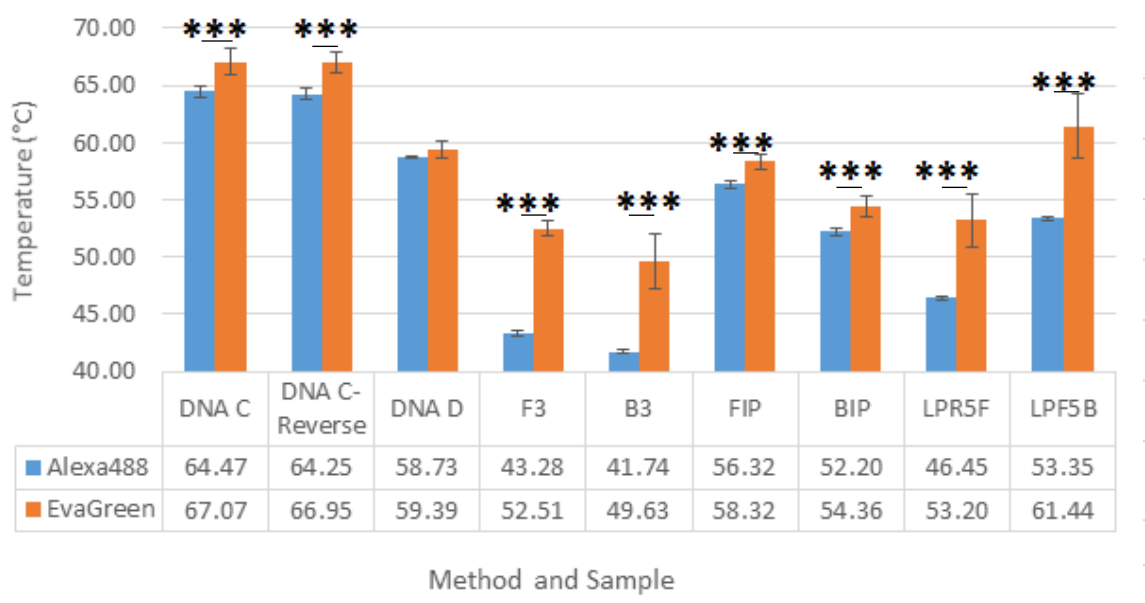


Figure 4-10 Comparison of melting temperatures of the DNA used to analyse the nearest base effect on the fluorescence. Melting temperatures were derived using the Alexa488 method (blue) and EvaGreen as a control (orange). Average of 10 10µl replicates of 10µM DNA in 7.8pH TE buffer measured in Applied Biosciences 7500 PCR Machine. EvaGreen experiments used 1µl of 20x EvaGreen per reaction. * shows P<0.05, ** P<0.01, *** P<0.001, the rest showed no significant difference.

controls. As these are produced due to different mechanisms, further investigation is required to determine the fundamental reason for the discrepancy in melting temperatures.

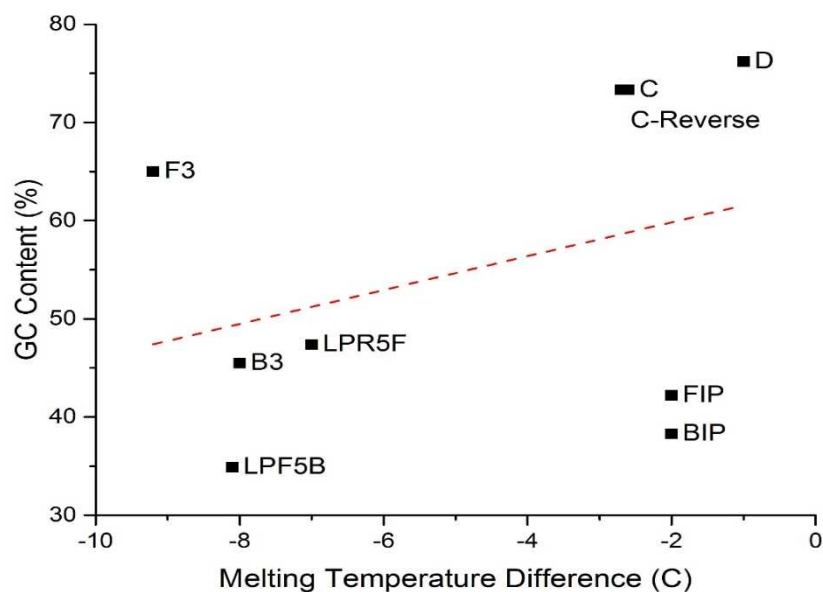


Figure 4-12 Comparison of GC content (%) and the difference in melting temperature (°C), statistical analysis found no strong correlation.

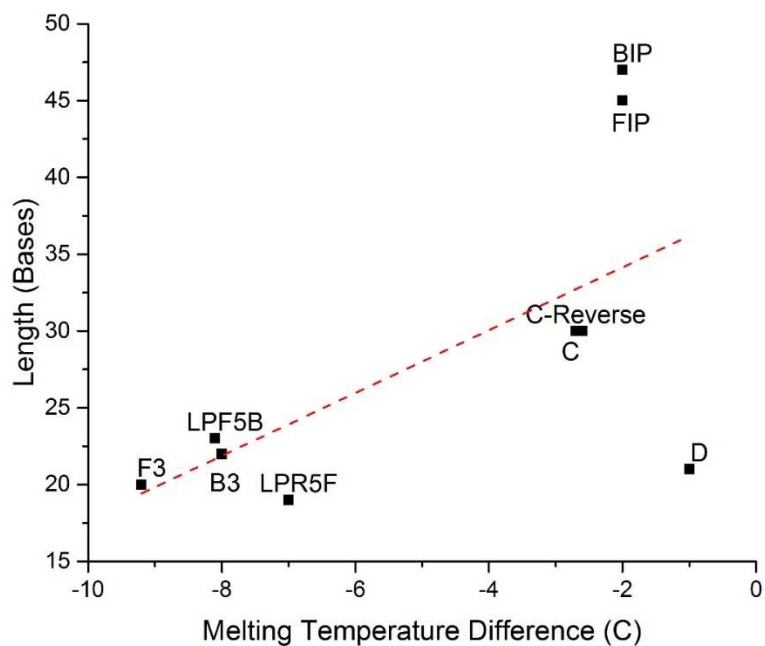


Figure 4-13 Comparison of DNA length (bases) and the difference in melting temperature (°C), statistical analysis found no strong correlation.

Further experiments should be done with DNA sequences with T and C base adjacent to the fluorophore (see Future Work), but the results suggest that there is quenching when the adjacent base is near which is relieved when the complement strand binds, or there is quenching when the complement strand binds which is relieved (resulting in an increase in fluorescence) when the labelled DNA is single-stranded. G bases are known to quench fluorescence, so the proposed model (see 4.3) is that G and A bases are quenching when adjacent or opposite the fluorophore, although further experiments would be needed to decide this with a high degree of certainty.

The Alexa488-derived melting temperatures are consistently below the EvaGreen controls, as seen in Figure 4-10 and Table 4-1. There is no obvious link between individual variables of GC content, nearest bases, or length and the difference in melting temperatures with the controls. Most are around 2°C below the controls, but some of the DNA oligonucleotides - particularly F3 and B3 but also LPR5F and LPF5B - showed large differences between the EvaGreen controls (Table 4-2). The strongest correlation was found between the difference in melting temperature as a percentage of EvaGreen-derived melting temperature, with a factor combining the length and GC content. This should be further investigated, as it could mean that the Alexa488 method for deriving melting temperatures is not reliable with short, low GC content DNA. Additional investigation into the mechanism would be required before this could be used as a new method.

	DNA C	DNA C - Reverse	DNA D	F3	B3	FIP	BIP	LPR5F	LPF5B
Difference (°C)	-2.6	-2.7	-1	-9.2	-8	-2	-2	-7	-8.1

Table 4-2 Difference between melting temperatures derived using EvaGreen and Alexa488

4.6. Absorption Studies Introduction

To further understand the quenching effects, which result in the Alexa488 DNA melting curves, the absorbance of the single- and double-stranded DNA was determined. The absorbance and emission spectra for reporter molecules such as EvaGreen have been well characterised, and consists of two distinct peaks at 470nm and 495nm [14]. EvaGreen changes confirmation in the presence of double-stranded DNA, resulting in an increase in the absorbance at 495nm and decrease at 470nm, see Figure 4-14 [14]. If there is a significant change in conformation of Alexa488, this could result in a similar multi-peak absorption spectra and comparable changes in the absorption and emission spectra.

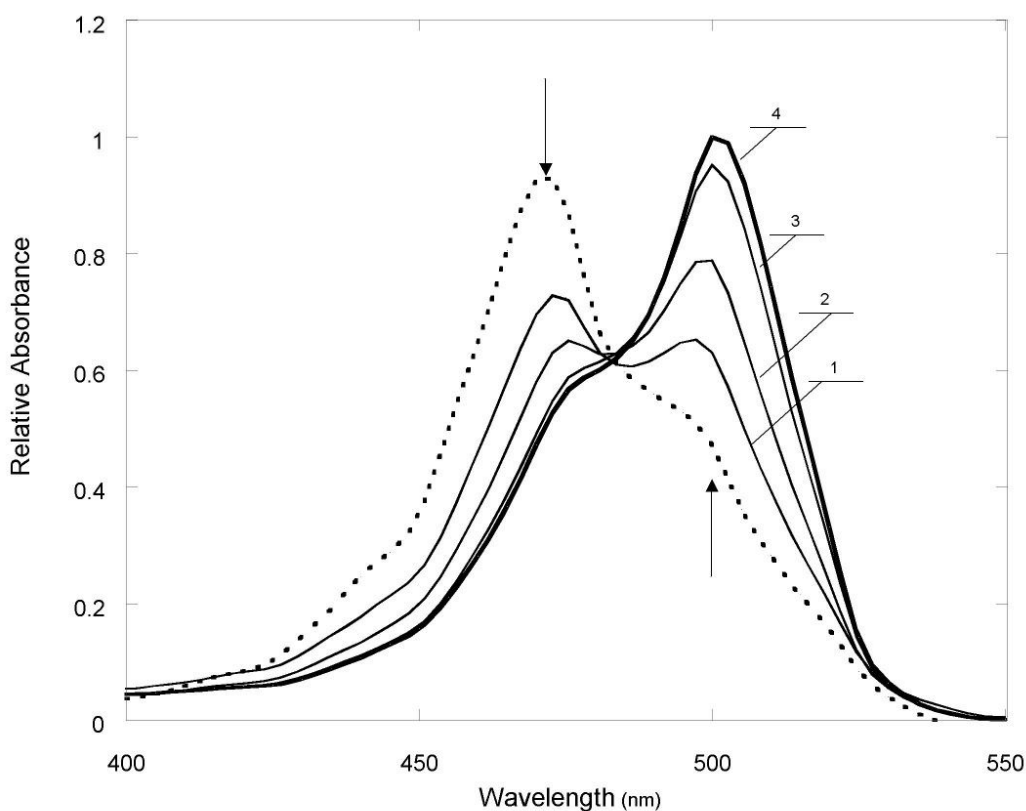


Figure 4-14 EvaGreen absorption in varying amounts of DNA, reproduced from [14].

Dotted line – 0ng/μl, Line 1 - 5 ng/μl, Line 2 - 10 ng/μl, Line 3 – 25 ng/μl, Line 4 – 100 ng/μl

Spectra measured with 11.15μM of EvaGreen, 100mM Tris buffer pH8.0

The quenched state is defined as that with the relatively lower fluorescence. If the fluorescence increases when the DNA melts, then the lower fluorescence at room temperature (25°C) when the DNA is double-stranded is defined as the quenched state whilst the higher fluorescence at 95°C when the DNA is single-stranded is defined as the unquenched state. If the fluorescence decreases when the DNA melts (as with EvaGreen), then the lower fluorescence at 95°C when the DNA is single-stranded is defined as the quenched state whilst the higher fluorescence at room temperature (25°C) when the DNA is double-stranded is defined as the unquenched state.

Based on the model that G and A bases are quenching Alexa488 when beside or opposite the fluorophore, it was expected that the absorption of single-stranded F3 and B3 will be more similar to the double-strand of FIP, BIP, LPR5F and LPF5B as these are unquenched, whilst the opposite will be true as the fluorophore is in a quenched state.

Results and Discussion

Absorbance spectra for F3, B3, FIP, BIP, LPR5F and LPF5B were obtained, F3 and BIP are shown in Figure 4-15. The spectra for F3 and B3 show increases in the total absorption area, when the complementary strand of DNA, as per the model in 0, whilst FIP, BIP, LPR5F and LPF5B all showed decreases, Figure 4-16 (A and B). The height of the absorption peak increased for F3 and B3, but decreased for FIP, BIP, LPR5F and LPF5B.

A shift in absorption peak is seen as shown in Figure 4-16 (C and D) when the fluorophore is unquenched, from $492.2\text{nm} \pm 0.4$ to $494.3\text{nm} \pm 0.7$, although this is significantly smaller than the shift seen in EvaGreen (from 470 to 495nm). This suggests that there is not a large conformational change as seen when EvaGreen binds to double-stranded DNA.

Absorption was only measured in 1nm steps, so a shift of only 2nm should be verified in future experiments with more accurate equipment, although this setup was able to previously identify the difference in absorbance of EvaGreen in ssDNA and dsDNA. As the fluorescence experiments were performed with a 488nm laser source, any shift away from 488nm will result in less energy absorbed by the fluorophore, and a corresponding reduction in fluorescence, although this would not account for the 20% reduction observed.

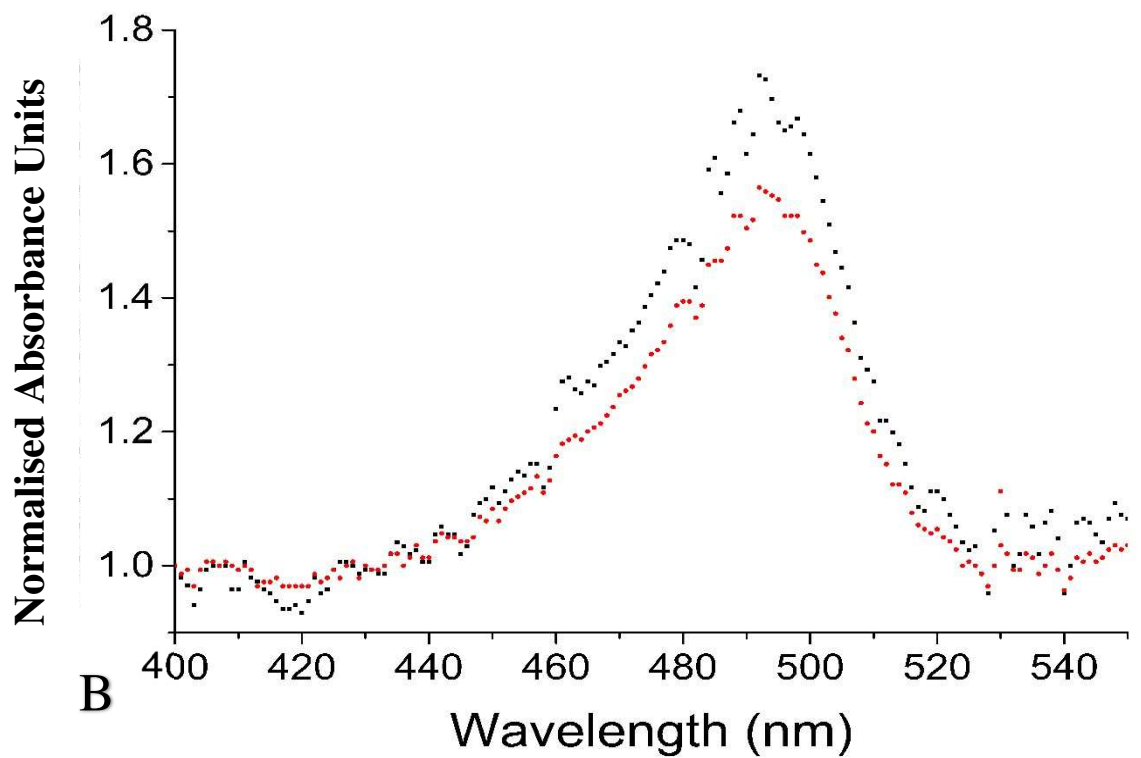
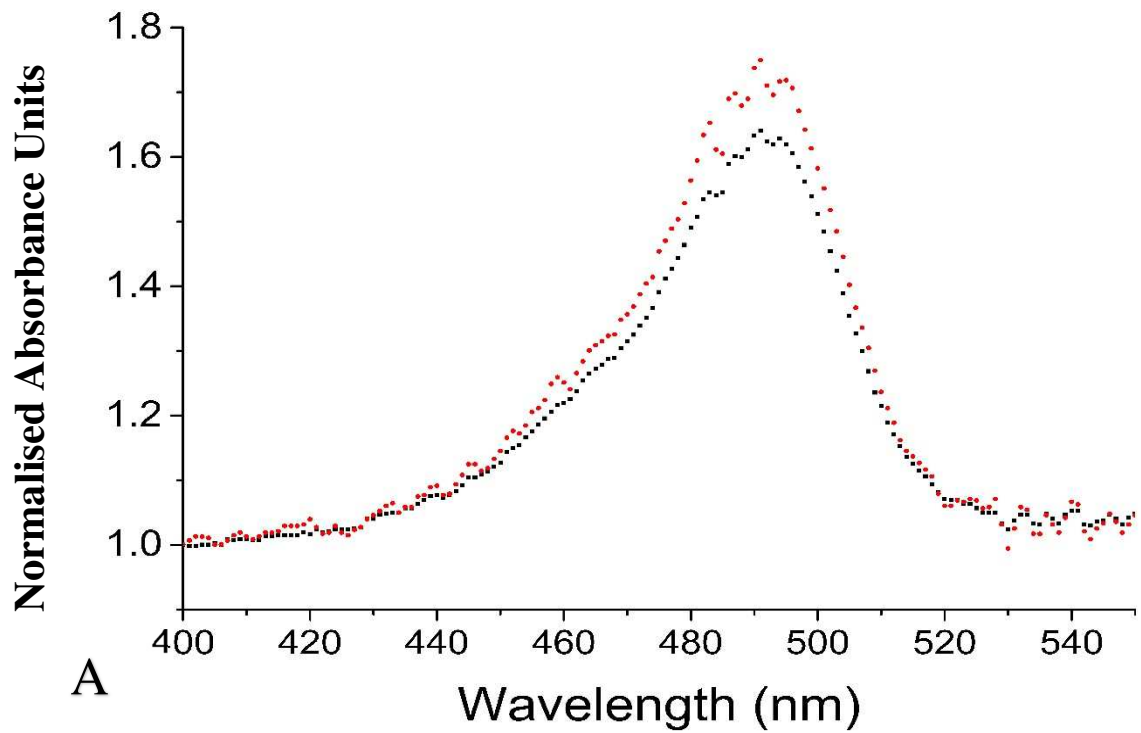


Figure 4-15 Averaged absorbance spectra of 1M F3(A) and BIP(B). Single-stranded DNA is shown with black squares, double-stranded DNA is shown with red diamonds. 10 μ l of 10 μ M DNA were prepared in 7.8pH Tris-EDTA buffer and absorbance measured in 1nm steps from 400-600nm (5 replicates of 1 μ l) using a BioTek Absorbance Reader. Readings were calibrated relative to 400nm and averaged with OriginPro(2016).

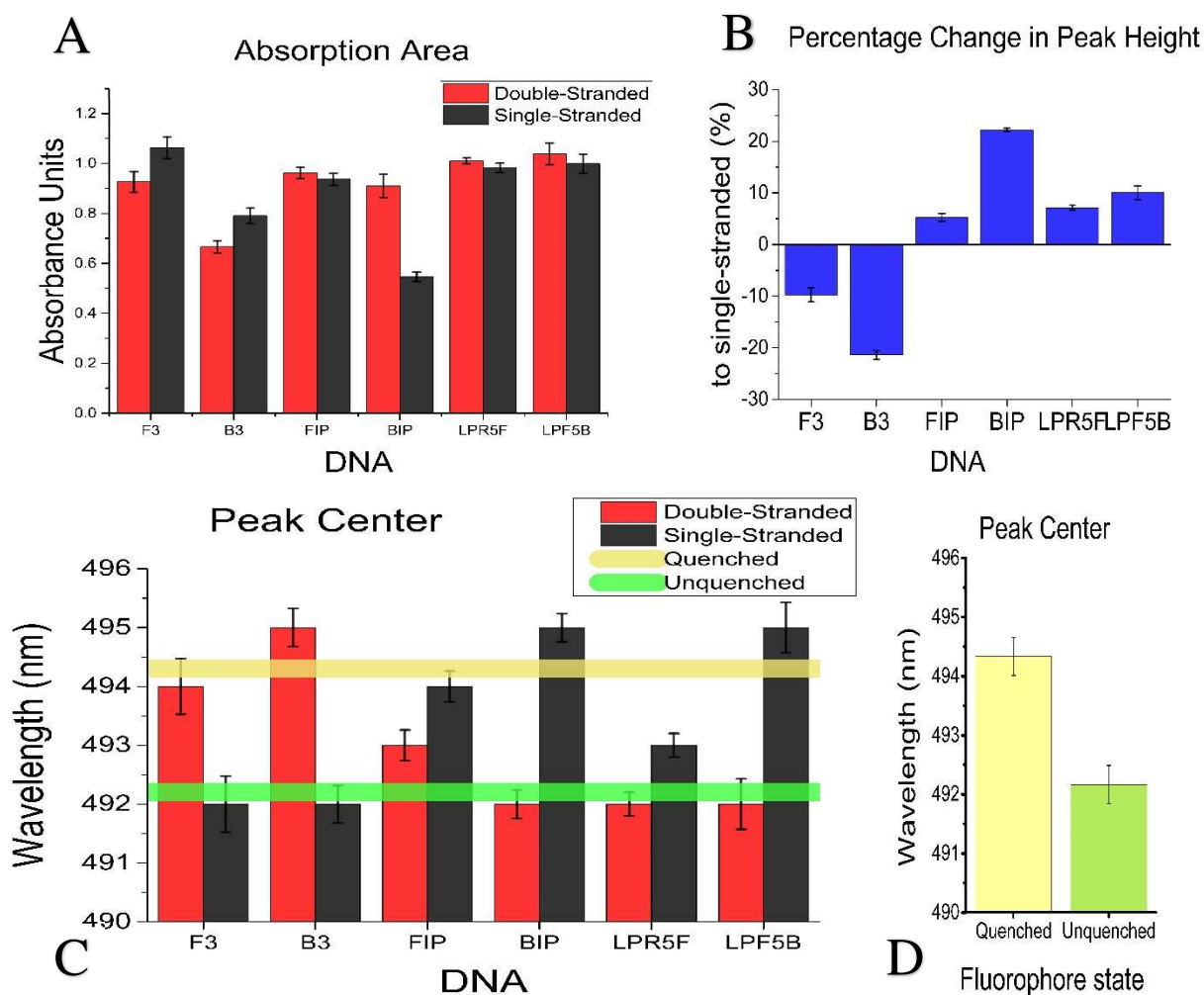


Figure 4-16 (A,C) Red shows double-stranded DNA, black shows single-stranded DNA.

(B, D) Yellow shows fluorophore in quenched state, green shows fluorophore in unquenched state.

(A) Absorption spectra of double- and single-stranded DNA. F3 and B3 show increases in absorption area in the single-stranded state compared to double-stranded. FIP, BIP, LPR5F and LPF5B show decreases in absorption in the single-stranded state compared to double-stranded.

(B) Percentage change in peak height from single-stranded to double-stranded DNA. F3 and B3 show decreases. FIP, BIP, LPR5F and LPF5B show increases.

(C) Absorbance spectra absorbance peaks. In the absolute peaks F3 and B3 show decreases in the wavelength of the highest peak centre in single-stranded DNA compared to double-stranded DNA, whilst FIP, BIP, LPR5F and LPF5B show increases.

(D) Shows the average wavelength of the highest peak, as per the model described in 0. Quenched includes the double-strand of F3, B3 and the single-strand of FIP, BIP,

4.7. Complementary Strand Effects

In order to discover how nucleotides on the complementary strand affect the Alexa488 fluorescence, several experiments were designed. The first group examined either fully double-stranded DNA, the second group examined DNA that is double-stranded adjacent to the fluorophore but with single-stranded portion at the opposite end, the third group examines the fluorophore adjacent to single-stranded DNA.

The model (section 4.3) predicts that the first and second group of DNA should produce quantifiable melting curves as the fluorophore can be affected directly by the change in charge on the nearest nucleotide. For the third group, it is expected that the further away the double-stranded DNA is from the fluorophore, the less the effect can be measured.

FRET has been known to work at distances of 1-10nm between the fluorophores, although the effectiveness reduces quickly with distance [43]. The 3, 6, 9 and 12 bases of single-stranded DNA between the fluorophore and the double-stranded sequence correlate to approximately 1nm, 2nm, 3nm and 4nm respectively. Previous experiments in the literature have noted that addition of TTT between double-stranded DNA and the fluorophore would eliminate the fluorescence effect [20], so this was also examined to confirm that this could remove the fluorescence effect when it is unwanted.

4.7.1. Completely Double-Stranded DNA

Alexa488-modified DNA (Table 4-3) was used to measure melting temperature of completely double-stranded DNA, and compared to the melting temperature of unmodified DNA measured with EvaGreen. For DNA C-Reverse, the Alexa488 fluorophore was on the 3' end of the DNA strand, which did not make a measurable difference to the melting temperature derived with EvaGreen or Alexa488 compared to the 5' end for DNA C and D. In all cases the Alexa488 derived melting temperatures were lower than the controls, and with less variation between readings (see Table 4-4).

DNA	Sequence and Fluorophore Position
C	Alexa488-GGGCCCCAGCGCCAACAGTCGGGCGCTTGTG
C-Reverse	GGGCCCCAGCGCCAACAGTCGGGCGCTTGTG-Alexa488
D	Alexa488-GGGCCCCAGCGCCAACAGTCG

Table 4-3 Sequences of DNA oligonucleotides

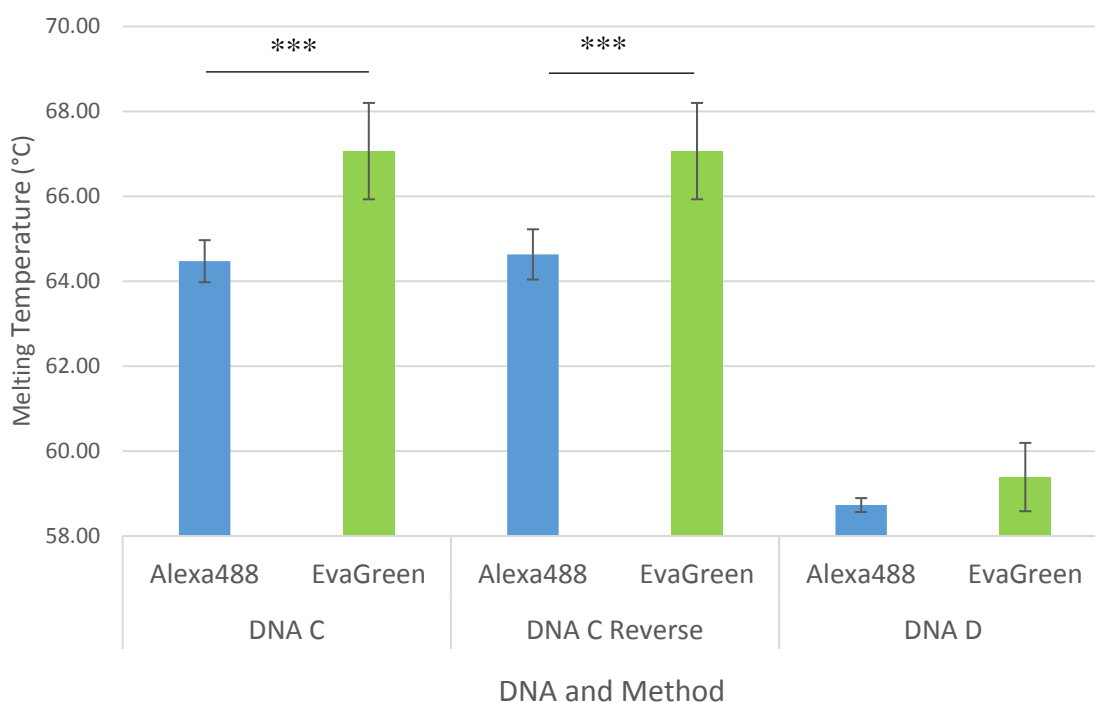


Figure 4-17 Melting temperatures of completely double-stranded DNA derived using EvaGreen or Alexa488 as a reporter molecule. Averages of 10 replicates of 10µM DNA in 7.8pH Tris-EDTA buffer, measured in Applied Biosciences 7500 PCR Machine. EvaGreen experiments used 1µl of 20x EvaGreen and unlabelled DNA oligonucleotides. * shows P<0.05, ** P<0.01, *** P<0.001, the rest showed no significant difference.

	DNA C		DNA C Reverse		DNA D	
Method	Alexa488	EvaGreen	Alexa488	EvaGreen	Alexa488	EvaGreen
Average	64.47	67.07	64.63	67.07	58.73	59.39
StDev	0.49	1.14	0.59	1.14	0.16	0.81

Table 4-4 Melting points and standard deviation between measurements by DNA and method.

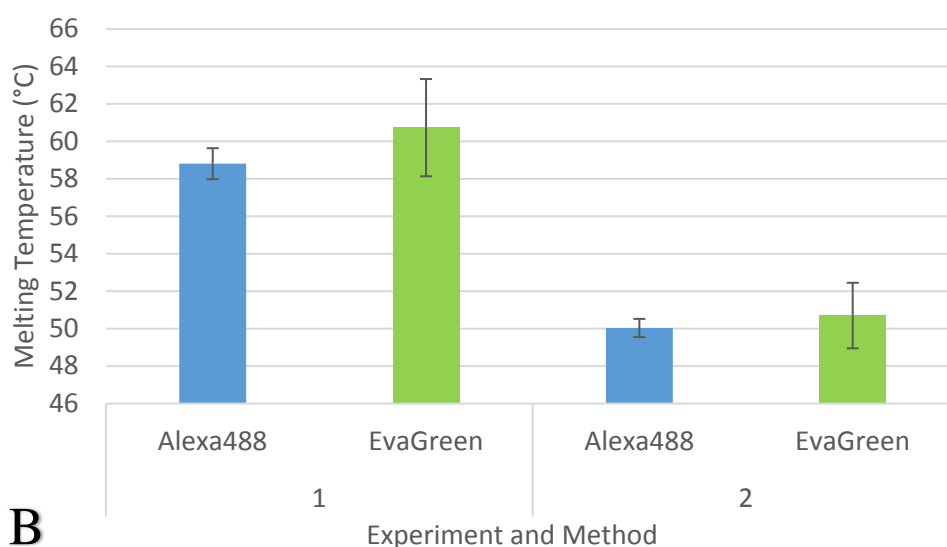
As discussed in 4.5, the reason for the difference in melting temperatures is not clear, although DNA D seemed to be closer than DNA C. DNA D is a truncated DNA C, 24 bases instead of 30, so length could be a factor. DNA C also has a slightly lower GC content, at 74.2% compared to 77.3% for DNA D. As T bases act as insulators, length and GC content will both be important.

4.7.2. Double-Stranded Adjacent to Fluorophore

The labelled strand is the same used for DNA C (1) and DNA C reverse (2) in 4.5. As in 4.5, the Alexa488-derived melting temperature is below that for the control, and showed less variability. For both experiments the nearest base adjacent to the fluorophore was G base, as in previous experiments. Figure 4-19 shows examples of the melting curves derived using Alexa488 fluorescence.

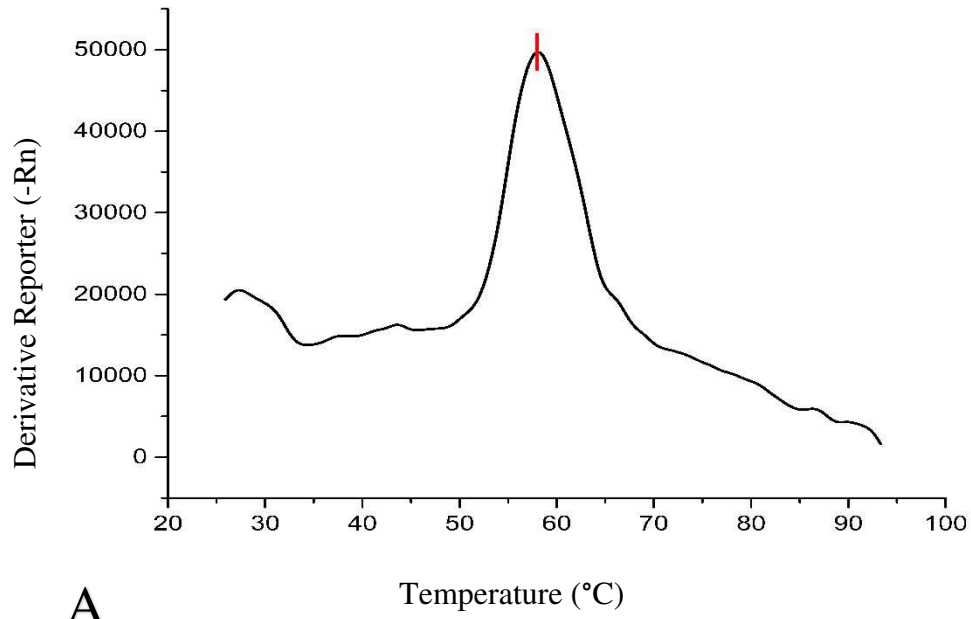
Experiment		1		5		10		15		20		25		30																								
1	Alexa488-	G	G	G	C	C	C	C	A	G	C	G	C	C	A	A	C	A	G	T	C	G	G	C	G	C	T	T	G	T	G							
		C	C	C	G	G	G	G	T	C	G	C	G	G	T	T	G	T	C	A	G	C																
2		G	G	G	C	C	C	C	A	G	C	G	C	C	A	A	C	A	G	T	C	G	G	C	G	C	T	T	G	T	G							
	Alexa488																					G	T	T	G	T	C	A	G	C	C	G	C	G	A	A	C	A

A

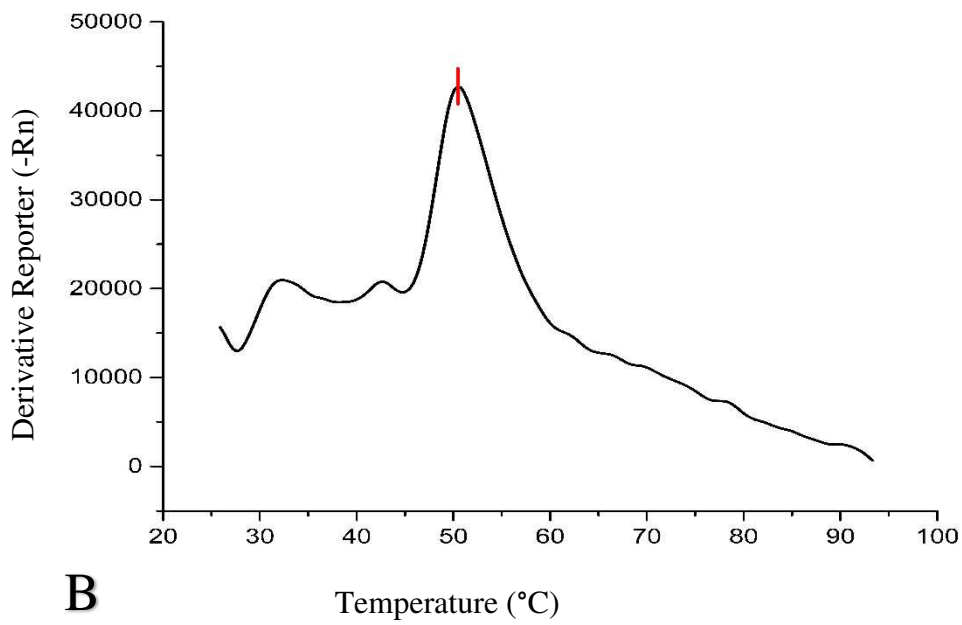


B

Figure 4-18 Sequence (A) and melting temperatures (B) of DNA that is double-stranded adjacent to the fluorophore derived using EvaGreen (green) or Alexa488 (blue) as a reporter molecule. Averages of 10 replicates of 10µM DNA in 7.8pH Tris-EDTA buffer, measured in ABI 7500. EvaGreen experiments used 1µl of 20x EvaGreen and unlabelled oligonucleotides. * shows P<0.05, ** P<0.01, *** P<0.001, the rest showed no significant difference.



A



B

Figure 4-19 (A) Example derivative curve from Experiment 1 and (B) Experiment 2 showing a melt peak at 58°C (A) and 50°C (B). 10 μ M DNA in 7.8pH TE buffer, measured in ABI 7500

Double-Stranded DNA Summary

A reliable melt curve was derived when the fluorophore was attached to completely double-stranded DNA, or if there was double-stranded DNA adjacent to the fluorophore. It should be noted that DNA C and D were originally chosen for this portion of the experiment as the Alexa488 derived melting temperatures were close to the controls derived using EvaGreen. Further experiments would be needed to ascertain the reason for the differences in melting temperatures seen with the BRCA1 LAMP oligonucleotides (section 4.5). DNA C and D will be used below to investigate the effects of partial single-stranded DNA between the fluorophore and double-stranded DNA.

4.7.3. Single-Stranded Adjacent to Fluorophore

These experiments examined the effect of short single-stranded DNA adjacent to the fluorophore. If the effect seen is due to photoinduced electron transfer, then the fluorescence will primarily be affected by the base closest to the fluorophore. The charge of that base will in turn be affected by the next adjacent base along the sequence, which in turn influences the fluorophore via the closest nucleobase.

EvaGreen can bind to ssDNA, so an increase in ssDNA was expected to increase the variability in these experiments.

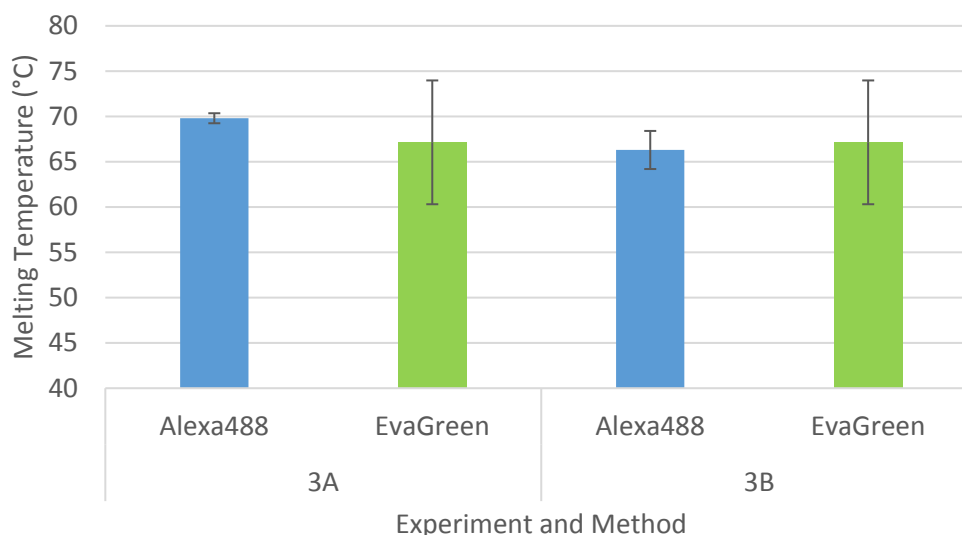
4.7.3.1. 3 Bases of Single-Stranded DNA, 1nm from Fluorophore

There were 3 bases (~1nm) of single-stranded DNA adjacent to the fluorophore. The melting temperature derived from Alexa488 is closer to that found with EvaGreen, but again with less variation. In 3A the melting temperature is above that found with EvaGreen, contrary to previous experiments, in 3B it is slightly lower. There is a slightly larger variation in 3B of $\pm 0.83^{\circ}\text{C}$ compared to $\pm 0.49^{\circ}\text{C}$ for 3A. The single-stranded sequence next to the fluorophore is GTG for 3A instead of GGG for 3B, if T bases reduce the quenching effect due to a different redox potential, this could explain the differences in the derived melting temperatures. Additionally, if T bases are having the opposite charge effect on the fluorophore, this could explain the larger variation in melting temperature.

Another possible reason could be the nearest base where the DNA is double-stranded. Both derivative curves (Figure 4-21) show a false melt peak due to signal noise just after the melt curve is begun, around 27°C, and numerous additional other peaks, which act as a comparison between the signal from the fluorophore and background noise. The false melt peaks appeared at the start of derivative curves where there is very little change in fluorescence, and can be used to determine how likely a melt temperature is to be true.

A

Experiment	1	5	10	15	20	25	30
3A	Alexa488-	G G G C C C C A G C G C C A A C A G T C G G C G C T T G T G					
		G G G G T C G C G G T T G T C A G C C G C G A A					
3B		G G G C C C C A G C G C C A A C A G T C G G C G C T T G T G					Alexa488
		G G G G T C G C G G T T G T C A G C C G C G A A					



B

Figure 4-20 Sequence (A) and melting temperatures (B) of DNA that has 3 single-stranded bases adjacent to the fluorophore derived using EvaGreen (green) or Alexa488 (blue) as a reporter molecule. Averages of 10 replicates of 10µM DNA in 7.8pH Tris-EDTA buffer, measured in ABI 7500. EvaGreen experiments used 1µl of 20x EvaGreen and unlabelled oligonucleotides. * shows P<0.05, ** P<0.01, *** P<0.001, the rest showed no significant difference.

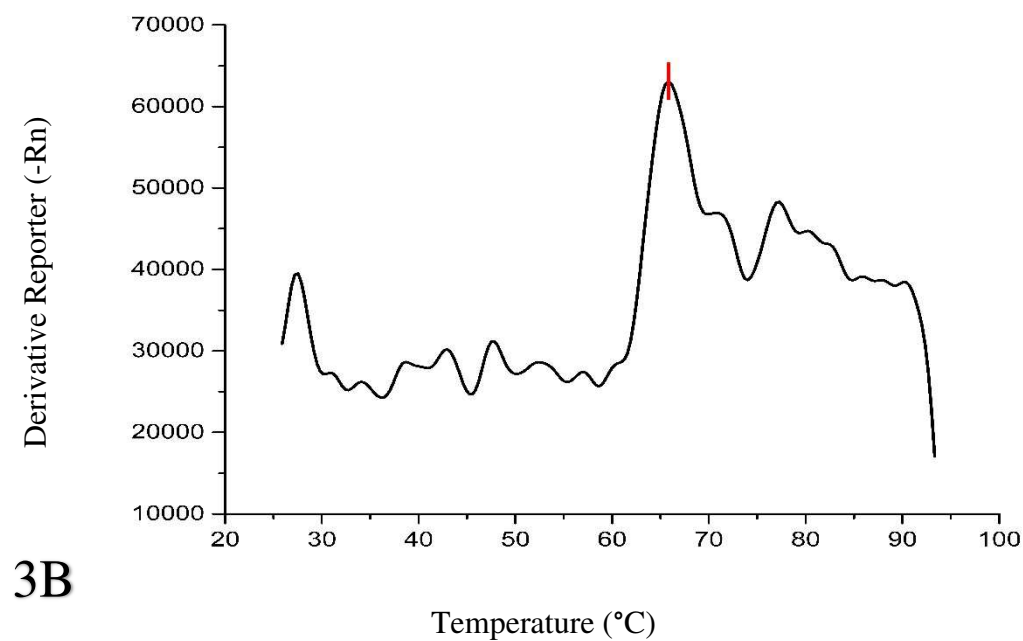
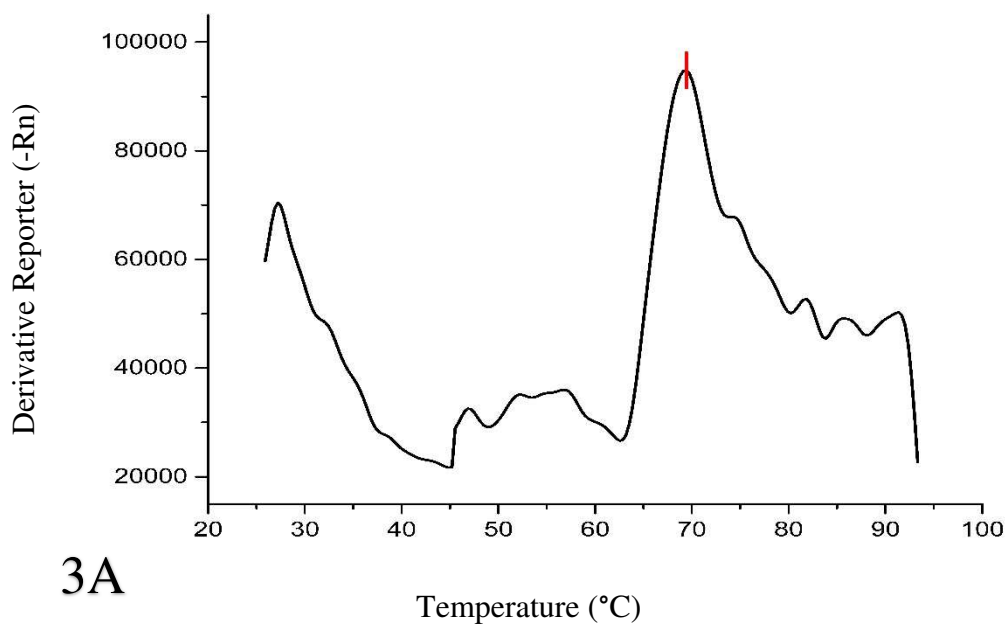


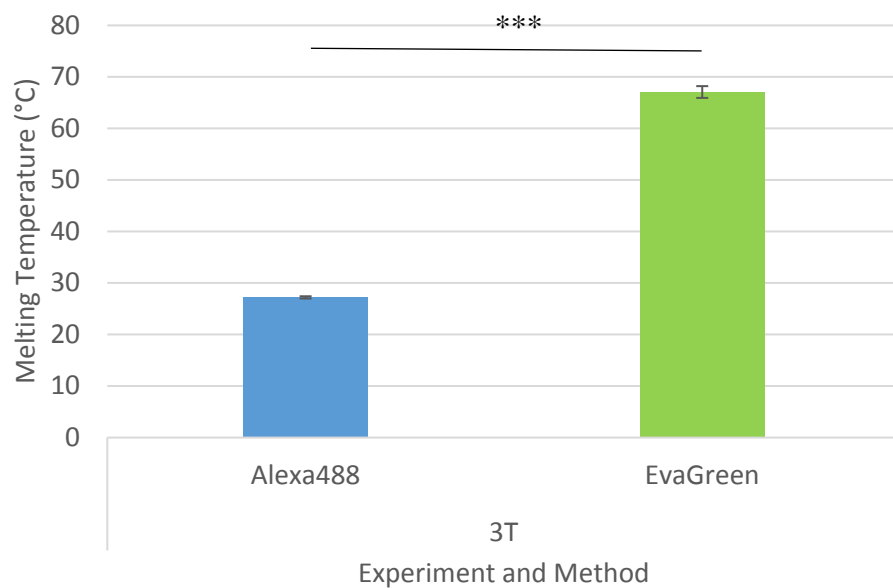
Figure 4-21 Example derivative curve from Experiment 3A (3A) and Experiment 3B (3B) showing a melt peak at 70°C (3A) and 66°C (3B). 10 μ M DNA in 7.8pH Tris-EDTA buffer, measured in ABI 7500

4.7.3.2. 3 Bases of Single-Stranded DNA consisting of T bases, 1nm from Fluorophore

The addition of 3T bases adjacent to the fluorophore to remove the photoinduced quenching effect has been noted in the literature. As predicted, single-stranded TTT adjacent to the Alexa488 fluorophore removed the fluorescence effect previously seen (Figure 4-22). The false peak due to signal noise at 27°C was predominant, and there were no peaks distinguishable in the background noise around the expected melting temperature (Figure 4-23)

Experiment	1	5	10	15	20	25	30	
3T	G G G C C C A G C G C C A A C A G T C G G C G C T T G T G T T T							Alexa488
	C C C G G G G T C G C G G T T G T C A G C C G C G A A C A C							

A



B

Figure 4-22 Sequence and melting temperatures of DNA that has 3 single-stranded T bases adjacent to the fluorophore derived using EvaGreen (green) or Alexa488 (blue) as a reporter molecule. Averages of 10 replicates of 10µM DNA in 7.8pH Tris-EDTA buffer, measured in ABI 7500. EvaGreen experiments used 1µl of 20x EvaGreen and unlabelled oligonucleotides. * shows P<0.05, ** P<0.01, *** P<0.001, the rest showed no significant difference.

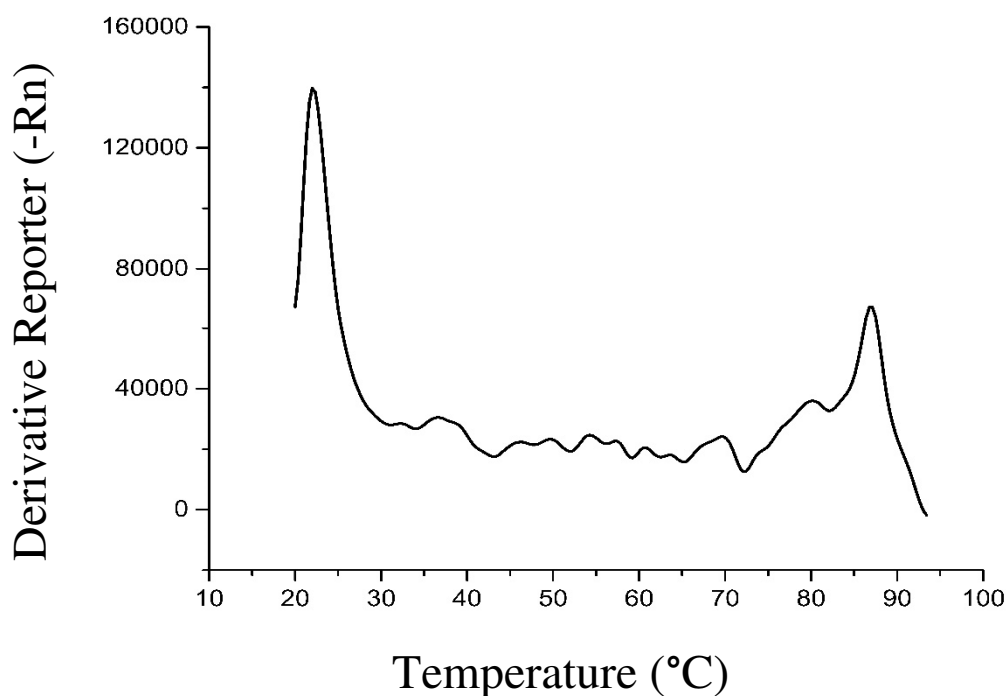


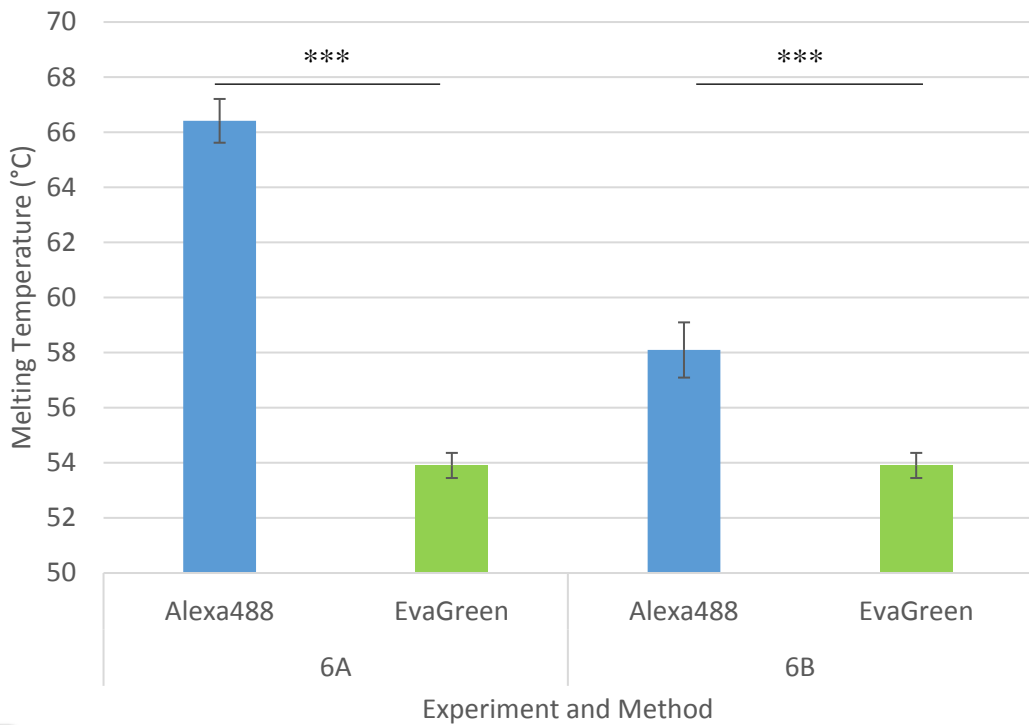
Figure 4-23 Averaged derivative curves from Experiment 3T showing a false peak around 27°C. 10 μ M DNA in 7.8pH Tris-EDTA buffer, measured in ABI 7500.

4.7.3.3. 6 Bases of Single-Stranded DNA, 2nm from Fluorophore

There are 6 bases (~2nm) of single-stranded DNA adjacent to the fluorophore. The melting temperature derived using Alexa488 were found to be higher than EvaGreen, and with higher variation, see Figure 4-24. The EvaGreen controls in this case were the same. Derivative peaks (Figure 4-25) are wide, with numerous additional peaks and a false peak due to signal noise at the start, suggesting that this is unreliable.

A

Experiment		1		5		10		15		20		25		30																
6A	Alexa488-	G	G	G	C	C	C	A	G	C	G	C	C	A	A	C	A	G	T	C	G	G	C	G	C	T	T	G	T	G
							G	T	C	G	C	G	G	T	T	G	T	C	A	G	C	C	G	C						
6B		G	G	G	C	C	C	A	G	C	G	C	C	A	A	C	A	G	T	C	G	G	C	G	C	T	T	G	T	G
								G	T	C	G	C	G	G	T	T	G	T	C	A	G	C	C	G	C					



B

Figure 4-24 Sequences (A) and melting temperatures (B) of DNA that has 6 single-stranded bases adjacent to the fluorophore derived using EvaGreen (green) or Alexa488 (blue) as a reporter molecule. Averages of 10 replicates of 10µM DNA in 7.8pH Tris-EDTA buffer, measured in ABI 7500. EvaGreen experiments used 1µl of 20x EvaGreen and unlabelled oligonucleotides.

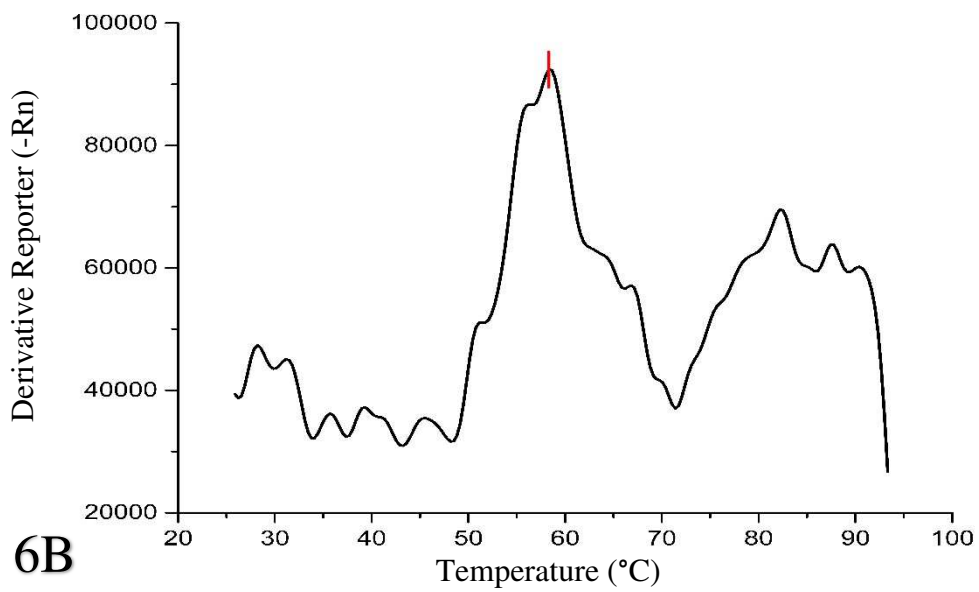
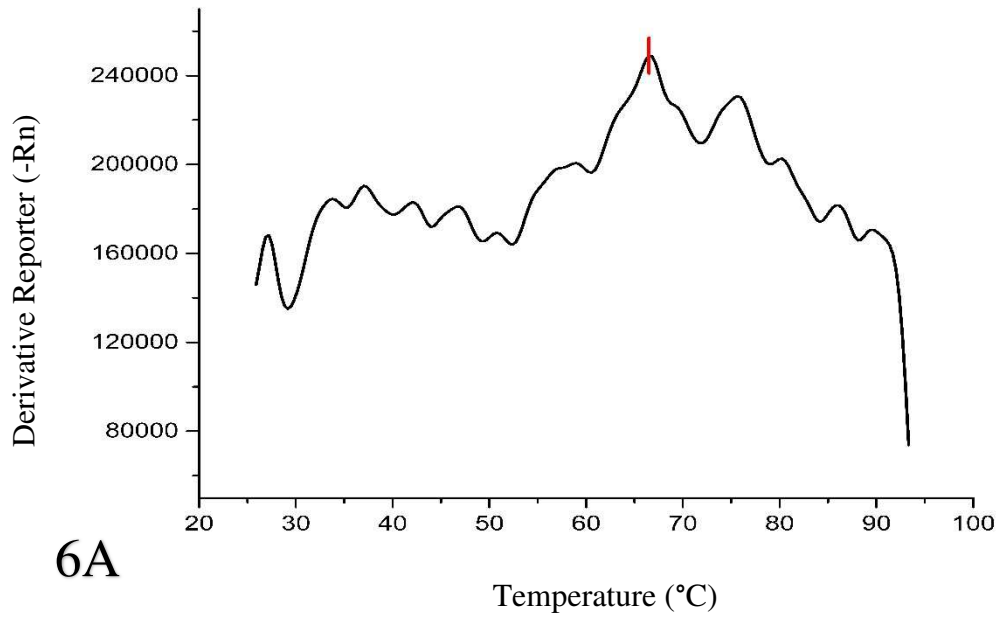


Figure 4-25 Example derivative curve from Experiment 6A and 6B with melt peak at 66°C (6A) and 58°C (6B). 10 μ M DNA in 7.8pH Tris-EDTA buffer, measured in ABI 7500

4.7.3.4. 9 Bases of Single-Stranded DNA, 3nm from Fluorophore

There are 9 bases (~3nm) of single-stranded DNA adjacent to the fluorophore. 9A is above the control melting temperature, with higher variation. The derivative curve of 9A has the 27°C false peak due to signal noise, and multiple additional peaks. In 9B, 9C and 9D the software called the false peak at the start. Further investigation would be required to determine if the signal derived from 9A can be used, it could be that the length of the double-stranded DNA is a factor in producing the background noise seen in 9B, 9C and 9D.

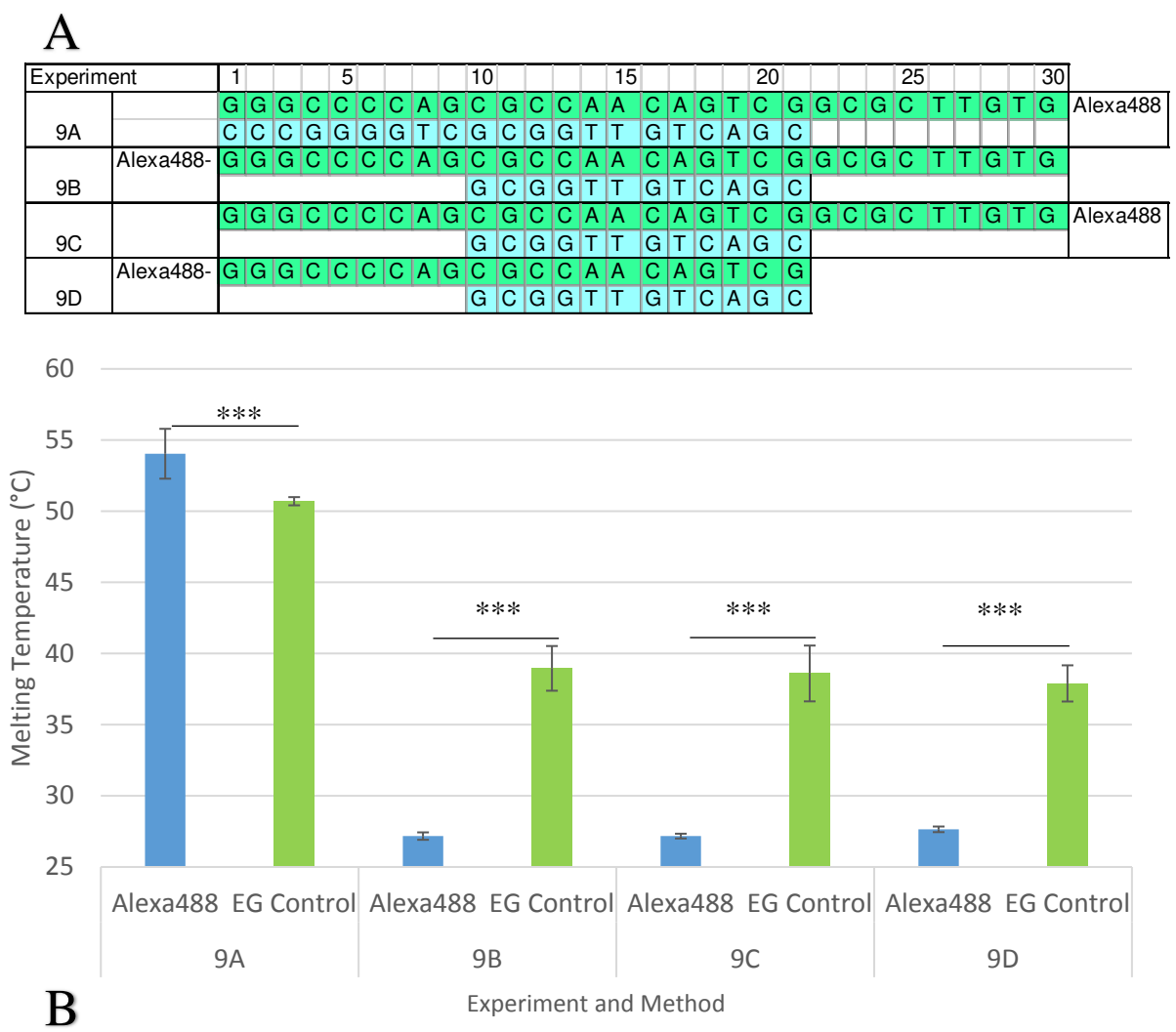
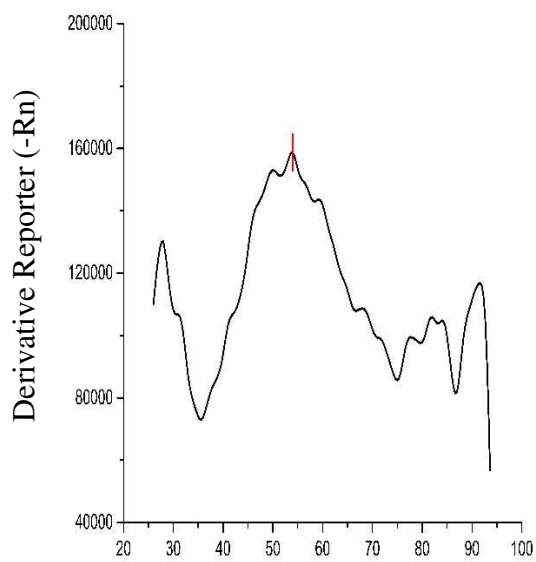
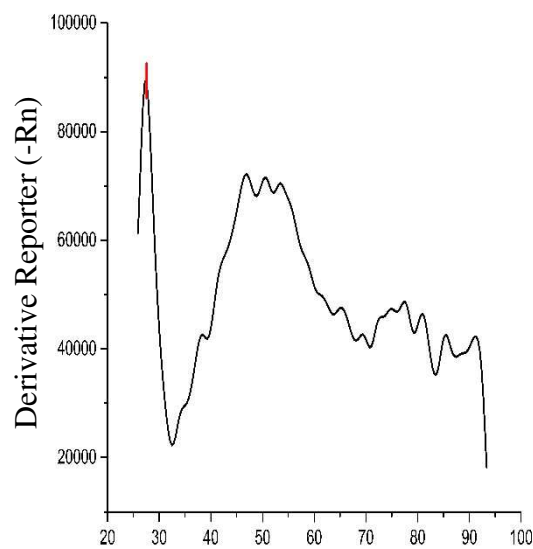


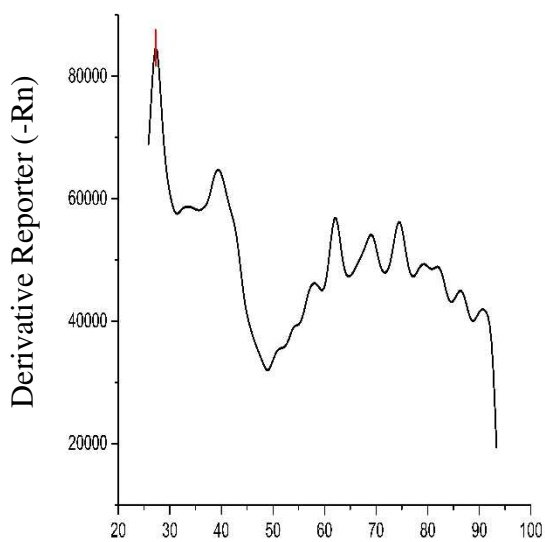
Figure 4-26 Sequence (A) and melting temperatures (B) of DNA that has 9 single-stranded bases adjacent to the fluorophore derived using EvaGreen (green) or Alexa488 (blue) as a reporter molecule. Averages of 10 replicates of 10µM DNA in 7.8pH Tris-EDTA buffer, measured in ABI 7500. EvaGreen experiments used 1µl of 20x EvaGreen and unlabelled oligonucleotides. T test P<0.001 shown by ***.



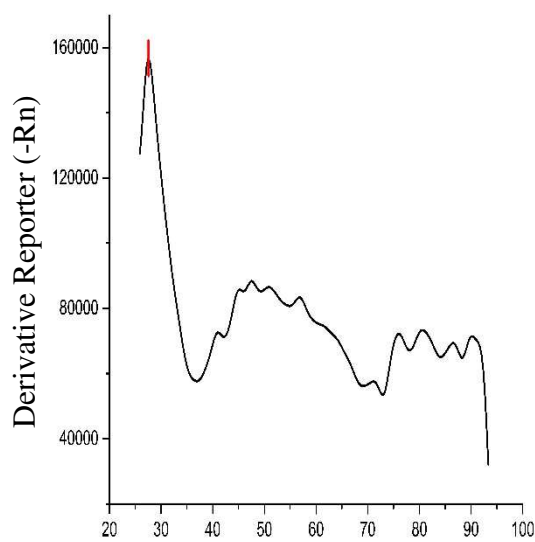
9A Temperature (°C)



9B Temperature (°C)



9C



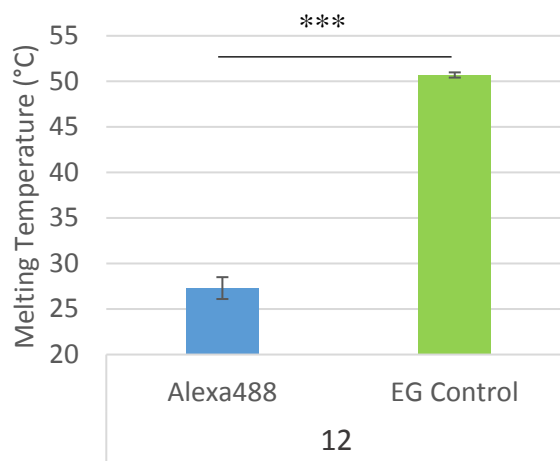
9D

Figure 4-27 Example derivative curves from Experiment 9A, 9B, 9C and 9D showing a melt peak at 54°C (9A) and false peaks due to signal noise around 27°C (9B/C/D). 10µM DNA in 7.8pH TE buffer, measured in ABI 7500

4.7.3.5. 12 Bases of Single-Stranded DNA, 4nm from Fluorophore

Experiment	1	5	10	15	20	25	30																							
Alexa488-	G	G	G	C	C	C	C	A	G	C	G	C	C	A	A	C	A	G	T	C	G	G	C	G	C	T	T	G	T	G
12												G	T	T	G	T	C	A	G	C	C	G	C	G	A	A	C	A	C	

A



B

Experiment and Method

Figure 4-28 Sequence (A) and melting temperatures (B) of DNA that has 12 single-stranded bases adjacent to the fluorophore derived using EvaGreen (green) or Alexa488 (blue) as a reporter molecule. Averages of 20 replicates of 10µM DNA in 7.8pH Tris-EDTA buffer, measured in ABI 7500. EvaGreen experiments used 1µl of 20x EvaGreen and unlabelled oligonucleotides. T test P<0.001 shown by ***.

This sequence, but with the fluorophore adjacent to the double-stranded portion at the 3' end was used above, as experiment 1 in 4.7.1, where it was found to function reliably and produce a quantifiable melt peak. Experiment 12 (Figure 4-28) was expected to fail to work, due to the 12 base / 4nm distance between the fluorophore and the secondary strand, although FRET is known to work over similar distances.

The 7500 FAST software reports the melting temperature of the false peak due to signal noise at the start of the heating run, suggesting that the data afterwards is background noise. In order to study this background noise in more depth, the melt curves were extracted using OriginPro and examined in more detail in Figure 4-29.

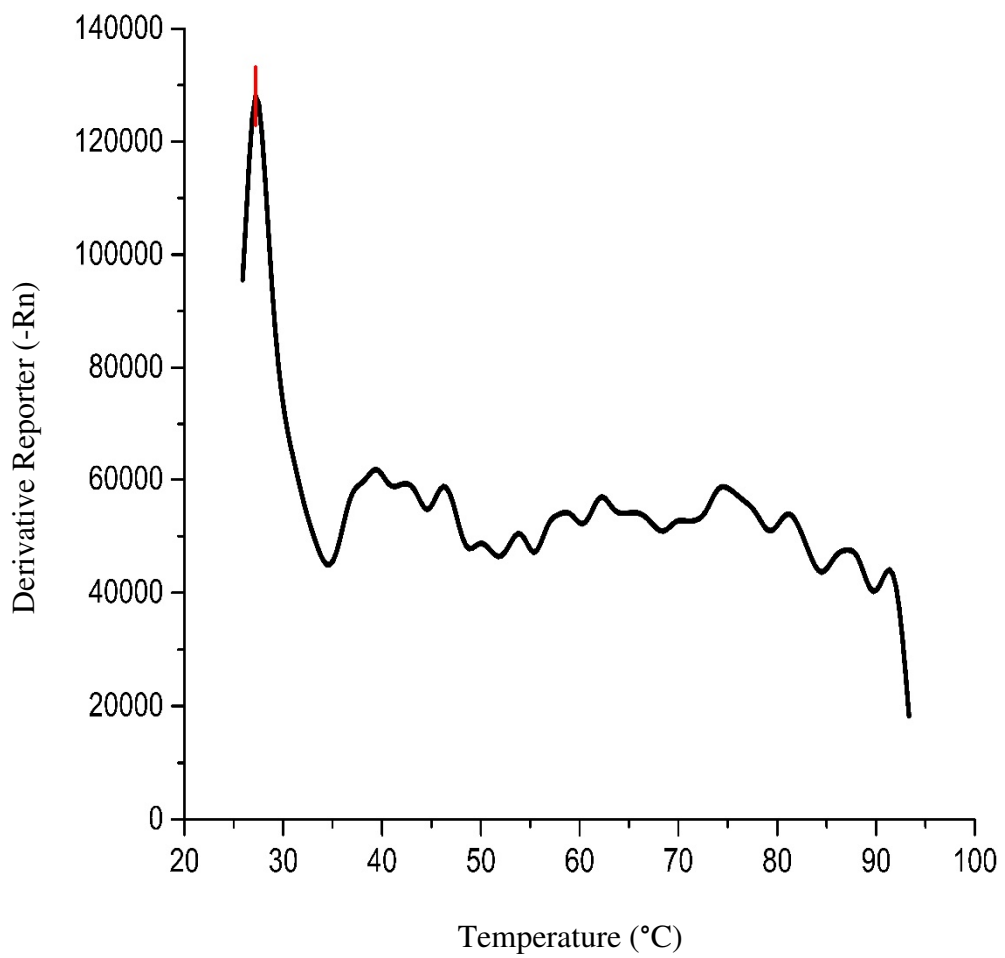


Figure 4-29 Derivative curve for 12 single-stranded base experiment showing a false peak due to signal noise around 27°C. 10 μ M DNA in 7.8pH TE buffer, measured in ABI 7500

4.7.3.6. Single-Stranded Adjacent to Fluorophore Summary

As other research has noted, addition of TTT bases adjacent to the fluorophore removes the observed fluorescent effect, whilst GTG does not. If, as predicted in the model, G or A bases are quenching the Alexa488 fluorophore, then T bases would alleviate that by distancing any quenching bases from the fluorophore. There was not a direct distance effect seen in the above experiments. If the effect were due to π -stacking between Alexa488 fluorophores, then the effect should have been lost immediately when the steric hindrance of a secondary strand was removed.

The distance between two DNA base pairs is 0.3nm, so the removal of 3 bases adjacent to the fluorophore would provide around the same space as an Alexa488 fluorophore [95,161]. In addition, GGG and GTG provide slightly different melt curves, with a different peak:false peak ratio, which suggests that the bases adjacent to the fluorophore are influencing the effect, rather than fluorophore-fluorophore interactions.

Further research will be required to discover if the fluorescence signal usually discarded as “background noise” could still yield valuable information as to the condition of the fluorophore, until then the rest of the work within this thesis will use the Alexa488 fluorescence effect only where the DNA is predicted to be completely double-stranded.

The peak height:median ratio was calculated for all of the above results, and summarised in . It is interesting to note that the results for the completely double-stranded DNA (0 bases of single stranded DNA) had ratios of 2.33 for Experiment 1 and 1.81 for Experiment 2. It could be that the difference seen is due to the difference in sequence – Experiment 1 is adjacent to GGG / opposite CCC, whilst Experiment 2 is adjacent to GTG / opposite CAC. As T base is known to insulate the quenching effect, this could explain the reduction in the strength of the melting temperature seen in the derivative curve. Further experiments examining this sequence effect should be studied, as this may lead to the use of this effect for sequencing in the future.

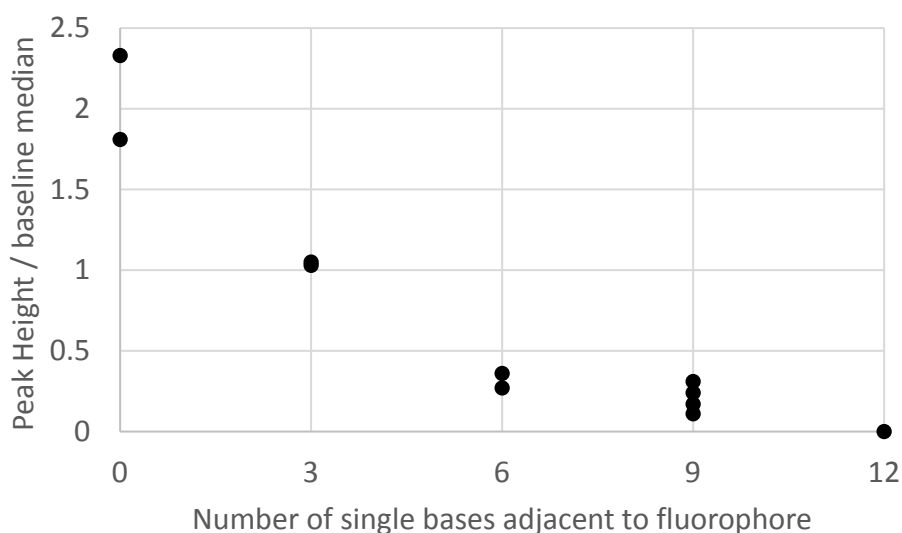


Figure 4-30 Peak height / baseline median for the melt curves for experiments detailed in 4.7.3 with partially single-stranded DNA adjacent with the Alexa488 fluorophore.

The model and literature predict that G base adjacent to the fluorophore will quench fluorescence, and the single-stranded experiments above show this is dependent on the bases adjacent to the G base, suggesting that electron transfer is involved rather than π -stacking between fluorophores.

4.8. Structural Similarities to Known Fluorophores

There are several structural similarities between Alexa488 and other known fluorophores. The results of the absorption experiments in 4.6 and the model proposed in 4.3 suggest that the fluorophore does not undergo a significant change in structure like EvaGreen. FITC and ATTO488 were chosen as they have similar chemical structures (Table 4.5) [66,72,165,166]. Due to similarities in structure, they both show similar absorption (Figure 4-31A) and emission spectra (Figure 4-31B) allowing melting curves comparison examined using an Applied Biosciences 7500 FAST PCR machine (triplicate of 10 μ l of 1M in TE pH 7.8 of DNA B modified with FITC and ATTO488). Note that these none of these fluorophores (Alexa488 included) were expected to produce DNA melt curves, it is not presumed that excitation/emission is directly responsible for this effect.

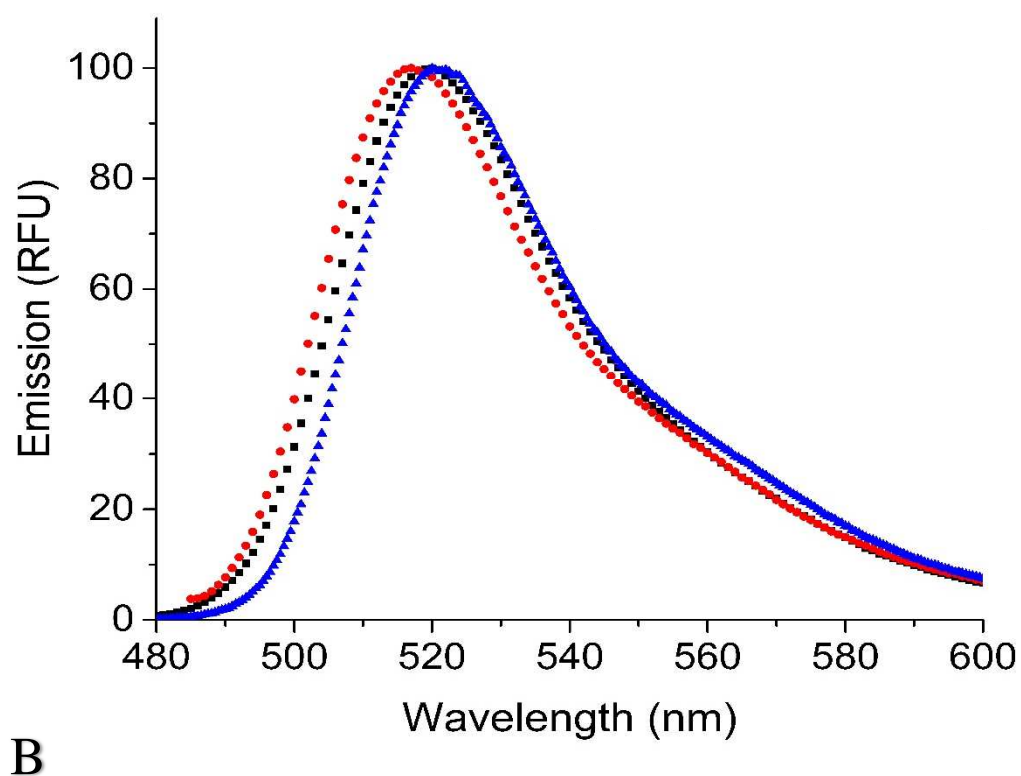
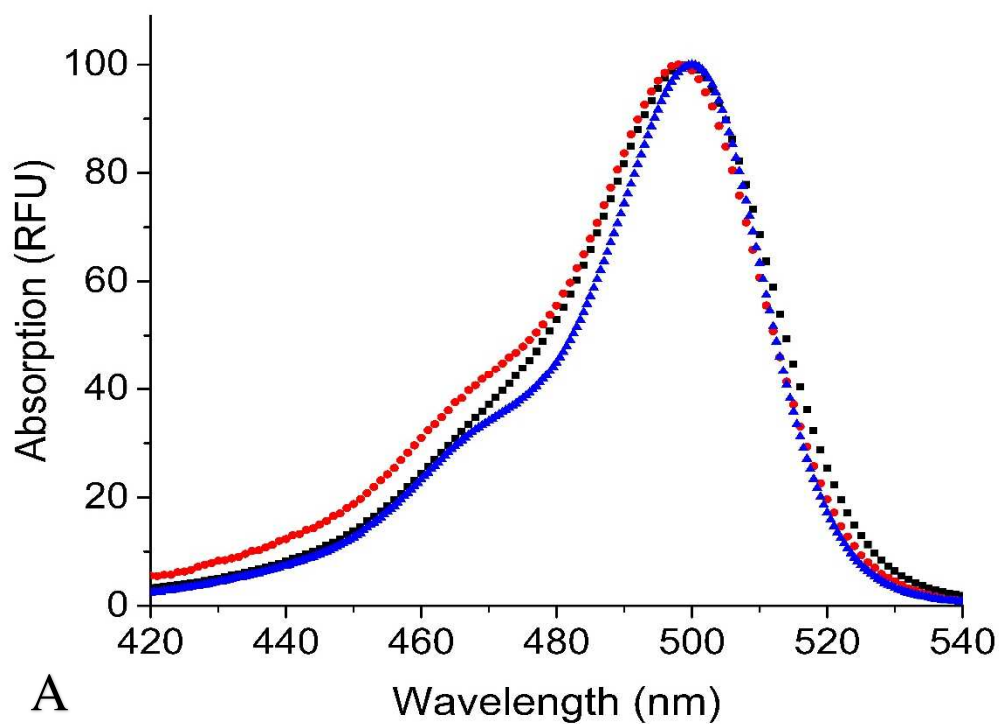


Figure 4-31 Absorption (A) and Emission (B) spectra of Alexa488 (black square), FITC (red circles) and Atto488 (blue triangles) fluorophores, drawn and analysed with OriginPro. The standard deviation between these fluorophores and an imaginary average was 3.22 for the absorption between 420-540nm and 3.46 for the emission between 480-600nm, showing the close alignment.

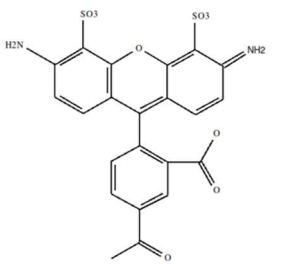
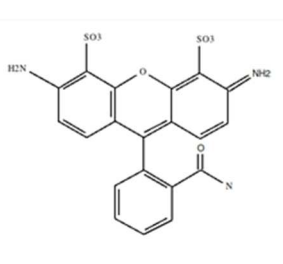
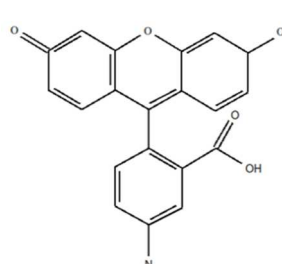
Fluorophore	Alexa488	ATTO488	FITC
Structure			
Melt curve	Yes	Yes	No

Table 4-5 Structures of Alexa488, ATTO488 and FITC fluorophores. Alexa488- and ATTO488-labelled DNA B exhibited the NB-S Quench effect, allowing the melting temperature to be derived, whilst FITC did not.

One theory was that π -stacking between fluorophores could explain the quenching of the fluorophores, this would suggest that FITC would show a similar pattern to ATTO488 and Alexa488 due to the similar chemical structures - π -stacking between the benzene rings would not depend on the side groups. FITC failed to produce a readable melt curve, instead exhibiting the expected temperature-dependent quenching, whilst ATTO488 produced a melt curve at the expected temperature (Table 4-5). Fluorophore-fluorophore interactions would not produce melt curves with negative peaks - these were accurately predicted based on the base nearest to the fluorophore, which is further evidence for nucleobase specific quenching, a very different mechanism from EvaGreen which cannot be predicted based on emission and excitation spectra alone.

The main structural differences between the fluorophores relate to the side groups of the benzene rings where light is absorbed and emitted [66]. The amine (NH₂) side group is also found in DNA bases and could act as a hydrogen bond donor between the fluorophores and DNA bases. The sulfonate (SO₃) group could act as a hydrogen bond acceptor, its presence itself is not known to significantly influence fluorescence alone. Electrochemically, Alexa488 and ATTO488 resemble Uracil, which may explain why the quenching effect is greater with Guanine and Adenine bases – both of these are found to pair with Uracil. Unbound SO₃ (electron-withdrawing group) and NH₂ (electron-donating group) allow photoinduced charge transfer across the molecule, which would be altered if one or both of these side groups were hydrogen-bonded to nearby molecules [66]. The position of the potential hydrogen acceptors and donors are mirrored, so potentially there could be

interactions at either side, with bases beside or across from the fluorophore. As expected, the emission and excitation spectra did not predict the NB-S quenching effect, although the SO_3 and NH_3 side groups may.

4.9. Conclusion

An early theory was that the EvaGreen-like melt curve could be due to FRET-like interactions between Alexa488 fluorophores although the experimental evidence does not suggest this. Negative melt curves were discovered - the Alexa488 fluorescence increases when the DNA strand melts - and this was found to be due to the base immediately adjacent to the fluorophore. Double-stranded DNA was analysed, which worked as expected although the melting temperature with Alexa488 was below that found with EvaGreen, sometimes by up to 9°C - as the Alexa488 melt curves are based on a different mechanism to a non-specific nucleic acid dye such as EvaGreen, more research will be needed to understand why these sequences produced different melting temperatures.

Single-stranded DNA experiments confirmed that the Alexa488 method should not be used to examine oligonucleotides with single-stranded DNA adjacent to the fluorophore without more research. The single-stranded DNA experiments suggested, as per the literature, photoinduced electron transfer between the adjacent nucleotides as this could explain that some effect was seen over longer distances, and this effect was different depending on how much of the oligo was double-stranded.

A model based on the literature and experimental results was produced, allowing predictions of the direction of the melt curve and additional melt-curve analysis based on the height and area of the peaks seen compared to a false peak due to signal noise seen when the melt curve is initiated.

Lastly, fluorophores with similar chemical structures (therefore producing similar emission and excitation spectra) were investigated to discover if this novel fluorescence effect could be explained based on chemical structure. Alexa488 and Atto488 both produce melt curves and contain NH_2 and SO_3 side groups, whilst FITC does not produce melt curves nor contain NH_2 and SO_3 side groups. Excitation and emission spectra alone cannot predict the nucleobase-specific quenching effect, further investigation is needed to ascertain how important the SO_3 and NH_2 side groups are for this mechanism.

Summary of Melt Curve Analysis for NB-S Quench Fluorescence

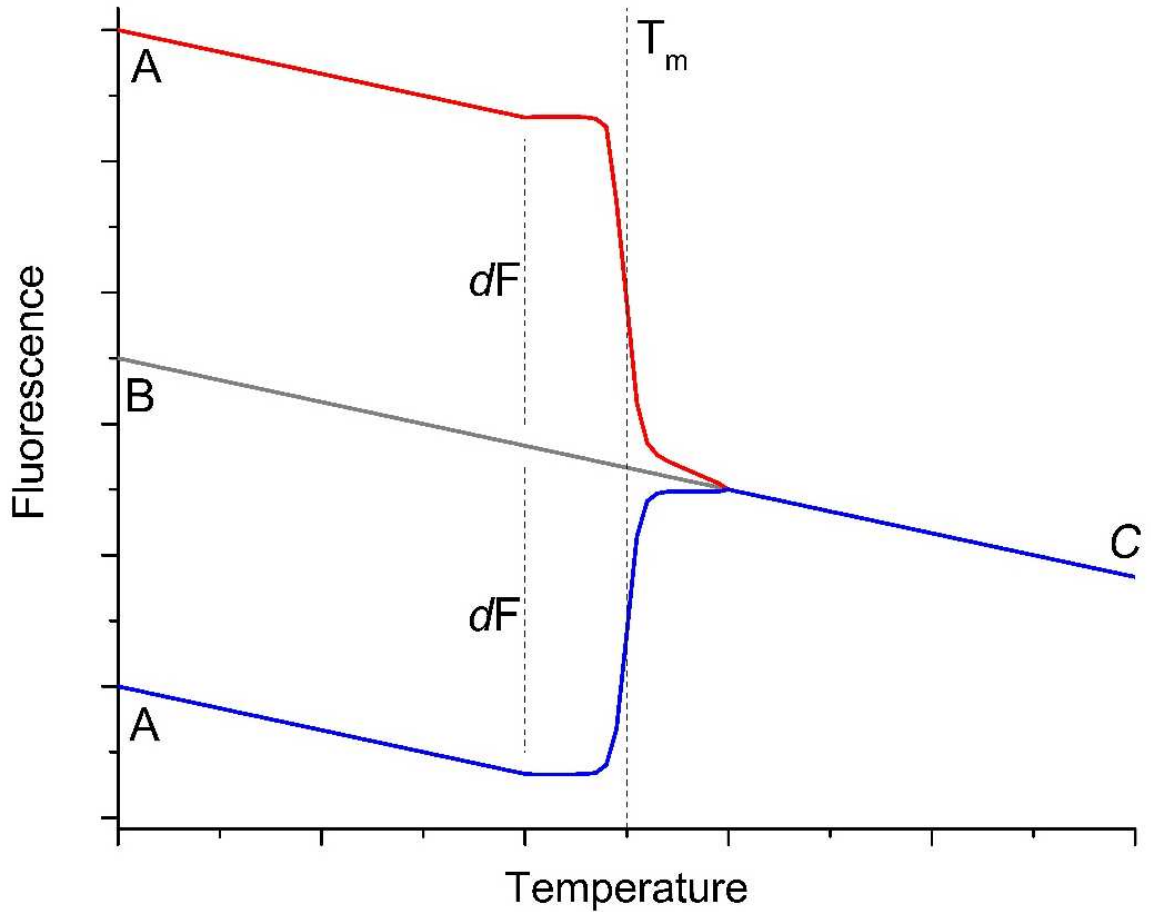


Figure 4-32 Model showing melt curves seen using the photo-induced fluorescence quenching effect. Red lines show the fluorescence signal seen when the fluorophore attached to double-stranded DNA is adjacent to a G or A base, blue line shows the fluorescence signal seen when the fluorophore attached to double-stranded DNA is opposite to a G or A base, grey shows the fluorophore attached to single-stranded DNA. dF shows the change in fluorescence between the double-stranded and single-stranded state. Points A show the absolute fluorescence when the DNA is double-stranded, B and C will be single-stranded. The melting temperature is shown by the dotted line, marked T_m

Various aspects of the DNA can be ascertained from the EvaGreen DNA melt curves, but in order to fully understand this with NB-S Quench additional experiments are needed to fully characterise the system. In order to discuss this, it is necessary to assume that the fluorophore has a completely unquenched state, experimentally it has been shown that $G > A > C > T$, so the quenching when DNA is single stranded adjacent to a T base would be the least quenching experimentally possible..

In the single-stranded state, the absolute fluorescence can be used to calculate the concentration of the single-stranded DNA. This depends on the nucleotide that is adjacent to the DNA, as experiments showed that the adjacent base quenched. If the quenching can be quantified for each of the nucleotides for a specific fluorophore, then this could allow accurate quantification, but would allow calculation of an idealised non-quenched state. Figure 4-32, shows a red model which is based on the higher quenching base (G or A) on the same strand, and a blue model with the higher quenching base (G or A) on the complementary strand. This idealised unquenched state would be at point A for the red model, and point B for the blue model.

The direction of the change in fluorescence from double-stranded to single stranded (shown by the dotted line and labelled dF) is dependent on the base directly adjacent to the fluorophore, G or A base result in a reduction in fluorescence as seen in the red model, whilst C or T base result in an increase in fluorescence as shown by the blue model. If the DNA is known to be complementary and double-stranded, then the change in fluorescence between A and C will be proportional to the concentration of the secondary strand of DNA.

The melting point T_m is dependent on both the sequence of the DNA (as discussed in Chapter 1.3), but also the environment that the DNA is found in. If the DNA is complementary and double-stranded, then a change in the melting point can be due to buffer pH, and salt concentration.

It was thought that the quenching effect could be constant across the DNA, proportional to the charge carried by each base. In this way, partial binding of the secondary strand could be monitored through a change in dF and a corresponding shift in the melting temperature. As there are 4 different bases, each with different quenching coefficients, this would require further experimentation. It is suggested that instead of a 3 base gap, which seemed to eliminate the charge effect seen with 3 T bases, this should be examined per base gap, with experiments examining the same single base gap with each of the 4 bases adjacent to the fluorophore.

5. Techniques Utilising the Nucleobase-Specific (NB-S) Quenching Effect

Chapter 4 investigated and characterised the Alexa488 fluorescence effect, this chapter examined novel potential applications. Non-specific intercalating nucleic acid dyes such as EvaGreen are used extensively in both medicine and science [14], NB-S Quench relies on a different mechanism and so could be a direct-label alternative – removing the possibility of contamination affecting results.

This chapter showed that the Alexa488 NB-S Quench effect could be used to quantify the total DNA product concentration and target/complement strand concentration. Techniques to amplify DNA such as Polymerase Chain Reaction (PCR) and Loop-Mediated Isothermal Amplification (LAMP) are mainstays of genetic and infectious diagnostics, this chapter showed that NB-S Quench could be applied to these methods without inhibiting PCR or LAMP reactions. After DNA amplification, melt curve analysis was used to differentiate products by sequence, information that is unavailable with FRET or EvaGreen.

In situations where intercalating dyes cannot be used, Fluorescence Resonance Energy Transfer (FRET) is commonplace utilising the transfer of fluorescence from the donor to the acceptor fluorophore specifically when they are in close proximity [35,43,67]. For DNA work, some FRET experiments could instead be performed with a single fluorophore, resulting in a faster, cheaper experiment. In order to work towards a LOC device, NB-S Quench was successfully incorporated into microfluidic devices [35].

Using the NB-S Quenching technique in laboratory applications is completely novel to this thesis.

5.1. Using the NB-S Quench Technique to Quantify DNA Concentration

Commonly used nucleic acid dyes such as EvaGreen are used not only to observe the melting point of a sample but also to quantify the concentration of genomic material in the sample.

5.1.1. Quantifying Concentration of Labelled DNA using Alexa488 Fluorescence

EvaGreen is useful for PCR and qPCR because it can be used to quantify the DNA present in the sample as it binds non-specifically to any DNA [14]. A drawback of this is that in addition to the amplified product, the template or genomic DNA in the sample will also cause fluorescence of EvaGreen, hence the requirement for amplification. The total fluorescent signal from Alexa488 labelled DNA is directly proportional to the concentration of the fluorophore. For these experiments, the dsDNA was labelled on one strand with Alexa488, and the fluorescence read using the ABI 7500. These experiments did not involve amplification of the DNA, and will investigate if this technique might be able to ascertain concentrations of the target DNA without qPCR. A potential use for this could be to determine the presence and concentration of plasmid DNA.

5.1.1.1. Results

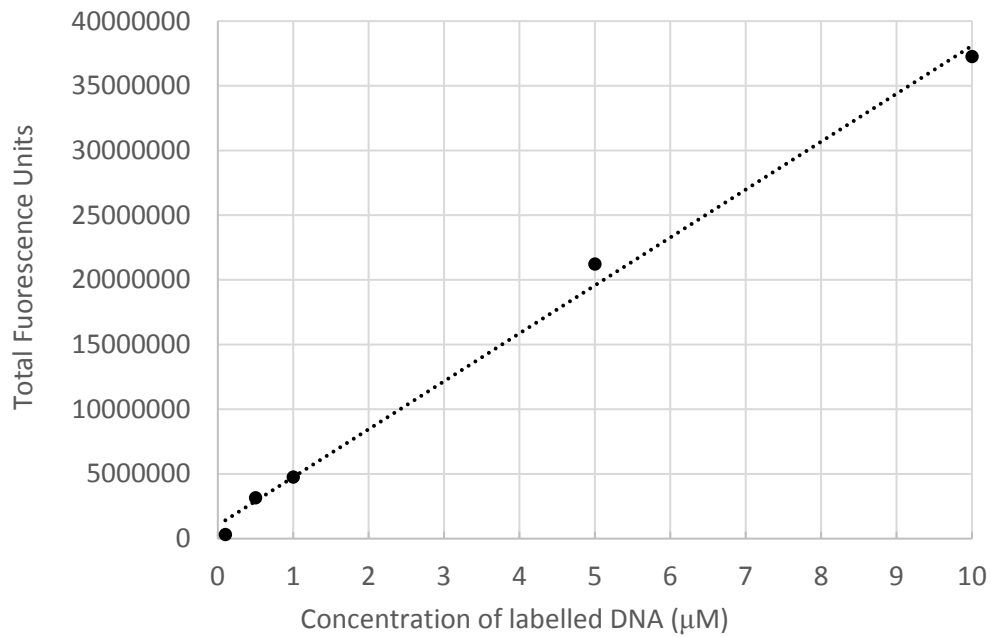


Figure 5-1 – Variations in concentrations (10 μM , 5 μM , 1 μM , 500 nM and 100 nM) of Alexa488-labelled DNA C in 7.8pH Tris-EDTA buffer. The concentration of the unlabelled complementary strand was the same as the DNA. Total fluorescence was measured using the Applied Biosciences 7500 Fast Real-Time PCR machine at 25°C. Each point shown is the average of 4 replicates, with the fluorescence for each read 10 times. Dotted line shows linear best fit, error bars show standard deviation.

5.1.1.2. Discussion

As can be seen in Figure 5-1 there is a linear correlation between the total fluorescence of Alexa488, with an R^2 of 0.995. The standard deviation for each point ranged from 0.24% to 0.54%. As discussed in Chapter 4, if the fluorescence effect was due to Alexa488 fluorophores interacting with each other, a non-linear relationship would be expected with higher concentrations resulting in additional quenching, but this was not seen. This linear relationship follows that of other fluorophores such as Cy5, as well as EvaGreen. One advantage of this technique over EvaGreen is that that the fluorescence seen is only the labelled DNA strand (and changes due to binding of its complement sequence), whereas EvaGreen fluoresces in the presence of contaminating and genomic DNA. Section 5.3 includes experiments with Alexa488 labelled BRAC primers, showing that there is no change in fluorescence with non-complementary DNA.

5.1.3. Quantifying Concentration of Complementary Strand using Alexa488 Fluorescence and Melt Curve Analysis

In addition to quantifying the concentration of the labelled strand, it would be useful to quantify the concentration of the complementary strand in experiments. As the fluorescent signal changes by up to 20% when the complementary strand binds, the small changes in the total fluorescence could be used to ascertain the concentration of the unlabelled complementary strand. Using the concentrations above however, the smallest change in fluorescence (100nM complementary with 10 μ M primary, 20°C) would likely be in the region of 0.1% - unlikely to be reliably measured with the Applied Biosciences 7500 PCR machine when the standard deviation of fluorescence readings is 0.24-0.54%.

In addition to measuring total fluorescence, or the change of fluorescence when the unlabelled complementary DNA is added, it could be possible to use the melting curves to measure the concentration of the complementary strand. The melt curve is due to double-stranded DNA melting to become single-stranded, lower concentrations of complementary strand results in a high proportion of the labelled DNA remaining single stranded, contributing a static background signal. Once there are sufficient complementary strands, at full binding saturation it would be possible for every single labelled strand to meet its complement and so the fluorescence of every fluorophore will change by the maximum possible. As the DNA strands are free in solution, the saturation point where every labelled strand binds to a complementary strand will require an excess concentration of the complementary strand, so this method has the potential to be calibrated so that concentrations above that of the primary strand could be measured – although the reliability will decrease above this saturation threshold.

5.1.2.1. Results

Figure 5-2 below shows the results of the fluorescence experiments to quantify the concentration of the complementary strand of DNA. The change in total fluorescence was not a reliable method of measuring the concentration of complementary DNA.

Figure 5-3 shows the derivative curves from the Applied Biosciences 7500 software. The measurements were extracted and analysed using Origin 2016 and the peak of the derived melt curve was compared to the background (at 60°C) to produce Figure 5-4. 60°C was chosen as any change in fluorescence at that temperature is not related to the DNA melting point. Logarithmic trend lines of 1µM and 500nM Alexa488-labelled DNA had the highest R² values at 0.99 and 0.98 respectively. Higher concentrations of Alexa488-labelled DNA showed lower R² values, 0.89 for 5µM and 0.81 for 10µM.

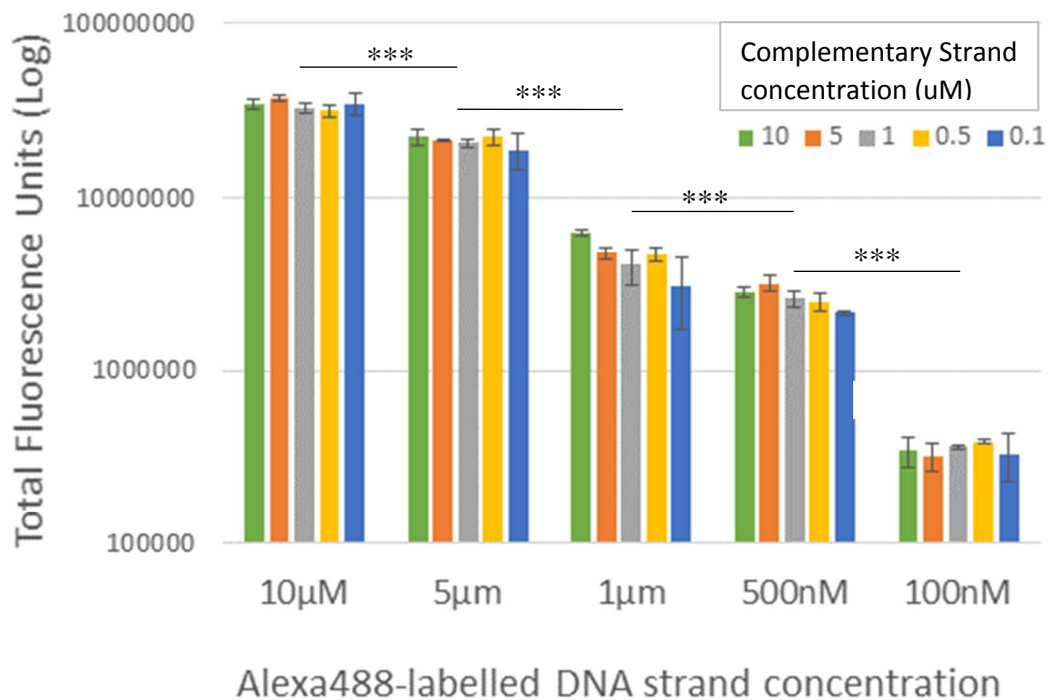


Figure 5-2 Varied concentrations of Alexa488-labelled DNA C with varied concentrations of unlabelled complementary DNA - 10µM (green), 5µM (orange), 1µM grey), 500nm (yellow) and 100nm (blue) - in pH 7.8 Tris-EDTA buffer. Total fluorescence was measured using the Applied Biosciences 7500 Fast Real-Time PCR machine at 25°C. 4 replicates, fluorescence for each read 10 times. Tukey ANOVA analysis for each group showed $P > 0.001$ showed by ***

10 μ M Primary (488-Labelled) DNA C

500nM Primary (488-Labelled) DNA C

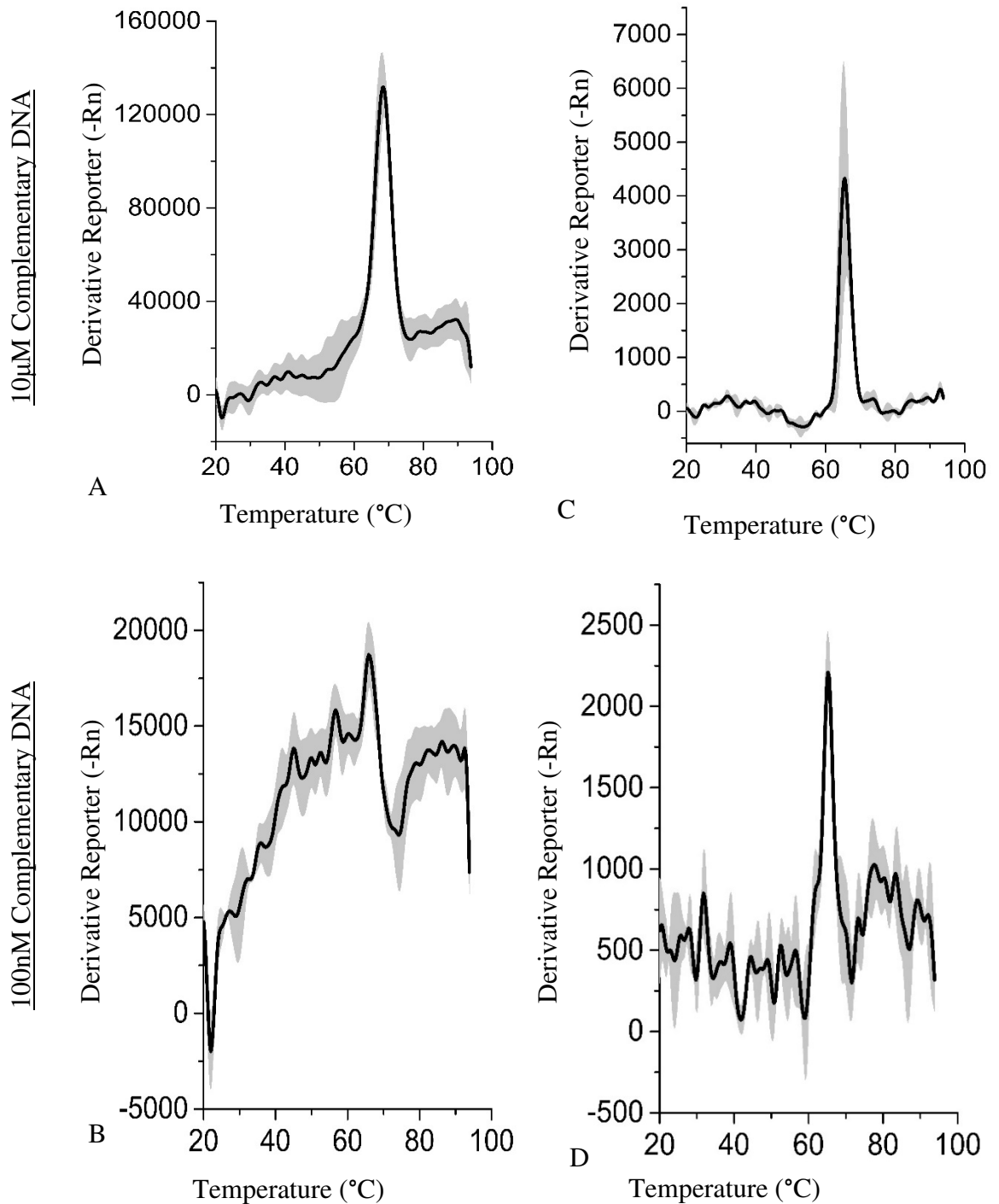


Figure 5-3 (A) and (C) are the derivative curves with high concentrations of complementary DNA (10 μ M) with 10 μ M (A) and 500nM (C) of Alexa488-labelled DNA C. (B) and (D) are the derivative melt curves with lower concentrations of complementary DNA (100nM) with 10 μ M (B) and 500nm (D) of Alexa488-labelled DNA C. Grey shaded area shows standard deviation between derived melt curves. All experiments were performed in quadruplicate with an Applied Biosciences 7500 Fast PCR machine at the 480nm excitation/530nm emission, measurements taken from 20-95°C.

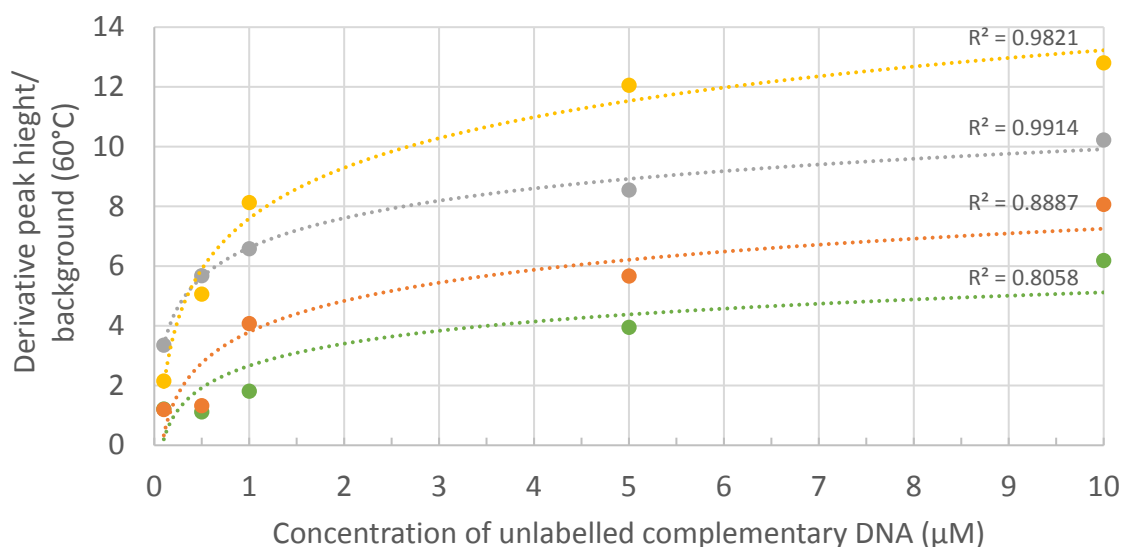


Figure 5-4 Derivative of the melt curve at the melting peak and 60°C. 10μM (green), 5μM (orange), 1μM (grey), 500nM (yellow).

Replicates of 5 in pH 7.8 TE buffer were performed in Applied Biosciences 7500 Fast PCR and analysed in Origin 2016. Experiments with 100nM of labelled DNA showed melting curves that were indistinguishable from background noise.

5.1.2.2. Discussion

The melt curve peak analysis results showed that lower concentrations of labelled DNA could accurately estimate concentration of the complementary strand. It suggested that the method would work with higher concentrations of the complementary strand than labelled strand, 500nM and 1μM Alexa488-labelled DNA C worked best (R^2 of 0.98 and 0.99 respectively) from 500nm-1μM but still within 10% at 5μM and 10μM. As previous experiments have shown that the concentration of the labelled strand can be obtained by the total fluorescence (if not known), and the melt peak analysis could then be used to estimate concentration of the complementary strand. 60°C was chosen to represent the background of the melt curve, it may be that another measure such as an average of the derivative could be more accurate –high temperature, low temperature, or a whole average excluding the expected melt peak. These weren't explored in this thesis but could be explored to improve this as a tool.

Further experiments with PCR in the following section examined this further to determine if the product concentration can be accurately measured.

5.1.3. Quantitative Polymerase Chain Reaction using Alexa488 fluorescence (qPCR)

Quantitative PCR (qPCR) is an amplification technique that allows quantification of the original concentration of template DNA in the sample. This is useful for determining gene expression, or quantifying severity of infection or bacterial contamination. qPCR can be performed using a reporter dye such as EvaGreen, or fluorescent probes utilising FRET (see sections 1.2 and 1.4). For this experiment, the amount of template DNA was varied, and qPCR performed in an ABI 7500 to amplify a modified BRCA1 (further experiments are discussed in 5.4) using unlabelled primers and EvaGreen as a control, or with B3 primer modified with Alexa488 (Figure 5-5). The last base of the template DNA and B3 primer was changed so that the higher quenching G base would be adjacent to the Alexa488, resulting in an increase in fluorescence instead of a decrease (see the model discussed in section 4.3).

Primer sequences:

F3: TCC TTG AAC TTT GGT CTC C

Modified B3: Alexa488-G*AG TTC ATA AAG GAA TTG ATA GC

Modified BRCA1 sequence:

```
1 TCCTGAACT TTGGTCTCC C AAAATGCTGG GATTATAGAT GTGAGCCACC  
1 AGGAACTTGA AACCAAGAGGG TTTTACGACC CTAATATCTA CACTCGGTGG  
  
51 TCGCCTGGCC TCTGGTTCTG TTATTATCCC AATTTACACAG ACTGGGGATA  
51 AGCGGACCGG AGACCAAGAC AATAATAGGG TTAAAGTGTC TGACCCCTAT  
  
101 CTGAAACTGT GCAGCAGAAA GATTATTAAC TTGGGAGGCA GATAGGCTTA  
101 GACTTTGACA CGTCGTCTTT CTAATAATTG AACCTCCGT CTATCCGAAT  
  
151 GACTCAAACC CTAATCTTCC ATTTACTTAC CAACTGTGCT ATCAATTCCT  
151 CTGAGTTTGG GATTAGAAGG TAAATGAATG GTTGACA CGA TAGTTAAGGA  
  
201 TTATGAACTC*  
201 AATACTTGAC*
```

Figure 5-5 Primer (F3 in red, B3 in Green) and template sequence of modified BRCA1 used to perform qPCR. Modified base indicated by *. Polymerase direction indicated by arrow.

5.1.3.1. Results

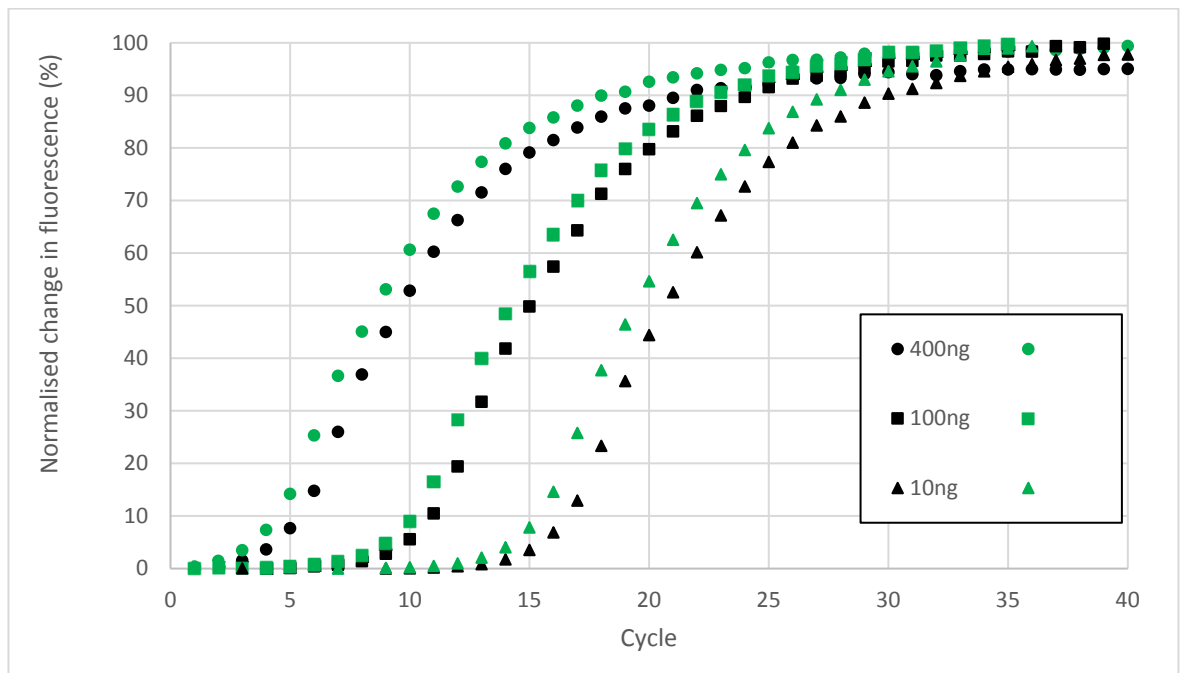


Figure 5-6 40 cycle qPCR performed in ABI 7500 using Alexa488-labelled primer (green) or unlabelled primers with EvaGreen (black) as a control. The amount of template DNA was varied, 400ng (circle), 100ng (square), 10ng (triangle). PCR was otherwise performed as described in 2.5.4.

5.1.3.2. Discussion

qPCR calibration curves are performed in order to quantify the concentration of DNA in an experimental sample. These were successfully performed as shown in Figure 5-6 using a commercial PCR machine (ABI 7500) using the fluorescence of Alexa488-labelled primers instead of the non-specific DNA dye EvaGreen. Early attempts using the ABI 7500 using Alexa488-labelled F3 and B3 failed as the higher quenching nucleotide (G, A) was on the complementary strand opposite the fluorophore, resulting in a decrease in fluorescence which the ABI 7500 software fails to recognise. It was decided that the template DNA and B3 primer would be changed to avoid this, although it would have also been possible to change the position of the primer so that the last nucleotide next to the fluorophore is a G or A base. An alternative solution could be to utilise the microscope setup used for other experiments or reprogram the ABI 7500 to recognise decreases in fluorescence during DNA amplification, these could form the basis of future work.

The Alexa488-derived amplification curves began sooner than the EvaGreen controls, this was noted too when LAMP is performed in section 2.4.1. As EvaGreen is a non-specific dye, it will fluoresce in the presence of the double-stranded template DNA and partially fluoresce due to unincorporated nucleotides, resulting in background fluorescence unrelated to the amplified product. Further experimentation will be needed to see if this finding is statistically relevant, measurements were taken every minute and so this may not always be true. The ABI 7500 software measures the change from this base background fluorescence, and so amplification of the target DNA is only seen once this has resulted in a relatively large change in fluorescence. In contrast, the fluorescence of Alexa488-labelled primers is not significantly affected by the free nucleotides in solution or the target DNA, as such there is lower background fluorescence to overcome.

5.2. Deriving Melting Temperatures of Partially Single-Stranded DNA

EvaGreen can bind to and fluoresce in the presence of single-stranded DNA. The results from Chapter 4.7 suggested that completely double-stranded DNA adjacent to the Alexa488 could accurately derive the melting temperature, but that this effect was reduced (but not removed entirely) by single-stranded DNA. 3 bases of single-stranded DNA produced an accurate melting temperature, but 6 bases of single-stranded DNA did not. It was decided for these experiments to take the sequences used in section 0 and increase the single-stranded DNA adjacent to the Alexa488 fluorophore by single bases to derive the melting temperature (Figure 5-7). These experiments are effectively investigating the effects of deletions on the complementary strand at the end near the Alexa488 fluorophore.

Experiment		1	2	3	4	5	6	7	8	9	10	11	12	13	14	15	16	17	18	19	20	21	22	23	24	25	26	27	28	29	30
		G	G	G	C	C	C	C	A	G	C	G	C	C	A	A	C	A	G	T	C	G	G	C	G	C	T	T	G	T	G
Double-Strand	Alexa488																														
Control																															
-1	Alexa488																														
-2	Alexa488																														
-3	Alexa488																														
-4	Alexa488																														
-5	Alexa488																														
-6	Alexa488																														

Figure 5-7 Figure showing the sequences of the DNA sequences used. The green strand is Alexa488 modified or unlabelled for the EvaGreen controls. The light blue represents the unlabelled complementary strand, which is the same for both the control and the Alexa488 experiments.

5.2.1. Results

Controls using the EvaGreen reporter molecule are shown in Figure 5-8. EvaGreen could not distinguish between double-stranded DNA, and -1, or -2. The -5 results do not fit with the overall trend. EvaGreen and Alexa488 differ in mechanism, EvaGreen can bind to single-stranded DNA and fluoresce, which will reduce the accuracy of melt curves.

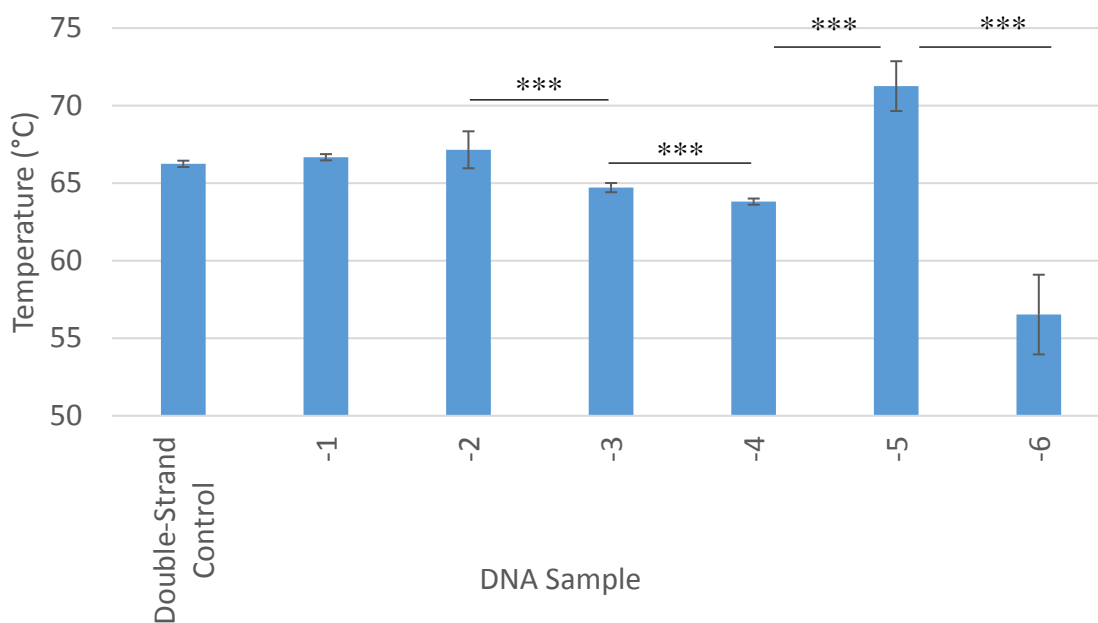


Figure 5-8 Melting temperatures of DNA with sequential deletions on the complementary strand derived using EvaGreen reporter molecule on the ABI 7500 PCR machine. * shows $P < 0.05$, ** $P < 0.01$, *** $P < 0.001$, the rest showed no significant difference.

Previous work in section 4.7.3 found increased variation in fluorescence readings as the proportion of single-stranded DNA increases, which fits with the literature. For simplicity, a linear relationship is assumed although $G \equiv C$ and $A = T$ will result in different binding and hence the difference in melting temperature is sequence dependant. The experiments here showed only a slight correlation, with an R^2 of 0.16, although the sequence in question (Figure 5-7) shows that the only bonds that are changed in -4, -5 and -6 are all $G \equiv C$. If -5 is removed the R^2 is substantially improved to 0.65, which is still below that obtained with Alexa488 NB-S Quenching.

Previous Alexa488 experiments in 4.7 showed that photoinduced electron transfer effect is most effective when the DNA is double-stranded adjacent to the fluorophore, less so at distances of 3 single bases / 1nm and ineffective at 6 single bases / 2nm, due to charge transfer across the DNA bases. The results of Figure 5-9 support this, the correlation seems to reduce from 5 to 6 single bases adjacent to the Alexa488 fluorophore and is shown in Table 5-1. A second order polynomial correlation was also modelled, with a stronger R^2 which also reduced from 5 to 6 single bases at which point the equation changed significantly (Table 5-2).

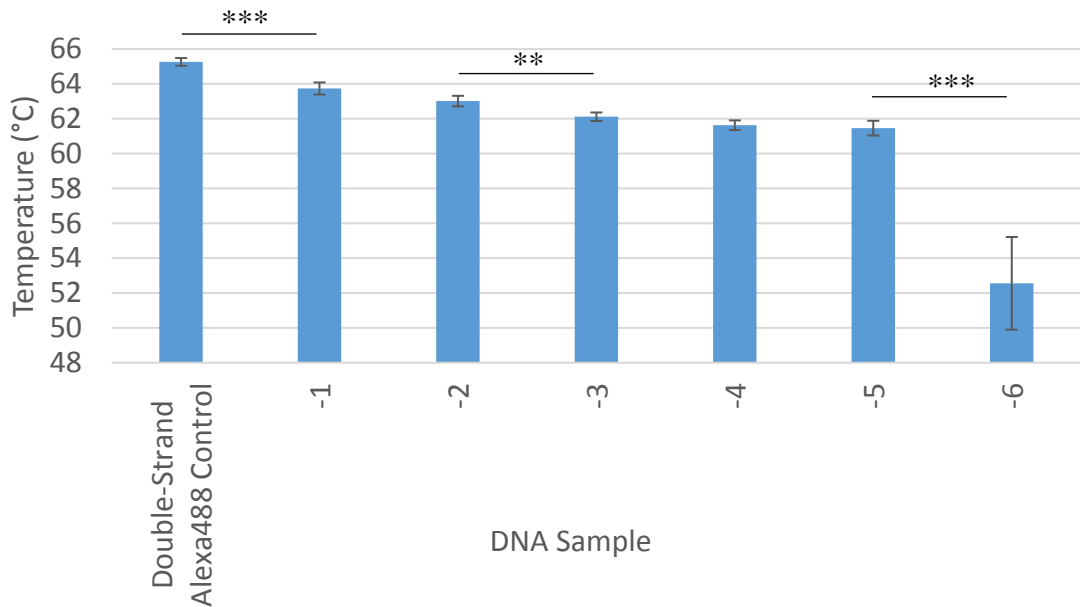


Figure 5-9 Melting temperatures of DNA with sequential deletions on the complementary strand derived using Alexa488 effect on the ABI 7500 PCR machine. -n indicates that a number of bases that have been removed from adjacent to the fluorophore on the complementary strand. * shows P<0.05, ** P<0.01, *** P<0.001, the rest showed no significant difference.

Points	DS to -2	DS to -3	DS to -4	DS to -5	DS to -6
R ²	0.96	0.97	0.96	0.93	0.68

Table 5-1 Linear correlation between the Alexa488 experiment (Figure 5-9), correlation reduces as the distance from the fluorophore increases.

Points	DS to -2	DS to -3	DS to -4	DS to -5	DS to -6
R ²	1	0.99	0.99	1	0.81

Table 5-2 Second order polynomial correlation between the Alexa488 experiments (Figure 5-9), correlation reduces as the distance from the fluorophore increases.

Points	DS to -1	-1 to -2	-2 to -3	-3 to -4
Melting Difference (°C)	1.5±0.3	0.7±0.3	0.9±0.3	0.2±0.3

Table 5-3 Difference in melting temperature with Alexa488 experiments with standard deviation between readings (averaged).

5.2.2. Discussion

When performing DNA amplification by PCR the primers are incorporated into the double-stranded DNA product, so ssDNA is not a common issue relevant to research or diagnostics. For multiplex PCR, the products are designed so that the melting temperatures are sufficiently different for them to be distinguished – usually a minimum difference of $\sim 5^{\circ}\text{C}$. As single base additions or deletions cannot be detected, reporter molecules such as EvaGreen cannot be used for DNA sequencing. Experiments to determine single point mutations are performed using specific primers which include the expected point mutation – if the sequence is as expected, the primers bind and PCR amplification is achieved, if there is a mutation then the primers do not bind and PCR amplification fails. If there is an unknown mutation, then sequencing is required as the alternative is to produce all possible primer sequences to see which results in DNA amplification.

The sequence for this experiment was chosen as the only bonds that are changed are $\text{G}\equiv\text{C}$, although it should be noted that DNA binding is additive (discussed in 1.1.1), and that the GC rich regions may form secondary structures within the same DNA strand or between DNA strands (see section 1.1.4). For the EvaGreen controls, it was expected that there would be a linear reduction in melting temperature and that single-stranded DNA would have a relatively small effect – increased variability in readings as the proportion of single-stranded DNA increased. This confirms current practice of ensuring that PCR products have a sufficient difference in melting temperature, or of designing primers over the expected single point mutation.

The Alexa488 experiments (Figure 5-9) do show significant difference to distinguish between single bases (Table 5-3). Both a linear, and a second order polynomial correlation were modelled (Table 5-1 and Table 5-2), with the second order polynomial correlation showing a higher R^2 value, although T-test analysis could not distinguish between many samples. The reduction in accuracy with distance isn't dissimilar to the reduction in fluorescence with distance with TIRF (see section 1.4.2 and Figure 1-12). As per the sequence (Figure 5-7), it is only $\text{G}\equiv\text{C}$ bonds that are removed, so the correlation should be linear. As the NB-S quenching effect is due to charge, the charge effect on the fluorophore will rely on distance and the charge of bases between the fluorophore and the double-

stranded DNA, which could explain the polynomial correlation and the fact that variation increases in a similar manner.

These results suggested that the Alexa488 effect could be used for sequencing of up to 4 bases near the fluorophore, addition or removal of a single base would change the fluorescence sufficiently for this to be differentiated, this is not possible with reporter molecules such as EvaGreen. With EvaGreen, the 5°C rule for designing PCR products means that the PCR products require a difference of ~6 bases depending on sequence, whereas Alexa488 derived melting temperatures could be more specific, potentially allowing differentiation of single base differences in products. An area of research where this could be used is restriction enzymes, some of which cut DNA resulting in short single-stranded “sticky ends”.

DNA amplification by PCR does not usually result in partially single-stranded products, a potential application for this is to differentiate products after PCR amplification. This is discussed in the following section.

5.3. Multiplex Target Sequence Identification

EvaGreen is used extensively to identify PCR products in solution, these experiments were based on previous work investigating differentiating single nucleotide variations with G-specific quenching in this thesis and in the literature [74]. These controls are also relevant for the DNA amplification experiments in section 5.4 and are discussed in the proceeding section, with the full sequences in Figure 5-15. Figure 5-10 shows the melt curves produced with the ABI 7500 when the primers are unlabelled – there is no distinguishable melt peak, the melting temperature of the primers cannot be observed.

Based on the BRCA1 LAMP primers (see section 4.5, Table 4-1, Figure 4-10, Figure 4-11 and Figure 5-15) controls were performed to measure the melt curves of Alexa488 labelled LPR5F and LPF5B. Melt curves of the unlabelled (or FITC-labelled) DNA produced no discernible melt curves with (Figure 5-10 A) or without (Figure 5-10 B) the complementary strand. OriginPro calculated 12-20 peaks, the most significant had a peak

area of 7-8%. Three sets of experiments were performed, the first used Alexa488-labelled LPRF5 and LPF5B, with one or both unlabelled complement strands added. Additional controls were performed individually for F3, B3, FIP and BIP, along with EvaGreen melt curves of the unlabelled variants of all 6 primers.

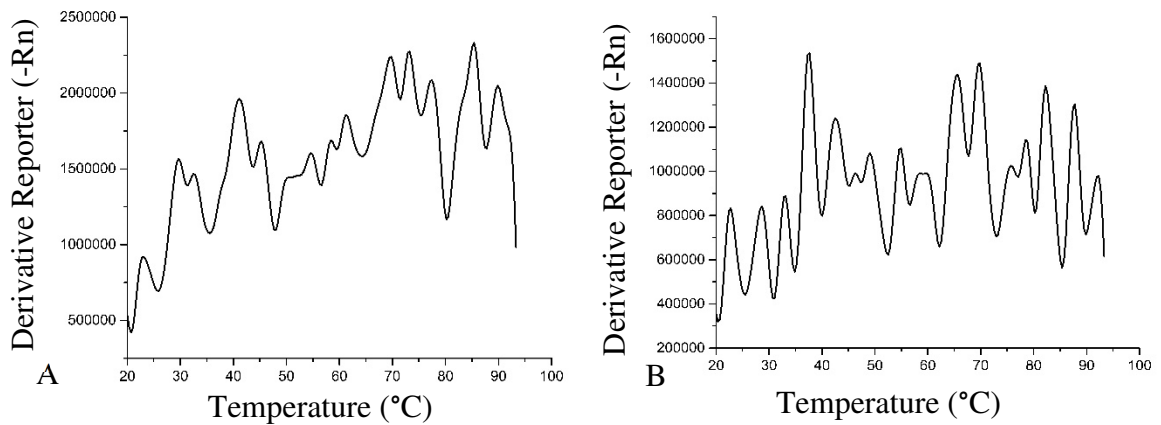


Figure 5-10 Derivative curves of standard unlabelled BRCA1 LAMP primers without (A) and with (B) LPR5F and LPF5B complement strands (see 0. for full sequences). No significant peak is observed.

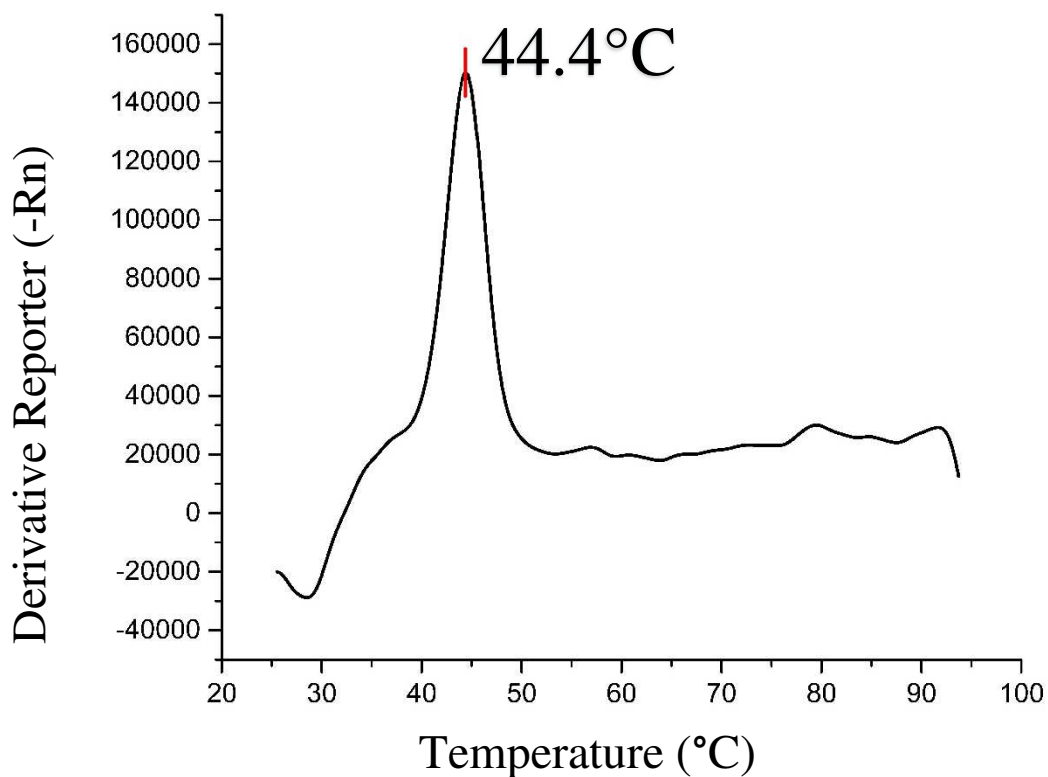


Figure 5-11 Averaged derivative curve of BRCA1 LAMP primers Alexa488-LPRF5 and Alexa488-LPF5B with the unlabelled LPR5F complement strand showing a distinct melt peak at 44.4°C. 10 μ M dsDNA in pH7.8 TE buffer

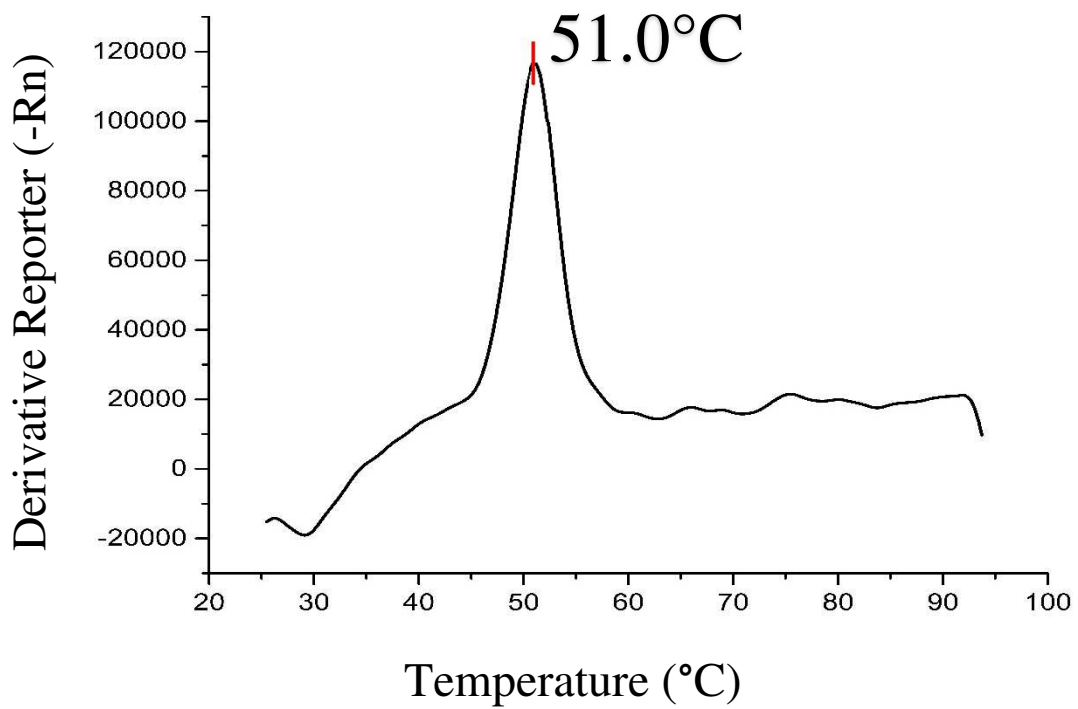


Figure 5-13 Averaged derivative curve of BRCA1 LAMP primers Alexa488-LPRF5 and Alexa488-LPF5B with the unlabelled LPF5B complement strand showing a distinct melt peak at 51.0°C. 10µM dsDNA in pH7.8 TE buffer

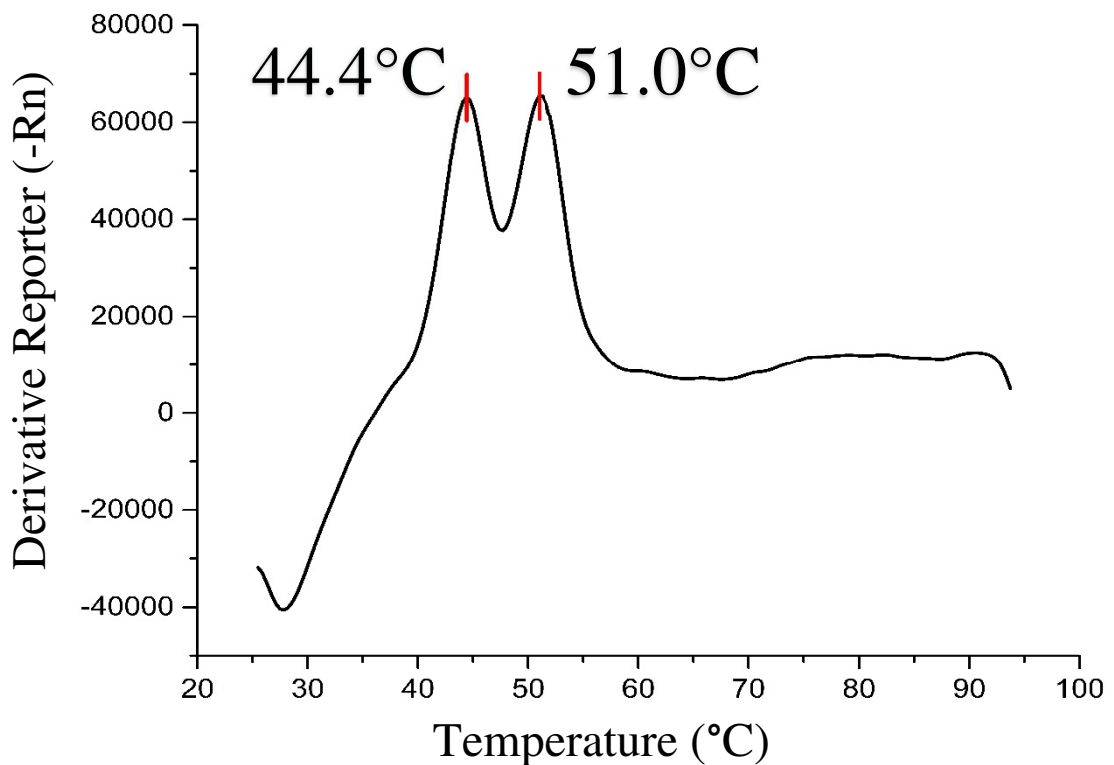


Figure 5-12 Average derivative curve of BRCA1 LAMP primers Alexa488-LPRF5 and Alexa488-LPF5B with their unlabelled complement strands showing two distinct melt peak at 44.4 °C and 51.0°C. 10µM dsDNA in pH7.8 TE buffer

Addition of the unlabelled LPF5B complement resulted in a melt curve with a peak at $44.4 \pm 0.19^\circ\text{C}$ (Figure 5-11), addition of the unlabelled complement LPF5B resulted in a melt curve with a peak at $51.0 \pm 0.16^\circ\text{C}$ (Figure 5-13), whilst addition of both resulted in a two-peak melt curve that allowed accurate identification of both complements (Figure 5-12). These experiments were repeated to mimic a LAMP reaction with the addition of the other unlabelled LAMP primers, Optigene ISO-004nd LAMP Mastermix and $5\mu\text{l}$ pH7.8 TE buffer instead of template DNA, which did not alter the melting curves. The peaks were analysed and integrated with OriginPro (an example of the separation of the dual peak is shown in Figure 5-14) so that the peak height, area, and area (%) could be calculated Table 5-4.

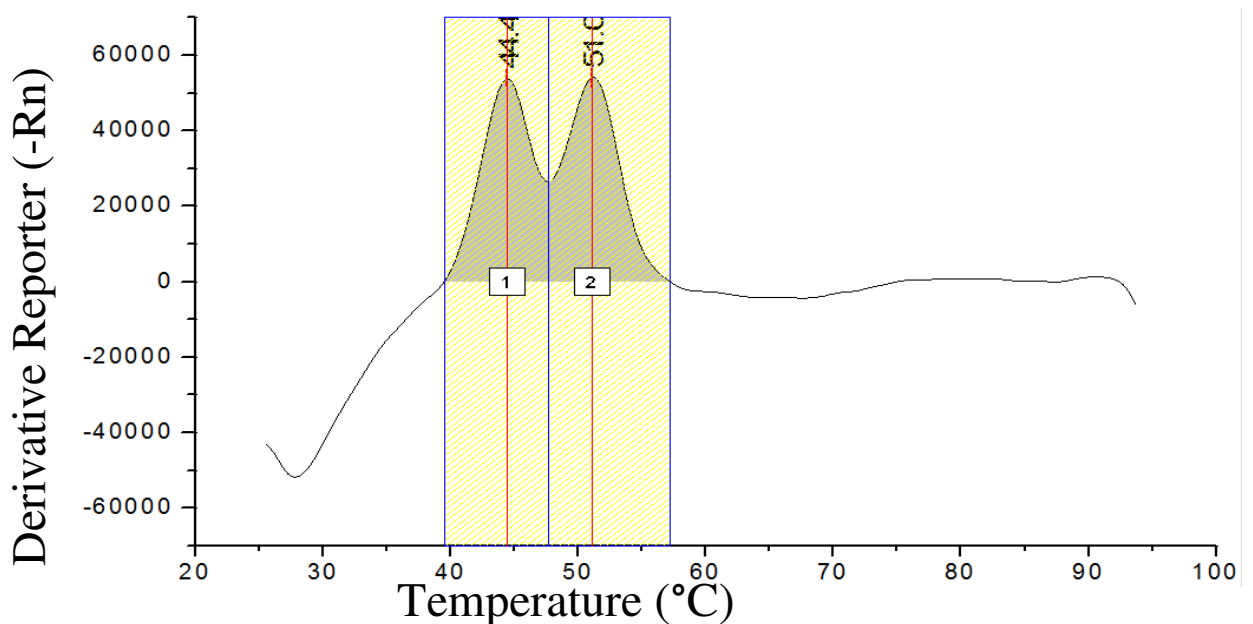


Figure 5-14 Example of analysis in OriginPro of the averaged melt curve of BRCA1 LAMP primers Alexa488-LPRF5 and Alexa488-LPF5B with their unlabelled complement strands. The centre points of the two peaks are shown by red lines and numbered, the separation line is in blue, and the areas are shaded in grey.

Number of peaks	Single		Dual	
Primer	LPR5F	LPF5B	LPR5F	LPF5B
Height	128000	99000	52000	52000
Area	634000	540000	250000	260000
Area (%)	58	57	24	26

Table 5-4 Peak attributes of Alexa488-LPR5F and Alexa488-LPF5R singularly and together for multiplex sequence identification. Analysis performed with OriginPro 2016 using averaged melt curves of data produced with an ABI7500.

As can be seen from Table 5-4, when the experiment is multiplexed (dual LPR5F and LPF5B) the peak attributes are approximately half the equivalent of the single peaks. This can be seen as the derivative in Figure 5-12 is roughly half that in Figure 5-13 and Figure 5-11. Whilst the negative controls above (Figure 5-10) found 12-20 peaks, with a maximum peak area of 7%, these experiments could be distinguished as OriginPro identified 1 significant peak in the single complement experiments and 2 significant peaks in the dual complement experiments.

5.4. DNA amplification using Alexa488 fluorescence

The Alexa488 fluorescence changes if the DNA is double- or single-stranded, this could be used for DNA amplification protocols, such as Polymerase Chain Reaction (PCR) and Loop-mediated Isothermal Amplification (LAMP).

5.4.1. Polymerase Chain Reaction (PCR) using Alexa488

Additional PCR experiments were planned to use BRCA1 in order to analyse the melt curves produced after PCR using NB-S quenching. Previous work in this chapter (5.1.3) showed qPCR with modified BRCA1 template and B3 primer. The F3 and B3 primers for BRCA1 LAMP reactions are routinely used to amplify the whole template sequence for

maintaining laboratory stocks, whilst the existing LPR5F and LPF5B LAMP primers were used to provide alternative PCR products.

Primers:

F3: TCC TTG AAC TTT GGT CTC C

B3: CAG TTC ATA AAG GAA TTG ATA GC

LPR5F: AGG CAG ATA GGC TTA GAC TCA A

LPF5B: AGA ACC AGA GGC CAG GCG AG

FIP: ATC CCC AGT CTG TGA AAT TGG GCA AAA TGC TGG GAT TAT AGA TGT

BIP: GCA GCA GAA AGA TTA TTA ACT TGG GAG TTG GTA AGT AAA TGG AAG A

BRCA1 sequence:

```

1  TCCTTGAACT TTGGTCTCC AAAATGCTGG GATTATAGAT GTGAGCCACC
1  AGGAACTTGA AACCAGAGGG TTTTACGACC CTAATATCTA CACTCGGTG
51  TCGCCTGGCC TCTGGTCTG TTATTATCCC AATTTACAG ACTGGGGATA
51  AGCGGACCGG AGACCAAGC AATAATAGGG TTAAAGTGTC TGACCCCTAT
101 CTGAAACTGT GCAGCAGAAA GATTATTAAC TTGGGAGGCA GATAGGCTTA
101 GACTTTGACA CGTCGTCTTT CTAATAATTG AACCTCCGT CTATCCGAAT
151 GACTCAAACC CTAATCTTCC ATTTACTTAC CAACTGTGCT ATCAATTCCT
151 CTGAGTTTGG GATTAGAAGG TAAATGAATG GTTGACACGA TAGTTAAGGA
201 TTATGAACTG
201 AATACTTGAC
  
```

Figure 5-15 BRCA1 template and primer sequences. Colour indicates primer sequences and arrow indicates amplification direction and strand. FIP and BIP were only used for LAMP DNA amplification (5.4.3) and so are not highlighted here.

Combination	Forward Primer	Reverse Primer	PCR Product length (base-pairs)	PCR Product Weight (kDa)	EvaGreen Melting Temperature (°C)
1	F3	B3	210	129.8	71.7±0.4
2	F3	LPF5B	69	42.7	79.4±0.1
3	LPR5F	B3	75	46.4	75.4±0.2

Table 5-5 BRAC1 PCR primer combinations, product length, weight and melting temperature.

As discussed in 4.7 and 4.8, F3 and B3 produce negative peak melt curves due to quenching by nucleotides present on the complementary strands (the target and primer sequence was altered in 1.2 to produce positive amplification curves). LPR5F and LPF5B give positive peak melt curves due to the quenching nucleotides on the labelled strands adjacent to the Alexa488 fluorophore. It was predicted that combination of a positive peak and negative peak primers would produce opposing melt curves, resulting in noisy, unreadable results, although as the efficiency and strength of quenching is different there may be one fluorophore that results in a greater change and so dominates.

Unlabelled F3, B3, LPR5F and LPF5B were used as controls, with the melt curves read by EvaGreen. Primer concentrations, or PCR Master Mix volumes can be used to limit the final product concentration. In order to keep the concentration of the labelled primer constant, and avoid the situation where there is skewed PCR amplification (by varying the concentration of the unlabelled complementary strand), it was decided to vary the volume of the MasterMix in order to limit the nucleotides present and so final concentration of the product. PCR product concentrations were measured using the melt curve analysis method described previously in 5.1.2, quantified using a ThermoFisher NanoDrop, and examined using the Agilent Bioanalyzer 1000, with the sizes as expected once the fluorophores were taken into account.

Results and Discussion

Using one Alexa488-labelled primer with one unlabelled primer, or two Alexa488-labelled primers resulted in PCR products the same size as the EvaGreen controls using two unlabelled primers. Melt curves as below in Figure 5-18, Figure 5-17 and in the correct melting temperatures, although F3 and B3 had negative peaks as previously discussed. As seen in Figure 5-16 there was not a significant difference between the temperatures measured using the Alexa488 fluorescence.

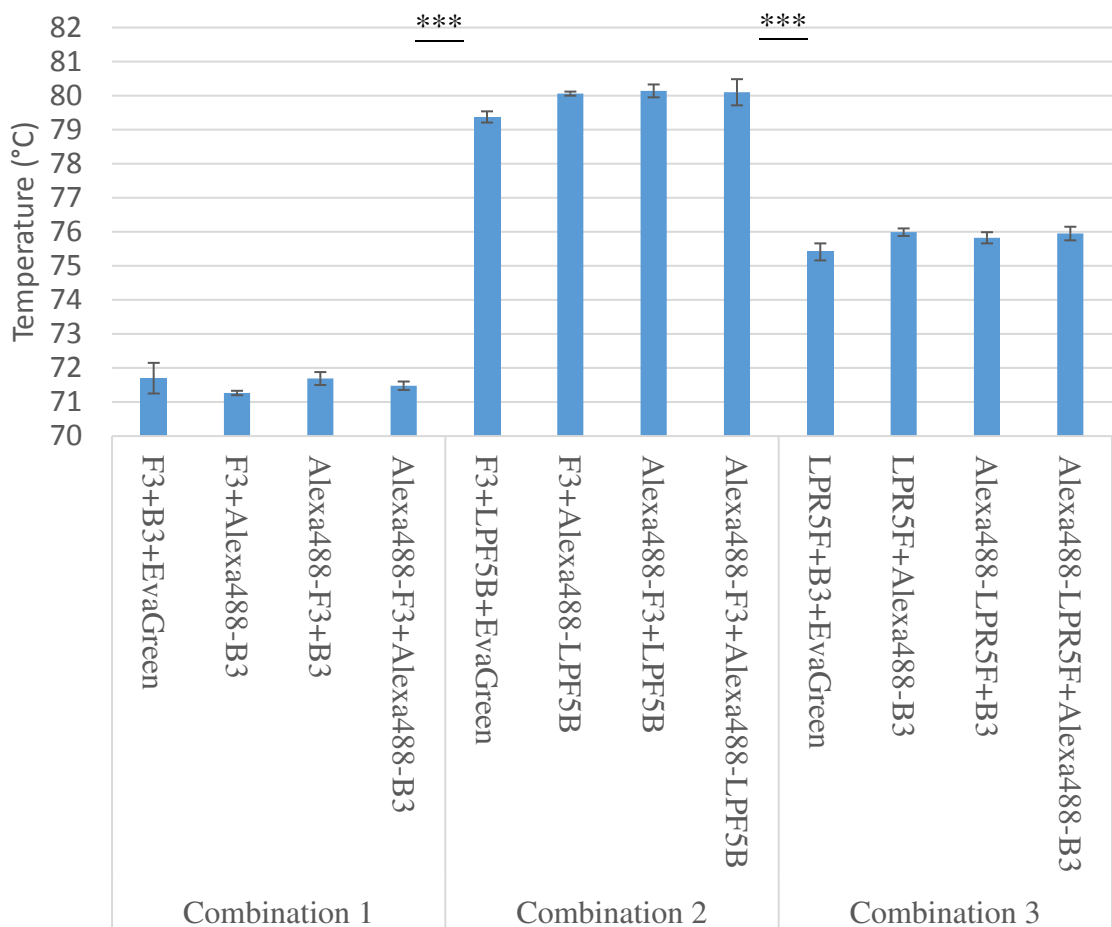


Figure 5-16 Melting temperature of BRAC1 PCR products measured with Alexa488 (blue) or EvaGreen (green) fluorescence in ABI 7500. EvaGreen with F3 and B3 are controls. *** shows $p < 0.001$ between combinations.

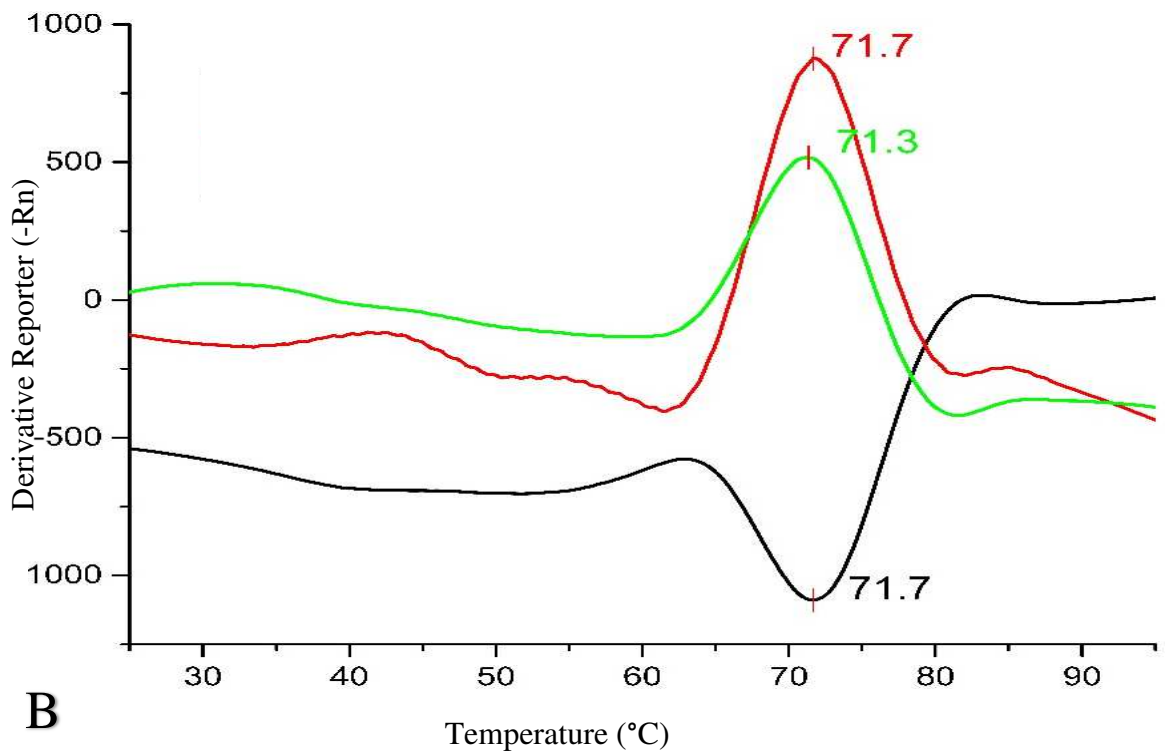
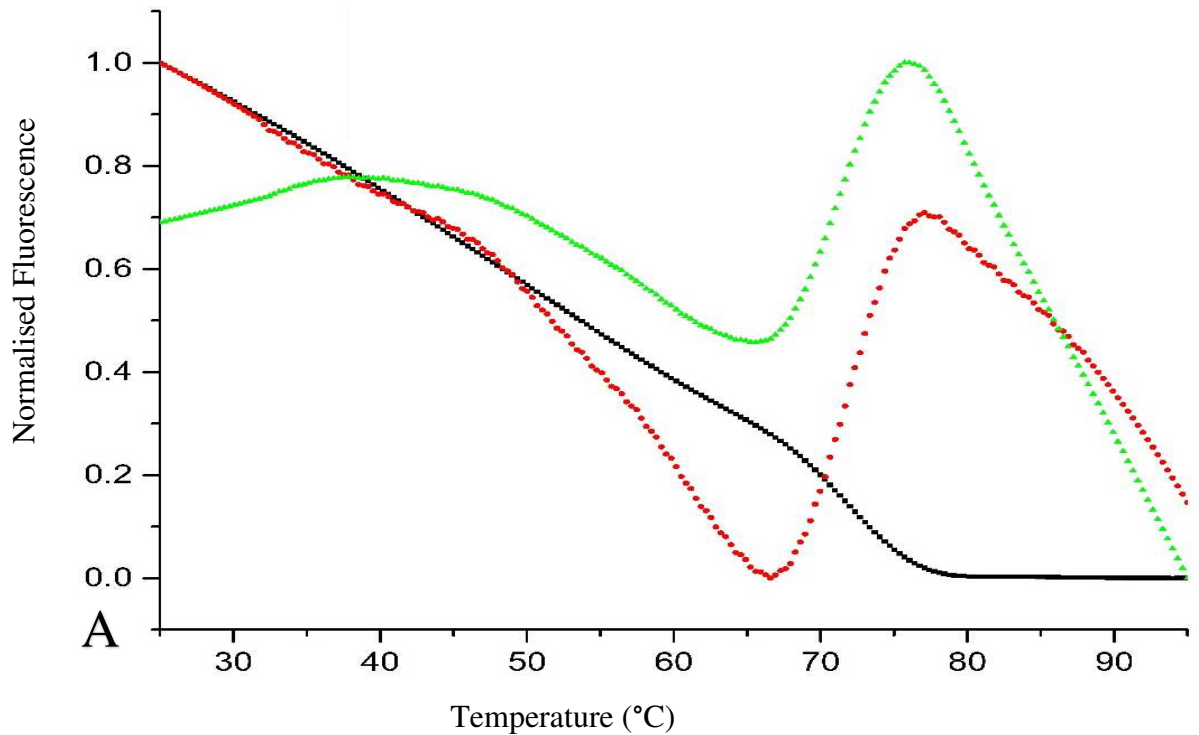


Figure 5-17 Spectra of normalised fluorescence (A) and derivative (B) curves of the products of Combination 1. In A and B, F3+B3+EvaGreen (control) is shown in black, Alexa488-labelled F3+B3 is shown in red, and F3+Alexa488-labelled B3 is in green. PCR was performed as described, with a melt curve performed between 25-95 °C. Origin 2016 performed smoothing with 10 point adjacent-averaging in Origin 2016, and derivative. Peakfinding function was limited to a single peak, shown.

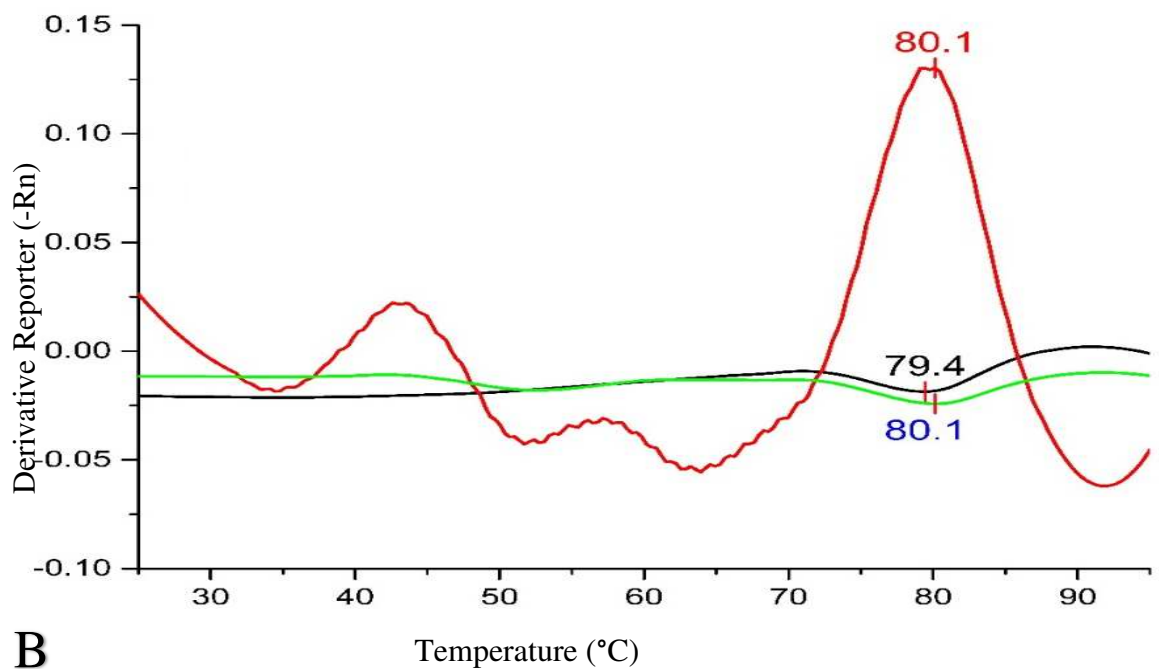
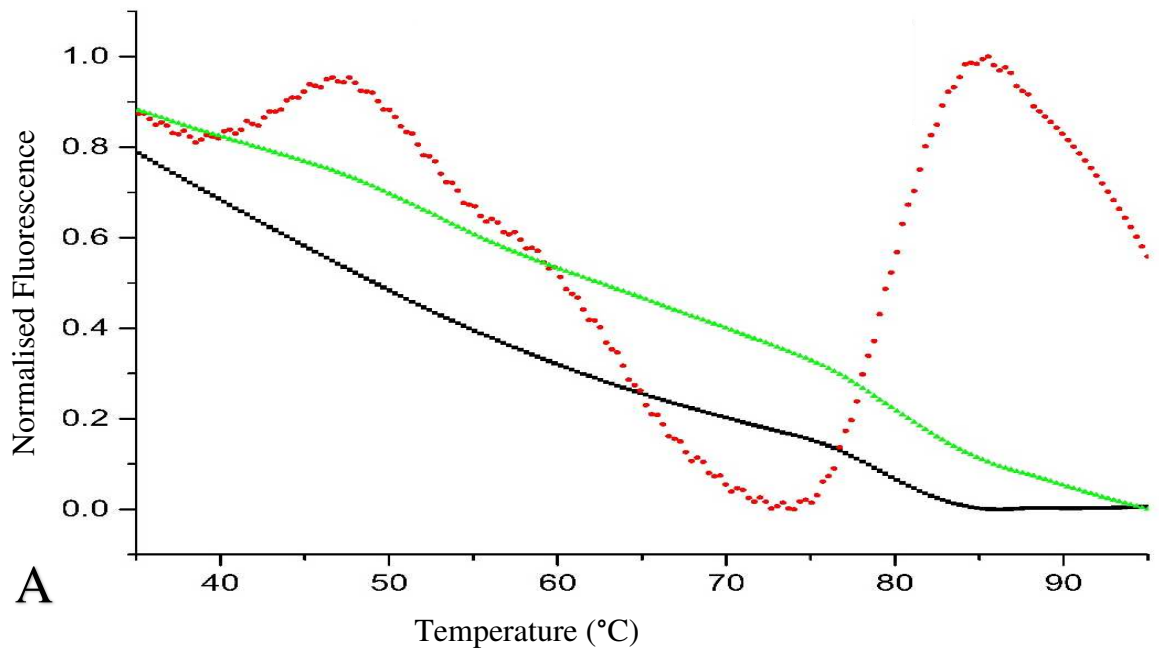


Figure 5-18 Spectra of normalised fluorescence (A) and derivative (B) curves of the products of Combination 2. In A and B, F3+LPF5B+EvaGreen (control) is shown in black, F3+Alexa488-labelled LPF5B is shown in green, and Alexa488-labelled F3+LPF5B is shown in red. PCR was performed as described, with a melt curve performed between 25-95 °C. Origin 2016 performed smoothing with 10 point adjacent-averaging in Origin 2016, and derivative plotted. Peakfinding function was limited to a single peak, shown.

5.4.2. Loop-Mediated Isothermal Amplification (LAMP) using Alexa488

LAMP is a method of DNA amplification requiring 3 pairs of primers and a constant temperature instead of PCR cycling [41–44]. The fundamentals of LAMP were discussed in section 1.2.2; the detailed reaction method is in 2.2.3.4. LPR5F and LPF5B were chosen from the 6 primers to be Alexa488-labelled as the fluorescence increases when double-stranded, so the amplification plot and melt curve should be similar to that seen with EvaGreen.

Experiments with primers with the lower quenching (T or C) base adjacent to the Alexa488 fluorophore resulted in a decrease in fluorescence each cycle which the ABI 7500 was not calibrated to measure.

EvaGreen controls were performed with and without template DNA. LAMP reactions A, B and C did not contain EvaGreen and relied on the single LPF5B (A), single LPR5F (B) or dual (C) Alexa488-labelled primers. After 20 minutes of amplification at 60°C, melt curves were performed and the products were run on agarose gels to confirm the products. LAMP produces large products due to the reaction producing multiple products of different lengths, whilst unreacted primers and template would have produced identifiable bands.

As there were differences seen in the LAMP products when the reaction was performed and melt curve derived using Alexa488-labelled primers, these products were photobleached for 24 hours at room temperature. After photobleaching EvaGreen was added, and the melt curves performed again.

Results and Discussion

The control experiments (Figure 5-19) worked as expected - without template DNA there was no increase in fluorescence in the amplification plot (1), nor a distinguishable melt curve (2). The EvaGreen control with template DNA showed amplification after 5 minutes with was complete after 10 minutes (3), producing a melt curve (4) with a single peak around 85°C.

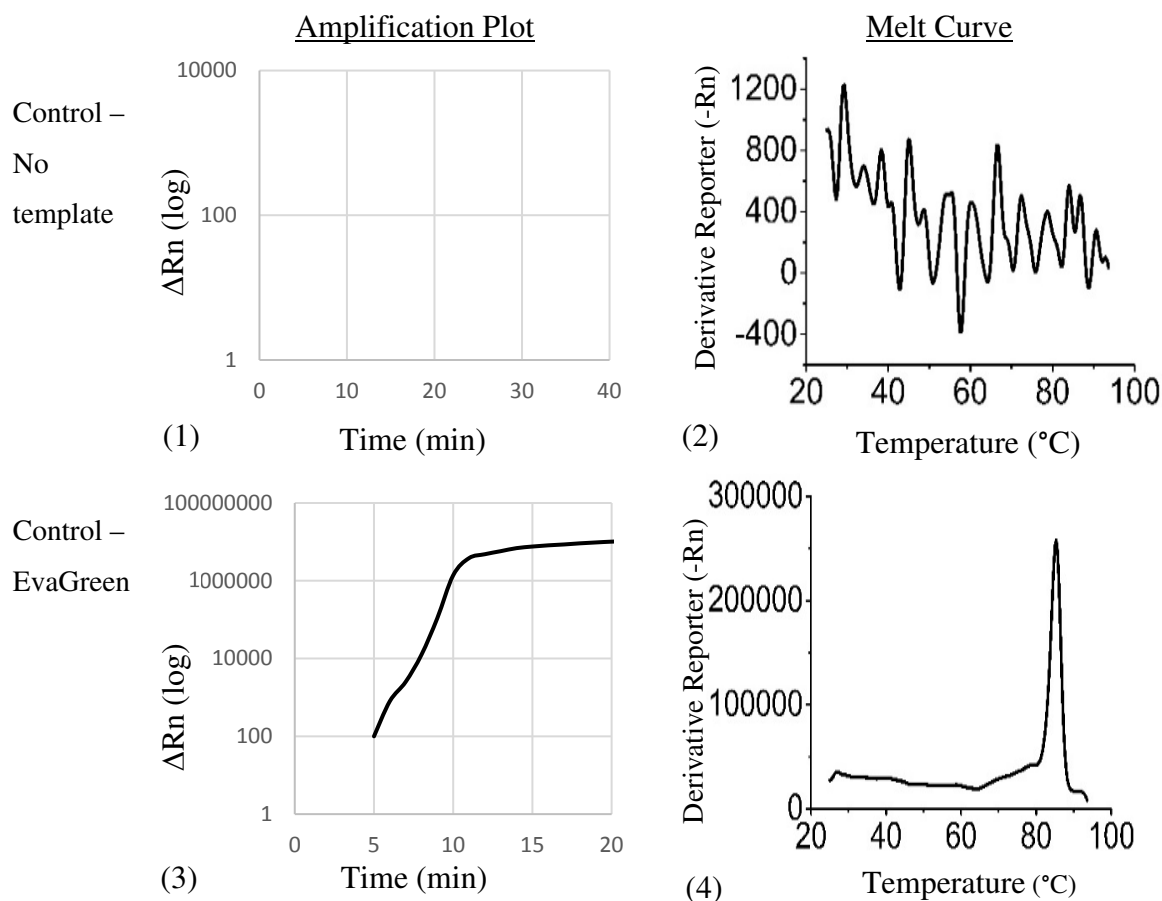


Figure 5-19 Amplification plots (left) and melt curves (right) of BRCA1 LAMP EvaGreen controls with (3 and 4) and without (1 and 2) template DNA performed on ABI 7500. Total reaction time was 20 min (40 cycles of 30 seconds). The control without template DNA showed no increase in fluorescence (1), nor a distinguishable melt curve (2). The EvaGreen control used unlabelled primers and worked as expected with positive LAMP amplification seen after 5 minutes and complete after 10 minutes (3), producing melt curve (4) with a single peak around 85°C.

The Alexa488 LAMP reactions (Figure 5-20) performed as expected, although the amplification appeared faster than the control, starting around 0.5-1 minutes and complete after 3-5 minutes (1, 3 and 5). The melt curves show 2-3 peaks, at the expected near 85°C but also at 80°C. The height of these secondary peaks depended on which primer was used, it is suggested that additional information specific to the location of these primers within the LAMP product is producing the differences in melt curves. When the Alexa488 fluorophore was photobleached, and melt curves performed with EvaGreen they were restored (Figure 5-21) suggesting that the altered melt curves are not due to different LAMP product structures, but due to the Alexa488 fluorophore position.

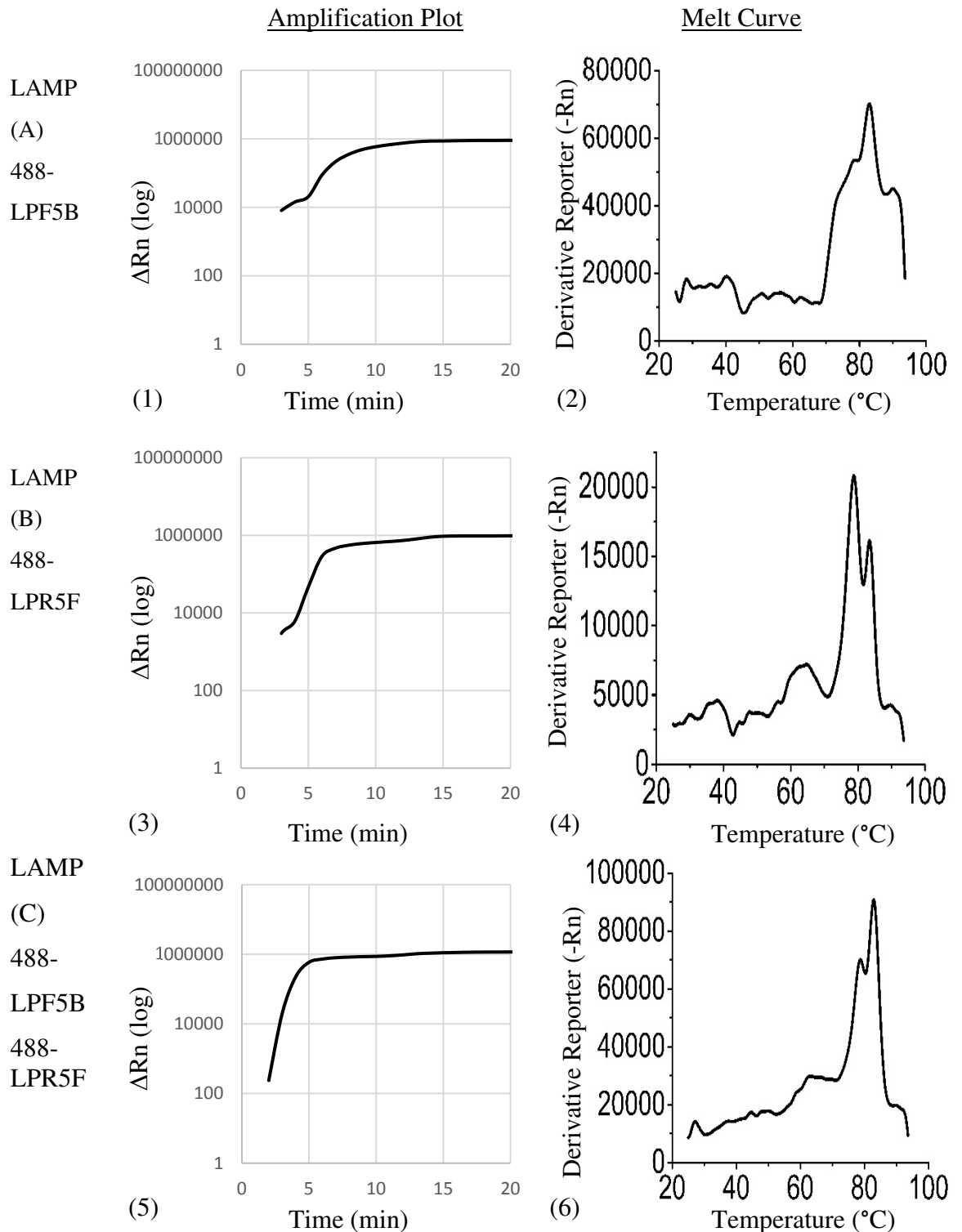


Figure 5-20 Amplification plots (left) and melt curves (right) of BRCA1 LAMP reaction performed using Alexa488-labelled primers in ABI 7500. Total reaction time was 20min (40 cycles of 30 seconds), with positive LAMP amplification seen after 0.5-1 minute and complete after 3-5 minutes, producing melt curves as seen on the right. LAMP (A) utilised Alexa488-labelled LPF5B (1 and 2), LAMP (B) utilised Alexa488-labelled LPF5B (3 and 4), LAMP (C) utilised Alexa488-labelled LPF5B (5 and 6).

Restored EvaGreen Melt Curves

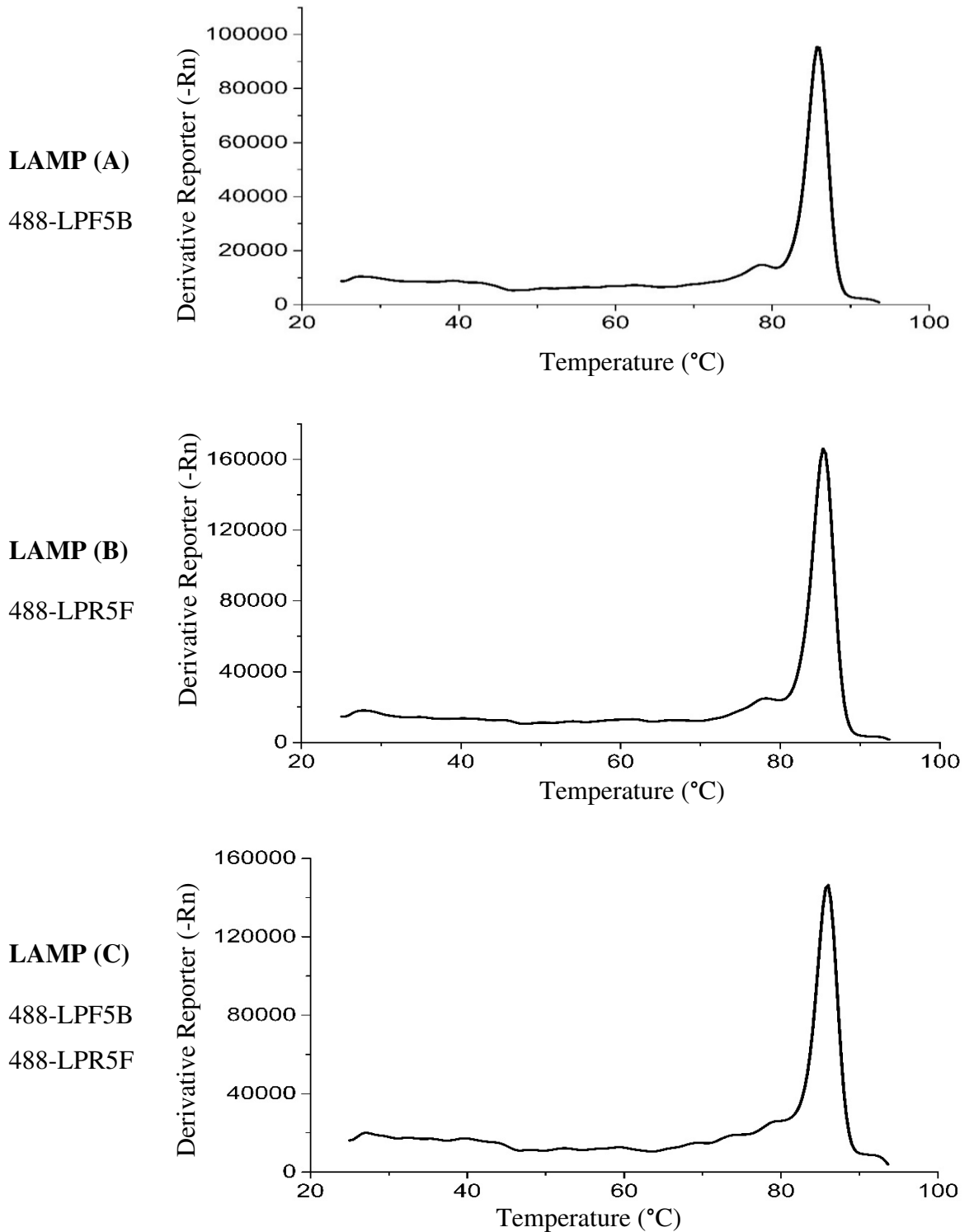


Figure 5-21 Restored averaged melt curves of Alexa488-labelled LAMP (A), (B) and (C) products – samples were photobleached and EvaGreen added to measure the melt curves in an ABI7500. The Alexa488 produced melt curves seen in the previous graph reverted to the expected curves, suggesting that the differences seen previously were due to specific position of the labelled primers within the overall LAMP product.

5.5. Incorporation of the Nucleobase-Specific Quenching Effect in a Reusable Microfluidic Lab-on-a-Chip Device

Lab-on-a-chip format devices can provide affordable diagnostics in low-resource environments [131,167]. There are several potential advantages to using Alexa488 for a microfluidic device. The first is that DNA binding could be analysed with a change in fluorescence (when the complement strand binds and the fluorophore is either quenched or unquenched), and additional sequence information could be gained by performing a melt curve. After that, the target DNA can be washed at temperatures above the melting temperature and collected, leaving the microfluidic chip able to be used for another sample, as shown in Figure 5-23.

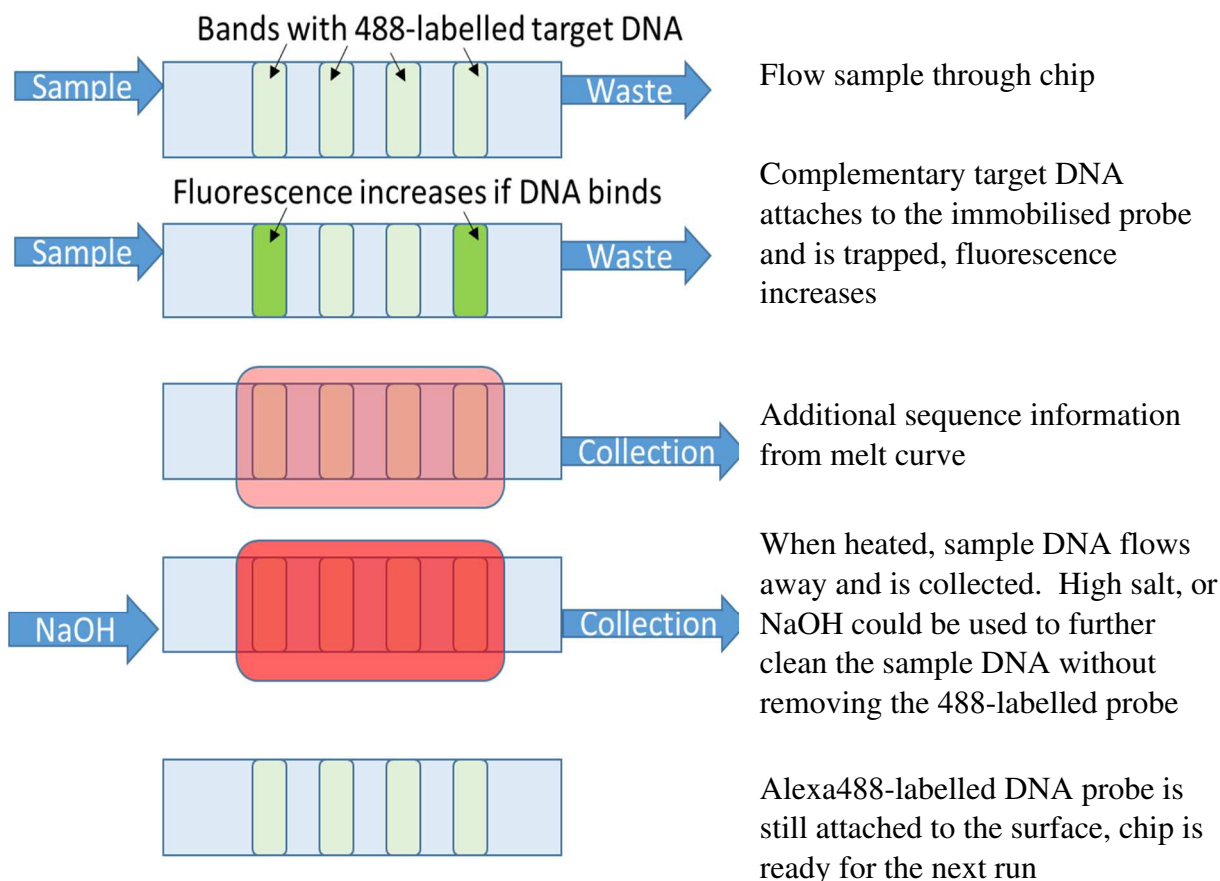


Figure 5-23 Schematic representation of the potential stages of a microfluidic DNA microarray using Alexa488 fluorescence to monitor DNA binding.

As this fluorescence effect was discovered in a microfluidic droplet system, it was a logical step to move it to an enclosed microfluidic system. For these two prototypes were created.

5.5.1. First Generation Microfluidic Device

The first generation device worked as expected, and accurate melt curves were obtained for DNA B (Figure 5-24). There were several drawbacks to the design, such as movement upon melting of the thermal paste (evident in the experiment shown in Figure 5-25 B) coupling the Peltier module and well. DNA was found in the well at 40°C and peaking at 95°C, suggesting that heating to 95°C could be used to remove the target strand from the probe in order to reuse the device. Trace amounts of DNA in the well before the target DNA was added will need to be investigated further, as this could be probe DNA that has detached from the surface of the glass coverslip. A further control experiment in the second-generation enclosed device will look at the rate that this DNA detaches from the surface.

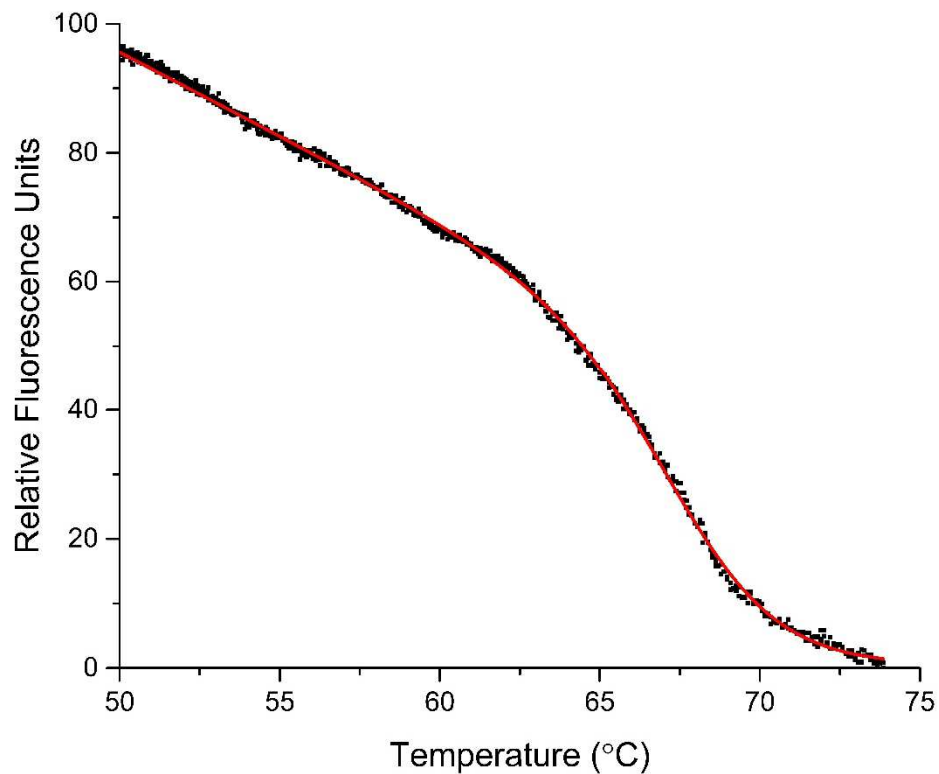


Figure 5-24 Melt curve derived using the First-Generation microfluidic device. Sigmoidal curve (red) fitted by OriginPro(2016).

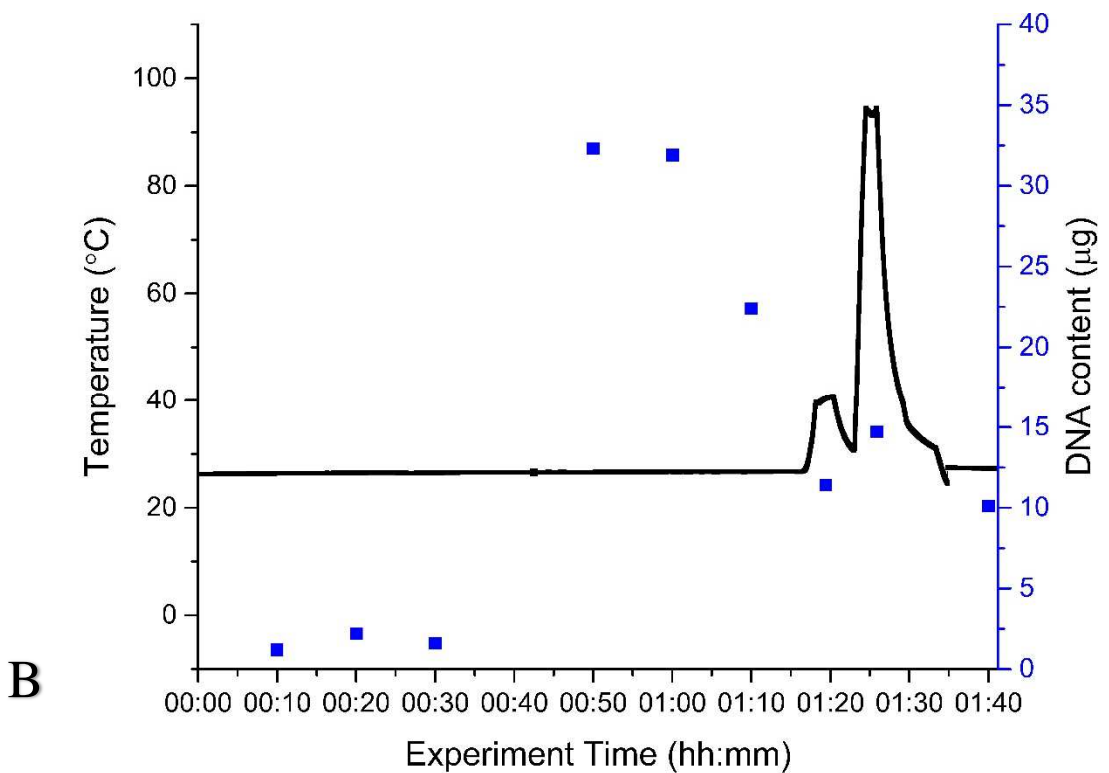
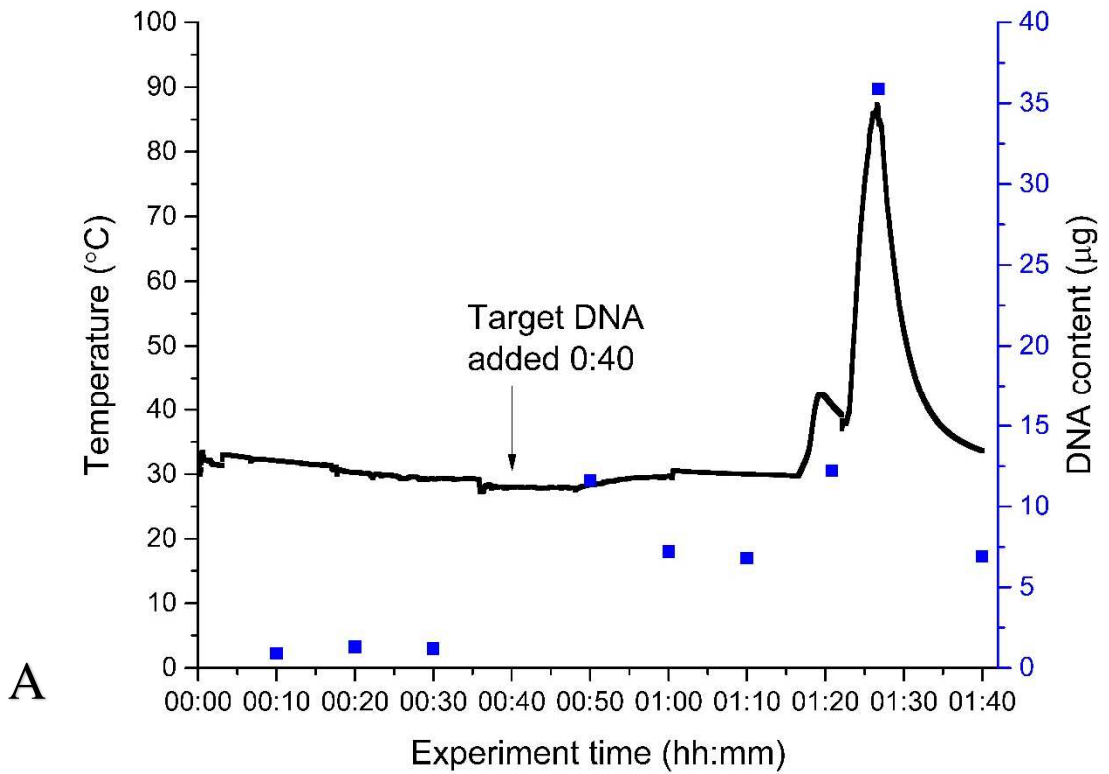


Figure 5-25 Testing the First-Generation Microfluidic device. Temperature (black line) and DNA content (blue squares) over the course of an experiment (A) and the control (B). Temperature measured using J-type thermocouple, fluorescence measured using the microscope and software previously described.

5.5.2. Second Generation Microfluidic Device

As in the first generation device, an 8mm by 8mm coverslip was coated with Alexa488-labelled DNA, and this was enclosed within a PDMS microfluidic chip as published previously [131,132,167,168]. For this experiment TE buffer was pumped at a constant rate of 20 μ l per minute with 10 μ l of 10mM unlabelled secondary DNA injected into the start of the chip, fluorescence measured using the upright fluorescence microscope with an EvaGreen / FITC filter set. As the device is fully enclosed, a thermocouple could not be used. It was noted that the coverslip with DNA had made contact with the device, as can be seen in Figure 5-26, which prevented buffer flow over the whole of the chip, and resulting in unreadable melt curves.

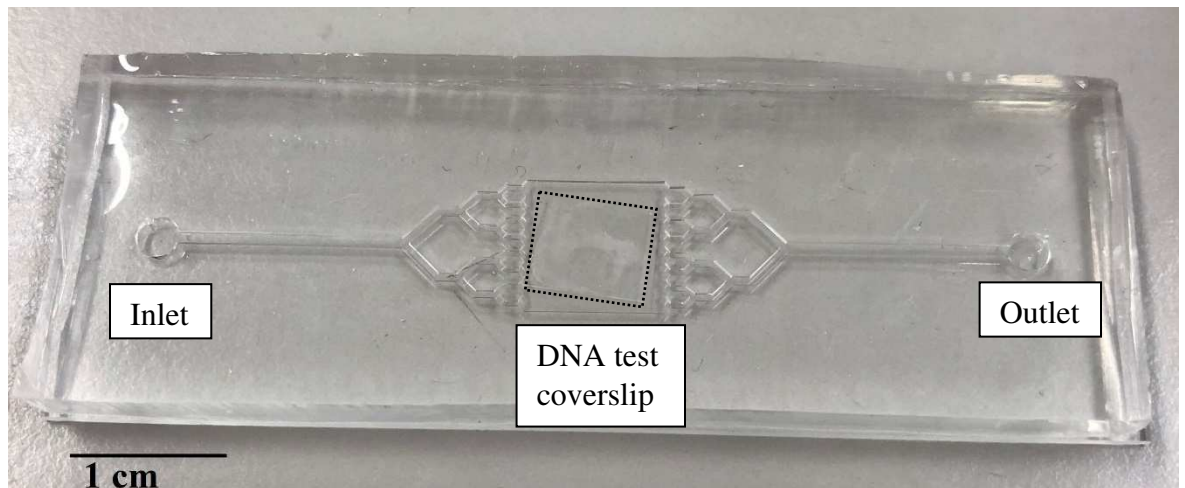


Figure 5-26 Complete Second Generation single input/output PDMS microfluidic device with DNA test chip enclosed in the centre (labelled). The inlet port and outlet ports are shown and are interchangeable.

There are several difficulties that will need to be overcome in order to improve this so that it has potential as a LOC diagnostics device. Firstly, there needs to be an integrated temperature sensor so that accurate melt curves can be derived. Secondly, an alternative fabrication protocol will need to be found as this device requires plasma ashing to bind the microscope slide to the PDMS chamber – this would remove unprotected DNA attached to the surface. These will be discussed in the future work, Chapter 6.

5.6. Conclusion

The Alexa488 sequence-specific photoinduced electron transfer NB-S quenching effect was used instead of EvaGreen to perform common biological techniques. Many protocols use a fluorophore to ascertain the presence or absence of a DNA strand, and a secondary fluorophore to analyse if the DNA is double-stranded or single-stranded - this could be a non-specific reporter molecule, such as EvaGreen, or a fluorophore attached to the complementary strand as discussed previously with FRET. By making use of the NB-S Quench effect, only a single fluorophore is needed to analyse presence/absence, single/double-stranded, and concentration of the secondary strand. Although at an early stage, Chapter 4 showed that binding of a partial complementary strand altered the fluorescent signal so this technique could provide additional information as to the sequence/length of the secondary strand with some additional research.

DNA amplification protocols PCR and LAMP using this technique were shown. When designing primers for DNA amplification it is important to know the expected sequence, as the melting of the DNA could cause either an increase or decrease in fluorescence (see Chapter 4). If two or more labelled fluorophores are to be used, it is recommended that they either all increase or all decrease fluorescence, as additive interference of fluorescence would increase the signal whilst reductive interference resulted in a poor fluorescent signal. In addition, PCR machines are programmed to look for increases in fluorescence, DNA amplification where the fluorescence decreases each cycle could be misinterpreted. The ABI 7500 software only recognises positive melt curve peaks, not negative, and so these had to be independently analysed using Origin2016.

Preliminary designs to incorporate this into a reusable microfluidic device were examined, results from the first-generation device suggest that the secondary strand could be removed by heating sufficiently to reuse the device for subsequent tests. Although difficulties with fabrication were noted, this seems to be a promising line of research, as there is the potential for multiple DNA diagnostic tests on a single chip.

6. Conclusion and Future Work

This thesis examined the effects of surface acoustic waves on DNA hybridization, with a view to integrate molecular diagnostic assays onto acousto-fluidic devices. The work used fluorescence to characterize the binding of DNA in a range of conditions, and revealed nucleobase-specific quenching (NB-S Quench) of fluorophores when attached to DNA as a double strand. This effect has been studied previously, but this is the first research into its potential applications for research and low-cost diagnostics. There is a potential for the effect to be used to simplify existing techniques, such as DNA melt curves, which also fulfilling other roles such as quantification and localisation which are usually reliant on non-specific DNA dyes such as EvaGreen. In short, this effect could be used to replace non-specific dyes or dye/quencher/FRET pairs in DNA amplification techniques entirely.

There will be additional impacts on research involving FRET, it was commonly expected that the emission of the acceptor fluorophore would only depend on the distance and excitation of the donor fluorophore but this research shows that the emission of either fluorophore may be increased or decreased by the DNA strand melting.

This work will have an impact on research into low-cost medical diagnostics, and improve the understanding of fluorescence of DNA modified with fluorophores, contributing to the understanding of future work in these areas. This chapter discusses the wider implications of the research in this thesis, and suggests further experimentation that could be implemented.

6.1. Surface Acoustic Waves and DNA

The experiments with SAW suggested a slightly lower melting temperature in some cases when using EvaGreen as a reporter molecule. EvaGreen has been characterised, and it is known that the molecule changes conformation with double-stranded DNA which also alters the absorbance and subsequent fluorescence [14,150]. Lower melting temperatures recorded with EvaGreen could have been due to the DNA itself melting at a lower temperature. Preliminary results in this thesis, where the FRET and Alexa488 measured melting temperatures did not change suggest that there may be something inherent to the reporter molecule.

Streaming within the droplet due to SAW may be affecting the binding of EvaGreen to the groove of DNA. Another theory is that Fluorescence Resonance Energy Transfer (FRET) and Alexa488 fluorescence are mainly affected by the binding of the whole molecule of DNA, whilst multiple copies of EvaGreen are known to bind along the length of DNA. If SAW are increasing local melting within a DNA strand, this might not affect FRET/Alexa488 fluorophores which are next to double-stranded DNA at one end of the DNA strand. In addition, if SAW are increasing the melting of the ends of DNA, this would only affect FRET/Alexa488 if it occurred at that end. In the case of FRET, the fluorescence is dependent on the distance between the acceptor and donor fluorophores [43], so partial melting of the DNA adjacent to the fluorophore which only slightly increases the distance between the acceptor fluorophore and the donor fluorophore would partially reduce the fluorescence signal.

In the case of Alexa488, partial melting of the DNA adjacent to the fluorophore which halved the quenching effect would change reduce the fluorescence of that fluorophore by 5-10%, and the experiments with complementary strand effects suggest that the photo-induced electron transfer effect may depend on the charge of more than just the adjacent nucleotide.

In both cases, if EvaGreen changes conformation when binding to the groove of double-stranded DNA, this partial melting would result in dislocation of the fluorophore, and changing of the conformation (and absorption/fluorescence) of that molecule, resulting in a large change in fluorescence, and requiring the molecule to again bind to the DNA groove and change conformation before the fluorescence signal recovers. If the DNA strand is relatively long, and the ends are affected more than the nucleotides within the strand, then there would be more EvaGreen bound to the unaffected nucleotides than affected at the end. The theory is that although the change in fluorescence is relatively large, on a long strand of DNA relatively few reporter molecules are affected, so this warrants further investigation if SAW and intercalating reporter molecules are to be used in the future.

Further to this, it was an aim of this thesis to investigate the difference of SAW on DNA in a microdroplet and DNA bound to the surface as the microenvironments will be different, with different pressure and streaming [52]. There was insufficient time to complete the experiments using FRET and Alexa488 fluorescence to evaluate DNA attached to the surface, so these were not included, but this research could provide interesting results and would improve understanding of SAW diagnostic devices. Current research is examining the preparation of DNA for sequencing with SAW, and the potential for the sequencing

reaction to be performed using SAW, if this is to be performed on a patterned surface then understanding the surface microenvironment will be essential. A thorough study could comparing DNA within the droplet, DNA attached to the surface, and DNA attached to bead, with saw would be relevant to past and future research [48,49,152,169].

6.2. Further Characterisation of Alexa488 Fluorescence Effect

There are still several important questions on the characterisation of the Alexa488 photo-induced electron transfer effect. ATTO488 was identified as also exhibiting this effect, whilst FITC does not, additional work could discover the chemical basis of this mechanism and allow additional fluorophores with these properties to be identified. It could be possible to engineer fluorophores to this end.

It is unknown why the melting temperature is almost always below that when measured with the EvaGreen control, there was no obvious correlation with DNA length, GC content, or the sequence of the nucleotides adjacent, further experiments could examine this in more detail. It could be as simple as the addition of the fluorophore on the end influencing the binding, perhaps through hydrogen bonding or other steric hindrance, although this would also be noted in FRET experiments – two fluorophores would also increase this effect. Additional work to discover if this is the case could utilise chemically similar fluorophores that do not fluoresce in the green channel, allowing use of intercalating dyes such as EvaGreen. In this thesis, Alexa488 fluorophores were photobleached and EvaGreen added to restore the expected melting peak, although it is unclear if this photobleaching would have destroyed the fluorophore so that it can no longer change the melting temperature. This theory may be disproven by additional experiments using partial complementary strands.

It was noted that the partial complement strands showed melting temperatures closer to the expected temperature, which could be simply due to the fact that the background signal increased along with the distance between the fluorophore and double-stranded DNA. Some experiments suggested that this did depend on the sequence of the nucleotides adjacent to the fluorophore – such as TTT eliminating the photo-induced electron transfer effect [20,76,163].

In order to understand the effects of deletions, mismatches, and insertions may have, 3 experiments are suggested. It is suggested that the experiments use the same sequence, but

with the fluorophore at either the 5' or 3' end, with a different nucleotide attached so as to produce melt curves in both directions, for example:

```
5'   GGG CCC CAG CGC CAA CAG TCG GCG CTT GTC 3'
      CCC GGG GTC GCG GTT GTC AGC CGC GAA CAG
```

Mismatches in the nucleotide closest to the fluorophore could be examined. This is predicted to increase quenching, with the fluorophore when double-stranded quenched by the fluorophore adjacent and opposite as this part is always single-stranded. This could mean that both the 5' and 3' fluorophore are relieved of quenching when the complementary strand has melted and is in solution. Examining mismatches as below could provide valuable information to improve the model:

3'-G	GAC AAG CGC CGA CTG TTG GCG CTG GGG CCG
3'-T	GAC AAG CGC CGA CTG TTG GCG CTG GGG CCT
3'-A	GAC AAG CGC CGA CTG TTG GCG CTG GGG CCA
5'-A	AAC AAG CGC CGA CTG TTG GCG CTG GGG CCC
5'-C	CAC AAG CGC CGA CTG TTG GCG CTG GGG CCC
5'-T	TAC AAG CGC CGA CTG TTG GCG CTG GGG CCC

Table 6-1 Example of sequences that could be used to investigate the effect of mismatches of the base closest to the Alexa488 fluorophore on the complementary strand.

Insertions/additions could be examined by adding a base opposite from the fluorophore. It is predicted that these results will be easier to interpret than the mismatches experiment detailed above as the effect of a quenching single base adjacent to the fluorophore will be removed. As G>C>A>T, the theory states that is the order of quenching that will be seen, and in all cases the overall quenching of the fluorophore will be removed when the DNA melts to become single-stranded.

6.3. Conventional Protocols with the Photo-induced Electron Transfer Effect

Additional research studying the fluorescence of Alexa488, or ATTO488, attached to, for example, antibodies would be interesting. If the binding of the antigen to the antibody near the fluorophore altered the fluorescence, this could lead to simpler antibody-based diagnostics. This could lead to improvements in histology, and antibody-based diagnostics such as Enzyme Linked Immunosorbent Assays (ELISA).

The compatibility of the photo-induced electron transfer effect with conventional DNA-based techniques would require more research on understanding complementary strand effects. Polymerase Chain Reaction (PCR) is a mainstay of genetic and infectious diagnostics, including lab-on-a-chip, and other DNA amplification techniques such as LAMP are used regularly in point-of-care diagnostics, including paper-based microfluidics [3,33,35,41,111].

The difference in melting temperature of some double-stranded DNA compared to the EvaGreen controls suggests that there may be other factors which require investigation before this technique could intercalating reporter molecules like EvaGreen. This thesis investigated using Alexa488 instead of EvaGreen for PCR and LAMP, although it was noted that there were difficulties (especially with LAMP) due to the fact that EvaGreen produces much larger changes in fluorescence, whereas Alexa488 only changes by 10-20%. For the ABI 7500 FAST PCR system, this meant that the software had difficulty during the amplification steps of the reaction as the increase (or decrease in the case of F3 and B3 primers) was of a magnitude smaller and much closer to the background than expected. Improving the sensitivity of the fluorescence sensors, and software changes, in these systems could lead this to become a commercially successful technique, although it was viable within our laboratory.

Experiments on surface-attached DNA were performed as an alternative to Fluorescence Resonance Energy Transfer (FRET)[67]. The advantages of FRET is there is a relatively large reduction in the signal from the donor fluorophore and increase in the signal from the acceptor fluorophore, and these can independently be monitored. Using the 10-20% quenching of a single fluorophore to monitor DNA binding requires relatively more sensitive equipment but there is potential for Alexa488 and similar fluorophores to be incorporated into DNA microarrays[3]. As the number of fluorophores is reduced in microarrays, the fluorescence is also reduced, so this technique may not be suitable for current high-density

microarrays without improving the sensitivity of the fluorescence sensor. In the long-term, microarrays may be completely replaced by sequencing.

There may also be a way for this technique to be incorporated into Next Generation Sequencing (NGS). As discussed before, some next generation sequencers rely on a fluorophore that is later cleaved [43], using dyes that exhibit the discussed fluorescence effect could allow additional information to be obtained, in turn allowing longer DNA probe binding to be studied and so increasing the efficiency of the sequencing.

Next generation sequencing, and Lab-on-a-Chip diagnostics often involves DNA attached to magnetic or fluorescent beads [170,171]. Experiments in this thesis used thiolated DNA attached to the surface of glass, which had no measurable effect on the fluorescence. Magnetic beads can be separately introduced, moved/kept in place, and later released, so this fluorescence technique could be combined with established protocols for Lab-on-a-chip diagnostics [82,83,168]. For example, the magnetic particles could be added to microfluidic devices with Alexa488-labelled DNA attached as a probe. If the target DNA is present in the sample, this is indicated by a change in fluorescence, and the particles with the target DNA can be collected.

It is likely that attachment to beads as is commonplace in NGS will not change the fluorescence effect discussed, although attachment to a fluorescent bead would still allow FRET. It is possible that this could improve current FRET bead techniques as the FRET signal would confirm that the probe DNA is attached, as well as providing information as to if it is double- or single-stranded. For example, if the fluorescent particle was a FRET donor, and the FRET acceptor Alexa488-DNA was attached to the bead within the FRET distance, then the existence of any signal would show that DNA binding had worked as expected. Addition, or removal of the complementary strand, would change the fluorescence giving a melting peak/annealing peak.

As current attachment chemistry can be used on the same DNA strand on the opposite end to the fluorophore, this could be used for surface attachment in microfluidic devices. This thesis contained preliminary work on integrating this technique into a droplet device, as well as two generations of microfluidic flow devices[131]. The second-generation flow device used a piece of coverslip with the DNA attached, due to difficulties noted in PDMS device fabrication – the microscope slide and PDMS must be processed in a plasma asher to ensure binding. This step would require protection of the DNA, with a resist coating for example, that would later require removal. There are some advantages to this, as the coating would prevent degradation of the DNA and photobleaching of the fluorophore, but alternative

fabrication methods such as “sticky” chambers, perhaps 3D printed, should be researched [88,172].

6.4. Second and Third Generation Microfluidic Devices

An RTD will be fabricated onto the microscope slide and calibrated before the device is sealed, this will need to be longer than those previously designed so that the contact points are outside of the device. It was noted that when the microfluidic device was sealed, part of it stuck to the DNA chip. There are several strategies to prevent this in the future, which could potentially aid in storage of the devices. A protective coating could be used between the DNA on the surface of the test chip and the microfluidic device that degrades with heat or a solvent that will not degrade the DNA or affect the DNA binding (nor interfere with the PDMS microfluidic chip). Agarose gel has been shown to work with lateral flow paper devices, and does not interfere with DNA including DNA amplification by LAMP or PCR. Another option would be to use a photoresist, such as S1818, which would be able to protect the DNA on the surface during the plasma asher bonding step during fabrication, before being broken down with ethanol when the chip is to be used. Both of these could be explored in the future, and would allow the DNA to be attached directly to the surface of the microscope slide instead of a coverslip in the device. If s1818 were used to fabricate the RTD to measure the temperature then it could be used for DNA patterning too.

An alternative would be to change the device fabrication, there are commercially available options that use an adhesive to attach to the microscope slide, removing the requirement plasma asher the surface to clean the surface before binding, such as the Ibidi sticky slides.

For these experiments, the buffer will be collected at several points during the run to show the levels of DNA are indistinguishable from water background. When the microfluidic chip is heated, more DNA is expected to be collected until it peaked at the melting temperature of the DNA. If multiple DNA binding sites were used, with differing melting temperatures, it would be possible to collect fractions as the DNA melts in order to use the sample DNA for other uses.

It is important to point out that the NB-S Quench effect seemed to work reproducibly when there was double-stranded DNA adjacent to the fluorophore, and this resulted in the ability to multiplex target sequence identification. If each spot on a DNA microarray were able to

differentiate between different similar target sequences, by length or perhaps by sequence if the experiments from 6.2 work as expected, then this would be a significant enhancement. An obvious use for this would be a negative control, where any unused primer binds to the same sequence attached to microarray. If there is successful PCR amplification, then this will be seen from the higher melting temperature. If there is no PCR, then the primers will be seen. A mixture could provide an insight as to the levels of original substrate DNA, which would link to disease severity. There would be the potential for multiple DNA tests along the length of a reusable microfluidic chip, limited only by the fabrication and fluorescence imaging.

7. References

1. Dunn P, Mckenna H, Murray R. Deficits in the NHS 2016. King's Fund [Internet]. 2016;(July):36. Available from: http://www.kingsfund.org.uk/sites/files/kf/field/field_publication_file/Deficits_in_the_NHS_Kings_Fund_July_2016_1.pdf
2. Laksanasopin T, Guo TW, Nayak S, Sridhara AA, Xie S, Olowookere OO, et al. A smartphone dongle for diagnosis of infectious diseases at the point of care. *Sci Transl Med.* 2015;7(273):273re1.
3. Sun Y, Dhumpa R, Bang DD, Høgberg J, Handberg K, Wolff A. A lab-on-a-chip device for rapid identification of avian influenza viral RNA by solid-phase PCR. *Lab Chip [Internet].* 2011;11(8):1457–63. Available from: <http://www.ncbi.nlm.nih.gov/pubmed/21369571>
4. Matatagui D, Fontecha JL, Fernández MJ, Gràcia I, Cané C, Santos JP, et al. Love-wave sensors combined with microfluidics for fast detection of biological warfare agents. *Sensors (Switzerland).* 2014;14(7):12658–69.
5. Park JY, Park SM. DNA hybridization sensors based on electrochemical impedance spectroscopy as a detection tool. *Sensors.* 2009;9(12):9513–32.
6. Länge K, Rapp BE, Rapp M. Surface acoustic wave biosensors: A review. *Anal Bioanal Chem.* 2008;391(5):1509–19.
7. Roh Y, Hur Y, Pak YE. SAW sensor for anti-human-immuno-globulin G molecule detection. *Proc - IEEE Ultrason Symp.* 2004;2(c):817–20.
8. Wyatt R, Kwong PD, Henrickson W a, Sodroski JG. Structure of the Core of the HIV-1 gp120 Exterior Envelope Glycoprotein. *Los Alamos Rev.* 1999;1–7.
9. Lai MMC. Cellular factors in the transcription and replication of viral RNA genomes: A parallel to dna-dependent RNA transcription. *Virology.* 1998;244(1):1–12.
10. Llangland JO, Cameron JM, Heck MC, Jancovich JK, Jacobs BL. Inhibition of PKR by RNA and DNA viruses. *Virus Res.* 2006;119(1):100–10.
11. Weber F, Wagner V, Rasmussen SB, Hartmann R, Paludan SR. dsRNA is produced

by dsDNA viruses.pdf. 2006;80(10):5059–64.

12. Rouzina I, Bloomfield VA. Heat capacity effects on the melting of DNA. 1. General aspects. *Biophys J* [Internet]. 1999;77(6):3242–51. Available from: <http://www.pubmedcentral.nih.gov/articlerender.fcgi?artid=1300595&tool=pmcentrez&rendertype=abstract>
13. Hur D, Kim MS, Song M, Jung J, Park H. Detection of genetic variation using dual-labeled peptide nucleic acid (PNA) probe-based melting point analysis. *Biol Proced Online* [Internet]. 2015;17(1):14. Available from: <http://www.biologicalproceduresonline.com/content/17/1/14>
14. Mao F, Leung WY, Xin X. Characterization of EvaGreen and the implication of its physicochemical properties for qPCR applications. *BMC Biotechnol*. 2007;7:76.
15. Holbrook JA, Capp MW, Saecker RM, Record MT. Enthalpy and heat capacity changes for formation of an oligomeric DNA duplex: Interpretation in terms of coupled processes of formation and association of single-stranded helices. *Biochemistry*. 1999;38(26):8409–22.
16. SantaLucia J. A unified view of polymer, dumbbell, and oligonucleotide DNA nearest-neighbor thermodynamics. *Proc Natl Acad Sci U S A* [Internet]. 1998;95(4):1460–5. Available from: <http://www.pnas.org/cgi/doi/10.1073/pnas.95.4.1460>
17. De Santis P, Scipioni A, Palleschi A, Savino M. Validity of the Nearest-Neighbor Approximation in the Evaluation of the Electrophoretic Manifestations of DNA Curvature. *Biochemistry*. 1990;29(39):9269–73.
18. Xia T, SantaLucia J, Burkard ME, Kierzek R, Schroeder SJ, Jiao X, et al. Thermodynamic parameters for an expanded nearest-neighbor model for formation of RNA duplexes with Watson - Crick base pairs. *Biochemistry*. 1998;37(42):14719–35.
19. Peyret N, Seneviratne PA, Allawi HT, SantaLucia J. Nearest-neighbor thermodynamics and NMR of DNA sequences with internal A·A, C·C, G·G, and T·T mismatches. *Biochemistry*. 1999;38(12):3468–77.
20. Wilson JN, Cho Y, Tan S, Cuppoletti A, Kool ET. Quenching of fluorescent nucleobases by neighboring DNA: The “insulator” concept. *ChemBioChem* [Internet]. 2008 Jan 17;9(2):279–85. Available from:

<https://doi.org/10.1002/cbic.200700381>

21. Manetto A. I-Modified Nucleosides as DNA-Sugar Centered Radical. II-DNA Excess Electron Transfer Studies. III-A new Direct DNA Detection Method: DNA-Photography. 2007;(January).
22. SantaLucia J, Allawi HT, Seneviratne PA. Improved nearest-neighbor parameters for predicting DNA duplex stability. *Biochemistry*. 1996;35(11):3555–62.
23. Allawi HT, SantaLucia J. Nearest neighbor thermodynamic parameters for internal G·A mismatches in DNA. *Biochemistry*. 1998;37(8):2170–9.
24. Antao VP, Tinoco Jr. I. Thermodynamic parameters for loop formation in RNA and DNA hairpin tetraloops. *Nucleic Acids Res [Internet]*. 2008;20(4):819–24. Available from: <http://www.pubmedcentral.nih.gov/picrender.fcgi?artid=312023&blobtype=pdf>
25. Brown T, Leonard GA, Booth ED, Kneale G. Influence of pH on the conformation and stability of mismatch base-pairs in DNA. *J Mol Biol*. 1990;212(3):437–40.
26. Spielmann HP, Wemmer DE, Jacobsen JP. Solution structure of a DNA complex with the fluorescent bis-intercalator TOTO determined by NMR spectroscopy. *Biochemistry*. 1995;34(27):8542–53.
27. Navarro E, Serrano-Heras G, Castaño MJ, Solera J. Real-time PCR detection chemistry. *Clin Chim Acta [Internet]*. 2015;439:231–50. Available from: <http://dx.doi.org/10.1016/j.cca.2014.10.017>
28. Bonnet G, Krichevsky O, Libchaber A. Kinetics of conformational fluctuations in DNA hairpin-loops. *Proc Natl Acad Sci U S A [Internet]*. 1998;95(15):8602–6. Available from: <http://www.pnas.org/content/95/15/8602.full.pdf>
29. Lewis FD, Letsinger RL, Wasielewski MR. Dynamics of photoinduced charge transfer and hole transport in synthetic DNA hairpins. *Acc Chem Res*. 2001;34(2):159–70.
30. Takahashi S, Sugimoto N. Effect of pressure on thermal stability of G-Quadruplex DNA and double-stranded DNA structures. *Molecules [Internet]*. 2013;18(11):13297–319. Available from: <http://www.ncbi.nlm.nih.gov/pubmed/24172240>
31. Siddiqui-Jain A, Grand CL, Bearss DJ, Hurley LH. Direct evidence for a G-

- quadruplex in a promoter region and its targeting with a small molecule to repress c-MYC transcription. *Proc Natl Acad Sci U S A* [Internet]. 2002;99(18):11593–8. Available from: <http://www.pnas.org/cgi/doi/10.1073/pnas.182256799>
32. Garavís M, González C, Villasante A. On the origin of the eukaryotic chromosome: The role of noncanonical dna structures in telomere evolution. *Genome Biol Evol.* 2013;5(6):1142–50.
 33. Wheeler EK, Hara CA, Frank J, Deotte J, Hall SB, Benett W, et al. Under-three minute PCR: Probing the limits of fast amplification. *Analyst.* 2011;136(18):3707–12.
 34. Otaguiri ES, Morguette AEB, Morey AT, Tavares ER, Kerbauy G, de Almeida Torres RSL, et al. Development of a melting-curve based multiplex real-time PCR assay for simultaneous detection of *Streptococcus agalactiae* and genes encoding resistance to macrolides and lincosamides. *BMC Pregnancy Childbirth.* 2018;18(1):1–11.
 35. Wang F, Burns MA. Performance of nanoliter-sized droplet-based microfluidic PCR. *Biomed Microdevices.* 2009;11(5):1071–80.
 36. Spiess AN, Feig C, Ritz C. Highly accurate sigmoidal fitting of real-time PCR data by introducing a parameter for asymmetry. *BMC Bioinformatics* [Internet]. 2008;9:221. Available from: <http://www.ncbi.nlm.nih.gov/pubmed/18445269>
 37. Lee C, Kim J, Shin SG, Hwang S. Absolute and relative QPCR quantification of plasmid copy number in *Escherichia coli*. *J Biotechnol.* 2006;123(3):273–80.
 38. Mestdagh P, Van Vlierberghe P, De Weer A, Muth D, Westermann F, Speleman F, et al. A novel and universal method for microRNA RT-qPCR data normalization. *Genome Biol.* 2009;10(6).
 39. Guttenberg Z, Müller H, Habermüller H, Geisbauer A, Pipper J, Felbel J, et al. Planar chip device for PCR and hybridization with surface acoustic wave pump. *Lab Chip.* 2005;5(3):308–17.
 40. Miller KR, Levine JS. *Prentice Hall biology*. Upper Saddle River, N.J.: Pearson/Prentice Hall; 2008.
 41. Tanner NA, Evans TC. Loop-mediated isothermal amplification for detection of nucleic acids. *Curr Protoc Mol Biol.* 2013;(SUPPL.105):1–14.

42. Tanner NA, Zhang Y, Evans TC. Simultaneous multiple target detection in real-time loop-mediated isothermal amplification. *Biotechniques*. 2012;53(2):81–9.
43. R. Kubota, A. M. Alvarez, W.W. Su, D. M. Jenkins. FRET-Based Assimilating Probe for Sequence-Specific Real-Time Monitoring of Loop-Mediated Isothermal Amplification (LAMP). *Biol Eng Trans*. 2011;4(2):81–100.
44. Tanner NA, Zhang Y, Evans TC. Visual detection of isothermal nucleic acid amplification using pH-sensitive dyes. *Biotechniques*. 2015;58(2):59–68.
45. Mamishev A V., Sundara-Rajan K, Yang F, Du Y, Zahn M. Interdigital sensors and transducers. *Proc IEEE*. 2004;92(5):808–44.
46. Andle JC, Vetelino JF. Acoustic wave biosensors. *Sensors Actuators A Phys*. 1994;44(3):167–76.
47. Barié N, Bücking M, Stahl U, Rapp M. Detection of coffee flavour ageing by solid-phase microextraction/surface acoustic wave sensor array technique (SPME/SAW). *Food Chem*. 2015;176:212–8.
48. Devendran C, Gunasekara NR, Collins DJ, Neild A. Batch process particle separation using surface acoustic waves (SAW): Integration of travelling and standing SAW. *RSC Adv* [Internet]. 2016;6(7):5856–64. Available from: <http://xlink.rsc.org/?DOI=C5RA26965B>
49. Bourquin Y, Reboud J, Wilson R, Zhang Y, Cooper JM. Integrated immunoassay using tuneable surface acoustic waves and lensfree detection. *Lab Chip*. 2011;11(16):2725–30.
50. Reboud J, Bourquin Y, Wilson R, Pall GS, Jiwaji M, Pitt AR, et al. Shaping acoustic fields as a toolset for microfluidic manipulations in diagnostic technologies. *Proc Natl Acad Sci U S A*. 2012;109(38):15162–7.
51. Huguet JM, Ribezzi-Crivellari M, Bizarro CV, Ritort F. Derivation of nearest-neighbor DNA parameters in magnesium from single molecule experiments. *Nucleic Acids Res*. 2017;45(22):12921–31.
52. Alghane MM. Surface Acoustic Wave Streaming in a Microfluidic System [Internet]. Heriot-Watt University; 2013. Available from: http://www.ros.hw.ac.uk/bitstream/10399/2645/1/AlghaneMM_0413_eps.pdf
53. Jarocka U, Sawicka R, Góra-Sochacka A, Sirko A, Zagórski-Ostojka W, Radecki J, et

- al. An immunosensor based on antibody binding fragments attached to gold nanoparticles for the detection of peptides derived from avian influenza hemagglutinin H5. *Sensors (Switzerland)*. 2014;14(9):15714–28.
54. Gallerano D, Wollmann E, Lupinek C, Schleder T, Ebner D, Harwanegg C, et al. HIV microarray for the mapping and characterization of HIV-specific antibody responses. *Lab Chip [Internet]*. 2015;15(6):1574–89. Available from: <http://dx.doi.org/10.1039/C4LC01510J>
55. Tajima N, Takai M, Ishihara K. Significance of antibody orientation unraveled: Well-oriented antibodies recorded high binding affinity. *Anal Chem*. 2011;83(6):1969–76.
56. Sarry F, Roux-Marchand T, Beyssen D, Elmazria O, Ait Aissa K. Dual Rayleigh and Love surface acoustic wave structures based on ZnO thin film for microfluidic applications. *IEEE Int Ultrason Symp IUS*. 2014;1517–20.
57. Klauke TN, Gronewold TMA, Perpet M, Plattes S, Petersen B. Measurement of porcine haptoglobin in meat juice using surface acoustic wave biosensor technology. *Meat Sci [Internet]*. 2013;95(3):699–703. Available from: <http://dx.doi.org/10.1016/j.meatsci.2013.03.028>
58. Guo F, Zhou W, Li P, Mao Z, Yennawar NH, French JB, et al. Precise Manipulation and Patterning of Protein Crystals for Macromolecular Crystallography Using Surface Acoustic Waves. *Small*. 2015;11(23):2733–7.
59. Qiu X, Tang R, Chen SJ, Zhang H, Pang W, Yu H. PH measurements with ZnO based surface acoustic wave resonator. *Electrochem commun [Internet]*. 2011;13(5):488–90. Available from: <http://dx.doi.org/10.1016/j.elecom.2011.02.028>
60. Luo J, Luo P, Xie M, Du K, Zhao B, Pan F, et al. A new type of glucose biosensor based on surface acoustic wave resonator using Mn-doped ZnO multilayer structure. *Biosens Bioelectron*. 2013;49:512–8.
61. Tripathy U, Giguère-Bisson M, Sangji MH, Bellemare MJ, Bohle DS, Georges E, et al. Optimization of malaria detection based on third harmonic generation imaging of hemozoin. *Anal Bioanal Chem*. 2013;405(16):5431–40.
62. Butykai A, Orbán A, Kocsis V, Szaller D, Bordács S, Tátrai-Szekeres E, et al. Malaria pigment crystals as magnetic micro-rotors: Key for high-sensitivity diagnosis. *Sci Rep [Internet]*. 2013;3:1431. Available from:

<http://www.pubmedcentral.nih.gov/articlerender.fcgi?artid=3594758&tool=pmcentrez&rendertype=abstract>

63. Bow HC. Microfluidic Devices for Analysis of Red Blood Cell Mechanical Properties. *Electr Eng.* 2010;126.
64. Gupta A, Akin D, Bashir R. Single virus particle mass detection using microresonators with nanoscale thickness. *Appl Phys Lett.* 2004;84(11):1976–8.
65. Wilfinger WW, Mackey K, Chomczynski P. Effect of pH and ionic strength on the spectrophotometric assessment of nucleic acid purity. *Biotechniques.* 1997;22(3):474–81.
66. Valeur B, Berberan-Santos MN. *Molecular Fluorescence: Principles and Applications, Second Edition.* Vol. 8, *Molecular Fluorescence: Principles and Applications, Second Edition.* Wiley-VCH; 2012.
67. Hoefling M, Lima N, Haenni D, Seidel CAM, Schuler B, Grubmüller H. Structural heterogeneity and quantitative FRET efficiency distributions of polyprolines through a hybrid atomistic simulation and monte carlo approach. *PLoS One.* 2011;6(5).
68. Bajar BT, Wang ES, Zhang S, Lin MZ, Chu J. A guide to fluorescent protein FRET pairs. *Sensors (Switzerland).* 2016;16(9):1–24.
69. Chen H, Puhl HL, Koushik S V., Vogel SS, Ikeda SR. Measurement of FRET Efficiency and Ratio of Donor to Acceptor Concentration in Living Cells. *Biophys J* [Internet]. 2006;91(5):L39–41. Available from: <http://dx.doi.org/10.1529/biophysj.106.088773>
70. Fish KN. Total internal reflection fluorescence (TIRF) microscopy. *Curr Protoc Cytom.* 2009;(SUPPL.50):273–5.
71. Axelrod D, Toomre D. Total Internal Reflection Fluorescent Microscopy. *Cell Biol Four-Volume Set.* 2006;3(1):19–28.
72. Lakowicz JR, Masters BR. *Principles of Fluorescence Spectroscopy, Third Edition.* *J Biomed Opt.* 2008;13(2):029901.
73. Bonnet G, Tyagi S, Libchaber A, Kramer FR. Thermodynamic basis of the enhanced specificity of structured DNA probes. *Proc Natl Acad Sci U S A* [Internet]. 1999;96(11):6171–6. Available from:

<http://www.pnas.org/cgi/doi/10.1073/pnas.96.11.6171>

74. Dohno C, Saito I. Discrimination of single-nucleotide alterations by G-specific fluorescence quenching. *ChemBioChem*. 2005;6(6):1075–81.
75. Torimura M, Kurata S, Yamada K, Yokomaku T, Kamagata Y, Kanagawa T, et al. Fluorescence-quenching phenomenon by photoinduced electron transfer between a fluorescent dye and a nucleotide base. *Anal Sci [Internet]*. 2001;17(1):155–60. Available from: https://www.jstage.jst.go.jp/article/analsci/17/1/17_1_155/_article
76. Doose S, Neuweiler H, Sauer M. Fluorescence quenching by photoinduced electron transfer: A reporter for conformational dynamics of macromolecules. *ChemPhysChem [Internet]*. 2009;10(9–10):1389–98. Available from: <https://doi.org/10.1002/cphc.200900238>
77. Herr AE, Hatch A V., Throckmorton DJ, Tran HM, Brennan JS, Giannobile W V., et al. Microfluidic immunoassays as rapid saliva-based clinical diagnostics. *Proc Natl Acad Sci U S A [Internet]*. 2007;104(13):5268–73. Available from: <http://www.pubmedcentral.nih.gov/articlerender.fcgi?artid=1828942&tool=pmcentrez&rendertype=abstract>
78. Chin CD, Laksanasopin T, Cheung YK, Steinmiller D, Linder V, Parsa H, et al. Microfluidics-based diagnostics of infectious diseases in the developing world. *Nat Med [Internet]*. 2011;17(8):1015–9. Available from: <http://www.ncbi.nlm.nih.gov/pubmed/21804541>
79. World Health Organization. World Health Organization Model List of Essential In Vitro Diagnostics. 2018;(November):29. Available from: http://www.who.int/medical_devices/diagnostics/EDL_ExecutiveSummary_15may.pdf
80. Tian WC, Finehout E. Microfluidics for biological applications. Vol. 16, *Microfluidics for Biological Applications*. Springer Science & Business Media; 2009. 1-416 p.
81. Kersaudy-Kerhoas M, Dhariwal R, Desmulliez MPY, Jouvét L. Hydrodynamic blood plasma separation in microfluidic channels. *Microfluid Nanofluidics*. 2010;8(1):105–14.
82. Gijs MAM, Lacharme F, Lehmann U. Microfluidic applications of magnetic particles for biological analysis and catalysis. *Chem Rev*. 2010;110(3):1518–63.

83. Choi JW, Oh KW, Thomas JH, Heineman WR, Halsall HB, Nevin JH, et al. An integrated microfluidic biochemical detection system for protein analysis with magnetic bead-based sampling capabilities. *Lab Chip* [Internet]. 2002;2(1):27–30. Available from: <http://xlink.rsc.org/?DOI=b107540n>
84. Lu R, Shi W, Jiang L, Qin J, Lin B. Rapid prototyping of paper-based microfluidics with wax for low-cost, portable bioassay. *Electrophoresis*. 2009;30(9):1497–500.
85. Martinez AW, Phillips ST, Wiley BJ, Gupta M, Whitesides GM. FLASH: A rapid method for prototyping paper-based microfluidic devices. *Lab Chip*. 2008;8(12):2146–50.
86. Liu H, Crooks RM. Three-dimensional paper microfluidic devices assembled using the principles of origami. *J Am Chem Soc*. 2011;133(44):17564–6.
87. Li X, Ballerini DR, Shen W. A perspective on paper-based microfluidics: Current status and future trends. *Biomicrofluidics*. 2012;6(1).
88. Jenkins G, Wang Y, Xie YL, Wu Q, Huang W, Wang L, et al. Printed electronics integrated with paper-based microfluidics: new methodologies for next-generation health care. *Microfluid Nanofluidics*. 2015;19(2):251–61.
89. Zhang AL, Zha Y. Fabrication of paper-based microfluidic device using printed circuit technology. *AIP Adv*. 2012;2(2).
90. Wang L, Li PCH. Microfluidic DNA microarray analysis: A review. *Anal Chim Acta*. 2011;687(1):12–27.
91. Liu WT, Wu JH, Li ESY, Selamat ES. Emission characteristics of fluorescent labels with respect to temperature changes and subsequent effects on DNA microchip studies. *Appl Environ Microbiol*. 2005;71(10):6453–7.
92. Sina AAI, Carrascosa LG, Liang Z, Grewal YS, Wardiana A, Shiddiky MJA, et al. Epigenetically reprogrammed methylation landscape drives the DNA self-assembly and serves as a universal cancer biomarker. *Nat Commun* [Internet]. 2018;9(1):4915. Available from: <https://www.nature.com/articles/s41467-018-07214-w>
93. Yang S, Ündar A, Zahn JD. A microfluidic device for continuous, real time blood plasma separation. *Lab Chip*. 2006;6(7):871–80.
94. Yang X, Forouzan O, Brown TP, Shevkoplyas SS. Integrated separation of blood

- plasma from whole blood for microfluidic paper-based analytical devices. *Lab Chip*. 2012;12(2):274–80.
95. Han D, Pal S, Nangreave J, Deng Z, Liu Y, Yan H. DNA origami with complex curvatures in three-dimensional space. *Science* (80-). 2011;332(6027):342–6.
 96. Voigt N V., Tørring T, Rotaru A, Jacobsen MF, Ravnsbæk JB, Subramani R, et al. Single-molecule chemical reactions on DNA origami. *Nat Nanotechnol* [Internet]. 2010;5(3):200–3. Available from: <http://dx.doi.org/10.1038/nnano.2010.5>
 97. Ding B, Deng Z, Yan H, Cabrini S, Zuckermann RN, Bokor J. Gold nanoparticle self-similar chain structure organized by DNA origami. *J Am Chem Soc* [Internet]. 2010;132(10):3248–9. Available from: <http://www.ncbi.nlm.nih.gov/pubmed/20163139>
 98. Douglas SM, Marblestone AH, Teerapittayanon S, Vazquez A, Church GM, Shih WM. Rapid prototyping of 3D DNA-origami shapes with caDNAno. *Nucleic Acids Res*. 2009;37(15):5001–6.
 99. WHO. Global Tuberculosis Report 2014. World Heal Organ [Internet]. 2014;306. Available from: http://apps.who.int/iris/bitstream/10665/91355/1/9789241564656_eng.pdf
 100. WHO. Global update on the health sector to HIV, 2014. 2014;(July):154. Available from: http://apps.who.int/iris/bitstream/10665/128494/1/9789241507585_eng.pdf?ua=1
 101. Miki Y, Swensen J, Shattuck-Eidens D, Futreal PA, Harshman K, Tavtigian S, et al. A strong candidate for the breast and ovarian cancer susceptibility gene BRCA1. *Science* (80-). 1994;266(5182):66–71.
 102. Sluis-Cremer N, Arion D, Abram ME, Parniak MA. Proteolytic processing of an HIV-1 pol polyprotein precursor: Insights into the mechanism of reverse transcriptase p66/p51 heterodimer formation. *Int J Biochem Cell Biol*. 2004;36(9):1836–47.
 103. Tang MW, Shafer RW. HIV-1 antiretroviral resistance: Scientific principles and clinical applications. *Drugs*. 2012;72(9):1–25.
 104. Glynn MT, Kinahan DJ, Ducreé J. CD4 counting technologies for HIV therapy monitoring in resource-poor settings-state-of-the-Art and emerging microtechnologies. *Lab Chip*. 2013;13(14):2731–48.

105. Maity S, Nandi S, Biswas S, Sadhukhan SK, Saha MK. Performance and diagnostic usefulness of commercially available enzyme linked immunosorbent assay and rapid kits for detection of HIV, HBV and HCV in India. *Virology*. 2012;9.
106. Bristow CC, Leon SR, Ramos LB, Vargas SK, Flores JA, Konda KA, et al. Laboratory evaluation of a dual rapid immunodiagnostic test for HIV and syphilis infection. *J Clin Microbiol*. 2015;53(1):311–3.
107. Dieye TN, Vereecken C, Diallo AA, Ondo P, Diaw PA, Camara M, et al. Absolute CD4 T-cell counting in resource-poor settings: Direct volumetric measurements versus bead-based clinical flow cytometry instruments. *J Acquir Immune Defic Syndr*. 2005;39(1):32–7.
108. Glynn MT, Kinahan DJ, Ducrée J. Rapid, low-cost and instrument-free CD4+ cell counting for HIV diagnostics in resource-poor settings. *Lab Chip [Internet]*. 2014;14(15):2844–51. Available from: <http://www.ncbi.nlm.nih.gov/pubmed/24911165>
109. Nathan AJ, Scobell A. How China sees America. *Foreign Aff*. 2012;91(5):1689–99.
110. Cole ST, Brosch R, Parkhill J, Garnier T, Churcher C, Harris D, et al. Deciphering the biology of mycobacterium tuberculosis from the complete genome sequence. *Nature*. 1998;393(6685):537–44.
111. Sekiguchi JI, Miyoshi-Akiyama T, Augustynowicz-Kopeć E, Zwolska Z, Kirikae F, Toyota E, et al. Detection of multidrug resistance in *Mycobacterium tuberculosis*. *J Clin Microbiol*. 2007;45(1):179–92.
112. Perdigão J, Macedo R, Malaquias A, Ferreira A, Brum L, Portugal I. Genetic analysis of extensively drug-resistant *Mycobacterium tuberculosis* strains in Lisbon, Portugal. *J Antimicrob Chemother*. 2009;65(2):224–7.
113. Kamerbeek J, Schouls LEO, Kolk A, Kuijper S, Bunschoten A, Molhuizen H, et al. Simultaneous Detection and Strain Differentiation of. *J Clin Microbiol*. 1997;35(4):907–14.
114. Shafer RW, Sierra MF. *Mycobacterium xenopi*, *Mycobacterium fortuitum*, *Mycobacterium kansasii*, and Other Nontuberculous *Mycobacteria* in an Area of Endemicity for AIDS. *Clin Infect Dis*. 1992;15(1):161–2.
115. Nagai H. Tuberculosis in patients with human immunodeficiency virus infection. *Japanese J Chest Dis*. 2015;74:S179–83.

116. Hill AN, Becerra JE, Castro KG. Modelling tuberculosis trends in the USA. *Epidemiol Infect.* 2012;140(10):1862–72.
117. Bryder L. “We shall not find salvation in inoculation”: BCG vaccination in Scandinavia, Britain and the USA, 1921-1960. *Soc Sci Med.* 1999;49(9):1157–67.
118. Dinnes J, Deeks J, Kunst H, Gibson A, Cummins E, Waugh N, et al. A systematic review of rapid diagnostic tests for the detection of tuberculosis infection How do I get a copy of HTA on CD? HTA Background. HTA Heal Technol Assess NHS R&D HTA Program www.hta.ac.uk Heal Technol Assess [Internet]. 2007;11(3). Available from: www.hta.ac.uk
119. DeRisi J, Penland L, Brown PO, Bittner ML, Meltzer PS, Ray M, et al. Use of a cDNA microarray to analyse gene expression patterns in human cancer. *Nat Genet.* 1996;14(4):457–60.
120. Smyth GK, Speed T. Normalization of cDNA microarray data. *Methods.* 2003;31(4):265–73.
121. Neiberghs H. Breast and ovarian cancer risks due to inherited mutations in BRCA1 and BRCA2. *Women’s Oncol Rev.* 2004;4(1):59–60.
122. Tao ZQ, Shi A, Lu C, Song T, Zhang Z, Zhao J. Breast Cancer: Epidemiology and Etiology. *Cell Biochem Biophys* [Internet]. 2015;72(2):333–8. Available from: <http://dx.doi.org/10.1007/s12013-014-0459-6>
123. Jemal A, Center MM, DeSantis C, Ward EM. Global patterns of cancer incidence and mortality rates and trends. *Cancer Epidemiol Biomarkers Prev.* 2010;19(8):1893–907.
124. Murray N, Winstanley J, Bennett A, Francis K. Diagnosis and treatment of advanced breast cancer: Summary of NICE guidance. *BMJ.* 2009;338(7695):b438.
125. Neal RD, Din NU, Hamilton W, GBRoumunne OC, Carter B, Stapley S, et al. Comparison of cancer diagnostic intervals before and after implementation of NICE guidelines: Analysis of data from the GBR General Practice Research Database. *Br J Cancer* [Internet]. 2014;110(3):584–92. Available from: <http://dx.doi.org/10.1038/bjc.2013.791>
126. The National Institute for Health and Care Excellence (NICE). Clinical Guideline Familial breast cancer: Classification and care of people at risk of familial breast cancer and management of breast cancer and related risks in people with a family

- history of breast cancer. Natl Collab Cent Cancer [Internet]. 2017;(March):1–254. Available from: <https://www.nice.org.uk/guidance/cg164/evidence/full-guideline-pdf-190130941>
127. Hess P. Surface Acoustic Waves. In: Kress W, de Wette FW, editors. Applied Physics A Materials Science & Processing [Internet]. Berlin, Heidelberg: Springer Berlin Heidelberg; 1995. p. 227. Available from: https://doi.org/10.1007/978-3-642-75785-3_2
 128. Daniel MR, Emtage PR. Acoustic radiation by interdigitated grids on LiNbO₃. *J Appl Phys*. 1972;43(12):4872–5.
 129. Kim J, Kim J, Shin Y, Yoon Y. A Study on the Fabrication of an RTD (Resistance Temperature Detector) by Using Pt Thin Film. *Korean J Chem Eng* [Internet]. 2001;18(1):61–6. Available from: <http://link.springer.com/10.1007/BF02707199>
<http://link.springer.com/article/10.1007/BF02707199>
 130. Baker B. Precision Temperature Sensing with RTD Circuits. *Appl Note, Microchip Technol* [Internet]. 1998;1–8. Available from: <http://ww1.microchip.com/downloads/en/AppNotes/00687c.pdf>
 131. Paterson DJ, Reboud J, Wilson R, Tassieri M, Cooper JM. Integrating microfluidic generation, handling and analysis of biomimetic giant unilamellar vesicles. *Lab Chip*. 2014;14(11):1806–10.
 132. Eddings MA, Johnson MA, Gale BK. Determining the optimal PDMS-PDMS bonding technique for microfluidic devices. *J Micromechanics Microengineering*. 2008;18(6).
 133. Zhou J, Ellis AV, Voelcker NH. Recent developments in PDMS surface modification for microfluidic devices. *Electrophoresis*. 2010;31(1):2–16.
 134. Fujii T. PDMS-based microfluidic devices for biomedical applications. *Microelectron Eng*. 2002;61–62:907–14.
 135. Jang MJ, Nam Y. Aqueous micro-contact printing of cell-adhesive biomolecules for patterning neuronal cell cultures. *Biochip J*. 2012;6(2):107–13.
 136. Shibuichi S, Yamamoto T, Onda T, Tsujii K. Super water- and oil-repellent surfaces resulting from fractal structure. *J Colloid Interface Sci*. 1998;208(1):287–94.

137. Durdureanu-Angheluta A, Ardeleanu R, Pinteala M, Harabagiu V, Chiriac H, Simionescu BC. Silane covered magnetite particles. Preparation and characterisation. *Dig J Nanomater Biostructures* [Internet]. 2008;3(1):33–40. Available from: <http://chalcogen.ro/Durdureanu-Pinteala.pdf>
138. Bourquin YPJ. Shaping surface waves for diagnostics. 2012;
139. Gunda NSK, Singh M, Norman L, Kaur K, Mitra SK. Optimization and characterization of biomolecule immobilization on silicon substrates using (3-aminopropyl)triethoxysilane (APTES) and glutaraldehyde linker. *Appl Surf Sci* [Internet]. 2014;305:522–30. Available from: <http://dx.doi.org/10.1016/j.apsusc.2014.03.130>
140. Kim M, Basarir F, Park J, Yoon T, Jang YH. Computational Calculation of thickness of Self-Assembled Monolayer of 3-aminopropyltriethoxysilane on Quartz (100). *Mol Simul.* 2014;(100):3–5.
141. Wei X, Kang C, Rong G, Retterer ST, Weiss SM. Porous silicon waveguide with integrated grating coupler for DNA sensing. *Front Pathog Detect From Nanosensors to Syst.* 2009;7553(February 2009):71670C.
142. Zhai J, Cui H, Yang R. DNA based biosensors. *Biotechnol Adv* [Internet]. 1997;15(1):43–58. Available from: <http://www.ncbi.nlm.nih.gov/pubmed/14539378>
143. Lawrie JL, Jiao Y, Weiss SM. Size-dependent infiltration and optical detection of nucleic acids in nanoscale pores. *IEEE Trans Nanotechnol.* 2010;9(5):596–602.
144. Lee S, Chon H, Lee J, Ko J, Chung BH, Lim DW, et al. Rapid and sensitive phenotypic marker detection on breast cancer cells using surface-enhanced Raman scattering (SERS) imaging. *Biosens Bioelectron* [Internet]. 2014;51:238–43. Available from: <http://dx.doi.org/10.1016/j.bios.2013.07.063>
145. Wu P, Hoglebe P, Grainger DW. DNA and protein microarray printing on silicon nitride waveguide surfaces. *Biosens Bioelectron.* 2006;21(7):1252–63.
146. Parak WJ, Gerion D, Zanchet D, Woerz AS, Pellegrino T, Micheel C, et al. Conjugation of DNA to silanized colloidal semiconductor nanocrystalline quantum dots. *Chem Mater.* 2002;14(5):2113–9.
147. Thermo Fisher Scientific. User guide: SMCC and Sulfo-SMCC. 2018;0747(22360). Available from: https://assets.thermofisher.com/TFS-Assets/LSG/manuals/MAN0011295_SMCC_SulfoSMCC_UG.pdf

148. Tip T. Attach an antibody onto glass, silica or quartz surface. ThermoCom [Internet]. 2015;0747(815):1–4. Available from: http://www.thermo.com/eThermo/CMA/PDFs/Articles/articlesFile_9376.pdf%5Cnpapers3://publication/uuid/0F5B8CEB-EA55-4975-B3B4-4966369A91EB
149. Dwight Z, Palais R, Wittwer CT. uMELT: Prediction of high-resolution melting curves and dynamic melting profiles of PCR products in a rich web application. *Bioinformatics*. 2011;27(7):1019–20.
150. Zipper H, Brunner H, Bernhagen J, Vitzthum F. Investigations on DNA intercalation and surface binding by SYBR Green I, its structure determination and methodological implications. *Nucleic Acids Res*. 2004;32(12).
151. Shilton RJ, Mattoli V, Travagliati M, Agostini M, Desii A, Beltram F, et al. Rapid and controllable digital microfluidic heating by surface acoustic waves. *Adv Funct Mater*. 2015;25(37):5895–901.
152. Roux-Marchand T, Beyssen D, Sarry F, Elmazria O. Rayleigh surface acoustic wave as an efficient heating system for biological reactions: Investigation of microdroplet temperature uniformity. *IEEE Trans Ultrason Ferroelectr Freq Control*. 2015;62(4):729–35.
153. Shugaev M V., Manzo AJ, Wu C, Zaitsev VY, Helvajian H, Zhigilei L V. Strong enhancement of surface diffusion by nonlinear surface acoustic waves. *Phys Rev B - Condens Matter Mater Phys* [Internet]. 2015;91(23):235450. Available from: <http://link.aps.org/doi/10.1103/PhysRevB.91.235450>
154. Seksek O, Bolard J. Nuclear pH gradient in mammalian cells revealed by laser microspectrofluorimetry. *J Cell Sci*. 1996;109(1):257–62.
155. Wixforth A. Acoustically driven planar microfluidics. *Superlattices Microstruct*. 2003;33(5–6):389–96.
156. Yeo LY, Friend JR. Ultrafast microfluidics using surface acoustic waves. *Biomicrofluidics*. 2009;3(1):1–23.
157. Williams MC, Wenner JR, Rouzina I, Bloomfield VA. Effect of pH on the overstretching transition of double-stranded DNA: Evidence of force-induced DNA melting. *Biophys J* [Internet]. 2001;80(2):874–81. Available from: [http://dx.doi.org/10.1016/S0006-3495\(01\)76066-3](http://dx.doi.org/10.1016/S0006-3495(01)76066-3)
158. Marras SAE, Kramer FR, Tyagi S. Efficiencies of fluorescence resonance energy

- transfer and contact-mediated quenching in oligonucleotide probes. *Nucleic Acids Res.* 2002;30(21):e122--e122.
159. Nazarenko I, Pires R, Lowe B, Obaidy M, Rashtchian A. Nazarenko, *NAR* 2002. 2002;30(9):7. Available from: [papers://15cdc10c-ce80-4a53-a8a2-a33202a26cc2/Paper/p642](https://pubmed.ncbi.nlm.nih.gov/11555555/)
 160. Ahsan SS, Chen H, Santiago-Berrios MB, Abruna HD, Webb WW. Quenching of Alexa Dyes by Amino Acids. *Biophys J.* 2010;98(3):583a.
 161. Panchuk-Voloshina N, Haugland RP, Bishop-Stewart J, Bhargava MK, Millard PJ, Mao F, et al. Alexa dyes, a series of new fluorescent dyes that yield exceptionally bright, photostable conjugates. *J Histochem Cytochem.* 1999;47(9):1179–88.
 162. Seidel CAM, Schulz A, Sauer MHM. Nucleobase-specific quenching of fluorescent dyes. 1. Nucleobase one-electron redox potentials and their Correlation with static and dynamic quenching efficiencies. *J Phys Chem.* 1996;100(13):5541–53.
 163. Behlke M a, Huang L, Bogh L, Rose S, Devor EJ. Fluorescence Quenching by Proximal G-bases. *Integr DNA Technol.* 2005;2–4.
 164. Wilson JN, Yin NT, Kool ET. Efficient quenching of oligomeric fluorophores on a DNA backbone. *J Am Chem Soc [Internet].* 2007 Dec 1;129(50):15426–7. Available from: <https://doi.org/10.1021/ja075968a>
 165. Imhof A, Megens M, Engelberts JJ, De Lang DTN, Sprik R, Vos WL. Spectroscopy of fluorescein (FITC) dyed colloidal silica spheres. *J Phys Chem B.* 1999;103(9):1408–15.
 166. Kiraz A, Doğanay S, Kurt A, Demirel AL. Enhanced energy transfer in single glycerol/water microdroplets standing on a superhydrophobic surface. *Chem Phys Lett.* 2007;444(1–3):181–5.
 167. Teles FRR, Fonseca LP. Trends in DNA biosensors. *Talanta [Internet].* 2008 Dec 15 [cited 2014 Sep 13];77(2):606–23. Available from: <http://linkinghub.elsevier.com/retrieve/pii/S0039914008005493>
 168. Foudeh AM, Fatanat Didar T, Veres T, Tabrizian M. Microfluidic designs and techniques using lab-on-a-chip devices for pathogen detection for point-of-care diagnostics. *Lab Chip.* 2012;12(18):3249–66.
 169. Destgeer G, Im S, Hang Ha B, Ho Jung J, Ahmad Ansari M, Jin Sung H.

Adjustable, rapidly switching microfluidic gradient generation using focused travelling surface acoustic waves. *Appl Phys Lett*. 2014;104(2):10–5.

170. Morandi A, Limousin M, Sayers J, Golwala SR, Czakon NG, Pierpaoli E, et al. X-ray, lensing and Sunyaev-Zel'dovich triaxial analysis of Abell 1835 out to R 200. *Mon Not R Astron Soc*. 2012;425(3):2069–82.
171. Lachance M, Daniel H, Meyer W, Prasad G, Gautam S, Boundymills K, et al. In vivo antiviral activity , protease inhibition and brine shrimp lethality of selected Tanzanian wild edible mushrooms. *J Appl Microbiol [Internet]*. 2012;2(1):1887–94. Available from:
<http://www.pubmedcentral.nih.gov/articlerender.fcgi?artid=91944&tool=pmcentrez&rendertype=abstract%5Cnhttp://www.pubmedcentral.nih.gov/articlerender.fcgi?artid=1594683&tool=pmcentrez&rendertype=abstract%5Cnhttp://www.ncbi.nlm.nih.gov/pubmed/18435743%5Cnht>
172. Stanton MM, Trichet-Paredes C, Sánchez S. Applications of three-dimensional (3D) printing for microswimmers and bio-hybrid robotics. *Lab Chip [Internet]*. 2015;15(7):1634–7. Available from: <http://dx.doi.org/10.1039/C5LC90019K>